TAMPEREEN TEKNILLINEN YLIOPISTO
TAMPERE UNIVERSITY OF TECHNOLOGY

Minna Kotilainen

Temperature-Induced Ageing Mechanisms and Long-Term Stability of Solar Thermal Absorber Coatings

Julkaisu 1222 • Publication 1222

Tampere 2014

Tampereen teknillinen yliopisto. Julkaisu 1222
Tampere University of Technology. Publication 1222

Minna Kotilainen

Temperature-Induced Ageing Mechanisms and Long-Term Stability of Solar Thermal Absorber Coatings

Thesis for the degree of Doctor of Science in Technology to be presented with due permission for public examination and criticism in Konetalo Building, Auditorium K1702, at Tampere University of Technology, on the 15th of August 2014, at 12 noon.

Tampereen teknillinen yliopisto - Tampere University of Technology
Tampere 2014

Doctoral candidate: Minna Kotilainen
Department of Materials Science
Tampere University of Technology. Finland

Supervisor: Professor Petri Vuoristo
Department of Materials Science
Tampere University of Technology. Finland

Pre-examiners: Associate Professor Luís Rebouta
Physics Department
University of Minho, Portugal

Professor Gunnar A. Niklasson
Department of Engineering Sciences, Solid State Physics,
Uppsala University, Sweden

Opponents: Associate Professor Luís Rebouta
Physics Department
University of Minho, Portugal

Professor Jari Koskinen
Physical Characteristics of Surfaces and Interfaces
Aalto University

ISBN 978-952-15-3313-6 (printed)
ISBN 978-952-15-3329-7 (PDF)
ISSN 1459-2045

ABSTRACT

The ageing mechanisms and long-term stability of different solar thermal absorber coatings were investigated at elevated temperatures of 200-500 °C. The absorbers were aged by means of thermal accelerated ageing studies and short-period heat treatments up to 500 °C for two hours.

The solar absorbers studied were various sputtered, evaporated, and electroplated industrial absorber surfaces on copper, nickel-coated copper, aluminium, anodized aluminium, and stainless steel substrates. The absorber coatings were based on chromium oxide, chromium oxy-nitride, titanium oxy-nitride, or titanium aluminium silicon oxy-nitride coating layers. The anti-reflection coatings were tin oxide or silicon oxide. The self-deposited, experimental absorber coatings were magnetron sputtered chromium oxide based or titanium aluminium silicon oxy-nitride coatings on copper with tantalum nitride or aluminium diffusion barriers between the substrate and the absorber coating.

The ageing mechanisms and degradation of the absorbers were analysed by optical measurements (solar absorptance with a UV/Vis/NIR spectrophotometer and thermal emittance by FTIR spectrophotometry), microstructural analysis using a field-emission scanning electron microscope (FESEM) equipped with an energy dispersive X-ray spectrometer (EDS) and transmission electron microscope (TEM) with selected area electron diffraction (SAED), and composition by time-of-flight elastic recoil detection analysis (TOF-ERDA) before and after the ageing studies.

The results clearly demonstrated the effect of the coating microstructure on the long-term stability of the absorber at elevated temperatures. Absorbers can suffer from an increase in the oxygen/metal ratio in the absorber coatings, diffusion of copper substrate atoms into the coating or through the coating to the surface, formation of copper oxide islands on the surface of the coating, formation of voids in the substrate surface, and chemical and structural changes in the coating or substrate during thermal ageing. The relation between optical degradation and ageing mechanisms was studied using optical modelling and simulation with CODE Coating Designer. The microstructure of the absorber coatings had a significant effect on stability at elevated temperatures. The dense sputtered chromium oxy-nitride coating on copper was clearly more stable than a similar coating material with large columns and open porosity between the columns.

PREFACE

This work was carried out during the years 2008-2013 at the Department of Materials Science, Tampere University of Technology (TUT). I wish to express my deep gratitude to my supervisor, Prof. Petri Vuoristo for his continuous encouragement and valuable advice. My sincere thanks go to my instructor, Dr. Petri Konttinen, for our long discussions and his valuable guidance during this work.

The research was funded by the Finnish Funding Agency for Technology and Innovation (TEKES) in the Functional Materials programme, in an industrial project "DiAd" of Aurubis Finland Oy (formerly Luvata Pori Oy), and the Graduate School for Advanced Materials and Processes (AMP). Jenny and Antti Wihuri Foundation, Emil Aaltonen Foundation, Aimo Puromäki Foundation by the Economic Sciences and Technology Foundation KAUTE, Walter Ahlström Foundation, Finnish Foundation for Technology Promotion, and Science Foundation of City of Tampere are gratefully acknowledged for their financial support.

My special thanks go to Dr. Mari Honkanen for the TEM evaluations and advice concerning the FESEM evaluations. For the TOF-ERDA analysis, I owe thanks to Dr. Kenichiro Mizohata from the University of Helsinki, for the XPS studies to Dr. Petri Jussila and Prof. Mika Valden, for the SAED patterns to Essi Sarlin, M.Sc., for the XRD studies to Leo Hyvärinen, M.Sc., and for the good advice concerning grazing incidence XRD to Lars Grieger, M.Res. For the help in optical modelling and simulations, I would like to thank Dr. Wolfgang Theiss, associated Prof. Tapio Niemi, Prof. Martti Kauranen and Dr. Turkka Salminen. I am grateful to Mikko Hahtala, M.Sc., for the preliminary experimental sputtering. I also want to thank the research assistants who have assisted me during this work. I wish to thank all of my past and present co-workers in the Surface Engineering Group and in the Department of Materials Science. I am especially grateful to Mr. Mikko Kylmälahti for assembling the vacuum deposition system and modifications to the circulating air furnace, Kirsi Lahtinen, M.Sc., for purchasing and testing the furnace, Jarmo Laakso, M.Sc., for proofreading the thesis, and Dr. Heli Koivuluoto for our discussions and her advice. I think Prof. Olof Forsén was right when he compared my thesis to a symphony orchestra where I would be the conductor directing a major concert. Many thanks to all my collaborators!

I also would like to thank the manufacturers of the industrial absorbers studied in this thesis for their cooperation. I have had valuable discussions with key persons in these companies. The fact that the companies found this study to be important was a driving force and encouraged me to study ageing behaviour in depth.

For their endless support, I wish to thank my parents Annu and Reijo, and also my parents-in-law Sinikka and Erkki. I wouldn’t have achieved this without my dear friends who have given me memorable moments to counterbalance the intensive work. My horses and cats have kept me sane! Finally, my warmest thanks go to my beloved husband Arttu and to my little son Ahti.

Kangasala, May 2014

Minna Kotilainen

TABLE OF CONTENTS

AUTHOR'S CONTRIBUTION

Minna Kotilainen is the main researcher and writer of this thesis. She planned and organized all the experiments, performed the ageing studies, carried out most of the characterizations, and analysed the results. Dr. Mari Honkanen and Essi Sarlin, M.Sc., performed the TEM studies, Dr. Kenichiro Mizohata the TOF-ERDA studies, Dr. Petri Jussila and Prof. Mika Valden the XPS studies, and Leo Hyvärinen, M.Sc., the XRD studies. Optical modelling was planned and performed together with Dr. Wolfgang Theiss. The experimental sputtered absorbers and diffusion barriers Ms. Kotilainen deposited together with Mikko Hahtala, M.Sc. Prof. Petri Vuoristo and Dr. Petri Konttinen gave advice on the experimental parts and commented on the manuscript.

LIST OF SYMBOLS AND ABBREVIATIONS

ɑ	Solar absorptance [-]
Δ	Change in variant [-]
Ɛ	Thermal emittance [-]
ʎ	Wavelength [µm or nm]
ρ	Reflectance [-]
τ	Transmittance [-]
ø	Diameter [mm]
a_n	Arrhenius accelerator factor [-]
e_A	Dielectric permeability of medium A [F m^{-1}]
e_B	Dielectric permeability of medium B [F m^{-1}]
e_{eff}	Dielectric permeability of effective medium [F m^{-1}]
E_T	Arrhenius' activation energy [J mol^{-1})
f	Volume fraction [-]
G(ʎ)	Solar spectral irradiance for air mass 1.5 [W m^{-2} K^{-1}]
k	Extinction coefficient [-]
n	Refractive index [-]
PC	Performance criterion function [-]
R	Ideal gas constant [R = 8.314 J K^{-1} mol^{-1}]
RMS	R_q, root mean square roughness, parameter for amplitude [µm]
T	Temperature [°C or K]
T_{eff}	Effective mean service temperature [°C or K]
T_m	Melting temperature [°C or K]
t	Time [h]

Ag	Silver
AISI 304L	Stainless steel type EN 1.4307, CrNi stainless steel
AISI 321	Stainless steel type EN 1.4541, CrNiTi stainless steel
Al	Aluminium
AlCuFe	Aluminium copper iron
AlN	Aluminium nitride
AlN_x	Aluminium nitride (sub-stoichiometric)
AlON	Aluminium oxy-nitride
Al_xO_y	Aluminium oxide (sub-stoichiometric)
Al_2O_3	Aluminium oxide, alumina
α-Al_2O_3	Alpha alumina phase
γ-Al_2O_3	Gamma alumina phase
AM	Air mass

AR	Anti-reflection
ARE	Activated reactive evaporation
At.%	Atomic percent
Au	Gold
a-Si:C:H	Amorphous and hydrogenated silicon
C	Carbon
Cr	Chromium
CrAlON	Chromium aluminium oxy-nitride
CrMoN	Chromium molybdenum nitride
CrN	Chromium nitride
CrO_xN_y	Chromium oxy-nitride
Cr_2O_3	Chromium oxide, chromia
Cu	Copper
CuO	Cupric oxide, copper oxide
CVD	Chemical vapour deposition
CSP	Concentrated solar power
DC	Direct current
DHV	Domestic hot water
e-beam	Electron beam
EDS	Energy dispersive spectroscopy
e.g.	exempli gratia
et al.	et alia
eV	electron volt
FESEM	Field-emission scanning electron microscope
FTIR	Fourier transform infrared spectroscopy
Ge	Germanium
h	hour
HfO_2	Hafnium oxide
HfC	Hafnium carbide
HfMoN	Hafnium molybdenum nitride
$HfMo_2O_8$	Hafnium molybdenum oxide
HfON	Hafnium oxy-nitride
HfO_x	Hafnium oxide (sub-stoichiometric)
HMVF	High metal volume fracture
HSS	High speed steel
H_2O_2	Hydrogen peroxide
IEA-SHCP	International Energy Agency - Solar Heating and Cooling Programme
i.e.	id est
ISO	International Organisation for Standardisation

IR	Infrared
LMVF	Low metal volume fracture
ln	Natural logarithm, $\log_e$
Ltd.	Limited liable company
MgO	Magnesium oxide
Mn	Manganese
Mo	Molybdenum
MoO_2	Molybdenum oxide
MoO_3	Molybdenum oxide
MSTC	IEA-SHCP Working Group “Materials in Solar Thermal Collectors”
N	Nitrogen
Nb	Niobium
NbAlN	Niobium aluminium nitride
NbAlON	Niobium aluminium oxy-nitride
NbTiON	Niobium titanium oxy-nitride
N_2	Nitrogen in its molecular form, nitrogen gas
NH_4	Ammonium
Ni	Nickel
NiO	Nickel oxide
NIR	Near infrared absorption spectroscopy
NREL	National Renewable Energy Laboratory in the USA
N/A	Not applicable
O	Oxygen
O_2	Oxygen in its molecular form, oxygen gas
P	Phosphorus
PbS	Lead sulphide
PE	Polyethylene
PECVD	Plasma-enhanced chemical vapour deposition
PP	Polypropylene
Pt	Platinum
PVD	Physical vapour deposition
RBS	Rutherford back scattering spectroscope
RF	Radio frequency
Ru	Ruthenium
S	Sulphur
sccm	Standard cubic centimetres per minute
SE	Secondary electrons
SF_6	Sulphur hexafluoride
Si	Silicon
SiO_2	Silicon dioxide, silica

SiON	Silicon oxy-nitride
Si_3N_4	Silicon nitride
Sn	Tin
SnO_x	Tin oxide
SPF	Institut für Solartechnik, solar technology institute in Switzerland
SS	Stainless steel
Ta	Tantalum
TaN	Tantalum nitride
TEM	Transmission electron microscope
Ti	Titanium
TiAl	Titanium aluminide
TiAlN	Titanium aluminium nitride
TiAlO	Titanium aluminium oxide
TiAlON	Titanium aluminium oxy-nitride
TiC	Titanium carbide
TiN_x	Titanium nitride (sub-stoichiometric)
TiN	Titanium nitride
TiO_xN_y	Titanium oxy-nitride
TOF-ERDA	Time-of-flight elastic recoil detection analysis
TUT	Tampere University of Technology
UHV	Ultra-high vacuum
UK	United Kingdom
USA	United States of America
UV	Ultraviolet absorption spectroscopy
U.S.	United States
Vis	Visible absorption spectroscopy
vol.%	Volume percentage
W	Tungsten
XPS	X-ray photoelectron spectroscope
XRD	X-ray diffraction
Zn	Zinc
ZnS	Zinc sulphide
ZrB_2	Zirconium diboride
ZrN_x	Zirconium nitride
ZrC_y	Zirconium carbide (sub-stoichiometric)
ZrC_xN_y	Zirconium carbonitride
ZrO_x	Zirconium oxide (sub-stoichiometric)
ZrO_xN_y	Zirconium oxy-nitride

1 INTRODUCTION

Solar thermal flat plate collectors are the most common solar collectors in Europe [1]. These kind of solar collectors are conventionally used for domestic hot water and space heating applications. A typical absorber surface of a flat plate collector consists of a substrate, absorber coating layers on the substrate and a possible anti-reflection coating. Substrate materials are typically copper or aluminium. Absorber coatings are usually made by sputtering, evaporation or electrochemically, or they can be sprayed or spread as a paint. At present, selective paints, electrochemically deposited black chromium coatings, sputtered or evaporated chromium oxy-nitride, titanium oxy-nitride or nickel/nickel oxide coatings with anti-reflection coating are common absorber surfaces.

Until the 1990s, the most common absorber coatings in flat plate collectors were electroplated black chromium coatings. The black chromium coatings consist of a Cr-Cr_2O_3 cermet absorber coating usually on copper and there could also be a thick nickel intermediate layer between the substrate and the absorber coating. The electrochemical deposition process from hexavalent chromium produces toxic and carcinogenic liquid waste. The optical properties of black chromium absorbers are suitable and production costs are low, so it is still used in flat plate collectors. [2-6] Nowadays, the black chromium coatings made from trivalent ions have also been investigated and the process is considered to be a promising and more environmentally acceptable replacement technology for hexavalent chromium plating [4, 7-9].

As a result of these environmental issues, physical vapour deposited (PVD) absorber coatings have been developed since the 1990s. Nowadays, magnetron sputtering is a widely used PVD deposition process for absorber coatings. Magnetron sputtering is suitable for large-area deposition of thin films and it has a relatively high deposition rate. This technique is used to deposit absorber coatings that produce less pollution than conventional electrochemical methods. In the last few years, magnetron sputtered chromium oxide or chromium oxy-nitride coatings have increased their market share significantly [10-17].

The first solar thermal collectors in the 1960s had a relatively low stagnation temperature [10]. The stagnation temperature means the highest temperature the coating could experience if the liquid circulation of the collector were turned off on a sunny day. Since the first collectors, new solar absorber coatings have been developed and used in advanced collector designs with improved efficiency.

There has also been active development of absorber surfaces. The progress of deposition processes and introduction of the PVD coating methods have improved the optical properties of the coatings. Nowadays, solar absorptance is about 0.95 and thermal emittance 0.04-0.05 in the most common high-quality commercial absorbers. Thanks to these innovations, the operating temperature and stagnation temperature have been increased. In particular, the highly selective new coatings have to withstand these stronger loads. With these kinds of PVD coatings, the modelled stagnation temperature is 200-215 °C. For conventional black chromium coatings (α = 0.95 and ε = 0.10-0.20), the modelled stagnation temperature would be 180-200 °C. [18] In the near future, operating temperatures of solar thermal applications of 80-250 °C have been predicted [1].

Further development of the collectors and new solar applications, like solar cooling and industrial process heating, continues to raise the operating temperatures of the absorbers. For example, food, wine and beverages, transport equipment, machinery, textiles and the pulp and paper industries need low and medium temperatures (< 250 °C), and the metal, mining, and chemical industries utilize high (> 250 °C) processing temperatures. These sectors have considered utilizing solar energy for process heating. [19, 20] There exist plenty of commercial solar thermal collectors for low temperatures (operating temperatures < 100 °C) and for high temperatures (> 250 °C, mainly used for electricity generation). Demands are now directed to the development of mid-temperature collectors, which can meet the requirements of most industrial processes. [20] One critical part of the development is impart stability to the absorber surface at elevated temperatures.

A procedure for accelerated life testing of solar absorber surfaces was developed within the framework of the MSTC working group (Materials in Solar Thermal Collectors) of the IEA-SHCP (International Energy Agency – Solar Heating and Cooling Programme). The procedure was formulated as a standard, and submitted to ISO at the beginning of 1997 as draft proposal ISO/CD 12592 Solar Energy - Materials for flat plate collectors - Qualification test procedures for solar surface durability [21]. It described in detail a procedure for the testing of the long-term stability of solar absorber coatings used in flat plate collectors. The minimum service lifetime for the absorber was estimated to be 25 years. Possible degradation was caused by the thermal load, condensation and high humidity, and air pollutants (sulphur dioxide). In a further project of the MSTC IEA-SHCP working group, Task X [22], and, in 2000, Brunold *et al.* [23] published the case studies of accelerated ageing testing of absorbers and differences in results at different independent testing laboratories. With the co-operation of the testing laboratories and several specialists, consensus was reached, and thus Köhl *et al.* [18] updated the high temperature testing procedure in 2004. The update of the accelerated temperature test conditions became necessary because of the improvements in the efficiency of solar absorber coatings. The new procedure depends explicitly on the optical performance of the absorber coatings. [18] A new standard draft ISO EN 12975-3-1 Thermal solar systems and components – Solar collectors, Part 3-1: Qualification of solar absorber surface durability [24] was published in 2011. According to [24], the accelerated ageing test is performed in a circulating air furnace at two different temperatures near the stagnation temperature of the coating. The maximum testing time is 600 hours. The ageing and degradation of absorber surfaces become significant at temperatures higher than about 300 °C. New investigations for developing accelerated ageing test procedures for solar thermal collectors in extreme climate conditions are in progress [25].

Generally, copper is used as the substrate for solar selective absorbers because copper has high thermal conductivity and high infrared (IR) reflectance. However, at temperatures greater than 300 °C, copper has been reported to diffuse into the absorber coating, creating degradation of the solar selective properties. [26] Solid state diffusion can be divided into bulk diffusion and grain boundary diffusion. Bulk diffusion is normally predominant in metals close to melting point. At lower temperatures with respect to the melting point, grain boundary diffusion is the significant mechanism. Diffusion of substrate material into the absorber coating can be prevented with a diffusion barrier layer having high thermal stability and good optical properties. The role of the diffusion barrier or denser coating structure is to slow down diffusion reactions, which may cause deterioration of the optical properties and adhesion. In microelectronic devices, diffusion of copper has been reported above 200 °C. Transition metal nitrides like TiAlN have been used as diffusion barriers for copper metallization in micro-electronic devices and packaging applications [27].

Degradation processes in solar absorbers have been reported to be caused by high temperature, high humidity, condensation of water, and/or sulphur dioxide as an airborne pollutant [22]. In the case of humidity, corrosion mechanisms in absorber coatings on aluminium substrates have been reported [28]. Between 2007-2011, the Institut für Solartechnik (SPF) tested 9 absorbers on aluminium substrate, where 4 of them passed and 5 failed, and 9 absorbers on copper substrate, where 7 passed and 2 failed. The failures were said to be caused by the condensation test. Therefore, moisture tests are of significant importance especially for aluminium substrates. It is likely that some of the studied absorbers here can degrade by moisture as in study [28]. All of these processes influence overall degradation, and this should be taken into account when evaluating absorber durability. This study is restricted to temperature-dependent ageing alone, and for future applications other ageing mechanisms should be studied as well.

2 AIM OF THE STUDY

This study is related to the materials science of thin solar absorber coatings. The aim of the thesis is to explain and deepen the knowledge of the thermal ageing mechanisms of solar absorbers. The scientific novelty of the thesis is the extensive study of microstructural and compositional changes and influences behind temperature-induced ageing phenomena. There is no such extensive study of thermal ageing of solar absorbers in the open literature. The study also includes investigations of the behaviour of diffusion barriers on copper substrate at elevated temperatures of 200-500 °C. Another target was to investigate and improve the stability of solar absorbers at elevated temperatures in advanced collectors where the operating temperature has been increased, and to provide a base for temperature-induced ageing phenomena investigations for future solar applications, like solar cooling and industrial process heat. This study is mainly focused on absorbers of advanced flat plate collectors at elevated temperatures.

The research questions were 1) what really happens in temperature-induced ageing phenomena in solar absorbers? 2) what effects are there on the thermal ageing rate? and 3) how to prevent ageing at elevated temperatures? Thermal ageing was investigated by means of accelerated ageing studies near the stagnation temperature and short-period heat treatments of up to 500 °C. The accelerated ageing procedure for solar absorbers is widely accepted and used for estimating the service lifetime of solar absorbers. However, in this study it was modified to investigate ageing phenomena: in prolonged periods and with additional exposures at higher temperatures. Service lifetime was defined according to the procedure for estimating the significance of ageing mechanisms. The ageing phenomena involved in solar absorbers was studied by techniques used in materials science research, particularly by microstructural, compositional and optical analysing techniques. Optical modelling and simulation was used to study the relation between optical degradation and ageing mechanisms. A summary of the research work is presented in Figure 1.

The literature review of this thesis presents solar thermal collectors and spectrally selective absorbers. The function and absorber coatings of flat plate collectors are introduced in section 3. Solar absorbers at elevated temperatures (> 250 °C) are discussed in section 4 considering the stability of absorber coatings and substrates.

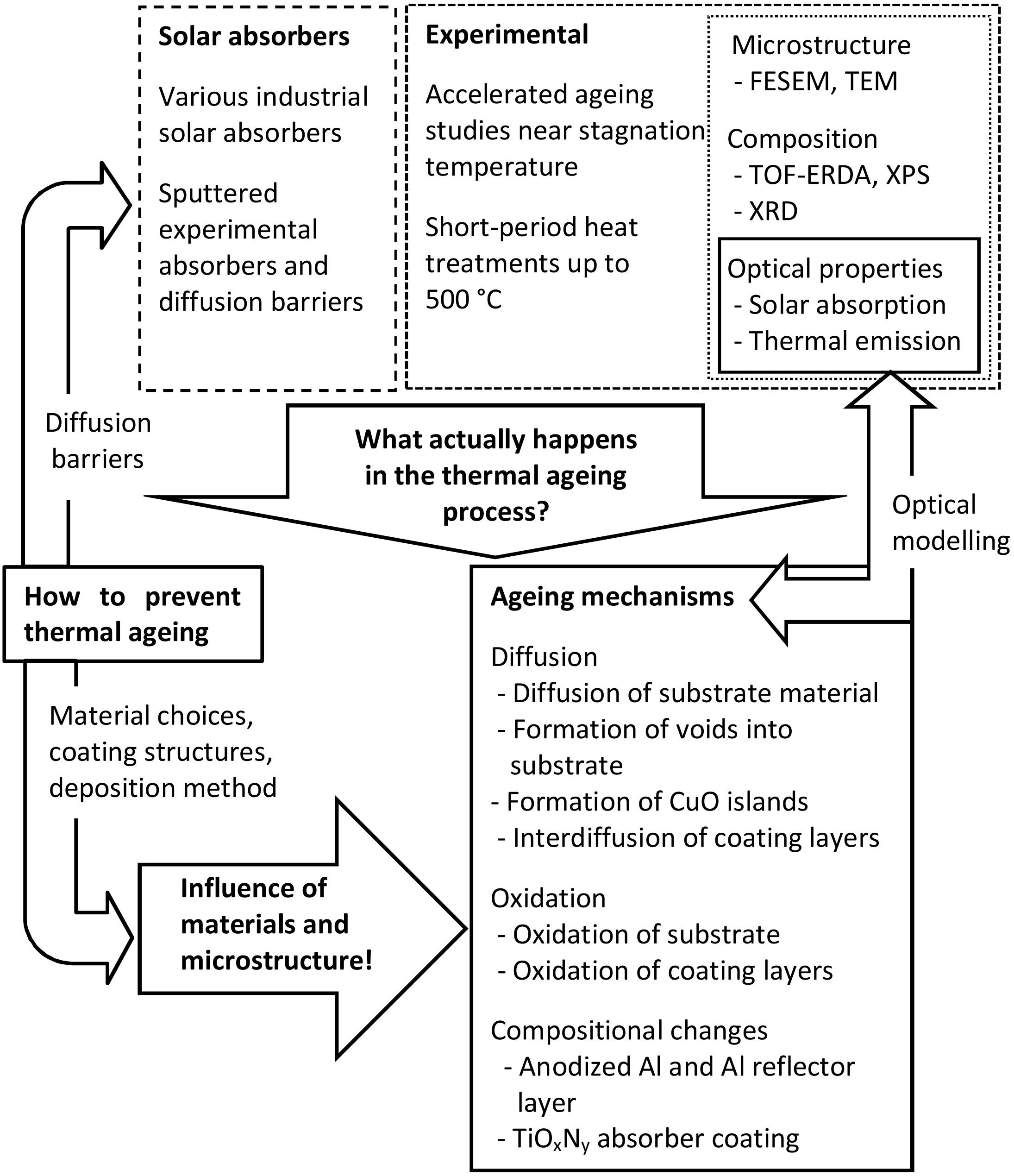

Figure 1. A summary of the research work.

3 SOLAR THERMAL COLLECTORS

Solar thermal collectors utilize sun radiation to produce heat. The absorber surface of a solar thermal collector is usually a spectrally selective absorber, as presented in this section.

3.1 Solar radiation and thermal energy

The sun is a continuous fusion reactor with a diameter of $1.4 \cdot 10^9$ m, and situated about $1.5 \cdot 10^{11}$ m from the Earth. [29] The yearly amount of solar energy incidents on the Earth's surface is about $1.5 \cdot 10^{18}$ kWh, which is approximately 10 000 times the current annual energy consumption in the world. [30]

The solar radiation incident at the surface of the Earth, after atmospheric absorption, is limited to the range between 0.3 and 3 µm, i.e. ultraviolet-visible-near infrared (UV/Vis/NIR) wavelengths. Figure 2 shows the hemispherical solar irradiance that reaches the surface of the Earth after passing through the atmosphere during clear sky conditions. This is adapted from the International Organization for Standardization (ISO) for air mass 1.5 (AM1.5), i.e. when the sun is about 42° above the horizon [31]. The spectrum consists of direct and diffuse radiation and both fluxes contribute to heating up flat plate solar collectors.

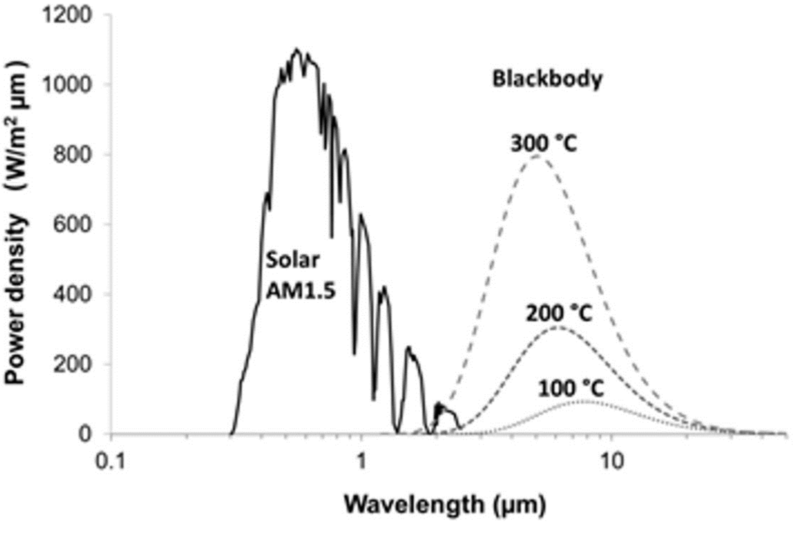

Figure 2. Solar AM1.5 spectrum and thermal spectrum of a blackbody at 100 °C, 200 °C and 300 °C.

All objects above absolute zero temperature emit thermal radiation. The wavelength and the intensity of the emitted radiation depend on the optical properties and the temperature of the body. [29] In theory, an ideal surface is a blackbody, which absorbs all the radiation from the entire wavelength range of the incident radiation and emits the maximum amount of energy according to Planck's law [32]. The dashed curves in Figure 2 indicate blackbody spectra at three temperatures. The optical properties of a real body can be characterised by its thermal emittance compared to the ideal blackbody in the infrared wavelength range. Thermal emittance is defined as a fraction of radiant energy emitted by the heated surface as compared with the radiation energy emitted by the blackbody at the same temperature and wavelength. For solar thermal applications, the most important radiation wavelength ranges are incident solar radiation from 0.3 to 2.5 µm covering UV-Vis-NIR and emitted thermal radiation from 2.5 to 50 µm. A rising blackbody temperature increases the amount of thermal energy emitted by the blackbody and shifts the location of the peak towards shorter wavelengths according to Wien's displacement law [29]. The thermal energy emitted by the blackbody is negligible for temperatures below 100 °C but at higher temperatures energy losses are unavoidable. Thermal losses from heated absorbers are due to conduction, convection and radiation [29].

Solar collectors must have at the same time high absorptance (low reflectance) for radiation in the short-wavelength solar energy spectrum, and low long-wavelength emittance (high reflectance) of the absorber to reduce heat losses. This is called a selective surface, as illustrated in Figure 3. An ideal reflectance spectrum for a spectrally selective surface is zero in the solar wavelength range and unity in the thermal infrared range and a sudden change between them. The wavelength from low to high reflectance is about 3 µm for temperatures below 100 °C and for higher temperatures (~300 °C) around 2 µm (see Figure 2). An efficient solar selective coating needs to have a high absorptance over the solar wavelength range and a low emittance to reduce thermal radiative heat losses. A material with high reflectance in the long-wavelength range is called an infrared (IR) reflector. In solar collectors, the purpose of the IR reflector is to send any unabsorbed radiation back into the absorption layer.

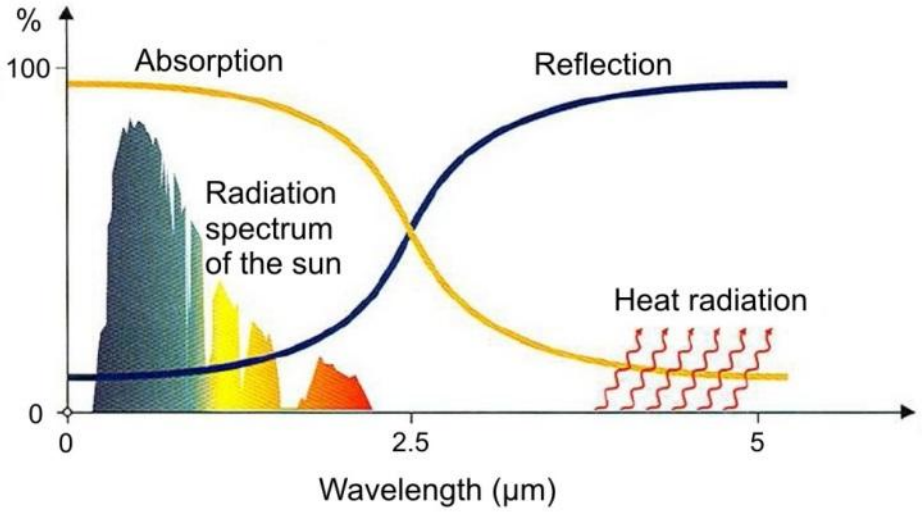

Figure 3. Absorption and reflectance in the wavelength of solar and thermal radiation in the solar thermal absorber. [33]

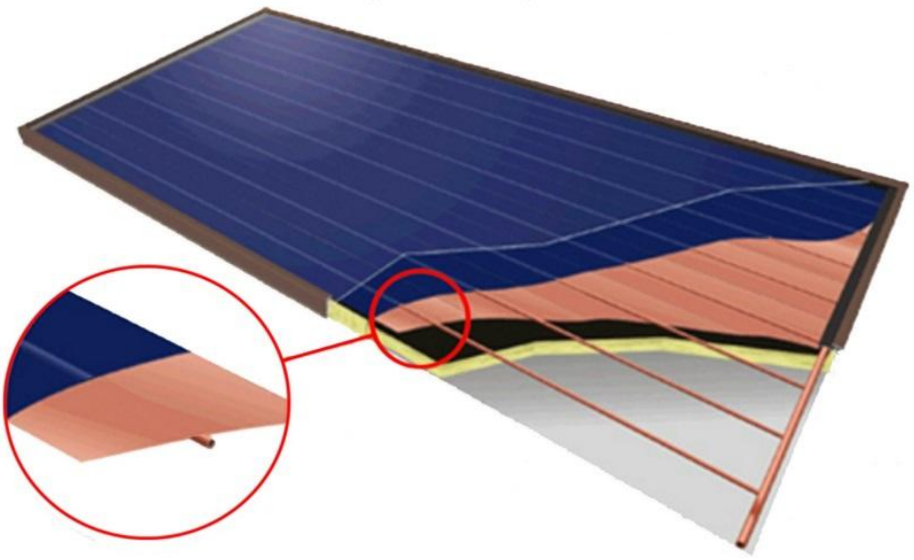

Figure 4. A flat plate collector. From top to bottom: transparent glazing, absorber coating, metal substrate, fluid tubes, insulation and collector frame. The absorber coating and the substrate together could be called an absorber plate. The fluid tubes behind the absorber plate are connected at both ends to large diameter header tubes.

3.2 Function of flat plate solar collectors

Solar thermal flat plate collectors are commonly used in Europe [1]. A typical flat plate solar collector is shown in Figure 4. Solar radiation hits an absorber surface after passing through a transparent cover. A large portion of this energy is absorbed by the absorption plate and then transferred to the transport fluid to be carried away along tubes for use or storage. The underside of the absorber plate is well insulated to reduce heat losses by conduction. The fluid tubes can be connected to the absorbing plate for example by ultrasonic welding or laser welding or they can be integrated to the plate structure [34]. The transparent cover is used to reduce heat losses by convection from the absorber plate. The cover also reduces heat losses by radiation from the collector, as glass is transparent to short-wave solar radiation, but nearly opaque to long-wave thermal radiation emitted by the absorber plate. [10]

The absorber surface absorbs as much of the solar irradiation as possible through the glazing, while losing as little heat as possible upwards to the atmosphere and downwards through the back of the collector frame. The absorber plate transfers the heat gained to the transport fluid in the tubes behind the plate. The absorptance of the absorber plate for short-wave solar radiation depends on the nature of the absorber coating. With suitable coatings on metal substrates, surfaces can be produced with high values of solar radiation absorptance and low values of thermal long-wave emittance. Typical selective surfaces consist of a thin absorber coating, which is highly absorbent to short-wave solar radiation but relatively transparent to long-wave thermal radiation. The absorber coating is deposited on a surface that has high reflectance and low emittance for long-wave radiation, i.e. the IR reflector. Selective surfaces are particularly important when the collector surface temperature is much higher than the ambient air temperature. [10] Different kinds of absorber coatings are presented in section 3.3.

The most common materials used for substrates in flat plate collectors are copper (Cu) and aluminium (Al). They both have high thermal conductivity and they act as good IR reflectors. The thermal conductivity for copper is 388 W/(m °C) at 225 °C and for aluminium 237 W/(m °C) [35], whereas it is about 20 W/(m °C) at the same temperature for chromium nickel stainless steel [36]. Nowadays, in Europe aluminium and copper substrates in flat plate collectors account for about 75 % Al and 25 % Cu, according to personal discussions during the InterSolar Europe 2013 exhibition with several absorber manufacturers and collector suppliers. A small part of the substrates is mild steel or stainless steel. Non-metallic all-polymeric collectors have been studied recently [37]. All-polymeric UV-resistant plastic extrusions are used for low temperature applications. [10] Currently, plastics such as polyethylene (PE) and polypropylene (PP) are mainly used for swimming pool absorbers [37-41].

3.2.1 Evacuated and noble gas filled flat plate collectors

Improving the stability of flat plate solar absorbers at higher temperatures may be the evacuation of the flat plate collector or filling the collector with noble gas. The oxygen in air oxidizes absorbers, thus reducing selectivity and lifetime. In comparison to evacuated tube collectors, benefits are expected concerning cost, reliability and building integration.

Evacuated collectors have been investigated because of their low thermal losses and the absence of humidity and condensation. Eaton and Blum [42] started the investigation of moderate flat plate collectors in 1975. In their studies, collectors were evacuated to pressures of approximately 10^2-10^4 Pa. [42] Benz *et al*. studied noble gases such as argon, krypton, xenon and sulphur hexafluoride (SF_6) for flat plate collectors for process heat and steam production, and solar cooling applications. Pressures were in the range of 10^3-10^4 Pa. The operating temperatures ranged between 100-150 °C. [43, 44]

Vestlund *et al*. [45, 46] studied sealed, gas-filled flat plate collectors theoretically and with some experiments. Argon, krypton and xenon gases were investigated. In these studies only the reduction in ageing due to the absence of humidity and dust [45, 46] were reported but the absence of oxygen was not considered.

BBT Thermotechnik GmbH, Buderus (Germany) markets the sealed, argon-filled flat plate collector Logasol SKS 4.0. The absorber consists of a PVD coating on a copper substrate. Solar absorptance is 0.95 ± 0.02 and thermal emittance 0.05 ± 0.02 at 100 °C. There is a gap between the cover glass and the absorber plate filled with an inert argon gas. The inert gas reduces heat transfer between the absorber plate and the cover glass by inhibiting convective heat loss. The sealed design protects the absorber coating from environmental influences such as moisture, dust and pollutants. This gives the collector a longer service life and consistently higher output. The stagnation temperature of the collector is reported to be 204 °C, and the maximum operating temperature 120 °C. [47] The effect of the argon gas atmosphere on the high temperature stability of the absorber has not been reported.

SRB Energy (Spain) together with CERN (Switzerland) has invented an evacuated flat plate collector in which the vacuum is maintained by a getter pump at the ultra-high vacuum (UHV) level of 10^{-6} Pa. The getter pump absorbs gases inside the collector, and holds the vacuum for more than 20 years, according to the manufacturer. An electroplated black chromium coating on a copper substrate has been used as an absorber. The stagnation temperature of the collector is reported to be 320 °C. Solar absorptance is > 0.90 and thermal emittance < 0.07 at 300 °C. The collector was designed for industrial process heating, district heating, solar field hybridization with biomass or fossil fuels for electricity production, and solar cooling applications. The SRB Energy evacuated collector can be equipped with concentrators of cylindrical mirrors to increase the operating temperature (Figure 5). [48] This kind of development regarding flat plate collectors can be expected to grow and increase operating temperatures. SRB Energy's evacuated collector with concentrating system was presented at the InterSolar Europe exhibition in Munich, Germany in June 2011.

Figure 5. An advanced evacuated flat plate collector with concentrating mirrors. [48]

TPV Solar (Switzerland) presented an evacuated flat plate collector called TPV Charged™ on June 2012 at the InterSolar Europe exhibition, and they won a solar award in 2012 with the invention. In TPV Solar's collector the vacuum is maintained with a getter pump at the UHV level of 10^{-6} Pa. The absorber is a PVD coating on a copper substrate. The expected lifetime of the collector is 20 years. It is designed for air conditioning and cooling, industrial process heating and residential heating applications at operating temperatures of 100-200 °C. The stagnation temperature of the collector is reported to be 325 °C. [49]

3.3 Spectrally selective absorbers

An energy efficient solar collector should absorb incident solar radiation, convert it to thermal energy and then deliver the thermal energy to a heat transfer liquid with minimum losses at each step. An ideal spectrally selective absorber has no reflectance in the visible region and high reflectance in the infrared region. There are many transition metals and semiconductors which show such selective characteristics, but their compositions need to be modified greatly to achieve the ideal characteristics. [10, 15, 50]

Spectrally selective absorbers can be created in many different ways. The first selective surfaces were oxide and sulphide layers on copper-based solar thermal systems [51]. It is possible to use several different design principles and physical mechanisms in order to create a selective solar absorber plate. Figure 6 shows the schematic designs of nine types of the absorber plates. The most interesting absorber types are presented below.

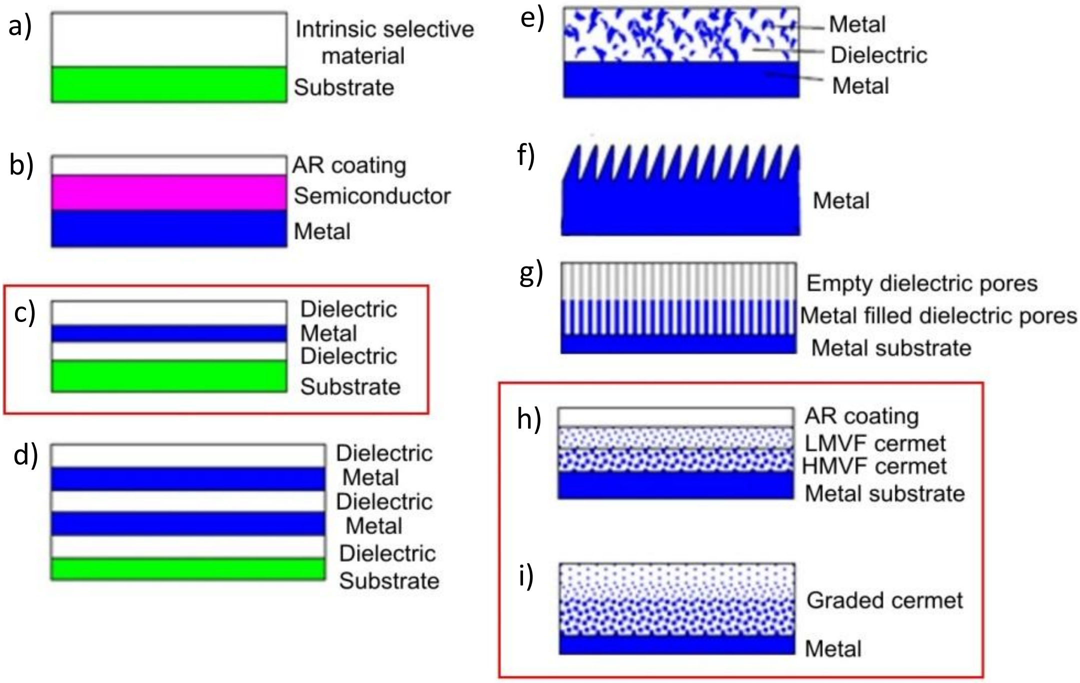

Figure 6. Cross-sectional schematic designs of different solar absorbers. [50] The absorbers boxed in red were studied in the present work.

3.3.1 Intrinsic selective absorbers and textured surfaces

The most straightforward way to produce a selective absorber is to use an intrinsic selective absorbing material (Figure 6 a) such as hafnium carbide (HfC) [52, 53] or zirconium diboride (ZrB_2) [54-56]. Intrinsic selective materials possess the desired kind of spectral selectivity naturally. Even though these intrinsic selective materials do exist, the selective properties have not been ideal for solar applications [15] or the materials require significant structural and/or compositional changes in the lattice or an anti-reflection (AR) coating on the intrinsic material in order to create the required properties [50]. For chemical vapour deposited (CVD) ZrB_2, the solar absorptance was 0.67-0.77 and thermal emittance (at 100 °C) was 0.06-0.09. A 70 nm anti-reflection silicon nitride (Si_3N_4) coating deposited onto the ZrB_2 coating led to an increase in absorptance to 0.93, while the emittance remained unchanged. [55] For HfC solar absorptance was about 0.70 and thermal emittance 0.10 [52]. The intrinsic selective absorbers are structurally more stable but optically less effective than multilayer absorbers. HfC could be useful as an absorbing selective surface at elevated temperatures because of its very high melting point (3316 °C) [57]. Historically, research into intrinsic absorbers has not given promising results because there are no ideal intrinsic materials, but intrinsic materials are finding use as a component in high-temperature composite absorber coatings and multilayer absorbers. [50]

Textured surfaces (Figure 6 f) can lead to high solar absorptance by means of multiple reflections against surface roughness, while thermal emittance is fairly unaffected by the texture. The spectral selectivity is obtained by the optical trapping of solar energy. A textured surface is usually needle-like, dendritic or porous in structure. The surface texture must be protected from damage caused by surface contact or abrasion. [15, 50] CVD deposited tungsten (W) has a dendritic structure [58]. Atom beam etched W coating with micropyramids and submicron holes developed for high-temperature solar applications has a solar absorptance of > 0.85 and thermal emittance at 500 °C of about 0.07 [59]. Sputter etching of copper, nickel and stainless steel leads to textured surfaces with a solar absorptance of 0.90-0.95 and thermal emittance at room temperature of 0.10-0.25 [60]. This geometrical selectivity is said to be more stable against environmental effects like oxidation and thermal shocks than multilayer absorbers [50].

3.3.2 Semiconductor-metal tandem absorbers

Metal-semiconductor tandem absorbers (Figure 6 b) are based on the short-wavelength absorbing ability of semiconductors with band gaps from about 0.5 eV (2.5 µm) to 1.26 eV (1.0 µm). The metal substrate under the semiconductor provides low emittance to give the desired spectral selectivity to the metal-semiconductor tandems. The most commonly used semiconductors are silicon (Si, band gap 1.1 eV) [53, 61-63], germanium (Ge, 0.7 eV) [63-65] and lead sulphide (PbS, 0.4 eV) [63, 66]. These semiconductors have high refractive indices, which result in large reflectance losses from the surface of the semiconductor. This is prevented by using thin and high-porosity semiconductor films or by using anti-reflection coatings. [50]

For optimum selectivity properties, typical layer thicknesses for Si and Ge are 1-10 µm. The layer thickness of PbS can be reduced to 0.1 µm because PbS is a direct-gap semiconductor with a larger absorption coefficient than Ge and Si (both indirect band-gap materials), and due to a unique surface morphology, which reduces the front surface reflection. [67] Ge and PbS coatings have obtained solar absorptance > 0.95 and thermal emittance (240 °C) of 0.48 and 0.14, respectively. Si coatings exhibited lower solar absorptance, of about 0.70. [63] CVD coated Si absorbers with silver (Ag) or molybdenum (Mo) IR reflectors on stainless steel substrates have been tested for several thousand hours at 500 °C without degradation of the optical properties [62]. The Si-based CVD coated absorbers are suitable for mid and high temperature applications [50]. PbS was said to be stable in a vacuum in operating temperatures of mid temperature applications up to 300 °C (the exposure conditions used are not specified in detail) [67], but it is not suitable for high temperature concentrated solar power (CSP) applications [50].

3.3.3 Multilayer absorbers

Multilayer absorbers known as interference stacks (Figure 6 c and d) are based on interference effects, and can be designed to be efficient selective absorbers. The desired effect of an interference stack is to trap energy between two reflective surfaces. The upper one is a thin semi-transparent metal layer and the lower is IR reflecting substrate or highly reflecting metal coating on substrate. Thickness of the dielectric layer is quarter of the desired wavelength, and with a multilayer stack is possible to broaden the region of high absorption. [68] The selective effect is caused by the multiple reflectance passes through the bottom dielectric layer and is independent of the selectivity of the dielectric layer. A thin metal semi-transparent reflective layer is located on the bottom dielectric layer. This metal layer has a high reflectance in the infrared region and is slightly less reflective in the visible region. On top of the reflective layer is the top dielectric layer, which reduces the visible reflectance. The thickness of the top dielectric layer determines the shape and position of the reflectance curve. [50]

Studies have been made of various multilayer absorbers using different metals, such as Mo [69-71], platinum (Pt) [69, 72, 73], Ni [69], chromium (Cr) [69], Al [74], tantalum (Ta) [69], and Cu [75] and dielectric layers, such as aluminium oxide (Al_2O_3) [69, 71-74], chromium oxide (Cr_2O_3) [76], hafnium oxide (HfO_2) [70], and zinc sulphide (ZnS) [75]. A triple-layer absorber Al_2O_3/Mo/Al_2O_3 was originally developed for the US space programme [77] and it has been produced by large-area sputtering for high-temperature applications [69]. Multilayered direct current (DC) reactive magnetron sputtered cermet films of Al_2O_3/Mo/Al_2O_3/Mo/Al_2O_3/... on a copper substrate have obtained a solar absorptance of 0.94 and thermal emittance of 0.05 for a film thickness of 200 nm [71].

Multilayer absorbers can be stable at mid to high temperatures depending on the materials used. At elevated temperatures, the multilayer absorbers can suffer from the oxidation of the metallic layers [76], interdiffusion between the multiple coating layers [50], or differences in the thermal expansion coefficients causing delamination [78].

3.3.4 Metal-dielectric composite tandems and gradient absorbers

Metal-dielectric composite coatings (Figure 6 e, g, h and i) are known as cermets (i.e. *ceramic-metallic*). They are highly absorbent in the solar region but transparent in the infrared. They are deposited onto a highly IR reflective metal substrate. Metal-dielectric composite consists of fine metal particles, which are in a dielectric or ceramic matrix. The high absorptance in the solar wavelength and transparency in the thermal infrared region are due to interband transition in the metal and the small particle resonance. The particle size should be much smaller than the wavelengths of solar radiation in order to absorb instead of scatter the solar radiation. The metal-dielectric concept offers a high degree of flexibility and the solar selectivity can be optimized using the right constituents, coating thickness, particle concentration, size, shape and orientation. [15, 50]

The highest solar absorptance is obtained when the absorber coating is a metal/dielectric graded composite. The idea of grading the structure is to change the refractive index (n) and extinction coefficient (k) in the structure. The refractive index of a material is defined as a dimensionless number that describes how radiation propagates through the material. For visible light most transparent materials have refractive indices between 1 and 2. The extinction coefficient relates to light absorption. The refractive index and the extinction coefficient depend on the wavelength and material properties. The graded composition should be designed with a continuously decreasing refractive index and extinction coefficient from the metal substrate towards the surface. This is because this type of composition suppresses coating interference and gives a low surface reflection, which increases the solar absorptance. In an ideal case, on the top of the coating there is a refractive index $n = 1$ and extinction coefficient $k = 0$. [79-81] The graded absorbers are reported to have higher absorptance and lower emittance when compared to homogeneous films of the same thickness [82]. Typical anti-reflection coatings in solar absorbers have relatively low refractive indices in the wavelength of 0.3-1.1 µm, for example about 1.5 for silicon dioxide (SiO_2), 1.5-1.6 for silicon oxy-nitride (SiON), and 1.7-1.8 for Al_2O_3 [83]. In the same wavelength range, for thermal evaporated Cr_2O_3 with a thickness of 70-300 nm refractive indices from 1.4 to 2.1 have been reported, depending on the deposition parameters [84]. Pure chromium (Cr) and titanium (Ti) have relatively high refractive indices, about 3.6 for Cr and 3.4 for Ti at a wavelength of 1.1 µm [83].

The lowest thermal emittance is achieved when the absorber coating has non-metallic properties, i.e. k does not increase with the wavelength. It means that a metal-dielectric composite coating should be so thin that thermal radiation cannot observe the composite coating. Metallic properties in the base of the cermet absorber coating cause reduction of the infrared reflectance, and thus increase thermal emittance. [79-81]

The graded composite absorbers can be produced by a variety of techniques, such as electroplating, anodizing, inorganic pigmentation of anodized aluminium, CVD, and PVD. The most widely used cermet absorbers are electroplated black chromium, evaporated titanium oxy-nitride and sputtered chromium oxy-nitride, and they are presented below in more detail.

Black chromium

Electroplated black chromium was the most common solar absorber coating in flat plate collectors until the 1990s. The electroplating bath contains chromic acid in the presence of catalyst ions such as sulphate or fluoride. In solar thermal applications, the electrolyte usually also contains nitrites. The nitrites can be reduced on the cathode, which results in the formation of black chromium oxides and nitrides. The electrochemical deposition process of chromium produces toxic and carcinogenic liquid waste, containing hexavalent chromium. Electroplated black chromium is still used in flat plate collectors and in receiver tubes of concentrated solar collectors because of its low production costs and high corrosion resistance [2-6].

Electroplated black chromium ($Cr-Cr_2O_3$) coating is a composite of metallic chromium and dielectric chromium oxide (see Figure 6 e). The content of metallic Cr is graded and increases with depth towards the substrate [15, 85]. Typically chromium crystallites are about 10 nm in diameter [15, 22, 86]. The size and packing density of the crystallites increases with depth [85]. Electroplated black chromium coatings have a rough surface layer which can improve anti-reflection properties [87]. Usually, a separate anti-reflection coating is not added onto the black chromium absorber coating. Typical metal substrates for black chromium absorber coatings are Cu [88, 89], Ni [88, 90], Ni-coated copper [2, 4, 91], and stainless steel [88, 92, 93]. Conventionally, the thermal emittance (100 °C) of black chromium coatings has been 0.10-0.20 [15] but the latest black chromium absorbers have a lower emittance, about 0.07-0.08. [91, 92] Kennedy suggested in [50] that improvements in the performance of black chromium absorber coatings are possible with the addition of an anti-reflection topcoat. [50]

Investigations to deposit black chromium coatings from trivalent ions have been proceeding and the process is considered to be a promising and more environmentally acceptable replacement technology for hexavalent chromium plating [4, 7-9]. In decorative and hard coating applications, many articles and patents in trivalent chromium plating have been published in the past 30 years. The commercial decorative trivalent chromium plating process has been in use since the mid-1970s [6, 94]. It has not yet been commercialized for solar thermal applications. The investigation results on electrochemically deposited trivalent black chromium are limited because nitrites exhibit harmful effects on trivalent chromium plating. Thus, in order to obtain trivalent black chromium coatings, it seems to be necessary to add to the electrolytes some chemical components, which play the same role as nitrite. Based on this, Hamid [7] and Bayati [8] investigated the addition of Co^{2+} and Fe^{2+} to improve the efficiency of the electroplating bath and the optical properties of black chromium coating [7, 8].

Electroplated black chromium coatings have been used as a selective solar absorber coating for applications requiring temperatures up to 300 °C. A nickel (Ni) layer between a Cu substrate and black chromium absorber coating increases thermal emittance but enhances thermal and corrosion resistance [22, 95]. A Ni layer on Cu has given stability up to 400 °C in air [96]. Black chromium absorber coating on stainless steel tubes is nowadays also used for high-temperature CSP applications [92].

The degradation process of black chromium selective coatings at high temperatures has been reported to be the oxidation of the metallic Cr crystallite and densification of the crystallites [22, 85, 88]. This results in optical degradation in the visible range and decrease of solar absorptance [85]. At elevated temperatures, the diffusion of substrate material through black chromium coating has been observed. Lee *et al.* [88] found diffusion of nickel, copper and iron from substrates after annealing at 450 °C for 24 h. The diffusion of substrate material played a major role in the decrease of solar absorptance. [88] The high-temperature stability of black chromium selective coating has been improved by admixing molybdenum (Mo) with chromium. Adding Mo affected the stability but not the optical response before heating. Absorptance was stable at a value of 0.95 at 425°C in air for 146 h with a Mo/Cr ratio of 0.05. The Mo percentage was very high near the surface of the coating. [97]

Chromium oxy-nitride

PVD processes have enabled more complex multilayer coatings and hence increased the optical selectivity of the absorbers. Nowadays, magnetron sputtering is a widely used PVD deposition process for absorber coatings. Magnetron sputtering is suitable for the large-area deposition of thin films and has a relatively high deposition rate. This technique is used to deposit absorber coatings that produce less pollution than conventional electrochemical methods. In the last few years, magnetron sputtered chromium oxy-nitride (CrO_xN_y) coatings have increased their market share significantly [10-17]. Figure 7 presents the X-ray photoelectron spectroscope (XPS) depth profile of a commercial CrO_xN_y/SnO_x absorber coating on a Cu substrate [16].

DC magnetron sputtered CrO_xN_y/SiO_2 coating on Cu obtained a solar absorptance of 0.95 and thermal emittance (80 °C) of 0.050. The absorber maintained its optical properties for 300 h at 278 °C in air but degraded (α_{aged} 0.91, ε_{aged} 0.135) after 600 h treatment at the same temperature. The degradation was attributed to the elemental diffusion of metallic Cu from the substrate into the coating and the formation of a cupric oxide (CuO) phase, and the interfacial reaction between the different layers (for example chromium oxide with silicon oxide) generating new phases, interfacial diffusion close to the interface region, chemical interactions adjacent to the interface and broadening of the interface width. [98]

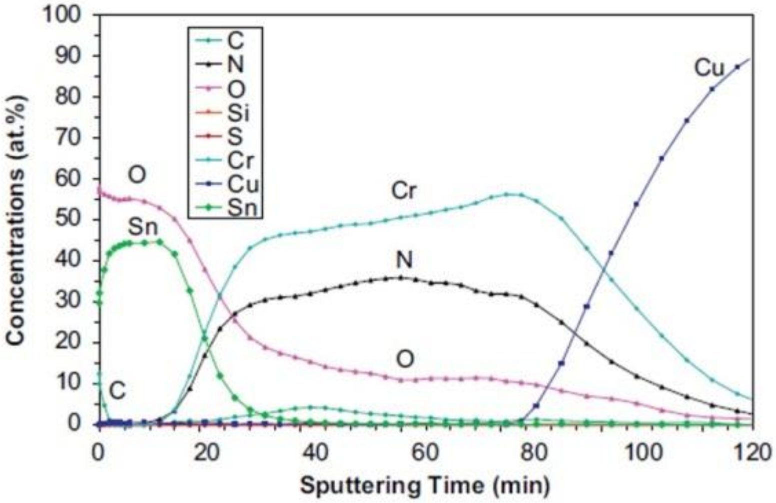

Figure 7. XPS depth profile of a commercial chromium oxy-nitride absorber. [16]

Titanium oxy-nitride

Titanium oxy-nitride (TiO_xN_y) cermet absorbers have been deposited by electron beam evaporation and by activated reactive evaporation (ARE) on copper substrates. They have been reported to be suitable for flat plate applications above 200 °C. TiO_xN_y absorbers have been reported to consist of columns with a metallic mixture of TiN and TiO, and a dielectric “vacuum” in the voids [99]. With a SiO_2 anti-reflection coating on the top, the solar absorptance was 0.94 and thermal emittance (100 °C) 0.044, and the absorber was thermally stable in a vacuum up to 400 °C (exposure time is not described) [100]. These coatings degrade quickly at elevated temperatures in air [101]. The SiO_2 anti-reflection layer has been reported to passivate the absorber and slow down the degradation in air [100, 102] but nevertheless the absorber is not suitable for high-temperature CSP applications [50].

A TiO_xN_y absorber on Cu has been reported to degrade first due to structural and chemical changes to the titanium nitride (TiN) and titanium oxide (TiO) without interacting with the substrate. Secondly, the TiN and TiO oxidize, and form crystalline rutile titanium dioxide (TiO_2), and the Cu becomes mobile and roughens the interface of the absorber and the reflector due to diffusion into the coating. Thirdly, a quasi-liquid coating-substrate mixture rises through the pores formed in the interface region and oxidizes on the surface of the film. This destroys the selective properties and mechanical stability of the film. The fourth and final step is the reconstruction of a chemically stable amorphous film of titanium oxides and crystalline copper oxides with a crater-like surface roughness located at previous pore sites. [101] However, in the operating range of about 350 °C, where degradation is apparent, the outer surface has been reported to be nitrogen-rich, not oxygen-rich. [103].

3.3.5 Substrate materials for selective surfaces

Most thin metal films show high reflectance in the infrared region. A high free electron density of a metal leads to high IR reflectivity, which results in the desired low emittance in the infrared region [104]. Free electron metals such as Cu [105-107], Ag [106, 107], and Au [106] show the lowest emittance values. These metals normally have very low emittance values of around 0.02-0.04. The thermal emittance values of the solar absorber substrate materials or infrared reflector coatings in current use or potentially in use are presented in Table 1. [108] The emissivity and reflectivity of most metals are presented in detail in the literature [106, 109-111]. The emittance values vary with surface conditions such as roughness and an oxide layer on the metal [106].

Farooq *et al*. [112] have investigated the thermal emittance of polished aluminium and copper substrates in solar absorbers. Aluminium substrates exhibited higher IR reflectance and reduced emittance. A cleaned Al substrate was 1 % more reflective than cleaned Cu, with $\varepsilon = 0.02$ while Cu had $\varepsilon = 0.03$. [112]

Sputtered nickel on a metal substrate acts as an oxidation barrier but has a lower reflectance in the thermal range than polished metal substrates, giving higher emittance values. A 300-nm-thick sputtered nickel layer increased the emittance on Al from 0.02 to 0.12, and on Cu from 0.03 to 0.13. [112]

Table 1. Thermal emittance of bulk metals used or possible for solar absorber IR reflectors. The values are approximate ranges at 500 °C from lowest to highest. [106]

Material	**Emittance**
Pure silver (Ag), polished	0.01-0.03
Pure copper (Cu), polished	0.02-0.03
Pure gold (Au), polished	0.02-0.03
Wrought copper (Cu)	0.02-0.03
Pure tungsten (W), polished	0.03
Pure aluminium (Al), polished, unoxidized	0.02-0-06
Wrought commercially pure aluminium (Al)	0.05
Pure iron (Fe), unoxidized	0.05
Pure nickel (Ni), polished	0.05-0.07
Commercially pure nickel (Ni), cleaned	0.04-0.09
Pure molybdenum (Mo), polished	0.07
Pure chromium (Cr)	0.06-0.1
Carbon steel, polished	0.1
Austenitic stainless steel, cleaned	0.2-0.3
Ferritic stainless steel, polished	0.2-0-4

4 SOLAR ABSORBERS AT ELEVATED TEMPERATURES

Temperature ranges of solar thermal collectors have been divided by operating temperature into low temperature (T < 100 °C), mid temperature (100 °C < T < 250 °C), and high temperature (T > 250 °C) [20]. Several different solar selective coatings have been investigated for mid and high temperature solar thermal applications, such as Cr, Ti, Al, W, Mo, Zr, Hf, Au, Ag, Pt and graphite-based absorber coatings. However, only a few of them are in commercial production, used in evacuated receiver tubes for solar thermal power generation. Archimede Solar Energy (Italy) under licence from ENEA (Italy's National Agency for New Technologies, Energy, and the Environment) produces Mo-SiO_2 and W/W-Al_2O_3/Al_2O_3 absorber coatings, which are stable at 580 °C in a vacuum [113-115], and Siemens (Germany) produces Mo- and W-Al_2O_3 absorbers, which are stable at 350-500 °C in a vacuum [116]. Table 2 gives a summary of absorbers which have been reported to maintain optical properties without significant changes at ≥ 250 °C either in air or a vacuum. The stability for a short time period at a certain test temperature can be used for comparing absorber samples with each other and for revealing the ageing mechanisms in the absorbers; the accelerated ageing test according to the ISO standard draft [24] is related to real operating temperatures and predicts service lifetime but was developed for mid temperature flat plate collectors.

It is notable that the stability of many of the selective coatings in Table 2 has been studied only in a vacuum. Some of the absorbers can easily degrade in air even if they are highly stable in a vacuum. For example, a sputtered Mo-Al_2O_3 selective absorber was stable in air only at < 300 °C but in a vacuum at as high as 500 °C [78], and sputtered Al_xO_y/Al/Al_xO_y coating was stable in air for two hours at 400 °C but in a vacuum for two hours at 800 °C [74]. The heating of the absorber in air can lead to oxidation, phase transformations, and interdiffusion [74].

In some of the studies presented in Table 2, the heat treatment period was short (a couple of hours or less). Exposure time has a great significance on the achieved temperature-stability, as in an Al_xO_y/Al/Al_xO_y coating, which was stable in air at 300 °C for 75 h but degraded at 400 °C after two hours [74], and a NbAlN/NbAlON/Si_3N_4 coating that was stable at 450 °C for 116 h but at 500 °C for two hours [117]. The relationship between exposure time and temperature is discussed in more detail in section 5.2.1.

Table 2. Thermal stability of different solar absorbers at ≥ 250 °C in air and/or in a vacuum. The absorbers have been reported to maintain optical properties without significant changes for a certain time period.

Absorber	Sub-strate	Deposition method	α	ε	Stability		Ref
					Air (°C)	Vacuum (°C)	
$Cr\text{-}Cr_2O_3$	Cu	DC sputtering	0.92-0.96	0.05-0.08 at 100 °C		300-400 (1 h)	[118]
$Cr\text{-}Cr_2O_3$	Ni coated Cu	Electro-plating	0.80	0.03 at 100 °C	350 (3 h)		[2]
$Cr\text{-}Cr_2O_3$	W	Electro-plating	0.98	0.10 at 100 °C		400 (2 h in argon)	[119]
$Cr\text{-}Cr_2O_3$	Ni	Electro-plating	0.90-0.96	0.25-0.30 at 100 °C	300 (1 h)		[88]
$Cr\text{-}Cr_2O_3$	SS	Electro-plating	0.88	0.24 at 100 °C	450 (24 h)		[88]
$Cr\text{-}Cr_2O_3$ with Cr_2O_3 AR coating	Ni coated SS	RF-sputtering	0.92	0.08 at 100 °C	300 (64 h)		[120]
$Cr_xO_y/Cr/Cr_2O_3$	Cu	Pulsed DC sputtering	0.89-0.91	0.05-0.06 at 100 °C	275 (50 h)	500 (2 h)	[76]
Cr_2O_3/CrN	Cu	DC sputtering	0.93	0.07 at 100 °C	250		[14]
$Cr\text{-}Al_2O_3$	Cu coated Glass	Vacuum evaporation	0.92	0.03 at 23 °C		500 (100 h)	[121]
$Al_2O_3/Cr/Al_2O_3$	Cr coated glass	RF and DC sputtering	0.89-0.95	0.14-0.25 at 537 °C	500-600 (100-150 h)	650-700	[69]
$CrMoN_{(HMVF)}/CrMoN_{(LMVF)}/CrON$	SS	DC sputtering	0.90-0.92	0.13-0.15 at 82 °C	400 (71 h), 425 (7 h)	500 (7 h)	[122]
$CrMoN_{(HMVF)}/CrMoN_{(LMVF)}/CrON$	Al	DC sputtering	0.89	0.08 at 82 °C	265 (600 h)		[122]
TiO_xN_y with SiO_2 AR coating	Cu	Sputtering or vacuum evaporation	0.95	0.05 at 100 °C	300		[101, 123]

TiN_x	Ag coated glass and SS	Sputtering	0.86-0.88	0.024-0.033 at 127 °C		600 (500 h)	[124, 125]
TiAlN/TiAlON/Si_3N_4	Cu	DC sputtering	0.93-0.95	0.05-0.08 at 82 °C	525 (50 h), 600 (2 h)	600 (2 h)	[126-128]
TiAlN/TiAlON/Si_3N_4	SS	DC sputtering	0.93-0.95	0.15-0.17 at 82 °C	525 (50 h), 600 (2 h)		[126-128]
TiAlN/AlON	Cu	DC and RF Sputtering	0.93-0.94	0.05-0.06 at 82 °C	400 (100 h), 600 (2 h)	900 (2 h)	[26]
TiAlN/AlON	SS	DC and RF Sputtering	0.91-0.94	0.18-0.20 at 82 °C	800 (2 h)		[26]
TiAlN/CrAlON/Si_3N_4	Cu	DC sputtering	0.94-0.95	0.05-0.07 at 82 °C	300 (150 h), 550 (2 h)	900 (2 h)	[129]
TiAl/TiAlN/TiAlON/TiAlO	SS, Cu	Multi arc ion plating	0.90	0.09-0.19 at 100 °C	650 (1 h)		[130]
Ti_xAl_{1-x}/TiN/(TiN-AlN)$_H$/(TiN-AlN)$_L$/AlN	Polished SS	DC and RF sputtering	0.94	0.08 at 82 °C	500 (2 h)		[131]
TiAlSiN/TiAlSiON with SiO_2 AR coating	Al, Cu	DC sputtering/PECVD	0.95-0.96	0.05 at 100 °C	278 (600 h)		[132-134]
Al/AlN	Al, glass	DC sputtering	0.93	0.04 at 23 °C	400		[135]
Al-AlN_x-Al_xO_y	Al coated quartz	DC sputtering	0.94-0.97	0.07 at 82 °C		400-600 (30 min), 450 (10 h)	[136]
SS-AlN with AlN AR coating	Al coated glass	DC sputtering	0.93-0.96	0.07-0.10 at 350 °C		500 (1 h)	[137]
Al_xO_y/Al/Al_xO_y	Cu	Pulsed DC sputtering	0.95-0.97	0.05-0.08 at 82 °C	400 (2 h)		[74]

$Al_xO_y/Al/Al_xO_y$	Mo	Pulsed DC sputtering	0.93-0.95	0.05-0.09 at 82 °C	300 (75 h), 400 (2 h)	800 (2 h)	[74]
$Al_2O_3/Cu/Al_2O_3/AlCuFe/Al_2O_3$	Cu coated Si wafer	Sputtering with Kaufman-type ion source	0.89-0.90	0.04-0.06 at 400 °C	400 (450 h)		[138]
Ni-NiO	Al	DC sputtering	0.96	0.10 at 100 °C		300	[139]
$Ni/Ni\text{-}Al_2O_3$	Cu	Vacuum evaporation	0.94	0.22 at 150 °C	300		[140, 141]
$Ni/Ni\text{-}Al_2O_3$	Ni, Pt or Ag coated quartz	Vacuum evaporation	0.96	0.22 at 150 °C	500 (100 h)		[140, 141]
$Al_2O_3/Ni/Al_2O_3$	Ni coated glass	RF and DC sputtering	0.89-0.95	0.14-0.25 at 537 °C	500-600 (100-150 h)	650-700	[69]
W-AlN with AlN AR coating	Al coated glass	DC sputtering	0.92-0.96	0.06 at 80 °C or 0.08-0.10 at 350 °C		500 (1 h)	[142]
$W/W\text{-}Al_2O_3$ with Al_2O_3 AR coating	SS	DC and RF sputtering	0.93	0.10 at 400 °C, 0.14 at 550 °C		580 (30 day)	[113-115]
$Mo\text{-}SiO_2$	Mo coated quartz	DC and RF co-sputtering	0.95	0.097 at 80 °C		800 (2 h)	[143]
$Mo\text{-}SiO_2$	SS	DC and RF sputtering	0.95	0.10 at 400 °C, 0.13-0.15 at 580 °C		580 (14 day)	[114, 115, 144]
$Mo\text{-}SiO_2$ with SiO_2 AR coating	SS	DC and RF sputtering	> 0.94	< 0.13 at 580 °C		580	[144]
$Mo\text{-}Al_2O_3$	SS	DC and RF sputtering	0.91-0.93	0.19-0.27 at 80 °C		500 (2 h)	[145]
$Al_2O_3/Mo/Al_2O_3$	Mo coated glass	RF and DC sputtering	0.89-0.95	0.14-0.25 at 537 °C	500-600 (100-150 h)	650-700	[69]

Al_2O_3/Mo/ Mo-Al_2O_3 with SiO_2 AR coating	SS	Sputtering	0.96-0.98	0.16-0.18 at 350 °C		650 (1 month)	[146]
Mo/HfO_x/Mo/ HfO_2	Cu	DC sputtering	0.90-0.92	0.07-0.09 at 82 °C	500 (2 h)		[70]
Mo/HfO_x/Mo/ HfO_2	SS	DC sputtering	0.90-0.92	0.17 at 82 °C	500 (2 h)	800 (2 h)	[70]
HfO_x/Mo/HfO_2	Cu	DC sputtering	0.90-0.92	0.07-0.09 at 82 °C	400 (2 h)	600 (2 h)	[70]
$HfMoN_{(HMVF)}$/ $HfMoN_{(LMVF)}$/ HfON with Al_2O_3 AR coating	SS	Pulsed DC sputtering	0.94-0.95	0.13-0.14 at 82 °C	475 (34 h), 500 (7 h)	650 (7 h)	[147]
ZrN_x	Ag coated glass and SS	Sputtering	0.86-0.88	0.024-0.033 at 127 °C		600 (500 h)	[124, 125]
ZrC_xN_y	Ag coated glass and SS	Sputtering	0.86-0.88	0.024-0.033 at 127 °C		600 (500 h)	[124, 125]
ZrO_xN_y	Ag coated glass and SS	Sputtering	0.88-0.93	0.08-0.30 at 327 °C		600 (500 h)	[124, 125]
Zr/ZrC_x/ZrO_x	SS	Vacuum evaporation	0.90	0.05 at 20 °C		600	[148, 149]
Zr/ZrC_x/ZrO_x	Quartz	Vacuum evaporation	0.90	0.05 at 20 °C		800	[148, 149]
Au-MgO	Mo coated SS	RF sputtering	> 0.90	< 0.10 at 100 °C	400 (64 h)		[121, 150]
Ag-Al_2O_3	Cu coated glass	Vacuum evaporation	0.90	0.03 at 100 °C		400 (100 h)	[121]
Pt/Pt-Al_2O_3	Cu	Vacuum evaporation	0.94	0.19 at 150 °C	400		[141]
Pt/Pt-Al_2O_3	Quartz	Vacuum evaporation	0.94	0.19 at 150 °C	600 (300 h)		[141]
Pt-Al_2O_3 multilayers	Pt coated quartz	RF sputtering	0.95	0.08-0.20 at 827 °C	700 (300 h)		[72]

$Al_2O_3/Pt/Al_2O_3$	Pt coated glass	RF and DC sputtering	0.89-0.95	0.14-0.25 at 537 °C	500-600 (100-150 h)	650-700	[69]
Al_2O_3-(Pt-Al_2O_3) with Al_2O_3 AR coating	Pt, Cr, Mo coated glass	RF and DC sputtering	0.89-0.91	0.13 at 20 °C	450-500 (100 h)		[151]
$Al_2O_3/Ta/Al_2O_3$	Ta coated glass	RF and DC sputtering	0.89-0.95	0.14-0.25 at 537 °C	500-600 (100-150 h)	650-700	[69]
NbAlN/NbAlON/Si_3N_4	Cu	DC sputtering	0.93-0.95	0.07 at 82 °C	450 (116 h), 500 (2 h)	600 (2 h)	[117]
$NbTiON_{(HMVF)}$/ $NbTiON_{(LMVF)}$ with SiON AR coating	Cu	Sputtering	0.95	0.07 at 100 °C		500 (40 h)	[152]
$NbTiON_{(HMVF)}$/ $NbTiON_{(LMVF)}$ with SiON AR coating	SS	Sputtering	0.91	0.13 at 100 °C		600 (40 h)	[152]
Cu-SiO_2	Cu coated glass	Vacuum evaporation	0.93	0.05 at 100 °C		277	[153]
Cu spinel	Cu coated glass	Vacuum evaporation	0.87	0.06 at 100 °C		300 (100 h)	[121]
Cu-C	Cu coated glass	DC sputtering	0.94	0.04 at 120 °C		500 (1 h)	[154]
SS-C (graded)	Cu coated glass	DC sputtering	0.94	0.03 at 100 °C		300	[155]
Graphite	Cu, Ag, Ni and Ti	Vacuum evaporation	0.71-0.80	0.01-0.02 at 100 °C		300 (100 h)	[156]
a-Si:C:H/Ti	Al	DC sputtering and PECVD	0.75	0.03 at 100 °C	250 (500 h)		[157]
NREL #6A	SS	Sputtering	0.95	0.08 at 500 °C	500		[57, 158]
NREL #6B	SS	Sputtering	0.95	0.10 at 500 °C	500		[57, 158]

High temperature solutions for flat plate collectors have been investigated by Barshilia *et al*. [26, 70, 74, 76, 117, 122, 126-129, 147, 159]. For example, they studied a TiAlN/TiAlON/Si_3N_4 coating on a copper substrate, which was stable at 625 °C for two hours in air and in longer tests at 525 °C for 50 h [127, 128], and a NbAlN/NbAlON/Si_3N_4 coating structure on a copper substrate, which remained stable at 500 °C for two hours in air or in longer tests at 450 °C for 116 h in air. The NbAlN/NbAlON/Si_3N_4 tandem absorber had a high oxidation resistance. [117] The NbN-based coating was thermodynamically stable towards Cu diffusion because of the absence of Cu-Nb compounds [160]. Selvakumar *et al*. [147] developed a new graded tandem absorber with a high and low metal volume fracture (HMVF, LMVF) of hafnium molybdenum (oxy)nitride coating $HfMoN_{(HMVF)}$/$HfMoN_{(LMVF)}$/ HfON/Al_2O_3 on a stainless steel substrate for high temperature solar thermal applications. The absorber was thermally stable in air at 475 °C for 34 h. At higher temperatures it was partially delaminated from the substrate, which was due to the formation of MoO_2, MoO_3 and $HfMo_2O_8$ phases. The Al_2O_3 anti-reflection coating on top of the absorber resulted in high oxidation resistance because Al_2O_3 is a very stable high temperature material and an excellent diffusion barrier for oxygen [141]. In a vacuum, the absorber remained stable up to 600 °C for 450 h and up to 650 °C for 100 h. [147] However, these coating structures are very complex and so far not commercially available.

4.1 Tool industry coatings as solar absorbers

With the exception of conventional solar absorber coating materials such as chromium oxide, titanium oxy-nitride or nickel doped anodized alumina, typical tool industry coatings have been developed for solar absorber applications. TiAlN and TiAlSiN have been reported to be very stable coatings on cutting and drilling tools [161], and they are also used as solar absorbers [132-134, 162].

TiAlN films were initially applied to hard coatings on cutting and drilling tools due to their excellent mechanical properties and good oxidation resistance at high temperatures [163, 164]. In solar thermal applications, Barshilia *et al.* [127, 128] reported a solar absorptance of 0.96 and thermal emittance of 0.07 at 82 °C achieved by a TiAlN/TiAlON/Si_3N_4 tandem absorber on a copper substrate which were very stable at high temperatures. The absorber remained stable at 625 °C for two hours in air and in longer tests at 525 °C for 50 h. The thermal stability of the absorber was attributed to its high oxidation resistance and the microstructural stability of the component materials at high temperatures. In addition, TiAlN was reported to act as a diffusion barrier for copper substrate atoms. Good diffusion barrier properties were gained due to effectively blocked diffusion paths for Cu by the formation of TiO, AlN, and Al_5Ti_2 compounds during the annealing of TiAlN/Cu at high temperatures. The interdiffusion between TiAlN/TiAlON and TiAlON/Si_3N_4 was very low up to 600 °C because of high melting points and stable microstructures. TiAlN, TiAlON, and Si_3N_4 exhibited very high oxidation resistances, at 750 °C, 900 °C, and 1400 °C, respectively. [127, 128]

Rebouta *et al.* [132, 162] studied a similar absorber layer stack but with a SiO_2 anti-reflection layer. The TiAlN/TiAlON/SiO_2 tandem absorber had a solar absorptance of 0.96 and thermal emittance of 0.05 at 100 °C. During continuous thermal annealing at 278 °C for 600 h, the optical properties remained almost unchanged. [132, 162] Zhu *et al.* [165, 166] have investigated TiAlN and TiAlN/TiAlON for coloured (black, blue, red, green, yellow, etc.) solar thermal applications [165, 166]. Yin *et al.* [167] have reported that DC magnetron sputtered TiAlN oxidizes easily, and is not recommended for use as a solar absorber in air for high temperature applications. Heat treatment in air at 450 °C for a few minutes resulted in a replacement of nitrogen with oxygen, mainly in a thin sub-layer on the top of the surface. The thickness of the oxide layer was about 25 nm, and it resulted in a significant degradation of the optical performance of the surface. [167]

In cutting tool applications, the TiAlSiN coating has been reported to have very good chemical stability [161], high oxidation resistance up to 900 °C [168, 169], and high corrosion resistance [163]. The TiAlSiN coatings on high-speed steel (HSS) showed no phase transformation in Raman spectra up to 850 °C in air, indicating that the coatings were stable up to 850 °C [170]. The addition of Si to TiAlN promotes the preferential formation of an Al_2O_3 barrier layer during oxidation at high temperatures due to the increased aluminium diffusion coefficient [171].

A newly developed commercially available $TiAlSiN_x/TiAlSiO_xN_y/SiO_2$ absorber coating has layer thicknesses of 60 nm, 45 nm, and 100 nm, respectively. The solar absorptance of the absorber is 0.96 and the thermal emittance is 0.05. The absorptance layers have been deposited by magnetron sputtering and the SiO_2 anti-reflection layer by plasma-enhanced chemical vapour deposition (PECVD). [133, 134] The absorber performed well in the accelerated ageing test at 278 °C for 600 h in air. [132]

4.2 Metal substrates of absorber coatings

Copper, aluminium, and stainless steel are widely used as absorber substrates in solar thermal collectors. In this section, the substrate materials are presented considering their use in high-temperature solar applications.

4.2.1 Copper as substrate material at elevated temperatures

Copper is traditionally used as a substrate in flat plate solar collectors because of its high thermal conductivity [35] and high IR reflectance [106]. The melting point of copper is 1083 °C [172]. However, at elevated temperatures, copper is quite mobile [173], and can penetrate through a coating layer without reacting with it [174]. The diffusion of copper at elevated temperatures has been widely studied in the electronics industry, such as in integrated circuits and computer chips. [175]

In microelectronics, copper has been found to diffuse easily into a silicon substrate and form a Cu_3Si compound at 200 °C and higher temperatures [176-179]. Various diffusion barriers have been investigated to prevent the diffusion processes between the copper and the silicon substrate. For example, refractory metals like Ta [174, 180-183], Mo [184-187], niobium (Nb) [188], W [183, 189-191], Cr [183, 192, 193], Ti [194-196], and ruthenium (Ru) [197, 198] have been investigated as diffusion barriers for copper. The barrier behaviour depended on the formation of binary compounds of the barrier material with copper. Mo, Ta and W did not form compounds with Cu, and thus they can act as good barriers. However, Cu has been observed to intermix substantially with W via structural defects even at temperatures of 260 °C [183, 199]. Titanium can form Ti_2Cu, TiCu, Ti_2Cu_3 and $TiCu_3$ phases, niobium $NbCu_2$ phase and chromium copper-rich Cr-Cu alloy. The binary compounds interfered in the multilayer structure, and led to the diffusion of copper through the diffusion barrier. [200, 201] Another physical factor which affected barrier properties was the self-diffusion coefficient of the barrier material. The smaller the self-diffusion coefficient, the better the barrier behaviour. The self-diffusion coefficients at 400-600 °C are in the order Ti>Cr>Nb>Mo>Ta>W. [202] However, the crystal structure of the barrier layer also had a significant role in barrier behaviour [203-206]. Materials with an amorphous structure have better thermal stability and diffusion barrier properties against copper diffusion. An amorphous structure has better diffusion barrier properties than polycrystalline materials because it is free of the grain boundaries which act as diffusion paths for copper. [207-210]. Ono *et al.* [202] have studied the sputtered transition metals (Cr, Ti, Nb, Ta and W) barriers between copper and silicon at 200-800 °C for 1 hour in a hydrogen atmosphere. The thickness of each barrier coating was 60 nm. Ta and W were the most stable barriers and they prevented copper diffusion up to 600 °C. [202] He and Feng [187] have reported a sputtered 50-nm-thick Mo barrier layer preventing copper diffusion to a silicon substrate at 675 °C for 30 min in a vacuum.

Nitrides and carbides of transition metals have been reported to provide more stable diffusion barriers for copper than pure transition metals in microelectronics applications. At low concentrations, nitrogen existed in the grain boundaries and thus filled the rapid diffusion paths. At high concentrations, nitrogen reduced the reactivity of the metal barrier layer by forming nitride phases. [187, 211] For example, TiAlN coatings have been used as a diffusion barrier in microelectronics because of their high thermal stability, chemical inertness and low electrical resistivity at high temperatures [27, 212]. Transition metal nitrides and carbides have been widely studied as diffusion barriers, for example TaN_x [194, 197, 213, 214], $TaSiN_x$ [207], $TaBN_x$ [204], TaC_x [215, 216], MoN_x [185, 186], WN_x [191, 217, 218], WC_x [189, 219], WC_xN_y [189], $WTiN_x$ [220], TiN_x [194, 195, 205, 212], ZrN_x [206], ZrC_xN_y [221], and NbN_x [222].

The barrier properties of a pure Ta layer might be improved by the addition of impurities to the coating. If the solubility limit is exceeded, solute atoms in a Ta grain would be expected to segregate in the grain boundaries, obstructing the fast pathways for copper diffusion. With the increase of N_2 partial pressure in Ar gas, the deposition rate decreases, while the content of N_2 increases, and the diffusion barrier properties of thin TaN_x films is improved [174, 223]. Holloway *et al.* [174] added nitrogen into a sputtered tantalum coating by adding N_2 to the Ar gas during sputter deposition. When the N_2 concentration was suitable (N_2 amount 5 vol.% of the Ar gas), a tantalum nitride compound, Ta_2N, was deposited. A 50-nm-thick Ta_2N was a more stable diffusion barrier (650 °C for 30 min in flowing He) for copper than a 50-nm-thick Ta layer (550 °C for 30 min in flowing helium). With lower N_2 concentrations (N_2 amount 0.25 vol.% of the Ar gas), a 50-nm-thick nitrogen-alloyed Ta was deposited that had very similar diffusion barrier properties to pure Ta. [174]

The thickness of the barrier coating has an effect on the stability. Generally, the thicker the diffusion barrier, the higher the stability achieved. Laurila *et al.* [215] have studied the influence of coating thickness on the barrier properties of reactively magnetron sputtered Ta_2N. Layer thicknesses were 10, 50 and 100 nm, and stability against copper diffusion for 30 min in a vacuum was 600 °C, 650 °C, and 750 °C, respectively. [215]

The effect of crystallinity and orientation on the diffusion barrier properties for copper has been investigated by Chung and Liu [224]. They studied reactively magnetron sputtered Ta_2N coatings. The amorphous and crystalline phases with different preferred orientation structures were produced by varying the substrate temperatures from room temperature to 200 °C. A 100-nm-thick Ta_2N layer deposited at room temperature was amorphous but at 200 °C had a totally crystalline hexagonal structure with the preferred (002) orientation. The diffusion mobility of atoms through layers depends on the grain size and grain boundary shape. The amorphous Ta_2N was stable up to 700 °C for 30 min in a vacuum, but degraded at 800 °C by the recrystallization of the amorphous structure to allow copper to diffuse through the crystallized structure along the grain boundaries, forming Cu_3Si and $TaSi_2$. The (002) oriented crystalline Ta_2N films acted as a diffusion barrier against Cu diffusion up to 800 °C for 30 min in a vacuum. The good stability of the totally crystallized polycrystalline structure is explained in Figure 8, which illustrates the differences in grain boundaries of preferred (002) orientation and randomly oriented grains. The preferred (002) orientation represents more closely packed and less defective grain boundaries than the randomly distributed grains. The randomly oriented grains include the greater mis-orientation and greater mis-registration between adjacent grains and thicker and more defective grain boundaries. The closely packed structure has fewer defects in the grain boundaries unlike random grain distribution, which has more open and defective grain boundaries. Atomic diffusion through the more open grain boundary structures in the randomly distributed grains appears to be much easier. The earlier degradation of the amorphous structure was attributed mainly to the random crystal nucleation in the amorphous Ta_2N layer during the heat treatments. [224]

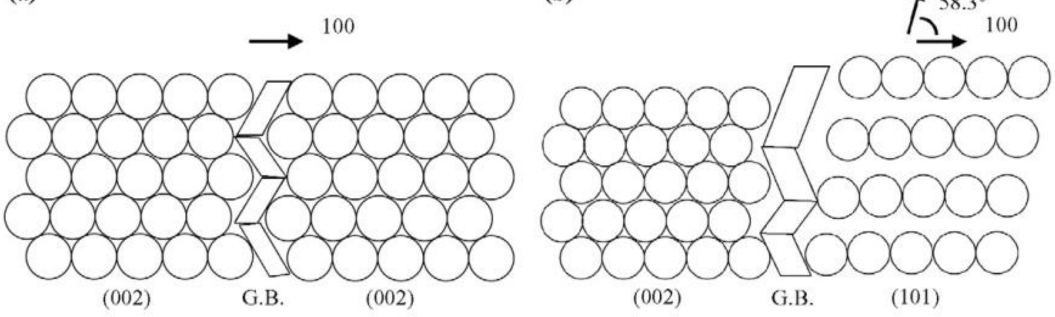

Figure 8. Schematic drawing of a grain boundary (G.B.) between two grains for a) both grains in (002) preferred orientation, and b) randomly oriented grains. [224]

In various solder joint applications, copper and other metals have been reported to diffuse by the Kirkendall effect with some other elements. The Kirkendall effect was named after its discoverer E. Kirkendall (1947) [225] after his experiments on the interdiffusion between Cu and Zn. It is defined by uneven interdiffusion between two materials if the atoms of one metal have a higher mobility and diffuse across the interface more rapidly than the atoms of the other material. This imbalance results in vacancies or voids at the interface between the two materials. The effect is commonly referred to as Kirkendall voids or Kirkendall porosity. With continuous exposure to high temperatures, the voids increase and coalesce causing porosity and loss of strength. Typically, the adhesion is low because the interfacial voids provide an easy fracture path. [226] This phenomenon has been observed widely in a variety of diffusion pairs, such as Cu-Zn [225], Cu-Au [227], Cu-Pt [228], Cu-Sn [229], Sn-Ag-Cu [228], Sn-Pb-Cu [230], Al-Au [231], Au-Sn [232, 233], Pb-Sn [233], Co-Si [234], and in many engineering components, such as solder joints [230, 233, 235], wire bonding [236, 237], and laminate composite materials [238, 239].

4.2.2 Aluminium as substrate material at elevated temperatures

The melting point of aluminium is 659 °C [240], and thus Al substrate cannot be utilized in solar applications at very high temperatures, near its melting point. High-temperature CSP systems have been reported to achieve operating temperatures of 400-1000 °C [241], so aluminium is not an optional receiver tube material at such high temperatures (> 600 °C).

Aluminium is known as a reactive metal that reacts readily with the oxygen present in the atmosphere and forms a natural ~1 to 10-nm-thick oxide layer. Typically, this oxide layer is very thin and dense. The oxide layer consists mainly of amorphous Al_2O_3 but > 500 °C both amorphous and crystalline alumina is presented. The oxide layer can prevent further dissolution of Al and thus provide an effective protective barrier. [242, 243] The oxide layer on polished aluminium in dry air at room temperature reaches a thickness of ~1 nm in a few minutes. Within some days the oxide layer grows with a decreasing growth rate to a thickness of about 2-3 nm. A 3-nm-thick aluminium oxide layer has been reported to act as a barrier and prevent the formation of a brittle intermetallic phase between an Al substrate and titanium carbide (TiC) coating. Higher temperatures accelerate and increase the growth rate of the aluminium oxide layer. [240, 243]

4.2.3 Stainless steel as substrate material at elevated temperatures

For most of the high-temperature (> 400 °C) solar applications, stainless steel (SS) is used as the substrate material [78]. For example, stainless steel has been used in concentrated solar power receiver tubes. The tubes have been coated usually by electroplating with black chromium. One commercial producer of electroplated black chromium on stainless steel tubing is Energie Solaire SA (Switzerland and Spain). The solar absorptance of the absorber is 0.94 ± 0.02 and thermal emittance (at 100 °C) 0.18. [92] The stainless steel substrate of the Energie Solaire absorber is a chromium nickel steel (AISI 304L) of 18-20 % Cr, 8-10 % Ni, 0.08 % C, 0.1 % Si, 2.0 % Mn, 0.05 % P, and 0.03 % S. [22]

Stainless steel has relatively high intrinsic emittance ($\varepsilon_{82\,°C}$= 0.10-0.12). The solar selective coating on SS substrates therefore exhibits low spectral selectivity. [78] The emittance values of the similar coatings deposited on stainless steel substrates were found to be 0.13-0.15 when the emittance on copper was 0.06-0.07.

Thermal emittance can decrease with a PVD coated metallic interlayer between the substrate and absorber coating, which acts as a good IR reflector. Table 1 in section 3.3.5 presented metals with low thermal emittance. In solar receiver tubes, for example Mo [144] and W [113, 114] have been used on stainless steel as a reflecting layer because they are also highly stable. The Mo/Mo-$SiO_{2(HMVF)}$/Mo-$SiO_{2\ (LMVF)}$/SiO_2 coating on stainless steel substrate had low emittance at high temperatures (0.13 at 580 °C) and a solar absorptance of 0.94. The thickness of the Mo layer was 500 nm. The structure showed good stability at 580 °C in a vacuum. [144] However, the metallic interlayer is not stable at high temperatures in air due to thermal oxidation and interdiffusion along the substrate and the absorber coating. [78]

Stainless steel substrate was stable at 450 °C for 24 h while other substrates (Cu, Ni, and Fe) suffered from diffusion of substrate atoms into the black chromium absorber coating. It was found that a black chromium coating on stainless steel suffered less optical degradation than a similar coating on other pure substrate materials at temperatures up to 450 °C. [88]

5 EXPERIMENTAL PROCEDURES

In this thesis, the absorber surfaces studied consisted of industrial solar absorbers and experimental coatings on metal substrates. The absorbers were aged at elevated temperatures in a circulating air furnace according to the accelerated ageing procedure and also heat-treated for a short period at up to 500 °C. The optical properties were characterized before and after the ageing by measuring the solar absorptance and thermal emittance using spectrometers with integrating spheres. The microstructure of the coatings was analysed by electron microscopes. The elemental concentration and diffusion was studied by time-of-flight electron recoil detection analysis (TOF-ERDA).

5.1 Studied selective absorber surfaces

The samples consist of various, widely available industrial solar absorbers and experimental, self-coated absorber surfaces. The industrial solar absorbers were supplied by some manufacturers for this study. The studied industrial solar absorbers represent products made by the most significant manufacturers in Europe and some new absorber developments from small-scale manufacturers. The experimental coatings were mainly deposited using the DC magnetron sputtering method at TUT.

5.1.1 Metal substrates

The substrates used in this study were established base materials for solar absorbers. The substrate materials were copper, nickel-coated copper, aluminium, anodized aluminium, and stainless steel. The copper sheets were cold-rolled and the thicknesses of the sheets were 0.12 mm or 0.2 mm. One of the copper sheets was nickel-coated with a 3-µm-thick Ni layer. The aluminium substrates were cold-rolled sheets with thicknesses of 0.4 mm, and extruded aluminium profiles with wall thicknesses of 0.5 mm (Figure 9). One of the aluminium sheets was an anodized aluminium sheet with a mirror-like surface and a total thickness of 0.4 mm. The thickness of the anodized aluminium oxide was about 140 nm, and on the anodized layer, a thin Al layer was used to act as an IR reflector. The stainless steel substrates were austenitic chromium nickel titanium stainless steel EN 1.4541 - AISI 321 of 18 % Cr, 11 % Ni, 0.08 % C, 1.0 % Si, 2.0 % Mn, 0.045 % P, 0.03 % S, and 0.15 % Ti sheets with a thickness of 0.3 mm, and austenitic chromium nickel stainless steel AISI 304L of 18 % Cr, 8 % Ni, 0.03 % C, 0.1 % Si, 2.0 % Mn, 0.05 % P, and 0.03 % S tubes with a diameter of 42.3 mm and a wall thickness of 2.0 mm.

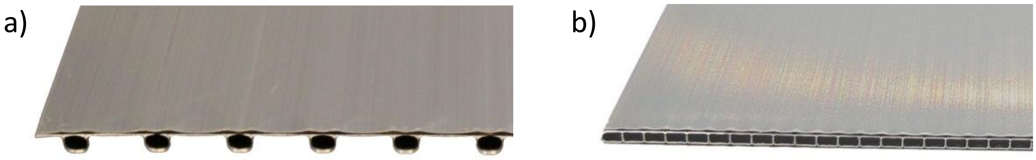

Figure 9. Extruded aluminium profiles: a) a profile with circular fluid channels behind the planar plate, and b) planar profile with rectangular fluid channels inside the shape.

The experimental substrates were cold-rolled copper sheets with a thickness of 0.2 mm. The substrate size was 70 mm x 70 mm. Before the coating process, the substrates were cleaned with acetone and ethanol, and then dried with a fanned air heater.

5.1.2 Absorber coatings

Table 3 presents the industrial coatings that were studied, which were typical solar absorbers from various manufacturers. The sputtered absorber coatings were chromium oxy-nitride (CrO_xN_y), chromium oxide (CrO_x) or titanium aluminium silicon oxy-nitride ($TiAlSiO_xN_y$) absorbers. The evaporated coating was a titanium oxy-nitride (TiO_xN_y) coating. The black chromium coatings were electroplated. All of the coatings had a graded structure from more metallic to dielectric towards the surface. The anti-reflection (AR) layers were tin oxide or silicon oxide, except in the electroplated absorbers where a rough surface acted as an anti-reflective layer [87]. Detailed information about the manufacturing technologies of industrial solar absorbers is not available from the suppliers for commercial reasons.

The most traditional technology used in the studied absorbers is the electroplating of black chromium. Sputtered chromium based absorbers have competed with and partly replaced electroplating since 2000s. The evaporation of TiO_xN_y has been widely used for a couple of decades. The sputtered CrO_xN_y on stainless steel has been developed to withstand outdoor conditions without glazing. The latest product studied is sputtered $TiAlSiO_xN_y$ on extruded Al profiles, which has been commercially available since 2011.

Table 3. Industrial solar absorber coatings studied. The coatings had a graded structure from metallic to dielectric towards the surface.

	Substrate	**Absorption layer**	**AR layer**	**Coating method**
1	Cu 0.2 mm	CrO_xN_y 100 nm	SnO_x 50 nm	Reactive sputtering
2	Al 0.4 mm	CrO_xN_y 100 nm	SnO_x 50 nm	Reactive sputtering
3	Cu 0.12 mm	CrO_xN_y 100 nm	SnO_x 50 nm	Reactive sputtering
4	Al 0.4 mm, anodized Al layer 140 nm, thin Al layer	CrO_x 120 nm	SiO_x 60 nm	Reactive sputtering and e-beam evaporation 1)
5	Cu 0.2 mm	TiO_xN_y 100 nm	SiO_x 100 nm	E-beam evaporation and PECVD 1)
6	Al 0.4 mm	CrO_xN_y 100 nm	SiO_x 80 nm	Reactive sputtering and PECVD 1)
7	Cu 0.2 mm Ni layer 3 000 nm	Cr in Cr_2O_3 200 nm	Rough CrO_x	Electroplating
8	SS AISI 304L 0.3 mm	CrO_xN_y 100 nm	SnO_x 50 nm	Reactive sputtering
9	SS AISI 321 tube ø 42.3 mm 2.0 mm	Cr in Cr_2O_3	Rough CrO_x	Electroplating
10	Al extruded profile a 2) 0.5 mm	$TiAlSiO_xN_y$ 100 nm	SiO_x 100 nm	Reactive sputtering and PECVD 1)
11	Al extruded profile b 2) 0.5 mm	$TiAlSiO_xN_y$ 100 nm	SiO_x 100 nm	Reactive sputtering and PECVD 1)

1) Absorption coating was sputtered or evaporated but the anti-reflection coating was coated by PECVD or using the electron-beam (e-beam) evaporation technique.

2) See Figure 9.

The experimental absorber coatings were multilayer absorbers (see section 3.3.3) based on chromium and chromium oxide layers, and gradient absorbers based on chromium nitride and chromium oxide layers. Chromium-based coatings were chosen because they are widely used in industrial solar absorbers. The experimental selective absorber coatings were deposited by DC magnetron sputtering with equipment designed and constructed at TUT. The chromium target (GfE Metalle und Materialien GmbH) had a purity of 99.7 %. The simulation software CODE Coating Designer of W. Theiss Hard- and Software [244] was used to determine the number of layers and thicknesses of the different layers in order to achieve an optically sufficient absorber with a simple and well reproducible coating layer stack. An optimized simulated 3-layer stack of $Cr_2O_3/Cr/Cr_2O_3$ on Cu would have layer thicknesses of 42.7 nm, 12.3 nm, and 44.6 nm, respectively, and a solar absorptance of 0.94 and thermal emittance of 0.01. However, apart from optimized simulation, the layer stack needed an absorber which could be deposited with sufficient repeatability with the existing sputtering equipment. The purpose of the chromium-based experimental absorbers on copper was to study the influence of diffusion barriers on stability at elevated temperatures as part of a larger study.

The experimental multilayer structure used contained three layers: a 45-nm-thick chromium oxide layer on a copper substrate, a 30-nm-thick metallic chromium layer in the middle and a chromium oxide layer with a thickness of 45 nm on the top. The simulated solar absorptance of the 3-layer stack of Cr_2O_3(45 nm)/Cr(30 nm)/Cr_2O_3(45 nm) was 0.86 and the thermal emittance 0.01. Figure 10 a) presents a schematic structure of the experimental $CrO_x/Cr/CrO_x$ multilayer absorber. Thermal studies were performed on the CrO_x(45 nm)/Cr(30 nm)/CrO_x(45 nm) multilayer absorber. It was demanding to produce the gradient structure for chromium oxide coatings (without nitrogen), and the structure obtained included only metallic Cr or oxygen-rich CrO_x because of the sudden transition mode from Cr to Cr_2O_3 (see Figure 11) despite altering the gas flows or the sputtering power during deposition. Similar behaviour has been reported for chromium earlier [118]. The deposition rate ratio for metals/composites is relatively small (3-4) for nitrides but achieves high (10-15) values for oxides [245]. The experimental deposition rate for metallic Cr was 3-4 nm/s with the parameters used and approximately 0.8 nm/s for oxygen-rich CrO_x.

The gradient profile in the stoichiometry of the experimental coatings was prepared with chromium nitride and chromium oxide layers. However, the experimental gradient structure included only two layers. The chromium nitride and oxide layers were deposited on copper substrates by using reactive DC magnetron sputtering with argon/nitrogen and argon/oxygen gas mixtures. Figure 10 b) presents a schematic picture of the experimental CrN_y/CrO_x gradient absorber. The coating layer thicknesses of CrN_y and CrO_x varied from 50 nm to 100 nm. The third experimental absorber was DC magnetron sputtered $TiAlSiO_xN_y$ with a PECVD SiO_x AR coating. The absorber was on a Cu substrate. Similar commercially available absorber coatings were studied on Al profiles in this thesis (absorbers 10 and 11 in Table 3). The experimental $TiAlSiO_xN_y/SiO_x$ absorber was deposited at the factory of the commercial manufacturer.

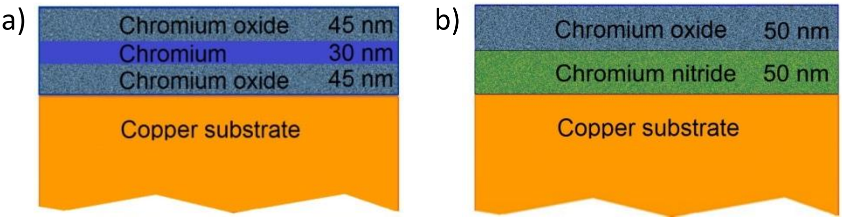

Figure 10. The DC magnetron sputtered experimental absorber coatings on copper substrate: a) $CrO_x/Cr/CrO_x$ multilayer absorber, and b) CrN_y/CrO_x absorber.

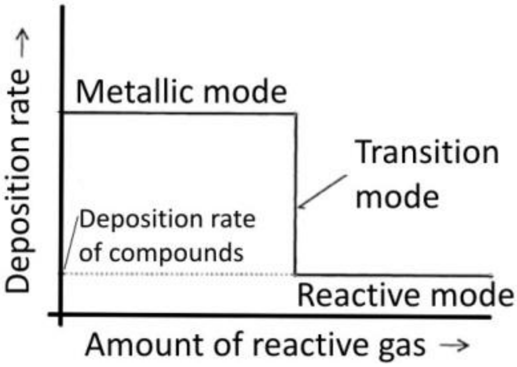

Figure 11. The reactive sputtering process is divided into three modes: metallic, transition and reactive mode, according to the amount of reactive gas used in the film deposition. Reactive magnetron sputtering has a low deposition rate of compounds compared to that of the pure metallic or alloyed films produced in the metallic mode. [245]

The deposition parameters of the experimental absorber coatings prepared at TUT are presented in Table 4. The sputtering magnetron targets were balanced type magnetrons. The substrates were at a floating potential, i.e. not grounded, during the deposition run. The substrate distance from the target was 80 mm. The repeatability of the experimental absorbers was appropriate according to visual inspection, measured optical properties and FESEM analysis. The range of variation in the deposition parameters (gas flows, total pressure and sputtering power) during deposition was negligible. The sources of error were the timing of the deposition and moving the substrate to the deposition area. The substrate was transferred to the deposition region after the glow discharge was initiated and out of the region after a certain coating layer had been deposited while the plasma was still on. During deposition, the substrate positioning was stationary. The estimated timing error was of the order of ± 2 s. The sputtering system was not equipped with a shutter between the target and the substrate.

Table 4. DC magnetron sputtering deposition parameters for the experimental absorber coatings.

Deposition parameters	**Experimental absorber coating layers**		
	Metallic Cr	**CrO_x**	**CrN_y**
Base pressure	$2\cdot10^{-5}$ mbar	$2\cdot10^{-5}$ mbar	$2\cdot10^{-5}$ mbar
Current	2 A	2 A	2 A
Voltage and power	420 V, 840 W	460 V, 920 W	410-420 V, 820-840 W
Argon (99.99 %) flow	200 sccm	200 sccm	200 sccm
Oxygen (99.999 %) flow	-	24 sccm (11 % of total flow)	-
Nitrogen (99.95 %) flow			25, 50 and 100 sccm (11-33 % of total flow)
Pressure during deposition (mbar)	$1.2\cdot10^{-2}$	$1.3\cdot10^{-2}$	$1.3\cdot10^{-2}$ - $3.0\cdot10^{-2}$
Deposition rate (nm/s)	~3-4	~1	~2 (25 sccm)… ~1 (100 sccm)
Target size Ø (mm)	150		

5.1.3 *Diffusion barrier coatings*

Two different experimental diffusion barriers were investigated: tantalum nitride and aluminium. The diffusion barriers were DC magnetron sputtered with the same equipment as the experimental absorber coatings. The deposition parameters are presented in Table 5.

Table 5. Sputtering deposition parameters for the experimental diffusion barrier coatings.

Deposition parameters	Experimental diffusion barriers	
	TaN_x	Al
Base pressure	$2\cdot10^{-5}$ mbar	$2\cdot10^{-5}$ mbar
Current	2 A	2 A
Voltage and power	420 V, 840 W	400 V, 800 W
Argon (99.99 %) flow	200 sccm	200 sccm
Nitrogen (99.95 %) flow	10, 25 and 50 sccm (5-20 % of total flow)	-
Pressure during deposition (mbar)	$1.2\cdot10^{-2}$ - $1.4\cdot10^{-2}$	$1.2\cdot10^{-2}$
Deposition rate (nm/s)	~2-3 (10 sccm)… ~2 (50 sccm)	~2
Target size Ø (mm)	150	150

The tantalum nitride (TaN_x) coatings were deposited on the copper substrates by reactive sputtering from the metallic Ta target in nitrogen gas (N_2). The tantalum target had a purity of 99.95 % (Kurt J. Lesker Company Ltd., UK). The N_2 flow was varied from 10 to 50 sccm while the argon flow remained constant at 200 sccm. In the absorbers for the ageing studies, a N_2 flow of 10 sccm (5 % of total flow) was used. For the ageing studies, the TaN_x coating thicknesses were 20 nm, 40 nm, and 60 nm. Two different absorber coatings were deposited on top of TaN_x diffusion barriers: a multilayer chromium oxide absorber coating CrO_x(45 nm)/Cr(30 nm)/CrO_x(45 nm) (Figure 10 a) and $TiAlSiO_xN_y/SiO_x$ absorber.

Another diffusion barrier coating studied was metallic aluminium (Al). Aluminium layers with thicknesses of 100 nm and 500 nm were experimentally sputtered on the top of copper substrate. The aluminium target had a purity of 99.99 % (Kurt J. Lesker Company Ltd., UK). During deposition, the argon flow was kept constant at 200 sccm. The experimental multilayer absorber (Figure 10 a) was deposited on the Al diffusion barrier.

In the industrial absorber coatings studied, the electroplated black chromium absorber on nickel-coated copper (absorber 7) can be considered to have a 3-µm-thick Ni layer as a diffusion barrier. The Ni layer has been reported to increase the thermal and corrosion resistance of black chromium coatings on Cu [22, 95].

5.2 Research methods and equipment

The thermal ageing properties of the solar absorbers were investigated by exposing samples to elevated temperatures in a circulating air furnace. Accelerated ageing studies near the stagnation temperature and short heat treatments up to 500 °C were performed. The ageing mechanisms were observed by studying changes in the optical properties, microstructures and compositions of the absorber surfaces before and after the thermal exposure. Ageing phenomena were investigated using several research instruments. Optical properties were measured with UV/Vis/NIR and FTIR spectrometers, microstructures were characterized using scanning and transmission electron microscopes, and composition by elastic recoil detection analysis and X-ray photoelectron spectroscopy.

5.2.1 Thermal accelerated ageing studies

Accelerated ageing tests at high temperatures are presented in ISO standard draft EN 12975-3-1 (2011) [24]. Detailed information about accelerated ageing studies are discussed in the following publications: [18, 22, 23, 246, 247]. The ageing studies were performed in a circulating air furnace (see section 5.2.3) at two different temperatures near the stagnation temperature of the absorber coatings.

In this study, the testing period was prolonged to 600 hours for all samples. The aim of the standard test proposal is to investigate whether the absorber reaches a lifetime of 25 years. We utilized the standard proposal in a way more appropriate for investigating the ageing processes in more detail. In the standard proposal [24], the test is completed after the performance criterion (PC) exceeds 0.05 but we continued the test to 600 hours in order to obtain more information about the ageing phenomena.

To pass the accelerated ageing test, the effect of degradation on the efficiency of the collector must be less than 5 % after 25 years [24]. The performance criterion (PC) is determined to quantify the ageing, and is calculated from the optical properties in the accelerated ageing test. Previously, PC values were calculated by equation (1):

$$PC = \Delta\alpha - 0.25 * \Delta\varepsilon \leq 0.05 \qquad (1)$$

where $\Delta\alpha$ and $\Delta\varepsilon$ are changes (as-deposited minus aged) in solar absorptance and thermal emittance [21, 22]. At low stagnation temperatures (<< 200 °C), the equation with a quarter of the weight of Ɛ is suitable. However, for modern collectors with higher stagnation temperatures the thermal load is higher, and thus the emittance weighs more in ageing behaviour [248]. The PC values for the modern solar thermal collectors are calculated by equation (2) [18, 24], which is the PC equation used in this work:

$$PC = \Delta\alpha - 0.5*\Delta\varepsilon \leq 0.05 \qquad (2)$$

The test temperature is dependent on the optical properties of the absorber [18, 24]. Table 6 presents the stagnation temperatures as a function of solar absorptance and thermal emittance. The calculation of the stagnation temperature is based on assumptions that the collector tilt angle is set equal to 45°, glass emittance 0.88, solar irradiation 1000 W/m^2, ambient temperature 30 °C, wind heat transfer coefficient 10 W/m^2K (as hot sunny days are usually windless), heat loss coefficient of the collector frame and back 0.9 W/m^2K, and solar transmittance of the glazing 0.9 (standard collector) and 0.95 (collector with AR-coated glass). The calculation of the stagnation temperature showed good agreement with experimental data recorded on a sunny day in Germany in a typical flat plate collector. The stagnation conditions have been assumed to occur 30 days per year [18, 22], and this period would then dominate the ageing load.

The effective mean temperature (T_{eff}) is the respective constant temperature load as a function of the maximum stagnation temperature and the activation energy. The effective mean temperature is dependent on the activation energy, which means that exposure periods with relatively high temperatures are crucial and dominate the ageing process. In [22], Carlsson *et al.* noticed that the period when a solar collector is operating at stagnation conditions determined the effective mean temperature of the absorber, although it represented only one month of the year. The effective mean temperature is evaluated from a yearly-based frequency function for the service temperature of the absorber surface with assumptions that the night temperature is 15 °C and the shape of temperature curve corresponds to the temperature curve of a selective absorber in a ventilated flat-plate collector measured on a sunny day in Freiburg during stagnation [18]. The effective mean temperature can be calculated by using re-scaling of a temperature histogram for 30 days of stagnation (Figure 12 a) but in this study, the measured data with stagnation temperature of 185 °C was used to determine the effective mean temperature (Figure 12 b). T_{abs} (°C) a)

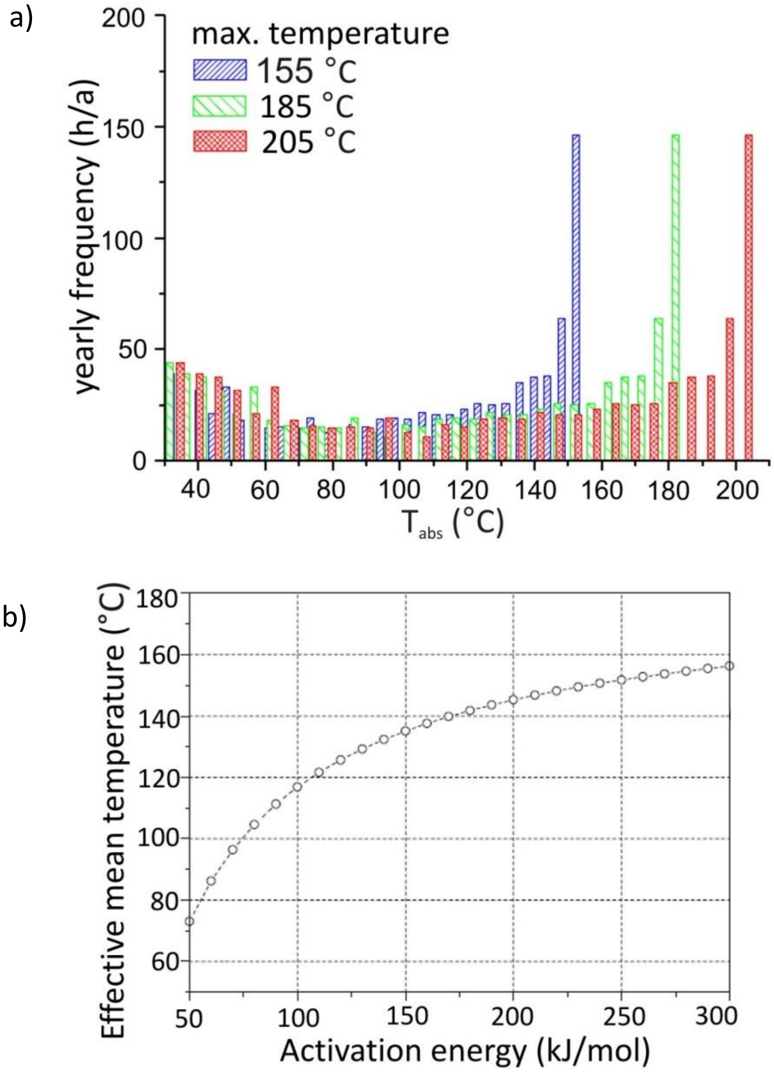

Figure 12. a) Histogram for flat-plate absorber temperatures for 30 days of stagnation. The measured data had stagnation temperature of 185 °C and other temperatures (155 °C and 205 °C) are computed according to the measured data [18], and b) effective mean temperature (T_{eff}) for the 30-day stagnation histogram for stagnation temperature 185 °C as a function of the activation energy of the dominating degradation process [18].

The same degradation can be achieved by exposure at a higher temperature for a shorter time interval. Equation (3) can be used to calculate the equivalent testing time for a high-temperature test at T_R corresponding to an in-service time of 25 years with the activation energy and the maximum stagnation temperature as parameters [18]. Test temperature T_1 ($T_1 = T_R$ in equation (3)) was defined to fulfil the requirements that the maximum t_1 is 600 h and activation energy is > 50 kJ/mol. Test first temperature T_1 can be calculated from equation (3) using assumptions of t_r = 600 h and E_T = 50 kJ/mol. Table 7 presents the testing temperatures as a function of stagnation temperature for accelerated ageing studies. For example, if the solar absorptance (α) is 0.95 and thermal emittance (ε) is 0.05, the stagnation temperature is 204 °C (see Table 6) and the first testing temperature is defined as 278 °C (see Table 7).

$$t_R = 25 \text{ years} \exp\left[-\frac{E_T}{R}\left(\frac{1}{T_{eff}} - \frac{1}{T_R}\right)\right] \tag{3}$$

In this work, the measured solar absorptance values of the industrial absorbers were 0.92…0.97 and the emittance values 0.03…0.23. The average of measured solar absorptance was 0.95 ± 0.02 and thermal emittance 0.08 ± 0.02. The thermal emittance of absorbers on stainless steel (absorbers 8 and 9) was disregarded because they were significantly higher (0.23 and 0.14, respectively) than the others, and stainless steel substrates have reported to withstand high temperatures well [2, 78]. Without the SS absorbers, the average thermal emittance was 0.06 ± 0.02. Thus, ageing studies were performed at 278 °C for all of the industrial absorber coatings in order to simplify the test and to obtain comparable results.

The absorbers were placed from room temperature into the furnace after the test temperature had been reached. Exposure periods were 36, 75, 150, 300 and 600 hours. After each period, three sample pieces of the absorber were removed from the furnace to cool down to room temperature on an insulating material. The samples were placed in the furnace at the same time but after each exposure period some of the samples were removed and others continued their exposure in the furnace, until 600 hours were reached. In the ISO standard draft [24], the test is stopped after reaching PC > 0.05 but in this work the test was prolonged to 600 h for all of the samples. Time t_1 was determined as the last testing time with PC < 0.05. The second test was performed at a temperature 30 °C higher (T_3 = 308 °C) or lower (T_2 = 248 °C) according to Figure 13 and Table 7. In order to obtain more information about the degradation process, the tests were also performed at the higher temperature T_3 for the absorbers which were determined to study at the lower temperature T_2. Testing time periods for T_2 and T_3 included the period from Table 7 and about half of that time period. The qualification procedure was determined by optical ageing in these temperatures according to Figure 13 [24] but adhesion was not measured in this study.

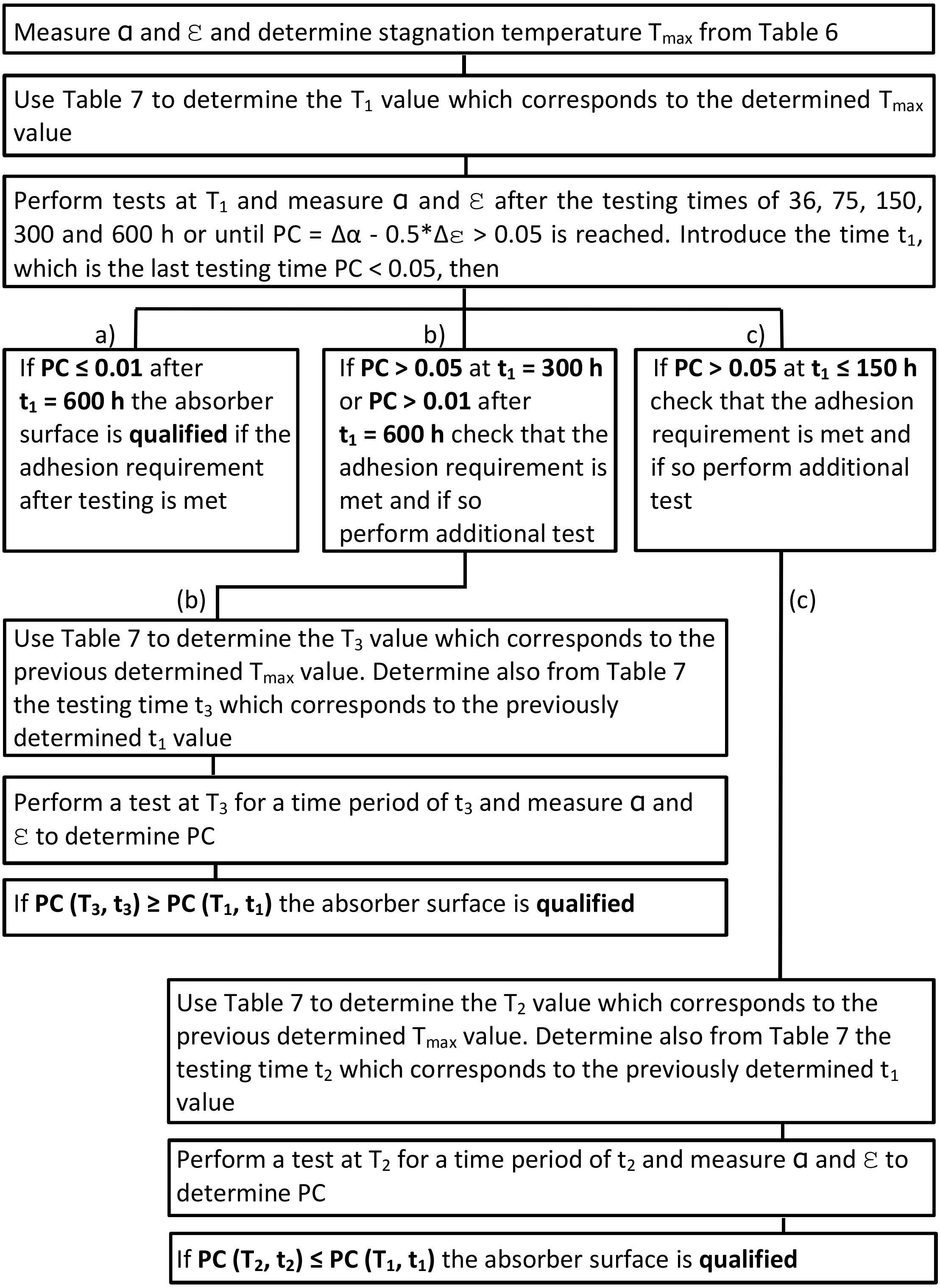

Figure 13. Accelerated ageing test procedure and qualification scheme for testing thermal stability of solar absorbers [24].

Table 6. Relation between optical properties of the solar absorber and stagnation temperature. The row α(AR) corresponds to the solar collectors with anti-reflecting glazing leading to higher stagnation temperatures. [24]

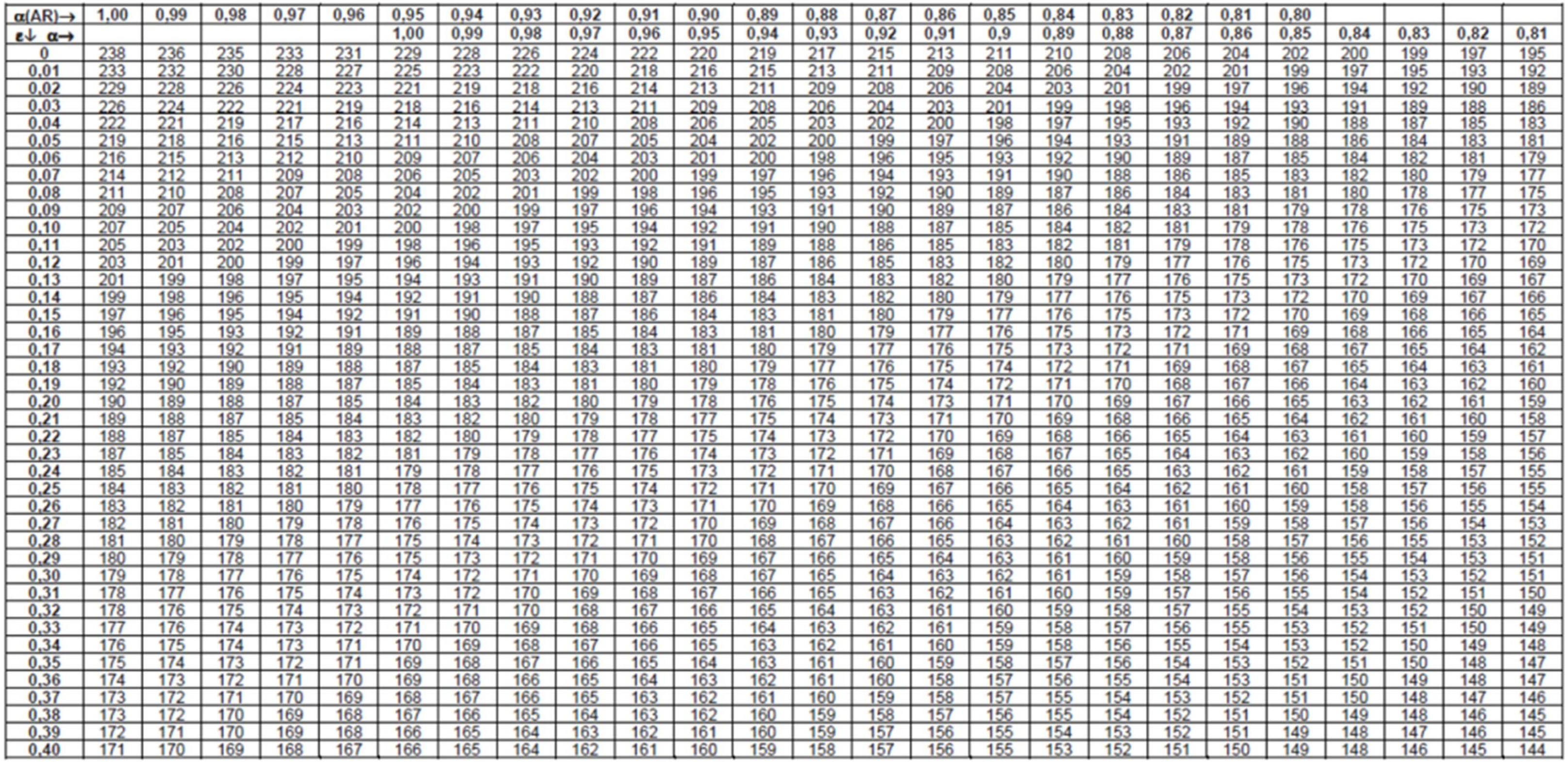

α(AR)→	1,00	0,99	0,98	0,97	0,96	0,95	0,94	0,93	0,92	0,91	0,90	0,89	0,88	0,87	0,86	0,85	0,84	0,83	0,82	0,81	0,80				
ε↓ α→						1,00	0,99	0,98	0,97	0,96	0,95	0,94	0,93	0,92	0,91	0,9	0,89	0,88	0,87	0,86	0,85	0,84	0,83	0,82	0,81
0	238	236	235	233	231	229	228	226	224	222	220	219	217	215	213	211	210	208	206	204	202	200	199	197	195
0,01	233	232	230	228	227	225	223	222	220	218	216	215	213	211	209	208	206	204	202	201	199	197	195	193	192
0,02	229	228	226	224	223	221	219	218	216	214	213	211	209	208	206	204	203	201	199	197	196	194	192	190	189
0,03	226	224	222	221	219	218	216	214	213	211	209	208	206	204	203	201	199	198	196	194	193	191	189	188	186
0,04	222	221	219	217	216	214	213	211	210	208	206	205	203	202	200	198	197	195	193	192	190	188	187	185	183
0,05	219	218	216	215	213	211	210	208	207	205	204	202	200	199	197	196	194	193	191	189	188	186	184	183	181
0,06	216	215	213	212	210	209	207	206	204	203	201	200	198	196	195	193	192	190	189	187	185	184	182	181	179
0,07	214	212	211	209	208	206	205	203	202	200	199	197	196	194	193	191	190	188	186	185	183	182	180	179	177
0,08	211	210	208	207	205	204	202	201	199	198	196	195	193	192	190	189	187	186	184	183	181	180	178	177	175
0,09	209	207	206	204	203	202	200	199	197	196	194	193	191	190	189	187	186	184	183	181	179	178	176	175	173
0,10	207	205	204	202	201	200	198	197	195	194	192	191	190	188	187	185	184	182	181	179	178	176	175	173	172
0,11	205	203	202	200	199	198	196	195	193	192	191	189	188	186	185	183	182	181	179	178	176	175	173	172	170
0,12	203	201	200	199	197	196	194	193	192	190	189	187	186	185	183	182	180	179	177	176	175	173	172	170	169
0,13	201	199	198	197	195	194	193	191	190	189	187	186	184	183	182	180	179	177	176	175	173	172	170	169	167
0,14	199	198	196	195	194	192	191	190	188	187	186	184	183	182	180	179	177	176	175	173	172	170	169	167	166
0,15	197	196	195	194	192	191	190	188	187	186	184	183	181	180	179	177	176	175	173	172	170	169	168	166	165
0,16	196	195	193	192	191	189	188	187	185	184	183	181	180	179	177	176	175	173	172	171	169	168	166	165	164
0,17	194	193	192	191	189	188	187	185	184	183	181	180	179	177	176	175	173	172	171	169	168	167	165	164	162
0,18	193	192	190	189	188	187	185	184	183	181	180	179	177	176	175	174	172	171	169	168	167	165	164	163	161
0,19	192	190	189	188	187	185	184	183	181	180	179	178	176	175	174	172	171	170	168	167	166	164	163	162	160
0,20	190	189	188	187	185	184	183	182	180	179	178	176	175	174	173	171	170	169	167	166	165	163	162	161	159
0,21	189	188	187	185	184	183	182	180	179	178	177	175	174	173	171	170	169	168	166	165	164	162	161	160	158
0,22	188	187	185	184	183	182	180	179	178	177	175	174	173	172	170	169	168	166	165	164	163	161	160	159	157
0,23	187	185	184	183	182	181	179	178	177	176	174	173	172	171	169	168	167	165	164	163	162	160	159	158	156
0,24	185	184	183	182	181	179	178	177	176	175	173	172	171	170	168	167	166	165	163	162	161	159	158	157	155
0,25	184	183	182	181	180	178	177	176	175	174	172	171	170	169	167	166	165	164	162	161	160	158	157	156	155
0,26	183	182	181	180	179	177	176	175	174	173	171	170	169	168	166	165	164	163	161	160	159	158	156	155	154
0,27	182	181	180	179	178	176	175	174	173	172	170	169	168	167	166	164	163	162	161	159	158	157	156	154	153
0,28	181	180	179	178	177	175	174	173	172	171	170	168	167	166	165	163	162	161	160	158	157	156	155	153	152
0,29	180	179	178	177	176	175	173	172	171	170	169	167	166	165	164	163	161	160	159	158	156	155	154	153	151
0,30	179	178	177	176	175	174	172	171	170	169	168	167	165	164	163	162	161	159	158	157	156	154	153	152	151
0,31	178	177	176	175	174	173	172	170	169	168	167	166	165	163	162	161	160	159	157	156	155	154	152	151	150
0,32	178	176	175	174	173	172	171	170	168	167	166	165	164	163	161	160	159	158	157	155	154	153	152	150	149
0,33	177	176	174	173	172	171	170	169	168	166	165	164	163	162	161	159	158	157	156	155	153	152	151	150	149
0,34	176	175	174	173	171	170	169	168	167	166	165	163	162	161	160	159	158	156	155	154	153	152	150	149	148
0,35	175	174	173	172	171	169	168	167	166	165	164	163	161	160	159	158	157	156	154	153	152	151	150	148	147
0,36	174	173	172	171	170	169	168	166	165	164	163	162	161	160	158	157	156	155	154	153	151	150	149	148	147
0,37	173	172	171	170	169	168	167	166	165	163	162	161	160	159	158	157	155	154	153	152	151	150	148	147	146
0,38	173	172	170	169	168	167	166	165	164	163	162	160	159	158	157	156	155	154	152	151	150	149	148	146	145
0,39	172	171	170	169	168	166	165	164	163	162	161	160	159	157	156	155	154	153	152	151	149	148	147	146	145
0,40	171	170	169	168	167	166	165	164	162	161	160	159	158	157	156	155	153	152	151	150	149	148	146	145	144

Table 7. The first accelerated ageing test temperature (T_1) is defined according to the stagnation temperature (T_{max}) of the absorber (see Table 6). The second test temperature (T_2 or T_3) and time period depends on the ageing in the first test temperature. [24]

T_{max} (°C)	T_1 (°C)	T_2 (°C)	t_2 (h) (t_1 = 18 h)	t_2 (h) (t_1 = 36 h)	t_2 (h) (t_1 = 75 h)	t_2 (h) (t_1 = 150 h)	T_3 (°C)	t_3 (h) (t_1 = 300 h)	t_3 (h) (t_1 = 600 h)
< 90	137	107	361	493	689	953	167	83	221
91–100	149	119	321	443	627	877	179	88	233
101–110	160	130	283	397	570	808	190	93	244
111–120	172	142	251	356	519	746	202	98	256
121–130	184	154	222	320	474	690	214	103	267
131–140	196	166	198	289	434	641	226	108	278
141–150	208	178	177	262	400	598	238	114	289
151–155	215	185	168	250	384	578	245	116	294
156–160	221	191	159	239	369	559	251	119	299
161–165	227	197	151	229	355	542	257	121	304
166–170	233	203	144	219	342	525	263	124	309
171–175	240	210	137	210	330	510	270	127	314
176–180	246	216	131	201	319	495	276	129	319
181–185	252	222	125	193	308	481	282	132	323
186–190	259	229	120	186	298	468	289	134	328
191–195	265	235	114	179	289	456	295	136	333
196–200	272	242	110	173	280	444	302	139	337
201–205	278	248	105	166	272	433	308	141	342
206–210	285	255	101	161	264	423	315	144	346
211–215	291	261	97	155	256	413	321	146	350
216–220	298	268	94	150	249	403	328	148	355
221–225	304	274	90	146	243	394	334	151	359
226–230	311	281	87	141	236	386	341	153	363

The thermal degradation processes can be accelerated by raising the temperature. The test procedure [24] is based on the assumption that the temperature dependence of degradation can be described by the Arrhenius relationship, which means that the degradation is caused by chemical processes, diffusion processes or desorption. Furthermore, it is presumed that only one mechanism of degradation is active at a time. [23] For ageing caused by chemical or diffusion or desorption processes, the kinetics of the degradation are temperature-dependent according to the Arrhenius relationship [23], as presented in equation (4).

$$a_n = \exp\left[\frac{E_T}{R}\left(\frac{1}{T_{ref}} - \frac{1}{T_n}\right)\right], \tag{4}$$

where E_T is the activation energy according to Arrhenius, R is the ideal gas constant (R = 8.314 J K^{-1} mol^{-1}), t_{ref} is the time period during which an absorber is exposed to a specific load (for example oxidation at temperature T_{ref}), and t_n is the time period during which the same absorber achieves the same degradation (oxidation at higher temperature T_n). The acceleration obtained by a temperature change from the time periods during similar degradations is defined by equation (5) [23]:

$$a_n = \frac{t_{ref}}{t_n} \tag{5}$$

The Arrhenius activation energy E_T can be defined from two known degradations at two different temperatures by combining equations (4) and (5):

$$E_T = R\,\frac{\ln(t_1) - \ln(t_2)}{{T_1}^{-1} - {T_2}^{-1}} \tag{6}$$

To define the Arrhenius activation energy for service lifetime estimation, Arrhenius behaviour was assumed. The known degradations were determined from PC = 0.05 regarding the two testing temperatures defined in the accelerated ageing procedure [24]. The equivalent time for PC = 0.05 was estimated from a PC versus time graph. The activation energy illustrates the degradation acceleration as a function of time and temperature: the higher the activation energy, the stronger the acceleration at elevated temperatures. The service lifetime was defined according to the procedure [24] to estimate the significance of ageing mechanisms. The failure time (i.e. service lifetime) of the absorber can be determined according to equation (7):

$$t_2 = t_1 \exp\left[-\frac{E_T}{R}\left(\frac{1}{T_1} - \frac{1}{T_{eff}}\right)\right] \tag{7}$$

Arrhenius behaviour was assumed, but the validity of the Arrhenius relationship can be evaluated with Arrhenius time-transformation for at least two test temperatures by equation (7). If the time-transformations are in good relation (located on the same curve), the Arrhenius relationship can be assumed to be valid.

According to the qualification procedure (Figure 13), qualification of the absorbers depends on the PC values in the two different test temperatures as explained with the example in Figure 14. In the example, PC = 0.05 is reached after 142 h at 278 °C. Activation energy has been assumed to be 100 kJ/mol (based on studies at other temperatures). When an absorber is used in a flat plate collector for DHW production, the absorber surface is exposed to an operating temperature range that may vary from about -20 °C up to the stagnation temperature (more than 200 °C). T_{eff} was evaluated to be 120 °C according to a new thermal load histogram (30 sunny stagnation days in a year, as in central Europe in the summer of 2003) for a stagnation temperature of 185 °C [249]. The service lifetime of 25 years is achieved if PC = 0.05 at 308 °C after ≤ 45 h. If the PC value is lower than 0.05 after 45 h (i.e. PC = 0.05 after a longer time period), the absorber has a lower activation energy, which leads to failure in the procedure because of a reduced service lifetime. Conversely, to pass at the lower temperature of 248 °C, the PC value needs to be 0.05 after ≥ 513 h.

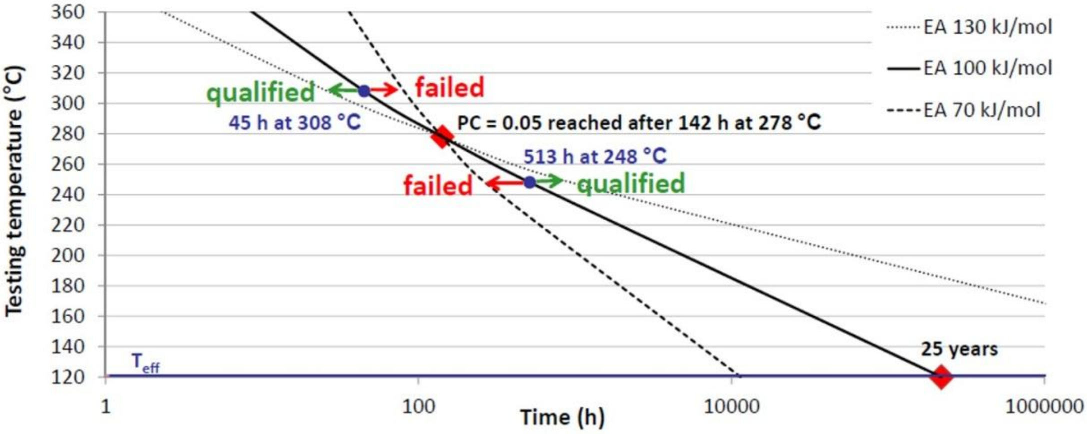

Figure 14. Qualification of the absorbers in accelerated ageing test depends on the PC values and activation energy.

In addition to the calculations of the activation energy from PC values as defined in the accelerated ageing test [24], the activation energy was determined separately for solar absorptance and thermal emittance. The activation energy was calculated from the slopes of ln(Δα) or ln(Δε) versus 1/T. The difference in absorptance and emittance during ageing is expressed for a specific time in measurement points and using interpolation in appropriate cases.

In addition to the testing temperatures of the accelerated ageing test [24], some of the absorbers (1-4) were investigated in preliminary study at 250 °C for 36 h, 75 h, 150 h, 300 h, and 600 h. The accelerated ageing test [24] recommends the assessment of the adhesion of aged samples using the pull-off or tape test but adhesion was not measured in the present study.

5.2.2 *Short-period heat treatments*

Short-period heat treatments were performed in a circulating air furnace at 300 °C, 400 °C and 500 °C for two hours for industrial absorbers, and also at 200 °C for experimental absorbers. 400 °C or 500 °C is an extreme temperature for flat plate collector absorber coatings for DHW or space heating applications. The purpose of the short-period heat treatments at these extreme temperatures was to obtain more information about the ageing mechanisms and to provide further information for the development of high-temperature absorber coatings. PC values were calculated for heat-treated samples using equation (2).

The absorber samples were placed in a cold furnace and then the furnace was heated to the testing temperature. The heating rates were 7.5 °C/min, 7.1 °C/min, 6.6 °C/min and 6.0 °C/min for 200 °C, 300 °C, 400 °C and 500 °C, respectively. The testing temperature was maintained for two hours. Then the samples were cooled to about 100 °C inside the furnace with air circulation on, heating off and fresh air was released into the furnace from an exhaust pipe. The cooling rates were 1.4 °C/min, 1.7 °C/min, 2.2 °C/min and 2.4 °C/min for 200 °C, 300 °C, 400 °C and 500 °C, respectively. The temperature curves for short-period heat treatments at 300-500 °C are presented in Figure 15. After the samples were cooled down to 100 °C, the furnace door was opened and the samples were taken out to room temperature and placed on a thermal insulating ceramic material.

The activation energy was determined for solar absorptance and thermal emittance for short-period heat treatments. The activation energy was calculated from the slopes of $\ln(\Delta\alpha)$ or $\ln(\Delta\varepsilon)$ versus $1/T$ for a time period of two hours.

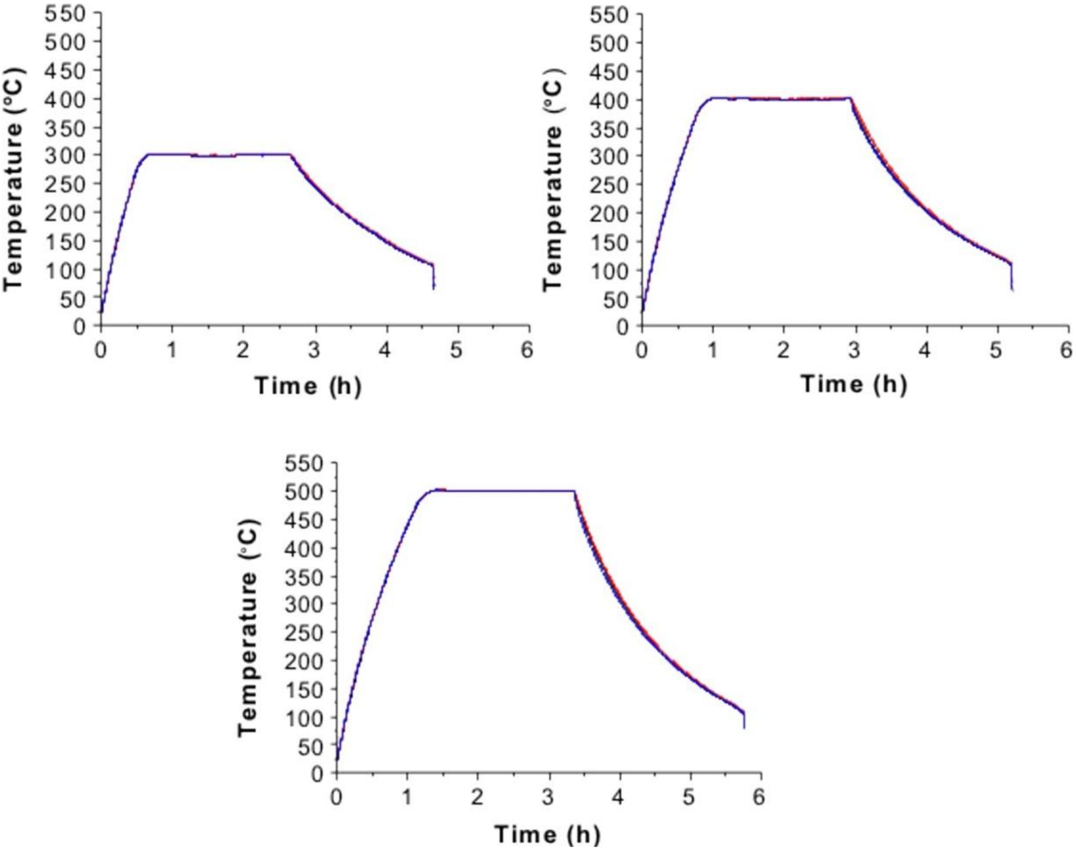

Figure 15. Temperature curves for short-period heat treatments at 300 °C, 400 °C, and 500 °C including heating, two hours of maintenance and cooling.

5.2.3 Circulating air furnace for ageing studies

The accelerated ageing studies and short heat treatments were performed in a Heraeus WU 6100 circulating air furnace at TUT. The maximum temperature was 500 °C. The dimensions of the furnace chamber are 475 mm x 475 mm x 420 mm and volume 95 l. The furnace has a K-type thermocouple for temperature measurements and the temperature was controlled with a Thermicon P microprocessor. For high-temperature studies of materials with special optical properties, the circulating air furnace is preferable because the turbulent stream of hot air creates a higher temperature uniformity inside and the samples and temperature sensors obtain the same temperature load [249].

To ensure accurate enough temperature measurements, modifications were made to the furnace: three Pt-100 temperature sensors were added inside the furnace along with a data recorder system with PromoLog Lite data acquisition software to measure and collect the temperature data from different positions in the furnace. The sensors were located in different places in the furnace to define the volume at which the temperature uniformity stays at the required ± 1 °C [24]. According to these temperature-control studies, it was decided to position the samples quite centrally in the furnace but not directly in front of the circulating propeller. The sensors were then placed around this volume of the furnace; one down in the front left corner (channel 3 in Figure 16), another up in the back right corner (channel 5) and a third in the middle (channel 7). After the temperature had settled, the temperature average of the three sensors was 248.0 °C, 278.0 °C, or 308.0 °C, depending on the setting adjustment in the accelerated ageing studies. When the furnace door was opened, the temperature decreased by about 50 °C. The exposure time at the lower temperature was approximately one minute. During the time that the furnace door was opened, the samples were removed from the furnace, the door was closed again and the temperature had reached the normal exposure temperature. The temperature uniformity in the volume where the samples were placed is presented in Figure 16 for the three temperature sensors at 278 °C. The temperature averages according to the sensors were 277.8 °C, 278.1 °C, and 278.0 °C for sensors 3, 5, and 7, respectively. Thus, in this work, the temperature uniformity was well within the required ± 1 °C. The standard proposal also requires a temperature accuracy of ± 1 °C after the temperature has settled [24]. In this work, the temperature accuracy after stabilization was about ± 1.5 °C as shown in Figure 16. For short-period heat treatments, the average from the three sensors after the temperature had settled was 200.0 °C ± 0.7 °C, 300.0 ± 0.8 °C, 401.0 ± 1.1 °C, and 500.5 ± 1.1 °C. The temperature stabilization in the ageing test has a significant effect on the ageing rate, as Köhl presented in [18]. In this work, the stability of the temperature created the biggest uncertainty in the results due to the temperature variation after stabilization and especially after the furnace door was opened and closed again.

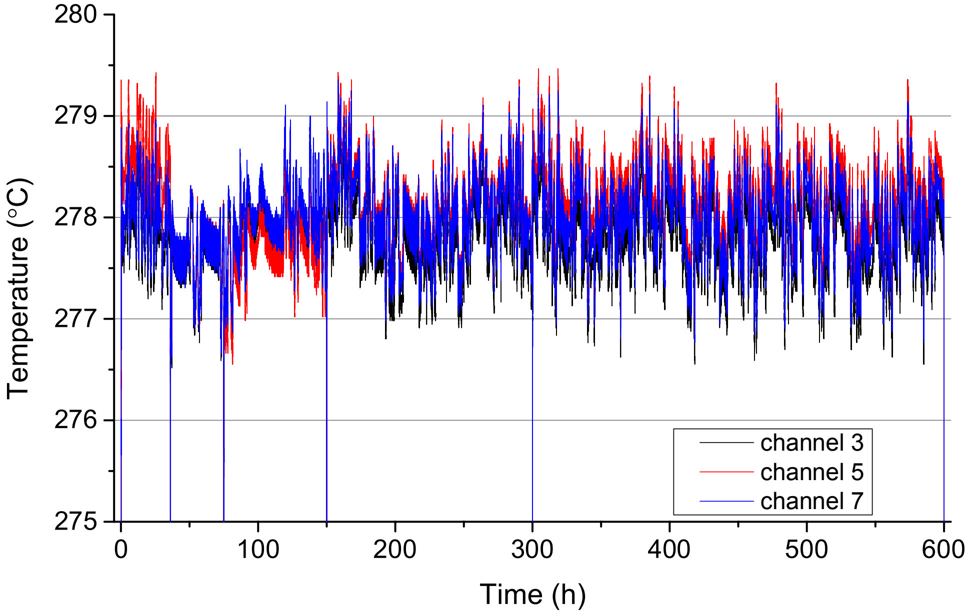

Figure 16. Homogeneity of the temperature inside the Heraeus furnace at 278 °C measured by three temperature sensors in different positions in the furnace (channels 3, 5 and 7). The temperature accuracy is about ± 1.5 °C. The furnace door was opened at 36 h, 75 h, 150 h, 300 h, and 600 h (vertical lines below normal variation).

The standard proposal 12975-3-1 states accurate limits for the temperature uniformity (± 1 °C) in the furnace and for the temperature-maintaining level (± 1 °C) after stabilized conditions have been reached after the start of the test [24]. A lot of effort was put into finding a furnace that would meet the requirements of the standard proposal but no such furnace was available commercially. Even the furnaces used in [22] were said to have a greater temperature variation than the required ± 1 °C. We were unable to find any furnaces fulfilling the ± 1 °C temperature accuracy requirement. The Heraeus WU 6100 furnace was the closest to reaching the requirements. In the furnace the maintaining level was said to be ± 0.5 °C, but the temperature uniformity inside the furnace was said to be only ± 1 °C at 100 °C, ± 1,5 °C at 200 °C, ± 2 at 300 °C, and ± 3 °C at 400 and 500 °C. The unavailability of a furnace that is accurate enough is problematic because small temperature variations create relatively significant uncertainties in the results, as presented in Figure 17.

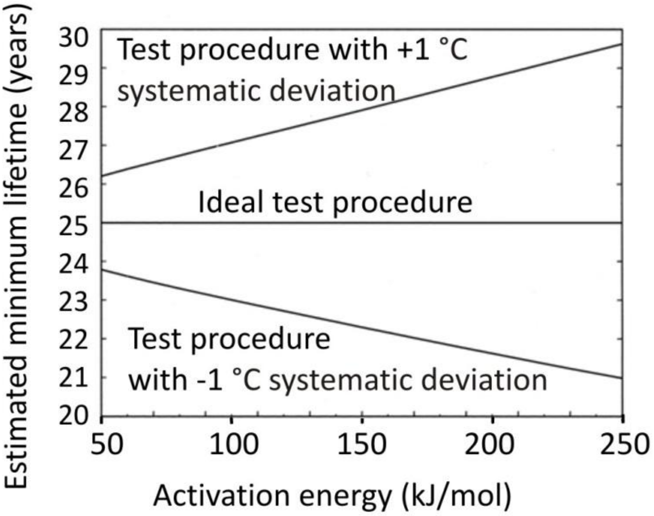

Figure 17. Change in the minimum lifetime resulting from test errors in the accelerated ageing test at high temperatures. For example, a test error of one degree Celsius in the accelerated test temperature affects the lifetime of the absorber. [249]

5.2.4 Spectroscopy to measure optical properties

The reflectance of absorber surfaces is typically measured with spectrophotometers with integrating spheres [250]. UV/Vis/NIR-spectrophotometers measure the solar spectrum range and IR spectrometers cover the infrared range. The optical properties of the absorbers were measured before and after the ageing studies. The performance criterion (PC) was calculated from the optical properties in the accelerated ageing test by means of equation (2).

UV/Vis/NIR spectrophotometer

Solar absorptance α was calculated for the AM1.5 spectrum from a hemispherical reflectance spectrum at a wavelength of 0.3-2.5 µm at a near-normal incident angle using a PerkinElmer Lambda 950 UV/Vis/NIR-spectrophotometer with an integrating sphere at the Optics and Molecular Materials laboratory of Aalto University, Espoo. In the integrating sphere, the inner walls and reference plate were made of Spectralon®. The absorptance of the Spectralon reference was effectively zero with a standard deviation of 0.002 (average of 10 measurements) covering the reproducibility of the measurements. The error of the spectrometer was estimated by measuring the same absorber sample five times on different days (over several years). The sample was originally chosen at random, and it was wrapped in silk paper at room temperature between the measurements. The solar absorptance average of five measurements was 0.944, the highest value was 0.963, the lowest 0.938, and the standard deviation 0.011. Although the error range was studied for only one absorber, the other absorbers were assumed to be in a similar range. Other error sources are discussed in the literature [250, 251]. In the results, solar absorptance values are presented as averages of (at least) three measurements.

The solar absorptance, α, was calculated from the measured reflectance ρ from 0.3 to 2.5 µm, as presented in equation (8):

$$\propto = (\int_{0.3\ \mu m}^{2.5\ \mu m} G(\lambda) * (1-\rho) d\lambda)/(\int_{0.3\ \mu m}^{2.5\ \mu m} G(\lambda) d\lambda) \qquad (8)$$

where G(Λ) is the solar spectral irradiance for air mass 1.5 [31], and a function of wavelength.

FTIR spectrophotometer

Thermal emittance ε measurements were performed at a near-normal incident angle using a Bruker Tensor 27 FTIR spectrometer (Bruker Optics, Germany) with a gold integrating sphere (Bruker A562-G/Q, Bruker Optics, Germany) with an MCT detector at TUT. The measuring wave number range was from 600 to 4000 cm^{-1} with a resolution of 4 cm^{-1}. The measurements were performed at room temperature. The emittance of the polished Cu reference was 0.040 ± 0.001 (average of 15 measurements) covering the reproducibility of the measurements. The error of the spectrometer was estimated by measuring the same absorber sample five times on different days (over several years). The sample was originally chosen at random, and it was wrapped in silk paper at room temperature between the measurements. The thermal emittance average of five measurements was 0.029, the highest value was 0.033, the lowest 0.022, and the standard deviation 0.005. The error range was studied for only one absorber, and the other absorbers were assumed to be in a similar range. Other error sources are discussed in the literature [250-253]. In the results, thermal emittance values are presented as averages of (at least) three measurements.

Thermal emittance was calculated from the reflectance measurements using a surface temperature of 100 °C. The infrared emittance, Ɛ, was determined by measuring the monochromatic reflectance ρ from 2.5 to 16.7 or to 22 µm by FTIR, as presented in equation (9):

$$\epsilon = \int_{2.5\ \mu m}^{16.7\ \mu m} E(\lambda, T) * (1 - \rho) d\lambda \,/ \int_{2.5\ \mu m}^{16.7\ \mu m} E(\lambda, T) d\lambda, \qquad (9)$$

where E is the Planck blackbody emittance at 100 °C, which is a function of the wavelength and the surface temperature. Equation (9) gives the normal emittance but the radiative heat losses of a solar absorber are given by the total hemispherical emittance. However, determining normal emittance is a commonly used procedure and it can often be converted to hemispherical by multiplication with a numerical factor [104].

The spectrometer measurements were calibrated with a similar Bruker Tensor 27 spectrometer at Uppsala University, Sweden. The main difference between the TUT and Uppsala Bruker equipment was that Uppsala has a broadband MCT detector (from 2.5 to 22 µm). At TUT the MCT detector was more accurate (less noise) but measured only up to 16.7 µm. Figure 18 presents emittance graphs of an absorber sample (3 pieces of the same absorber) and polished copper as reference measured by the FTIR spectrometers at Uppsala and TUT. The thermal emittance Ɛ was determined by measuring the spectral reflectance ρ from 2.5 to 16.7 µm. The graphs have been shifted to different levels but the shapes of the graphs were uniform. TUT’s equipment had higher emittance results than Uppsala’s, and the shift in the results was about 0.034. All of the pieces of the same absorber sample had similar emittance graphs with the same equipment. In this work, we use the emittance results calculated from TUT’s measurements without any correction coefficients. The measurements with the same equipment were comparable to each other.

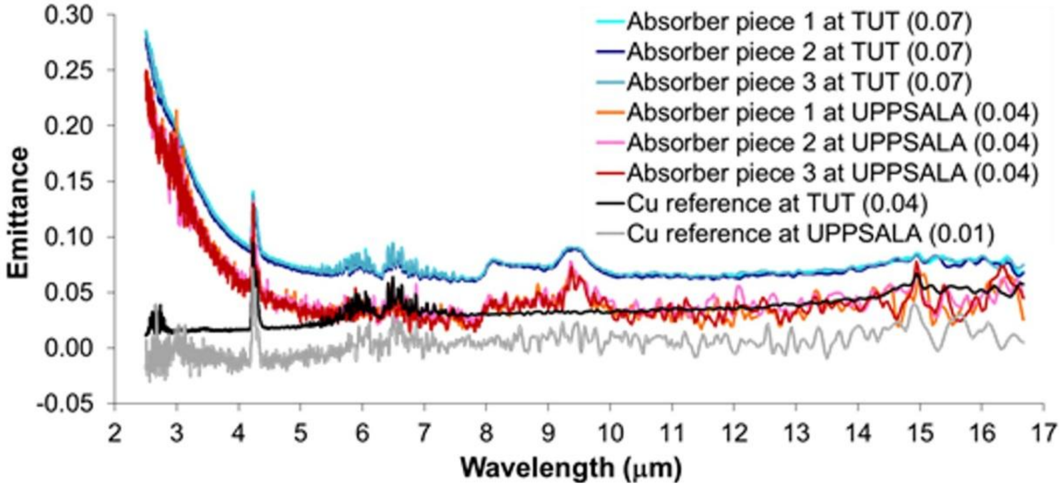

Figure 18. Calibration emittance measurements using FTIR spectrometers at TUT and Uppsala. The graphs have shifted to different levels but otherwise their shapes are similar. TUT's measurements had less noise than Uppsala's.

Error estimation of PC value

The error range of the PC value was calculated from the total differential of equation (2) according to the error ranges of solar absorptance and thermal emittance, as in equation (10):

$$\Delta_e PC = \left|\frac{dPC}{d\alpha}\right|\Delta_e\alpha + \left|\frac{dPC}{d\varepsilon}\right|\Delta_e\varepsilon = \Delta_e\alpha + 0.5\Delta_e\varepsilon, \qquad (10)$$

where $\Delta_e\alpha$ is error range of solar absorptance and $\Delta_e\varepsilon$ is the error range of thermal emittance. The error of solar absorptance and thermal emittance was estimated by measuring one random absorber sample five times independently (over several years) with both UV/Vis/NIR and FTIR spectrometers. The standard deviation of reproducibility measurements was 0.011 for solar absorptance and 0.005 for thermal emittance. Thus, the error range of PC is calculated by equation (11):

$$\Delta_e PC = 0.011 + 0.5*0.005 = 0.014 \qquad (11)$$

Even though the error range was estimated for only one absorber, it was considered to cover all of the absorber samples.

5.2.5 Microscopy for microstructural and layer thickness analyses

Investigations of the ageing mechanisms include microstructural and layer thickness analyses by Field-Emission Scanning Electron Microscope (FESEM) and Transmission Electron Microscope (TEM). Further information about the microscopes is given below.

Field-Emission Scanning Electron Microscope (FESEM)

Microstructural and morphological analyses were performed using a Zeiss ULTRAplus (Carl Zeiss SMT AG, Germany) ultra-high resolution field-emission scanning electron microscope (FESEM) with an energy dispersive X-ray spectrometer (EDS, INCA Energy 350 analyzator with INCAx-act detector, Oxford Instruments, UK) at TUT. FESEM analyses were performed for all of the industrial and experimental absorbers. The microstructures were analysed from cross-sectional samples and the morphology from the surfaces of the absorber coatings. A secondary electron (SE) and in-lens secondary electron detectors were used. The microstructures and morphology were analysed from as-deposited and aged samples.

The cross-sectional samples were prepared by bending the absorber coating with the substrate plate until the coating cracked from the top. The bent samples were glued with carbon glue to sample holders. The samples were tilted in a microscope chamber to see the cross-section of the coating. The large cracks in the fracture cross-sectional FESEM images came from sample preparation. Layer thicknesses and microstructures were analysed from the cross-sectional samples. The deposition rate for experimental coatings was calculated from the layer thickness and deposition time. EDS analyses were performed on surfaces from flat (not bent) samples, which were glued to the sample holders. Also, polished cross-sectional samples were prepared from the aged industrial Cu-substrate absorbers. The samples were ground with 800-4000 SiC papers, and then polished with a 3 µm diamond suspension (DiaPro Mol, Struers) and 0.04 µm SiO_2 polishing liquid (96 % OP-S, Struers) with 2 % NH_4 and 2 % H_2O_2. The polished cross-sectional samples were coated with a thin carbon layer to prevent charging.

The coverage area of CuO islands in the absorber surface was determined from FESEM images using image processing. For each aged sample, FESEM images were taken from extensive locations on the surface. The coverage area was calculated by means of image analysis software (UTHSCSA Image Tool).

Transmission Electron Microscope (TEM)

The microstructures, layer thicknesses, and elemental analysis were studied with a JEM-2010 (Jeol, Japan) transmission electron microscope (TEM) at TUT. The microscope was equipped with an energy dispersive X-ray spectroscope (EDS) analyser (Noran Vantage with Si(Li) detector, Thermo Scientific, USA). TEM analyses were performed for as-deposited and aged samples of industrial absorbers 1-7. TEM selected area electron diffraction (SAED) patterns were used to analyse the amorphous/crystalline structure of coating layers for industrial absorbers 1-6. Cross-sectional samples were prepared from the as-deposited and aged industrial absorbers. The samples were cut into small pieces of about 1.5 mm x 1 mm. The pieces were attached to a titanium grid by carbon glue with the coating layers face-to-face. The carbon glue was hardened in a furnace at 150 °C for one hour. The grid was pre-thinned mechanically by hand to a thickness of about 100 µm and then with a dimple grinder (Model 656, Gatan Inc., USA) to a thickness of about 50 µm. The final polishing was made with a precision ion polishing system (PIPS, Model 691, Gatan Inc., USA).

5.2.6 TOF-ERDA, XPS and XRD for composition and phase analysis

The depth profiles of the compositions and phase analysis were studied by time-of-flight elastic recoil detection analysis (TOF-ERDA), X-ray photoelectron spectroscope (XPS) and X-ray diffraction (XRD). Further information about the techniques is given below.

Time-of-flight elastic recoil detection analysis (TOF-ERDA)

The time-of-flight elastic recoil detection analysis (TOF-ERDA, Figure 19) of the elemental concentration profiles was performed with the EGP-10-II 5-MV tandem accelerator at the University of Helsinki [254] for industrial absorbers 1-7. The depth profiles were used to compare differences in the compositions of the absorbers before and after ageing. In the measurements, an ion beam of 43 MeV ^{79}Br was used. The detector was at a recoil angle of 40° and the angle of incident ion beam was 20° relative to the sample surface. The elemental concentration profiles were calculated using known geometry and SRIM-2003 stopping powers [255] in energy loss calculations. The results of the depth profiling should be regarded as indicative only. The multiple scattering and surface roughness broadened the detected layers. In the ERDA measurements, traces of impurities

(C, H, Ar, P, F, Mg, Na, S) were detected. However, the total amount of these impurities was negligible, and thus they are not presented in the graphs. Oxidation of the absorber coating layer was determined from the TOF-ERDA measurements by subtracting the oxygen content of the AR layer and possible anodized layer from the total oxygen content. The oxygen/metal ratios of certain coating layers were calculated by dividing the determined oxygen content of a certain layer by the measured metal content of the same layer. Densities of absorption and anti-reflection layers were calculated from TOF-ERDA data by using microscopically analysed layer thickness and atom weights for the elements.

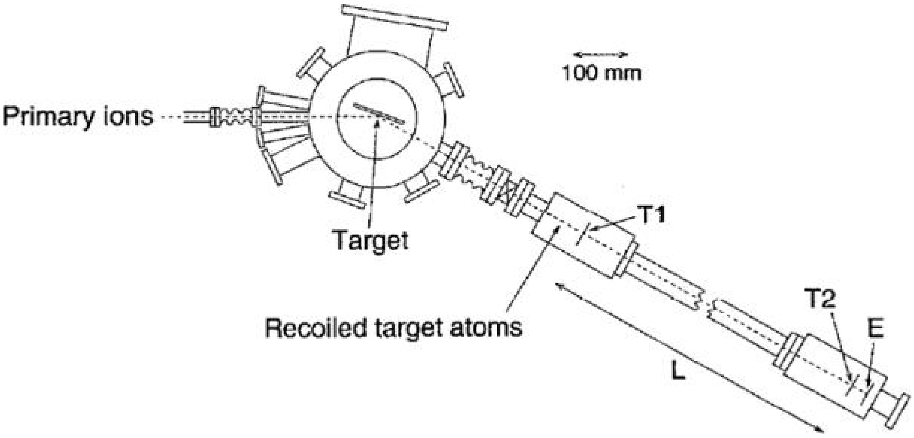

Figure 19. Schematic drawing of the configuration of the TOF-ERDA measurements. Timing detectors T1 and T2 were used for measuring the time-of-flight over flight path L. E denotes the energy detector. [254]

X-ray photoelectron spectroscope (XPS)

The chemical states and compositions were studied with an XSAM 800 (Kratos Analytical, UK) X-ray photoelectron spectroscope (XPS) at TUT, Surface Science Laboratory for as-deposited industrial absorbers 1-4. The XPS was used for analysing the chemical states of compounds of the anti-reflection layers and to ensure the composition measurements of the TOF-ERDA from as-deposited absorbers 1-4. A depth profile was measured from the sample by using the Ar ion sputtering associated with XPS measurements in order to study how the elemental composition changes as a function of depth. Prior to the measurements, the analysis chamber was pumped down to the base pressure of $1 \cdot 10^{-10}$ mbar. Average element concentrations were determined from the circular detection area, which is approximately 600 µm in diameter. The information was acquired from depths up to ~5 nm with a relative surface sensitivity of ~0.1 atomic-%. Ar ion sputtering during depth profiling can change the chemical state of the compounds. It should be noted that sputtering time is not directly proportional to total sputtering depth, since oxides are generally removed much faster than metals. The depth profile results were identical with the TOF-ERDA measurements, and in further studies TOF-ERDA was used for analysing the composition.

X-ray diffraction (XRD)

Phase identification for industrial absorber 4 was carried out by grazing incidence X-ray diffraction (XRD) with a Panalytical Empyrean system using Cu Kα radiation. The incidence angles used were 0.2-2.0°. The diffraction profiles are acquired in the angular range of 20-80° (angle 2-Theta). Grazing-angle incidence in a parallel beam arrangement with a Goebel mirror in the incident beam and a parallel plate collimator and monochromator in the diffracted beam was used. Phase identification was performed using the Panalytical X'Pert High Score Plus software using the ICDD PDF-4 database (International Centre for Diffraction Data, Newtown Square, PA, USA).

5.2.7 Optical modelling and simulation

The simulation software CODE Coating Designer of W. Theiss Hard- and Software [244] was used to determine the experimental absorber coating layer stack and to study the relation between ageing mechanisms and the degradation of optical properties.

The spectral optical constants used in the simulations were taken from a database of the CODE Coating Designer [244]. Most of the materials studied (Cr, Cr_2O_3, CuO, TiN, TiO_2, Al_2O_3) needed extrapolation of optical constants to cover a wavelength range up to the infrared region. In the extrapolations, the last values of the complex refractive index were used for higher wavelengths. Cu, Al and SiO_2 used in the simulations had refractive index data available up to 25 µm. For Cr, the extrapolation created significant uncertainties because the refractive index data was available only up to 1 µm in the CODE database, and the refractive index values were not stabilized in the available range. In [256] it was noted that reliable long-wavelength data is not available for Cr and that different measurements do not agree well with each other, probably because of weak structures or oxidation.

For CuO and Cr_2O_3 the extrapolation can be assumed to be more valid because the refractive index data were near constant for CuO from 1 µm to the highest available value of 2.5 µm, and for Cr_2O_3 from 0.5 µm to the highest available value of 1 µm. For CuO, the refractive index data in the CODE database was entirely consistent with the data presented in [257]. Refractive index values in the infrared region for CuO have not been published but CuO has been reported to exhibit an intense single band around 20 µm, which is the only significant band in the long-wavelength region [257] but therefore out of the measurement range in this study (thermal emittance measurements up to 16.7 µm, see section 5.2.4). For Al_2O_3, TiO_2 and TiN, refractive index data were available up to 2.5 µm, 1 µm, and 0.9 µm respectively in the CODE database, and the refractive indexes were not fully regularised towards the highest available data. It has been reported that there are difficulties in defining the optical properties of oxidised titanium, since there are so many oxides of Ti [258]. Using TiN and amorphous TiO_2 instead of TiN, TiO and rutile TiO_2 in the simulations of TiO_xN_y imparted uncertainties to the models. More accurate simulations of the absorber or diffusion barrier coatings were limited because the optical data for CrO_xN_y, CrO_x, CrN, TiO_xN_y, TiO, γ-Al_2O_3, SnO, SnO_2 and TaN were not available in the CODE database or in the Handbook of Optical Constants of Solids [259].

The Bruggeman effective medium theory [260] was used to simulate composite structures. The Bruggeman model is used for cermets [261, 262]. The Bruggeman model included a random mixture of two spherical media with a certain volume factor like presented in equation (12):

$$f\,\frac{e_A - e_{eff}}{e_A - 2e_{eff}} + (1-f)\,\frac{e_B - e_{eff}}{e_B + 2e_{eff}} = 0, \qquad (12)$$

where e_A is dielectric permeability of the medium A with probability of f and e_B is dielectric permeability of the medium B with probability of 1 – f. This spherical cell is embedded in an effective medium which effective dielectric permeability is e_{eff}. [262]

A CrO_x coating layer was simulated by using data of stoichiometric Cr_2O_3 and the Bruggeman model with Cr in Cr_2O_3, and black chromium using the Bruggeman model with Cr particles in a Cr_2O_3 matrix with a graded structure. A TiO_xN_y absorber coating was simulated using mixtures of TiN and amorphous TiO_2 with the Bruggeman model and a layer structure. A SiO_x anti-reflection coating was simulated using SiO_2 data. An anodized aluminium oxide layer before and after thermal exposure was simulated by using α-Al_2O_3. Voids in Cu substrate were simulated in two different ways: using the Bruggeman model with air in the Cu matrix and using a Drude free electron theory model for a damaged Cu substrate by damping a very large amount of electrons in Cu (i.e. shorten relaxation time) and converting Cu into oxidized Cu by reducing the density of electrons (i.e. smaller plasma frequency in CODE). The Drude model is a classical model and can be used to describe both the electrical and optical behaviour of metals. It is based on that some electrons in a metal can be considered to be free and the free electron density is equal to the density of metal atoms multiplied by their valency. The free electrons are constantly scattered at crystal defects and grain boundaries. The time between two collisions represents an average relaxation time τ. [263]

The industrial and experimental absorbers studied were complex gradient or multilayer structures which complicated optical modelling of the absorbers. The simulations performed were simplifications but sufficiently reliable to indicate a certain degradation behaviour. Fitting accurate simulations of the absorbers will be discussed and proposed in section 9.

6 RESULTS

The results presented in this thesis include optical measurements, microstructural and compositional analysis of the studied solar absorbers before and after ageing studies at elevated temperatures. The focus was on investigating ageing mechanisms during thermal exposure.

6.1 As-deposited solar absorbers before ageing

As-deposited absorbers include industrial and sputtered experimental absorbers before thermal exposure. The optical properties, microstructures and compositions of the as-deposited absorbers are presented in this section.

6.1.1 Optical properties of the as-deposited industrial absorbers

The measured optical properties of the industrial as-deposited absorbers were compared to the values recorded by the absorber manufacturers (Figures 20 and 21). A summary of the solar absorptance (α) and thermal emittance (ε) values is presented in Table 8. The measured solar absorptance and thermal emittance values are the averages of 21 measurements. The standard deviation of α and ε include only the reproducibility of the absorber, not the absolute accuracy of the measurement. ISO standard draft EN 12975-3-1 (2011) requires a standard deviation of $\Delta_{st.dev}\alpha < 0.01$ and $\Delta_{st.dev}\varepsilon < 0.04$ to be qualified to the accelerated ageing testing to ensure that samples are uniform enough for the studies [24]. On the whole, the absorbers had a very uniform quality, even a magnitude lower standard deviation than required. Only the sputtered CrO_xN_y on SS (absorber 8) had a higher standard deviation than required for absorptance values, because the standard deviation was 0.010 and requirement was *less than* 0.01. Nevertheless, we included absorber 8 in these studies.

The measured solar absorptances were well within the reported values by manufacturers, except for the sputtered CrO_xN_y on Al (absorber 6), which had a lower solar absorptance (0.92) than reported (0.95 ± 0.02). Other absorbers had either higher or lower measured solar absorptance than the reported value but the values were inside the error range.

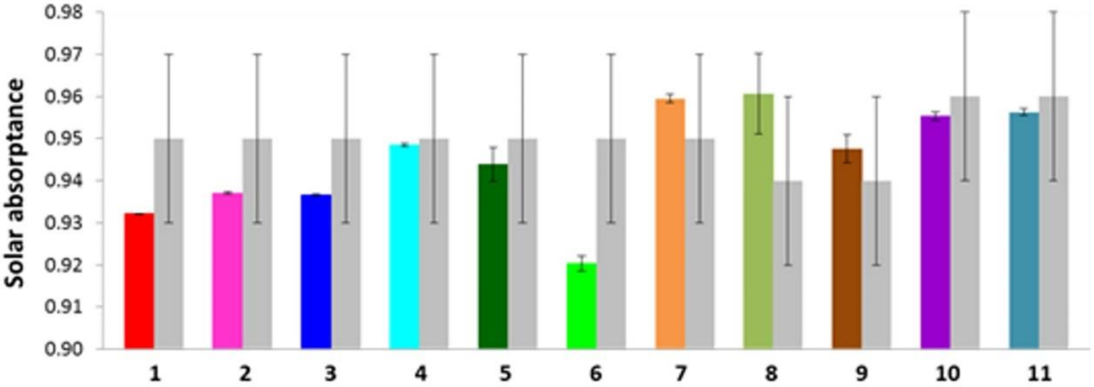

Figure 20. Solar absorptances of the industrial solar absorbers studied. The measured values of each absorber are on the left (different colours). Next to the measured values in grey are the reported absorptances by the manufacturers with the standard deviations they have reported.

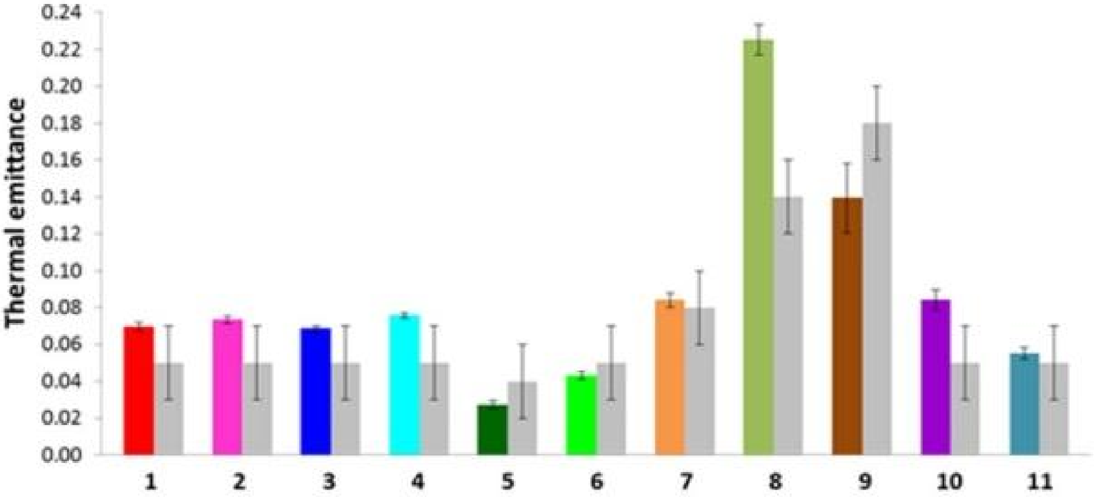

Figure 21. Thermal emittances of the industrial solar absorbers studied. The measured values of each absorber are on the left (different colours). Next to the measured values in grey are the reported emittances by the manufacturers with the standard deviations they have reported.

The thermal emittances measured had more variation than solar absorptance when compared to the reported emittance values. The sputtered CrO_x on anodized Al (absorber 4) and sputtered $TiAlSiO_xN_y$ on an extruded Al profile (absorber 10) had a slightly higher measured thermal emittance (0.076 and 0.084, respectively) than reported (0.05 ± 0.02 for both absorbers 4 and 10). A higher mismatch was in the sputtered CrO_xN_y on SS (absorber 8) in which the measured ε value was 0.225, and the reported 0.14 ± 0.02. However, it is notable that even though absorber 8 had a higher measured thermal emittance, it also had a higher measured solar absorptance (measured 0.96, reported 0.94 ± 0.02) than reported by the manufacturer. The measured α/ε ratio was 4.3 whereas the reported values were 6.7. The higher the α/ε ratio, the more selectively the absorber surface acts. The electroplated black chromium on SS (absorber 9) had a lower measured thermal emittance (0.140) than reported (0.18 ± 0.02). Other thermal emittances of the absorbers were inside the error range of reported values with either higher or lower values.

Table 8. A summary of the measured optical properties of the as-deposited industrial solar absorbers.

Absorber	Solar absorptance	Thermal emittance	α/ε ratio
1	0.932 ± 0.001	0.069 ± 0.003	13.4
2	0.937 ± 0.001	0.073 ± 0.002	12.8
3	0.937 ± 0.001	0.069 ± 0.002	13.7
4	0.948 ± 0.001	0.076 ± 0.001	12.5
5	0.944 ± 0.004	0.027 ± 0.002	34.5
6	0.920 ± 0.002	0.043 ± 0.002	21.3
7	0.959 ± 0.001	0.084 ± 0.004	11.4
8	0.96 ± 0.01	0.225 ± 0.008	4.3
9	0.948 ± 0.003	0.14 ± 0.02	6.8
10	0.955 ± 0.001	0.084 ± 0.006	11.3
11	0.956 ± 0.001	0.055 ± 0.003	17.3

6.1.2 *Optical properties of the as-deposited experimental absorbers*

The solar absorptance of the multilayer CrO_x(45 nm)/Cr(30 nm)/CrO_x(45 nm) absorber was approximately 0.87 ± 0.01 and its thermal emittance 0.05 ± 0.02. According to the simulation software CODE Coating Designer of W. Theiss Hard- and Software [244], the optical properties of the ideal described structure are α = 0.86 and ε = 0.01. Figure 22 presents measured reflectance spectra for the experimental CrO_x/Cr/CrO_x absorber and simulated spectra for Cr_2O_3(45 nm)/Cr(30 nm)/Cr_2O_3(45 nm) and for the Cr_2O_3(40.8 nm)/Cr(34.5 nm)/Cr_2O_3(76.8 nm) absorber roughly fitted to the experimental data.

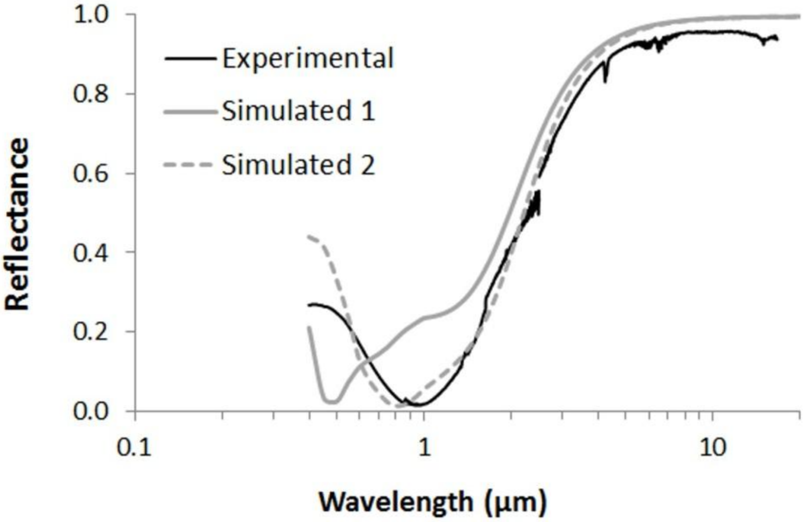

Figure 22. Measured reflectance spectra for the experimental CrO_x/Cr/CrO_x absorber on a cold-rolled Cu sheet and simulated reflectance spectra by CODE Coating Designer for the Cr_2O_3(45 nm)/Cr(30 nm)/Cr_2O_3(45 nm) absorber (Simulated 1) and the Cr_2O_3(40.8 nm)/Cr(34.5 nm)/Cr_2O_3(76.8 nm) absorber roughly fitted to the experimental data on Cu (Simulated 2).

The reproducibility of the experimental absorbers was acceptable according to six CrO_x/Cr/CrO_x samples. With the same set up of deposition parameters, the absorbers had a solar absorptance (α) of 0.87 with a standard deviation ($\Delta_{st.dev}\alpha$) of 0.01 and a thermal emittance (ε) of 0.05 with a standard deviation ($\Delta_{st.dev}\varepsilon$) of 0.02. The absorber passed the requirement of the ISO standard draft EN 12975-3-1 (2011) [24] for the standard deviation of $\Delta_{st.dev}\alpha < 0.01$ and $\Delta_{st.dev}\varepsilon < 0.04$ to be uniform enough.

The optical properties of the gradient CrN_y/CrO_x absorbers varied significantly depending on the thickness of the absorber and the gas flow of reactive nitrogen gas. The optical properties of the experimental absorbers are summarized in Table 9. A flow of 25 sccm of N_2 (Ar 200 sccm) in the CrN_y layer imparted a metallic grey colour to the CrN_y/CrO_x absorber, and the solar absorptance was only 0.60. With a higher N_2 content, the solar absorptance increased and the colour of the absorbers was blue. Thermal emittance remained low if the thickness of the absorber was thin enough to remain invisible in the IR range [79].

Table 9. Optical properties of the experimental absorbers.

Experimental absorber	Solar absorptance	Thermal emittance	Layer thickness (nm)
$Cu/CrO_x/Cr/CrO_x$	0.87	0.05	45/30/45
Cu/CrN_y (25 sccm N_2)/CrO_x	0.60	0.02	120/50
Cu/CrN_y (50 sccm N_2)/CrO_x	0.93	0.18	110/50
Cu/CrN_y (50 sccm N_2)/CrO_x	0.93	0.06	50/50
Cu/CrN_y (100 sccm N_2)/CrO_x	0.80	0.04	50/50
$Cu/TiAlSiO_xN_y/SiO_x$ 1)	0.95	0.05	100/100

1) Deposited at the factory of a commercial manufacturer.

6.1.3 *Microstructures of the as-deposited industrial absorber coatings*

The microstructures of the industrial absorbers were mainly typical structures for certain deposition methods. Sputter deposited coatings (absorbers 1-4, 6, 8, and 10-11) had a columnar structure which is in agreement with Thornton's zone model [69]. The differences between the columnar structures of the different absorber coatings were revealed in the FESEM and TEM studies. Figures 23 and 24 show the microstructures of the sputtered chromium oxy-nitride on copper (absorbers 1 and 3). The absorption coating of absorber 1 was dense and no porosity could be found. In the absorption layer of absorber 3 there seemed to be some porosity between the columns. Densities calculated from the TOF-ERDA amount of material measurements were 6.5 ± 0.1 g/cm^3 for absorber 1 and 4.1 ± 0.1 g/cm^3 for absorber 3. In comparison, Figure 25 presents the microstructures of the sputtered chromium oxide and chromium oxy-nitride absorption layers of absorbers 2, 4, and 6 on Al and anodized Al substrates. The densities were 5.0 ± 0.1 g/cm^3 for absorber 2, 5.4 ± 0.1 g/cm^3 for absorber 4, and 5.2 ± 0.1 g/cm^3 for absorber 6.

The sputtered CrO_xN_y (absorber 6) on cold-rolled Al substrate and $TiAlSiO_xN_y$ (absorbers 10 and 11) on extruded Al profiles were columnar but had defects in the coating layers. Figure 26 presents the FESEM images of the as-deposited surface and cross-section of absorbers 2, 4, and 6 on cold-rolled Al sheets. For absorber 6, numerous craters in the CrO_xN_y absorber coating and SiO_x AR coating were observed. Some of the craters were located only in the AR layer but some of them were deeper and extended through the whole coating stack. Similar defects were rare in absorbers 2 and 4 but single craters were noticed. For absorbers 10 and 11, the Al profile substrates had scratches from the extrusion process, which are likely to have been reproduced in the coating and created a rough surface and some defects in the coating (Figure 27).

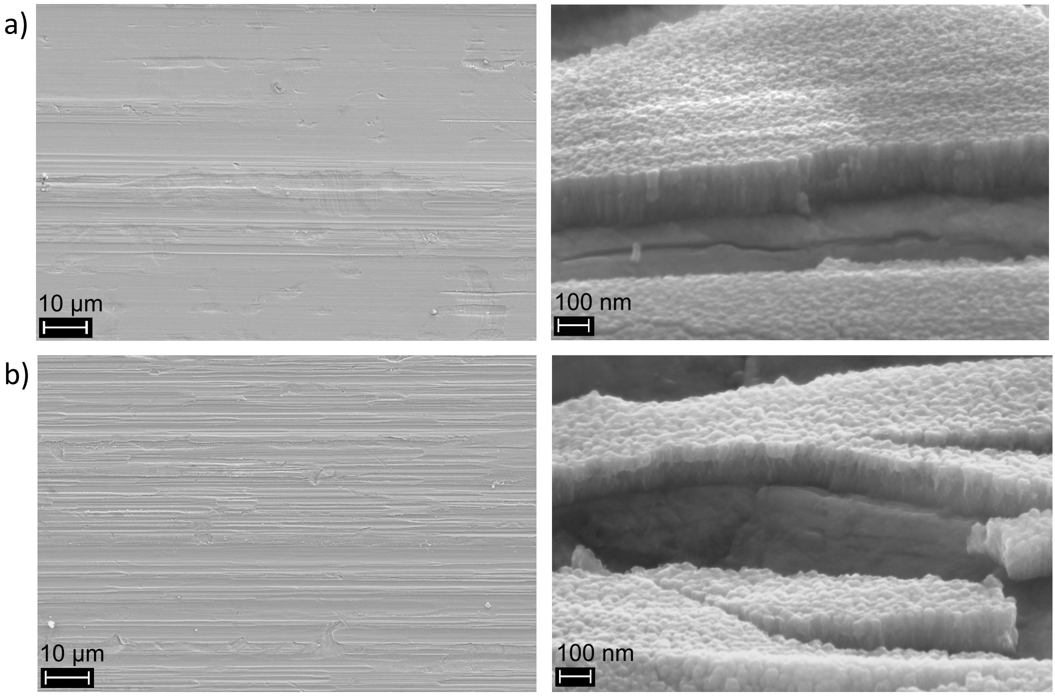

Figure 23. FESEM images of as-deposited sputtered CrO_xN_y/SnO_x coatings on Cu: a) absorber 1 and b) absorber 3. On the left, a surface image and on the right, a cross-sectional image in which the cracking of the coatings is due to sample preparation. Absorber 1 has a denser columnar structure and the columns are smaller than in absorber 3.

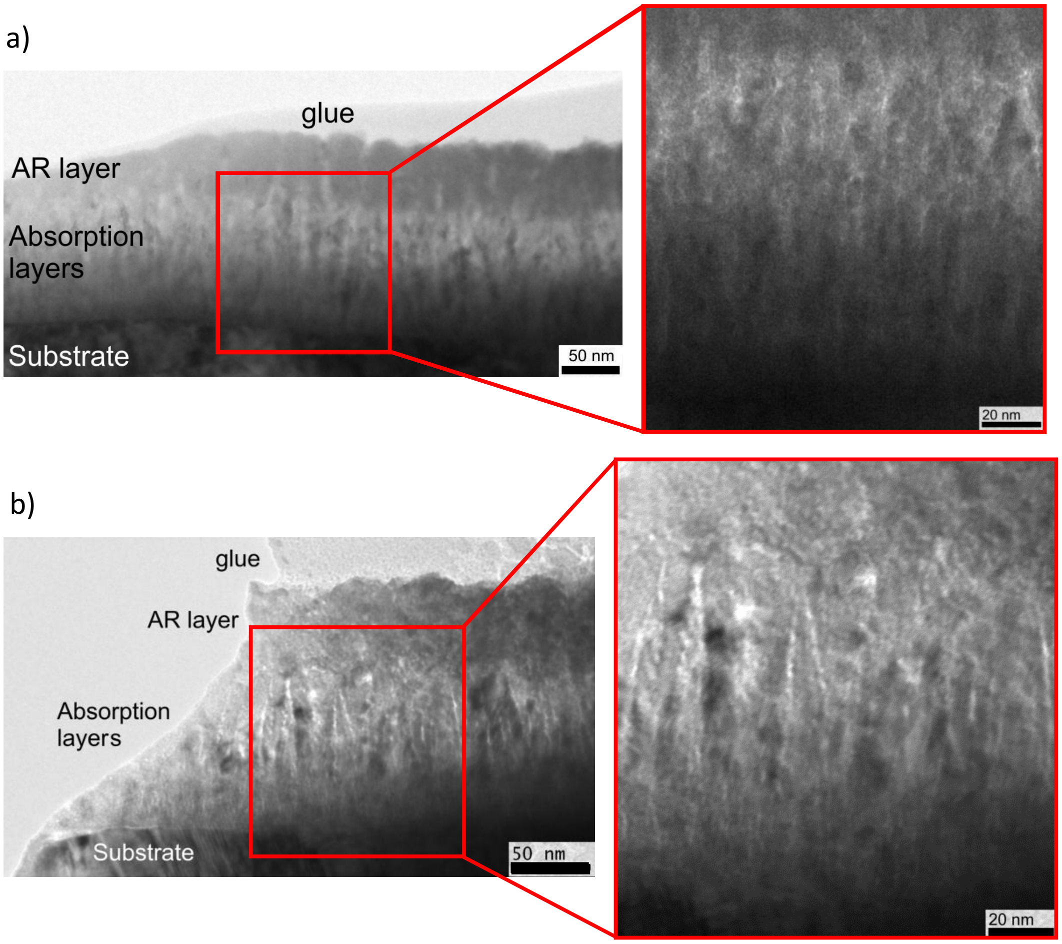

Figure 24. TEM images of as-deposited CrO_xN_y/SnO_x on Cu a) absorber 1 and b) absorber 3. On the left, all the coating layers and on the right, an insert of the CrO_xN_y absorption coating. The absorption coating of absorber 3 has porosity between the columns but absorber 1 has a denser structure.

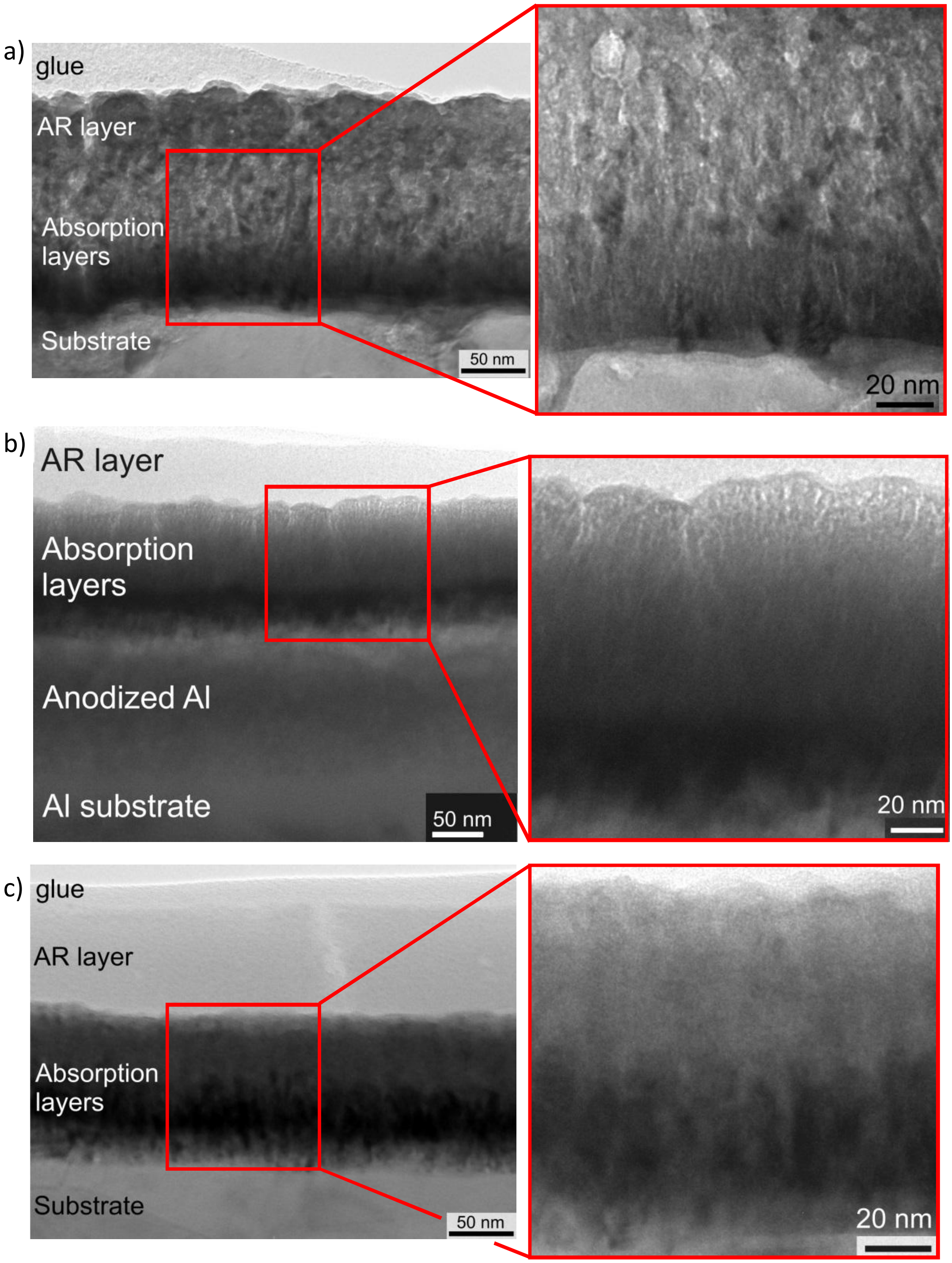

Figure 25. TEM images of an as-deposited CrO_xN_y absorber coating on Al: a) absorber 2, b) absorber 4 (on anodized Al), and c) absorber 6. On the left, all the coating layers and on the right, an insert of the absorber coating.

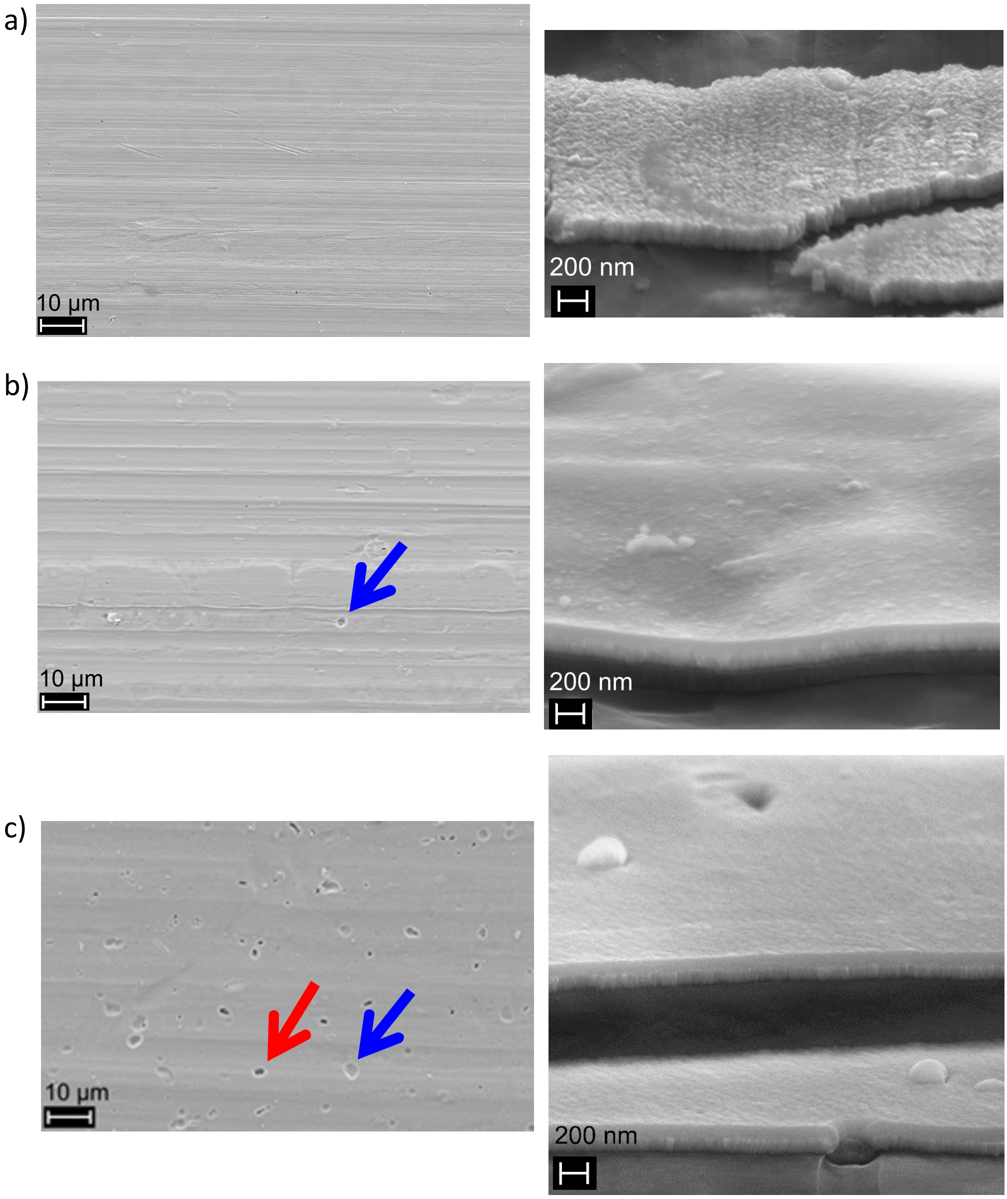

Figure 26. FESEM images of as-deposited CrO_xN_y absorber coatings on cold-rolled Al sheets a) absorber 2 with SnO_x AR coating, b) absorber 4 with SiO_x AR coating and anodized Al substrate, and c) absorber 6 with SiO_x AR coating. Defects or craters in the coatings can penetrate the SiO_x AR layer (blue arrow) or through the whole coating (red arrow). On the left, a surface image and on the right, a cross-sectional view in which sample preparation had created horizontal cracks in the coating.

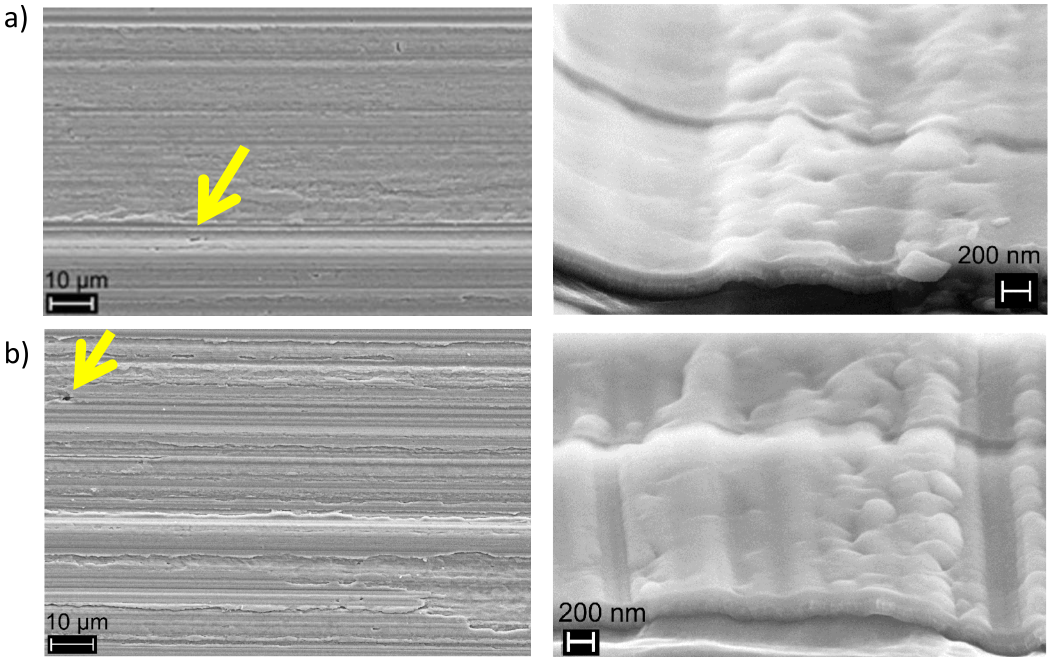

Figure 27. FESEM images of $TiAlSiO_xN_y/SiO_x$ on extruded Al profile: a) absorber 10 and b) absorber 11. Absorbers 10 and 11 had a rough substrate surface from the extrusion process reproduced in the coating structure and some defects in the coating (yellow arrow). On the left, a surface image where the extrusion direction is horizontal and on the right, a cross-sectional view where the extrusion direction is vertical but sample preparation had created horizontal cracks in the coating.

The sputtered CrO_xN_y/SnO_x absorber on SS (absorber 8) had a different macrostructure in the coating surface (Figure 28) compared to the other sputtered absorbers studied. The coating was not distributed evenly on the substrate but it included thicker spherical areas and thinner parts between them. The size of the spherical areas was approximately 5-20 µm in diameter. The sections between the thicker spherical areas were not cracks, as shown in Figure 28 c). The microstructure inside the spherical areas was columnar (Figure 28 d) as in the other sputtered absorbers in this work. It is possible that the substrate had been cleaned by electrochemical etching which revealed the coarse grain structure of the stainless steel [264, 265], and the thin coating would probably have reproduced the structure.

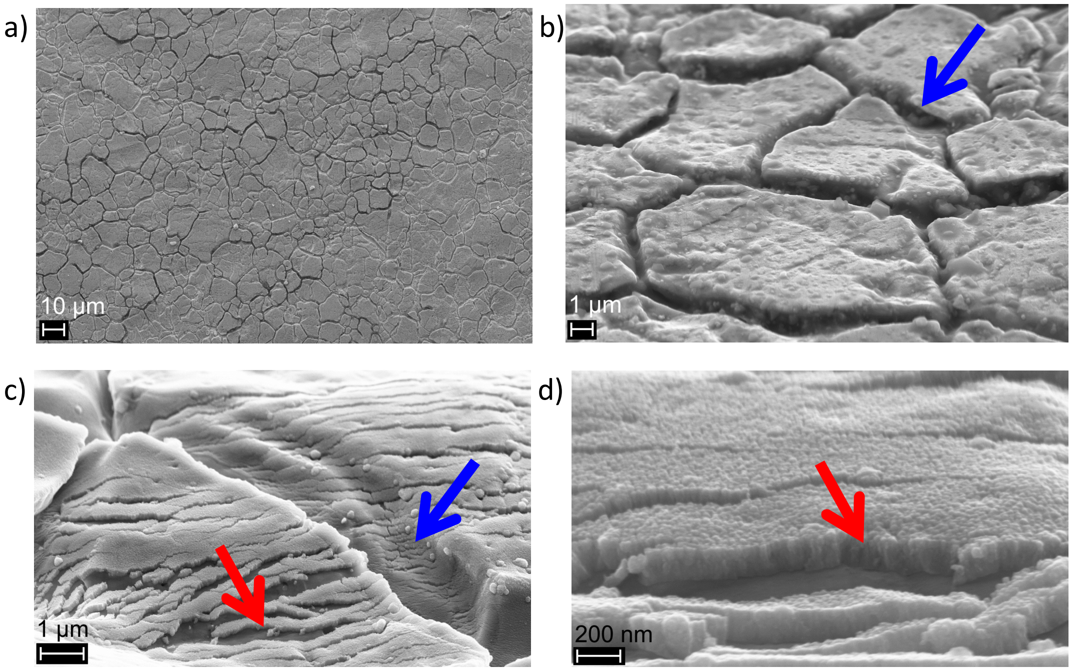

Figure 28. FESEM images of as-deposited CrO_xN_y absorber on SS (absorber 8). A) the surface topography of the absorber consists of spherical areas, b) spherical areas and the thinner sections between them (blue arrow), c) the thinner sections between the spherical areas are not cracks (blue arrow) but sample preparation had created horizontal cracks in the coating (red arrow), and d) the cross-section of the absorber coating is columnar. Sample preparation had created horizontal cracks in the coating (red arrow).

The evaporated TiO_xN_y absorber coating (absorber 5) also had a columnar structure, as expected according to Movchan and Demchishin's structure zone model for evaporated coatings [266]. Figure 29 shows the structure of absorber 5. The density calculated from the TOF-ERDA measurements for the absorption coating of evaporated TiO_xN_y (absorber 5) was 4.7 ± 0.1 g/cm^3.

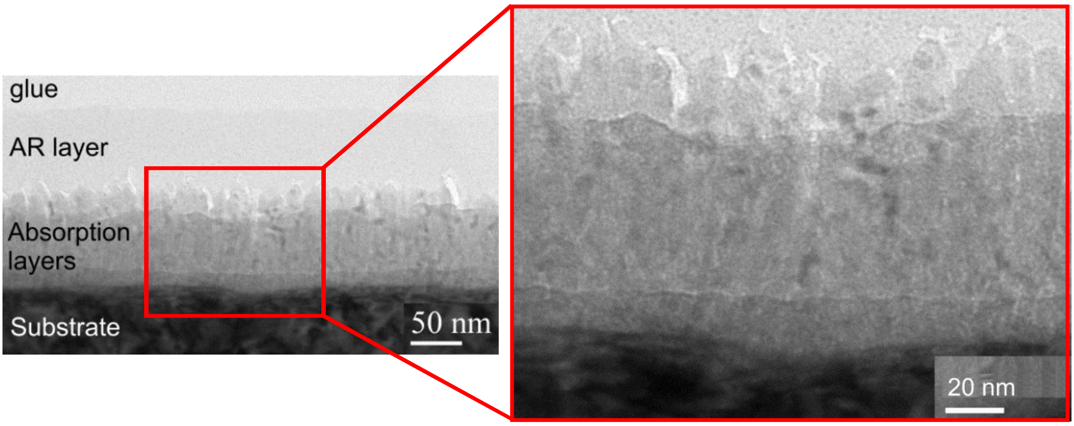

Figure 29. TEM images of the as-deposited evaporated TiO_xN_y/SiO_x on Cu (absorber 5). On the left, all the coating layers and on the right, an insert of the TiO_xN_y absorber coating. The evaporated TiO_xN_y absorber coating had a columnar structure and a porous top layer.

The electroplated black chromium absorbers 7 and 9 had a flake-like rough surface, as illustrated in Figure 30 for absorber 7 (the surface topography of absorber 9 was similar). The structure is typical for electrodeposition because electroplated black chromium consists of a very fine metallic distribution of Cr particles within the matrix of a chromium oxide. The particles have agglomerated into larger particles within the 0.05-0.3 µm size range. These larger particles form a network which constitutes the surface coating [267]. A similar particle network was observed in absorbers 7 and 9. For electroplated black chromium absorber 7, the density of 1.6 ± 0.1 g/cm^3 was calculated from the TOF-ERDA measurements.

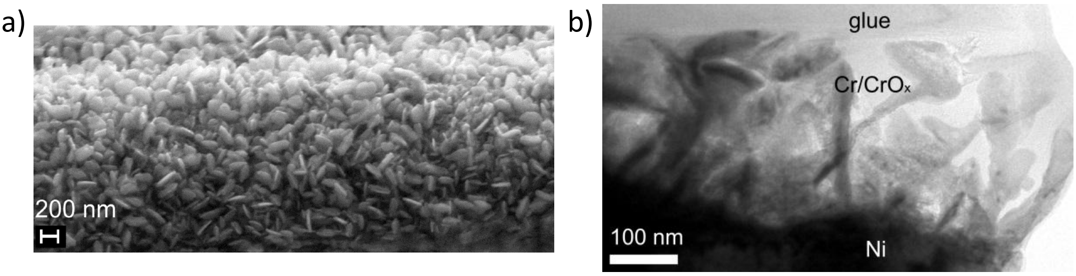

Figure 30. Surface topography and microstructure of electroplated black chromium absorber 7 a) FESEM image of a rough surface, and b) TEM image of a cross-section of the coating. The microstructure was a flake-like particle network, which is typical for electroplated black chromium coatings.

6.1.4 Compositions of the as-deposited industrial absorber coatings

The amounts of the main elements in the absorber coatings are presented in Table 10. The values are measured by TOF-ERDA. The densities of the absorption layers have been calculated and the error of the density calculations is ± 0.1 g/cm^3. It should be noted that the density values are averages for the whole absorber coating (assuming a homogeneous structure) even though the absorbers have gradient structures.

The densities of sputtered CrO_xN_y and CrO_x absorber coatings (absorbers 1-4 and 6) were 4.1-6.5 g/cm^3 while electroplated black chromium (absorber 7) had a density of 1.6 g/cm^3. Evaporated TiO_xN_y had a density of 4.7 g/cm^3.

Table 10. Amounts of elements determined by TOF-ERDA and calculated densities of absorber coatings for absorbers 1-7.

Absorber	**Amount ($1*10^{15}$ at/cm^2)**			**Layer thickness [1] (nm)**	**Density (g/cm^3)**
	Cr or Ti	**O**	**N**		
1 CrO_xN_y	643.5	173.3	201.3	100	6.5
2 CrO_xN_y	467.8	154.4	240.2	100	5.0
3 CrO_xN_y	439.3	115.8	321.6	100	4.1
4 CrO_x	604.5	488.6	0	120	5.4
5 TiO_xN_y	306.7	488.4	6.4	100	4.7
6 CrO_xN_y	426.6	343.8	243.9	100	5.2
7 CrO_x	310.1	213.0	0	200	1.6

1) Based on FESEM and TEM observations.

The XPS results of the atomic concentrations of the elements, the measured binding energies of the XPS transitions and possible chemical compounds on the as-received surface and sputtered depth profiled surfaces for absorbers 1-4 are presented in Table 11. CrO_xN_y absorber coatings (absorbers 1-3) included metallic Cr, Cr_2O_3, and CrN compounds. The CrO_x absorber coating (absorber 4) had metallic Cr and Cr_2O_3 compounds. Adventitious carbon is due to organic chemicals captured from the atmosphere, containers, etc. In absorber 4, the electrically isolated areas of SiO_x and Al_2O_3 became positively charged during XPS measurement, resulting in a binding energy shift of approximately 1-2 eV. The binding energy scales were corrected by setting the Si 2p oxide peak to 104.0 eV and the Al 2s oxide peak to 120.4 eV. This correction was not applied at 70 min sputtering time since the O 1s and Al 2s oxide peaks were split due to differential charging; these are marked with * in Table 11.

Table 11. XPS results of atomic concentrations of elements, measured binding energies of XPS transitions and possible chemical compounds on as-received surface and sputtered depth profiled surfaces for absorbers 1-4.

Absorber 1	**Transition**	**E_B (eV)**	**Relat. conc. (At.%)**	**Possible compounds**
As-received surface	C 1s	284.5	26.1	Adventitious carbon
	O 1s	530.5	43.2	Tin oxides (SnO, SnO_2), adsorbed oxygen
	Sn $3d_{5/2}$	486.8	30.7	Tin oxides (SnO, SnO_2)
Sputtered 12 min	C 1s	281.8	4.8	Adventitious carbon
	O 1s	530.8	21.0	Cr_2O_3, adsorbed oxygen
	Sn $3d_{5/2}$	486.4	1.8	Tin oxides (SnO, SnO_2)
	Cr $2p_{3/2}$ met.	574.1	15.3	Metallic chromium
	Cr $2p_{3/2}$ ox.	575.5	27.5	Cr_2O_3, CrN
	N 1s	396.7	29.6	CrN, N in solid solution
Sputtered 30 min	O 1s	530.4	22.2	Cr_2O_3, adsorbed oxygen
	Cr $2p_{3/2}$ met.	574.0	64.2	Metallic chromium
	Cr $2p_{3/2}$ ox.	576.4	7.3	Cr_2O_3
	N 1s	397.2	6.2	CrN, N in solid solution
Sputtered 35 min	C 1s	282.7	4.9	Adventitious carbon
	O 1s	530.4	8.7	Cr_2O_3, adsorbed oxygen
	Sn $3d_{3/2}$	495.1	0.2	Tin oxides (SnO, SnO_2)
	Cu $2p_{3/2}$	932.5	20.7	Metallic copper
	Cr $2p_{3/2}$ met.	574.0	58.6	Metallic chromium
	Cr $2p_{3/2}$ ox.	576.5	3.9	Cr_2O_3
	N 1s	396.9	3.1	CrN, N in solid solution

Absorber 2	Transition	E_B (eV)	Relat. conc. (At.%)	Possible compounds
As-received surface	C 1s	284.7	61.9	Adventitious carbon
	O 1s_1	530.6	9.8	Tin oxides (SnO, SnO_2)
	O 1s_2	532.0	15.7	Metal hydroxides, organic compounds
	Sn $3d_{5/2}$	486.8	12.6	Tin oxides (SnO, SnO_2)
Sputtered 3 min	O 1s	530.5	48.2	Tin oxides (SnO, SnO_2)
	Sn $3d_{5/2}$	486.7	51.8	Tin oxides (SnO, SnO_2)
Sputtered 12 min	C 1s	284.7	1.3	Adventitious carbon
	O 1s	530.4	42.1	Metal oxides (Cr_2O_3, SnO)
	Sn $3d_{5/2}$	486.5	29.0	Tin oxides (SnO, SnO_2)
	Cr $2p_{3/2}$ met.	574.2	1.0	Metallic chromium
	Cr $2p_{3/2}$ ox.	576.1	18.0	Cr_2O_3, CrN
	N 1s	396.7	8.6	CrN, N in solid solution
Sputtered 30 min	C 1s	282.9	5.1	Adventitious carbon
	O 1s	530.6	19.6	Metal oxides (Cr_2O_3, SnO)
	Sn $3d_{5/2}$	486.8	0.5	Tin oxides (SnO, SnO_2)
	Cr $2p_{3/2}$ met.	574.0	20.9	Metallic chromium
	Cr $2p_{3/2}$ ox.	575.4	25.8	Cr_2O_3, CrN
	N 1s	396.8	28.1	CrN, N in solid solution
Sputtered 45 min	C 1s	282.6	5.4	Adventitious carbon
	O 1s_1	530.4	6.0	Metal oxides (Cr_2O_3, SnO)
	O 1s_3	532.1	8.0	Al_2O_3
	Sn $3d_{5/2}$	487.1	0.3	Tin oxides (SnO, SnO_2)
	Cr $2p_{3/2}$ met.	573.9	49.5	Metallic chromium
	Cr $2p_{3/2}$ ox.	576.0	4.1	Cr_2O_3, CrN
	N 1s	397.3	10.6	CrN, N in solid solution
	Al 2s met.	117.5	10.2	Metallic aluminium
	Al 2s ox.	120.2	6.0	Al_2O_3
Sputtered 60 min	C 1s	282.1	2.6	Adventitious carbon
	O 1s_1	530.7	0.5	Cr_2O_3
	O 1s_3	532.3	12.5	Al_2O_3
	Cr $2p_{3/2}$ met.	574.0	3.7	Metallic chromium
	Cr $2p_{3/2}$ ox.	575.6	0.8	Cr_2O_3
	Al 2s met.	117.4	72.3	Metallic aluminium
	Al 2s ox.	120.3	7.5	Al_2O_3

Absorber 3	**Transition**	**E_B (eV)**	**Relat. conc. (At.%)**	**Possible compounds**
As-received surface	C 1s	284.6	24.4	Adventitious carbon
	O 1s_1	530.6	21.8	Tin oxides (SnO, SnO_2)
	O 1s_2	531.7	24.8	Metal hydroxides, organic compounds
	Sn $3d_{5/2}$	486.9	29.1	Tin oxides (SnO, SnO_2)
Sputtered 3 min	O 1s	530.6	47.6	Tin oxides (SnO, SnO_2)
	Sn $3d_{5/2}$	486.7	52.4	Tin oxides (SnO, SnO_2)
Sputtered 6 min	O 1s	530.3	43.9	Metal oxides (Cr_2O_3, SnO)
	Sn $3d_{5/2}$	486.5	40.7	Tin oxides (SnO, SnO_2)
	Cr $2p_{3/2}$ ox.	576.3	10.3	Cr_2O_3, CrN
	N 1s	396.5	5.1	CrN, N in solid solution
sputtered 9 min	C 1s	282.5	8.5	Adventitious carbon
	O 1s	530.7	19.8	Metal oxides (Cr_2O_3, SnO)
	Sn $3d_{5/2}$	486.5	3.0	Tin oxides (SnO, SnO_2)
	Cr $2p_{3/2}$ met.	574.1	16.8	Metallic chromium
	Cr $2p_{3/2}$ ox.	575.6	23.5	Cr_2O_3, CrN
	N 1s	396.7	28.4	CrN, N in solid solution
Sputtered 12 min	C 1s	282.3	5.0	Adventitious carbon
	O 1s	530.5	18.2	Metal oxides (Cr_2O_3, SnO)
	Sn $3d_{5/2}$	486.4	1.5	Tin oxides (SnO, SnO_2)
	Cr $2p_{3/2}$ met.	574.1	18.4	Metallic chromium
	Cr $2p_{3/2}$ ox.	575.5	27.1	Cr_2O_3, CrN
	N 1s	396.9	29.8	CrN, N in solid solution
Sputtered 45 min	C 1s	282.6	6.5	Adventitious carbon
	O 1s	530.7	6.3	Metal oxides (Cr_2O_3, SnO)
	Cu $3d_{5/2}$	932.6	15.4	Metallic copper, Cu_2O
	Cr $2p_{3/2}$ met.	573.9	36.5	Metallic chromium
	Cr $2p_{3/2}$ ox.	575.4	13.2	Cr_2O_3, CrN
	N 1s	397.1	22.3	CrN, N in solid solution

Absorber 4	**Transition**	**E_B (eV)**	**Relat. conc. (At.%)**	**Possible compounds**
As-received surface	C 1s	285.4	47.7	Adventitious carbon
	O 1s	533.3	31.5	Silicon oxides (SiO_x)
	Si 2p	104.0	20.7	Silicon oxides (SiO_x)
Sputtered 30 s	C 1s	284.7	2.1	Adventitious carbon
	O 1s	533.5	55.0	Silicon oxides (SiO_x)
	Si 2p	104.0	42.9	Silicon oxides (SiO_x)
Sputtered 18 min	C 1s	284.7	0.7	Adventitious carbon
	O 1s_1	533.5	50.5	Silicon oxides (SiO_x)
	O 1s_2	530.8	5.8	Cr_2O_3
	Si 2p	104.0	38.8	Silicon oxides (SiO_x)
	Cr $2p_{3/2}$ ox.	576.2	4.2	Cr_2O_3
Sputtered 25 min	C 1s	284.1	1.9	Adventitious carbon
	O 1s_1	532.3	12.5	Silicon oxides (SiO_x)
	O 1s_2	530.6	45.3	Cr_2O_3
	Si 2p	102.7	3.9	Silicon oxides (SiO_x)
	Cr $2p_{3/2}$ ox.	576.2	36.4	Cr_2O_3
Sputtered 45 min	C 1s	282.7	1.3	Adventitious carbon
	O 1s	530.8	50.9	Cr_2O_3
	Cr $2p_{3/2}$ met.	574.1	16.8	Metallic chromium
	Cr $2p_{3/2}$ ox.	576.0	31.0	Cr_2O_3
Sputtered 60 min	C 1s	282.7	1.9	Adventitious carbon
	O 1s_2	530.7	25.1	Cr_2O_3
	O 1s_3	532.8	8.2	Al_2O_3
	Cr $2p_{3/2}$ met.	573.9	31.1	Metallic chromium
	Cr $2p_{3/2}$ ox.	575.9	15.6	Cr_2O_3
	Al 2s met.	117.2	14.0	Metallic aluminium
	Al 2s ox.	120.4	4.3	Al_2O_3
Sputtered 70 min	O 1s	532.1	4.2	Al_2O_3
	O 1s *	534.1	40.5	Al_2O_3
	Cr $2p_{3/2}$ met.	573.7	6.2	Metallic chromium
	Cr $2p_{3/2}$ ox.	575.4	1.4	Cr_2O_3
	Al 2s met.	117.5	15.7	Metallic aluminium
	Al 2s ox.	120.2	3.0	Al_2O_3
	Al 2s ox. *	122.1	29.0	Al_2O_3
Sputtered 80 min	O 1s	532.6	55.6	Al_2O_3
	Al 2s ox.	120.4	43.0	Al_2O_3
	S 2p	162.5	1.4	Sulphur, sulphides

6.1.5 Microstructures of the as-deposited anti-reflection coatings

The studied sputtered and evaporated absorbers had either tin oxide (absorbers 1-3, and 8) or silicon oxide (absorbers 4-6, and 10-11) anti-reflection coatings. As a comparison of anti-reflective layers, the microstructures of the two sputtered CrO_xN_y absorber coatings on aluminium (absorbers 2 and 6) are presented in Figure 31. As an AR coating, absorber 2 has a sputtered tin oxide layer and absorber 6 a PECVD-coated silicon oxide layer. The absorber coating layers had columnar structures in the both of the absorbers.

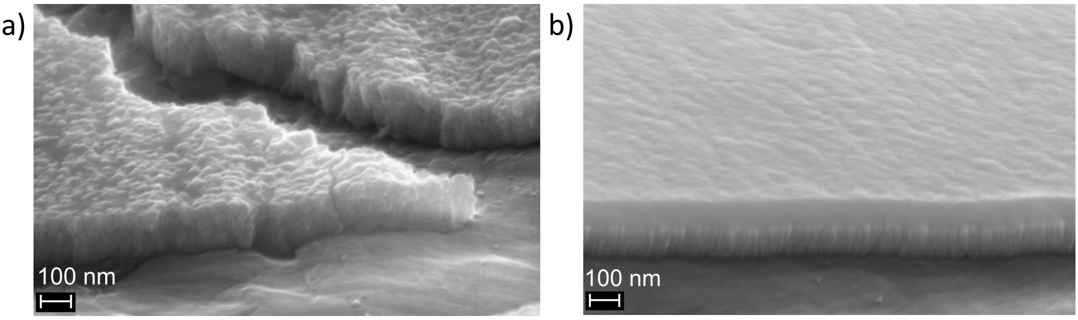

Figure 31. FESEM images of the microstructures of sputtered CrO_xN_y absorber coatings on aluminium: a) absorber 2 with a sputtered tin oxide AR layer, and b) absorber 6 with a PECVD-coated silicon oxide AR layer. The absorber layers seemed to have a very similar columnar structure but the tin oxide AR layer had a columnar structure, and the silicon oxide AR layer was relatively smooth and homogenous. The cracking of the coatings is due to sample preparation.

Figure 32 presents the AR layers of sputtered CrO_xN_y/SnO_x coatings on Cu (absorbers 1 and 3). The AR coating of absorber 1 was fine-grained but absorber 3 had larger columns (see also Figure 23).

Figure 33 presents TEM images of the AR layers of absorbers 1-6. The PECVD-coated or e-beam evaporated silicon oxide layers were quite smooth and homogeneous, and the sputtered tin oxide layers had a columnar structure. All of the silicon oxide AR layers had a dense and homogenous structure (see Figure 31 b and 33), except for some defects or roughness, which were observed in absorbers 6, 10, and 11 (see Figures 26-27). There were no additional AR coatings on the electroplated absorbers surfaces. The rough surface (see Figure 30) of electroplated black chromium (absorbers 7 and 9) has been reported to act as an AR coating [87].

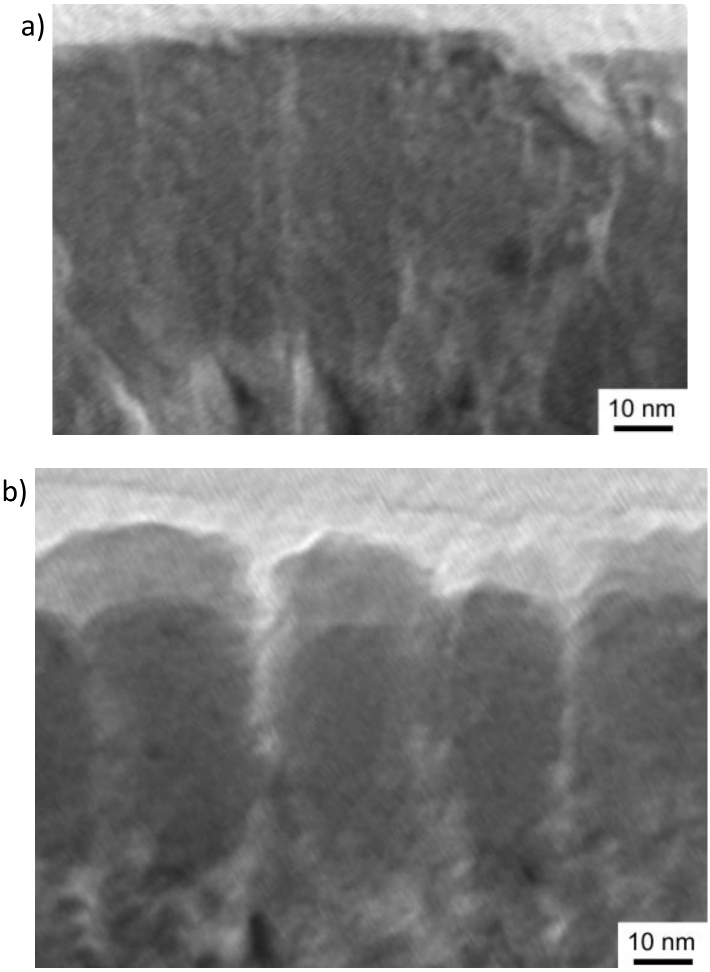

Figure 32. TEM images of as-deposited SnO_x anti-reflection layers on CrO_xN_y absorber coatings on Cu a) absorber 1 and b) absorber 3. The AR layer of absorber 3 has large columns and porosity between the columns.

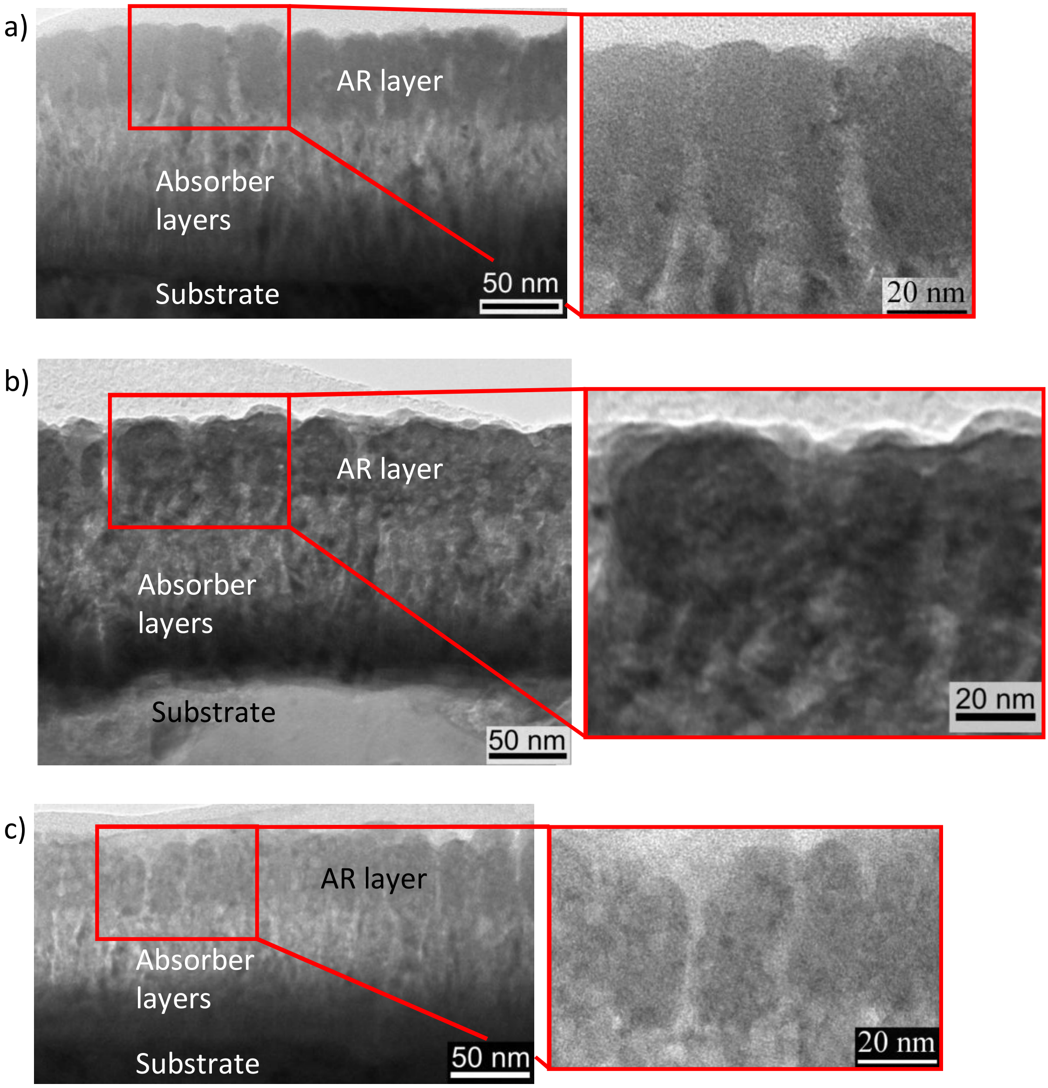
a)
AR layer
Absorber layers
Substrate
50 nm
20 nm
b)
AR layer
Absorber layers
Substrate
50 nm
20 nm
c)
AR layer
Absorber layers
Substrate
50 nm
20 nm

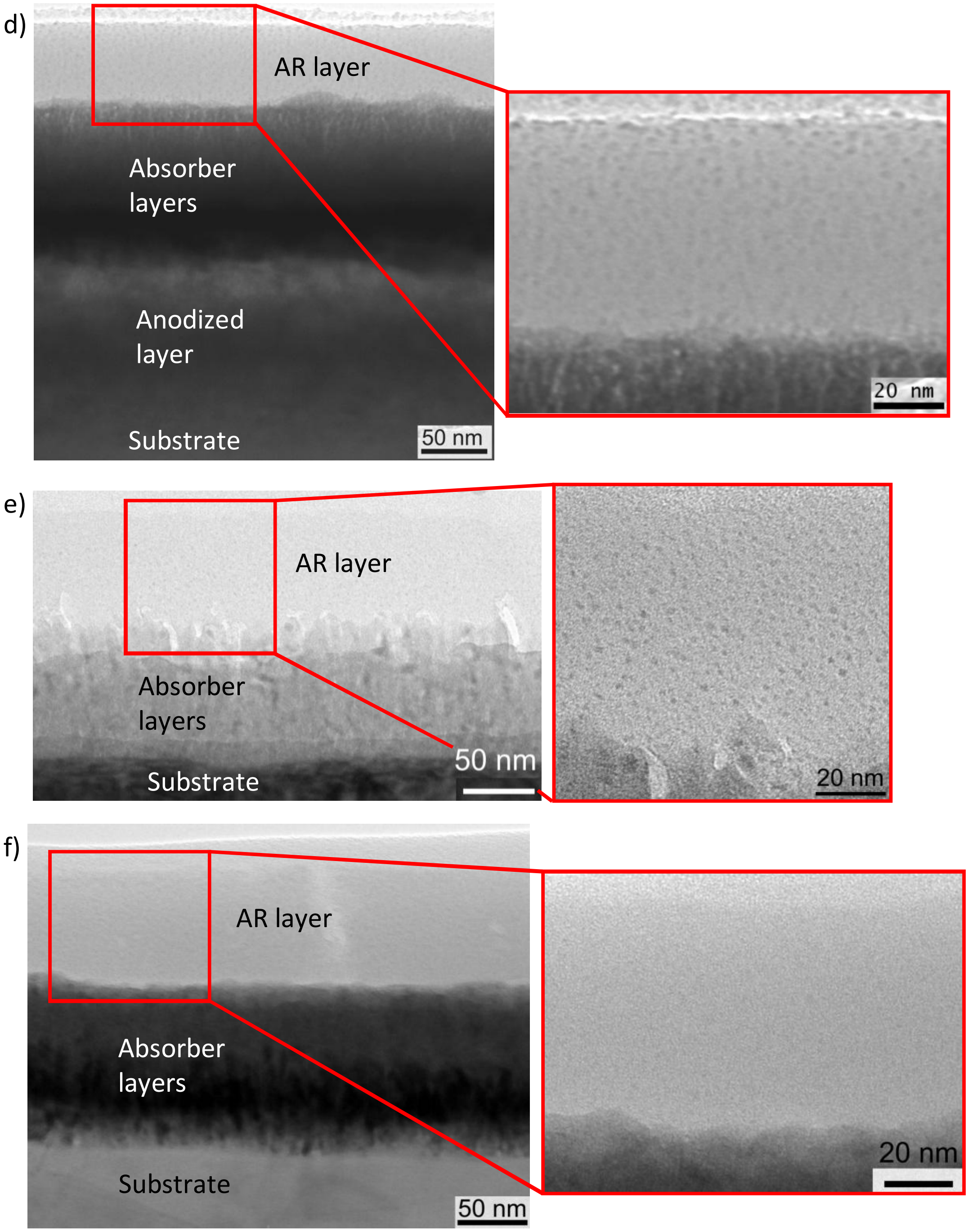

Figure 33. TEM images of as-deposited industrial absorbers and their anti-reflection layers: with a sputtered SnO_x AR layer a) absorber 1, b) absorber 2, and c) absorber 3, and with PECVD or e-beam evaporated SiO_x AR layer d) absorber 4, e) absorber 5, and f) absorber 6. On the left, all the coating layers and on the right, an insert of the anti-reflection coating.

6.1.6 Compositions of the as-deposited anti-reflection coatings

The tin oxide anti-reflection layers included compounds of SnO and SnO_2 (for absorbers 1, 2, and 3), according to XPS analysis (Table 11). The silicon oxide AR layer of absorber 4 included sub-stoichiometric SiO_x, as presented in Table 11.

The TOF-ERDA measurements revealed the O/Sn and O/Si ratios of the AR layers to be near 2 (Table 12). The amounts of main elements measured by TOF-ERDA and the calculated densities of the anti-reflection coatings are presented in Table 12. The error range of the density calculations is ± 0.2 g/cm^3. All of the sputtered tin oxide AR layers (absorbers 1-3) have a density of 6.2-6.5 g/cm^3. A PECVD-coated silicon oxide AR layer on the evaporated TiO_xN_y absorber coating has a density of 1.8 g/cm^3 while the other SiO_x coatings (absorbers 4 and 6) have a density of 2.5-2.8 g/cm^3.

Table 12. Amounts of elements determined by TOF-ERDA and calculated densities of anti-reflection coatings for absorbers 1-6.

Absorber	**Amount (1*10^{15} at/cm^2)**			**O/Sn or O/Si ratio**	**Layer thickness [1] (nm)**	**Density (g/cm^3)**
	Sn	**Si**	**O**			
1 SnO_x	129.4	0	265.8	2.05 ± 0.05	50	6.5
2 SnO_x	130.5	0	250.3	1.92 ± 0.04	50	6.4
3 SnO_x	126.0	0	242.8	1.93 ± 0.04	50	6.2
4 SiO_x	0	177.4	324.6	1.83 ± 0.04	60	2.8
5 SiO_x	0	169.0	369.3	2.19 ± 0.05	100	1.8
6 SiO_x	0	196.5	396.3	2.02 ± 0.03	80	2.5

1) Based on FESEM and TEM observations.

6.1.7 *Microstructures of the experimental as-deposited absorber coatings*

Sputtered experimental absorbers consisted of a columnar structure, which is typical for coatings sputtered at room temperature [69]. Figure 34 presents the microstructures of an experimental ~100-nm-thick $CrO_x/Cr/CrO_x$ multilayer absorber and a ~200-nm-thick gradient CrN_y/CrO_x absorber. The microstructures of the experimental absorbers were quite similar to the sputtered industrial solar absorbers (see Figure 23). Please note that the experimental absorbers have only an absorber layer, not an AR layer.

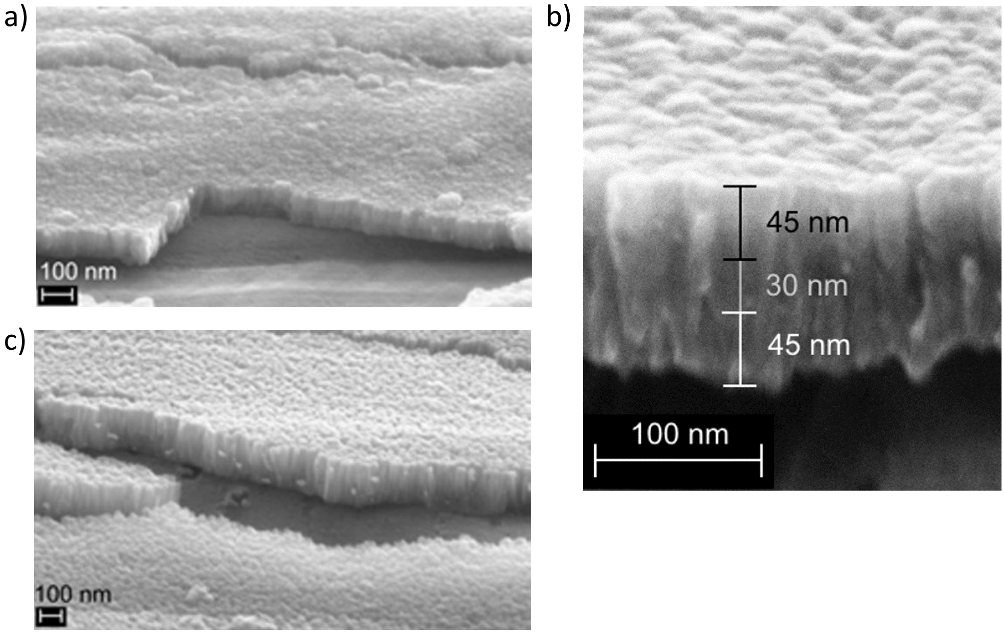

Figure 34. Microstructure of sputtered experimental absorber coatings: a) $CrO_x/Cr/CrO_x$, b) $CrO_x/Cr/CrO_x$ with a higher magnification of FESEM to reveal the coating layers, and c) CrN_y/CrO_x. The cracking of the coatings is due to sample preparation.

6.2 Solar absorbers during thermal accelerated ageing studies

The accelerated ageing studies were performed for the industrial solar absorbers. The optical properties were studied after each exposure period. The microstructures, compositions, and surface topography were analysed after 600 h exposure at 278 °C.

6.2.1 Changes in optical properties during thermal ageing

Solar absorptance values showed negligible or very small changes in most of the studied industrial absorbers (Table 13) during the accelerated ageing test at 278 °C. Only the evaporated TiO_xN_y absorber coating on Cu (absorber 5) suffered a significant decrease in solar absorptance (30 %, from 0.94 to 0.65 after 600 hours). A smaller change was observed in the electroplated black chromium coating on Ni-coated Cu (absorber 7) where solar absorptance decreased by 7 % from 0.96 to 0.89. Figure 35 shows graphs of the solar absorptance values in the accelerated ageing studies.

Changes in thermal emittance were more common in the studied industrial absorbers during the accelerated ageing studies. A change in the thermal emittance values was calculated as as-deposited minus aged. A significant increase in thermal emittance after 278 °C for 600 h was observed in one of the sputtered CrO_xN_y absorber coatings on Cu (absorber 3: $\Delta\varepsilon$ = -30 % from 0.069 to 0.368), the sputtered CrO_x coating on anodized Al with a thin Al layer as the IR reflector (absorber 4: $\Delta\varepsilon$ = -14 % from 0.076 to 0.218) and the evaporated TiO_xN_y coating on Cu (absorber 5: $\Delta\varepsilon$ = -11 % from 0.027 to 0.140). A small decrease ($\Delta\varepsilon \leq$ 3 %) in thermal emittance was observed in absorbers 7-11. The same kind of slight decrease in thermal emittance values, i.e. enhanced selectivity, has been reported earlier in the literature [70, 73, 268, 269]. Thermal emittance values remained unchanged ($\Delta\varepsilon$ = 0-1 %) in all of the sputtered CrO_xN_y and $TiAlSiO_xN_y$ coatings on aluminium (absorbers 2, 6, and 10-11), whereas emittance decreased slightly ($\Delta\varepsilon$ = 3 %) in the absorbers on stainless steel substrates (absorber 8 from 0.225 to 0.194, and absorber 9 from 0.140 to 0.109). Figure 36 shows graphs of the thermal emittance values in the accelerated ageing studies for the studied industrial solar absorbers.

Table 13. Absorptance and emittance values before and after ageing at 278 °C for 600 h, and PC values after 600 h. The values are averages of 21 measurements for as-deposited and 6 measurements for aged absorbers.

Absorber	$\alpha_{\text{as-deposited}}$	α_{aged}	$\Delta\alpha$	$\varepsilon_{\text{as-deposited}}$	$\varepsilon_{\text{aged}}$	$\Delta\varepsilon$	**PC**
1	0.932	0.930	0.00	0.069	0.123	-0.05	0.029
2	0.937	0.931	0.01	0.073	0.075	0.00	0.004
3	0.937	0.907	0.03	0.069	0.368	-0.30	0.179
4	0.948	0.930	0.02	0.076	0.218	-0.14	0.091
5	0.944	0.645	0.30	0.027	0.140	-0.11	0.354
6	0.920	0.913	0.01	0.043	0.046	0.00	0.009
7	0.959	0.886	0.07	0.084	0.061	0.02	0.062
8	0.960	0.933	0.03	0.225	0.194	0.03	0.012
9	0.948	0.941	0.01	0.140	0.109	0.03	-0.008
10	0.955	0.947	0.01	0.084	0.079	0.01	0.006
11	0.956	0.939	0.02	0.055	0.050	0.01	0.015

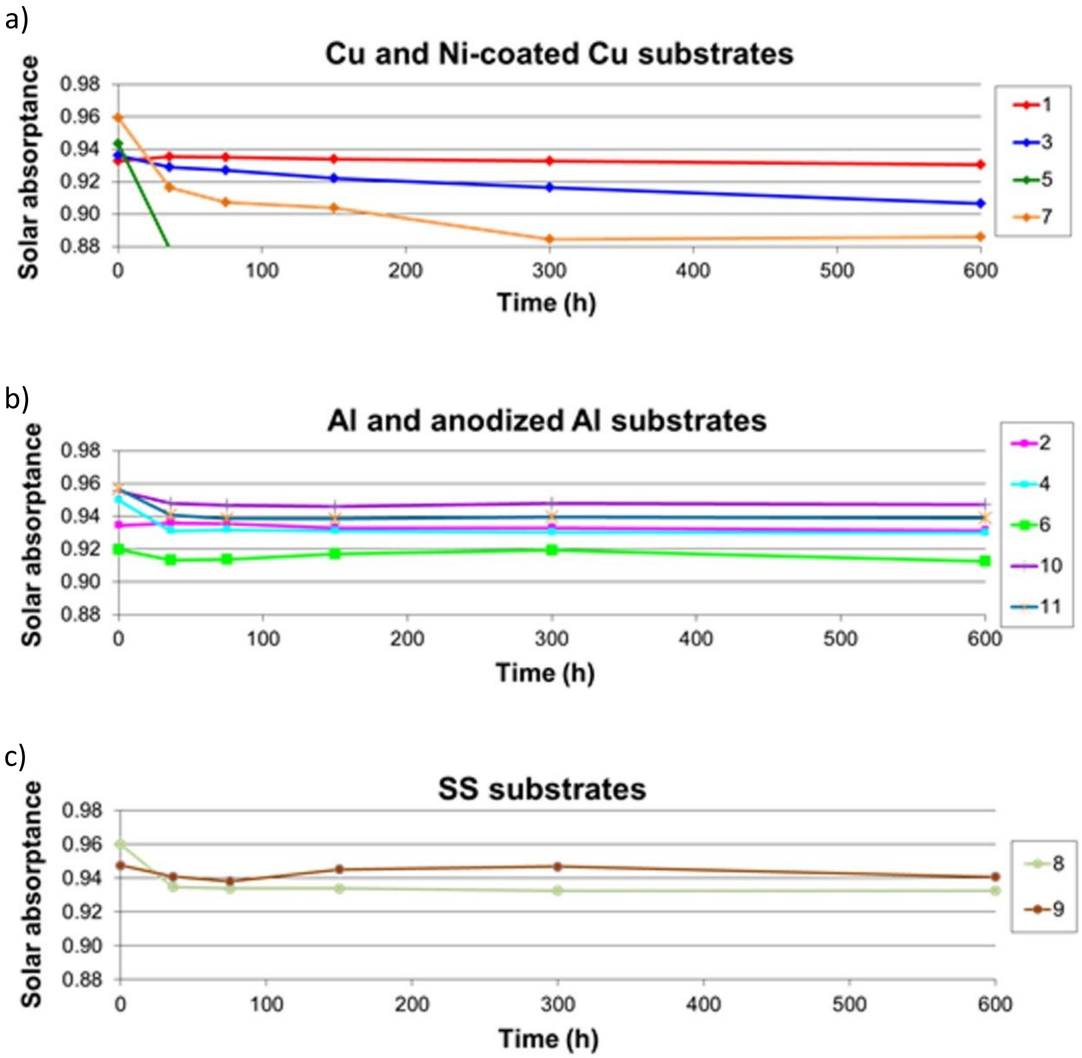

Figure 35. Solar absorptance during the accelerated ageing studies at 278 °C for absorbers on a) Cu and Ni-coated Cu, b) Al and anodized Al, and c) stainless steel substrates. The absorptance values of as-deposited coatings are shown at the beginning of the x-axis (0 h).

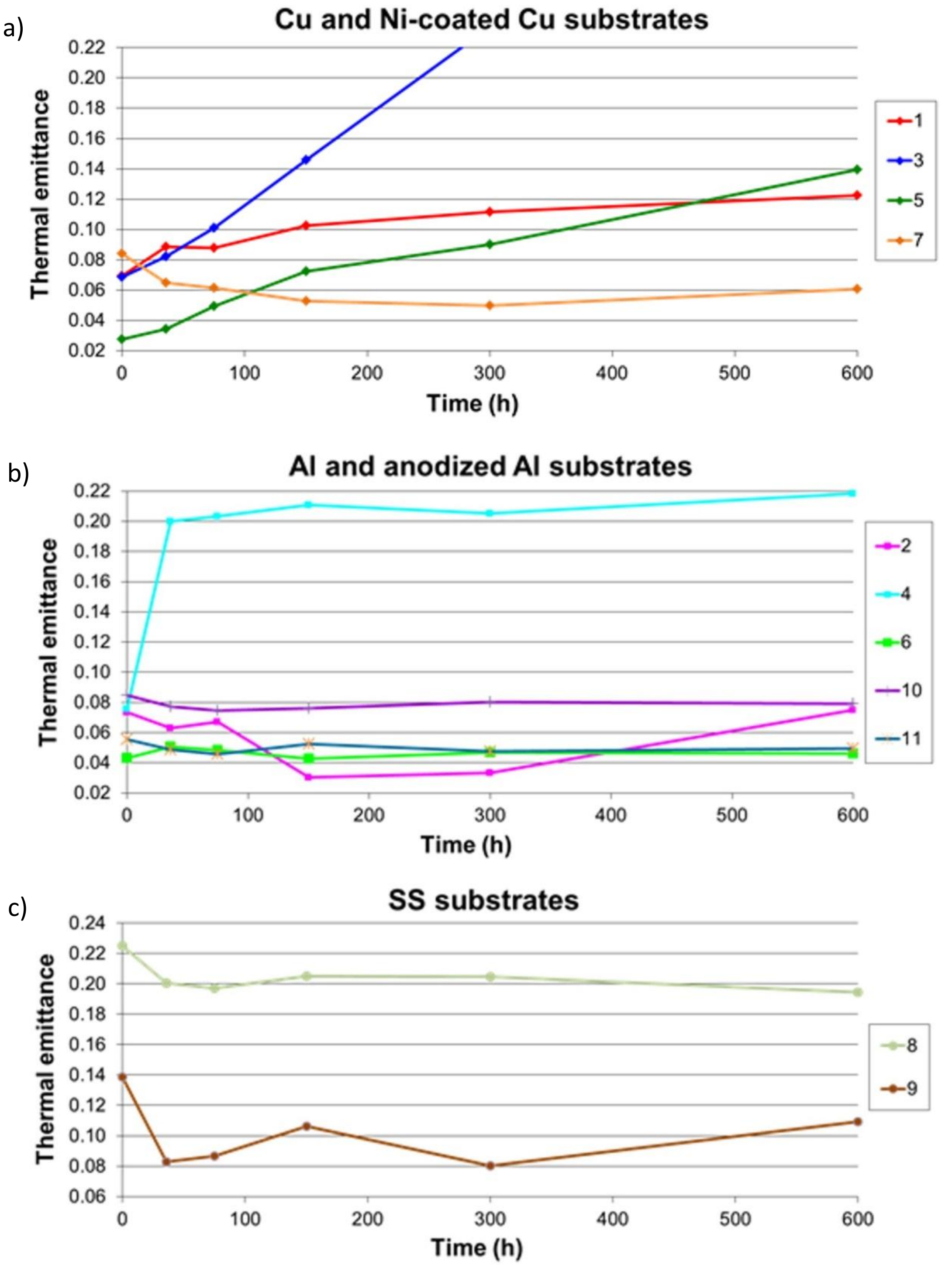

Figure 36. Thermal emittance during the accelerated ageing studies at 278 °C for absorbers on a) Cu and Ni-coated Cu, b) Al and anodized Al, and c) stainless steel

substrates. The emittance values of as-deposited coatings are shown at the beginning of the X-axis (0 h).

The reflectance curves of CrO_xN_y on Al and SS substrates (absorbers 2, 6, and 8), and $TiAlSiO_xN_y$ on Al (absorbers 10 and 11) remained almost unchanged during the accelerated ageing studies (Figures 37 and 38). Only a very slight shift of reflectance towards lower wavelengths was observed. Figure 39 presents the reflectance curves of CrO_xN_y on Cu (absorbers 1 and 3) before and after ageing at 278 °C. During ageing, reflectance at long wavelengths (IR range) decreased, i.e. thermal emittance increased. However, the change for absorber 1 was very small. The decrease in IR reflectance was significant in absorber 3. A similar behaviour was observed in CrO_x on anodized Al with a thin Al layer as the IR reflector on the anodized aluminium oxide (absorber 4) but at 278 °C the absorber degraded after only 36 h and longer exposure did not change the reflectance spectra (Figure 40). At a lower temperature of 250 °C, a decrease in reflectance at long wavelengths was observed as a function of exposure time, as presented in Figure 40. For the black chromium absorbers on Ni-coated Cu (absorber 7) and on SS (absorber 9), reflectance curves shifted towards lower wavelengths (Figure 41), as in [85, 113, 144, 270]. A small shift of reflectance towards lower wavelengths was also observed for CrO_xN_y on SS (absorber 8). More severe changes of reflectance were observed in TiO_xN_y on Cu (absorber 5), in which the reflectance curve has increased in both the visible and NIR ranges, shifted towards lower wavelengths and decreased in the IR range, as presented in Figure 42.

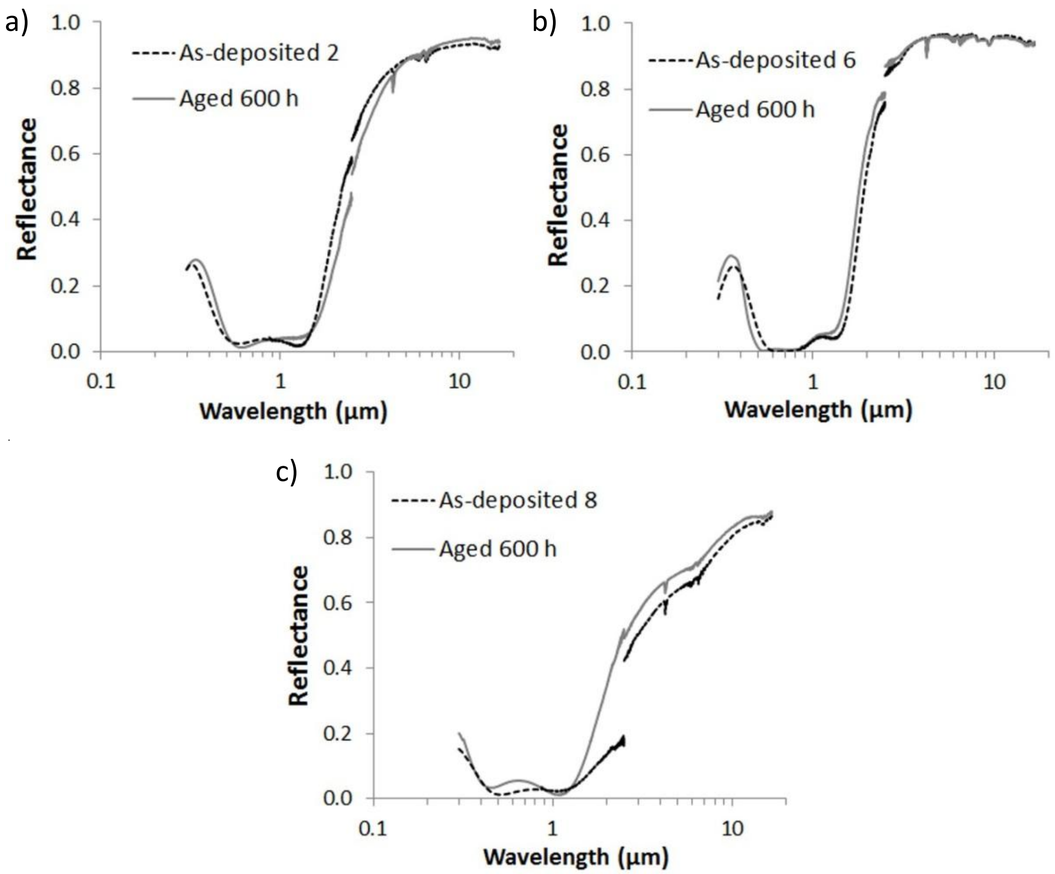

Figure 37. Reflectance curves for CrO_xN_y on Al for a) absorber 2 and b) absorber 6, and on SS for c) absorber 8.

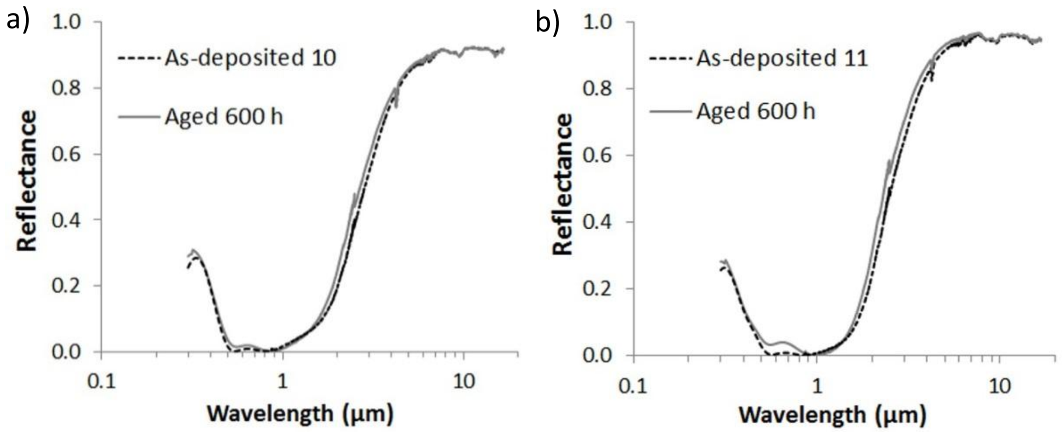

Figure 38. Reflectance curves for $TiAlSiO_xN_y$ on Al for a) absorber 10 and b) absorber 11.

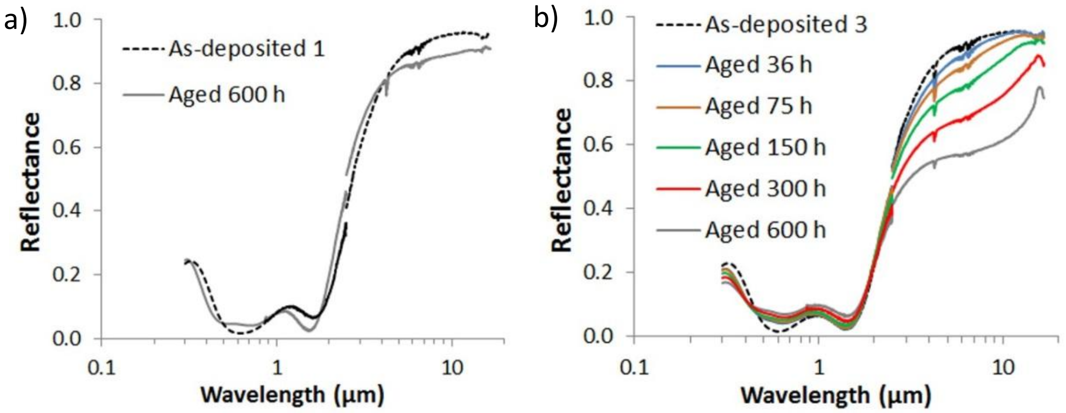

Figure 39. Reflectance curves for CrO_xN_y/SnO_x on Cu for a) absorber 1, and b) absorber 3.

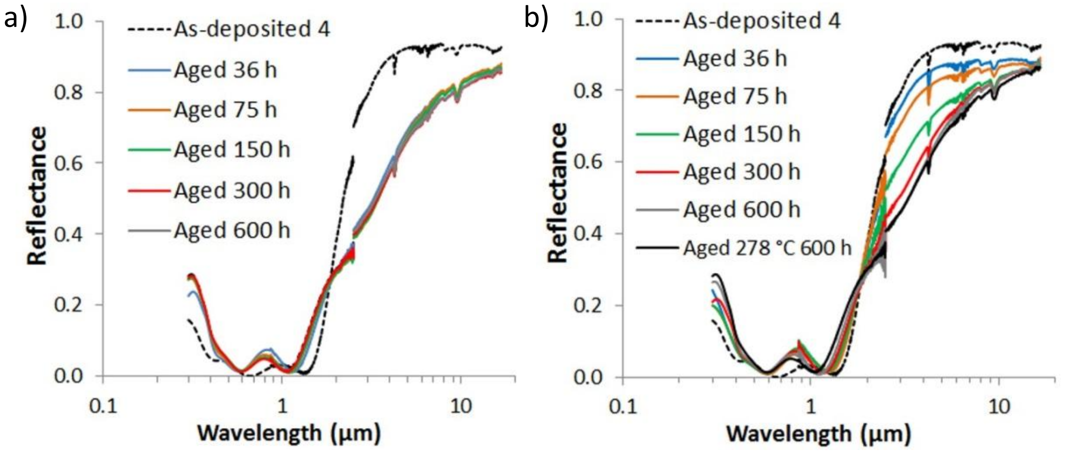

Figure 40. Reflectance curves for absorber 4, $Al/CrO_x/SiO_x$ on anodized Al for thermal exposures at a) 278 °C and b) 250 °C.

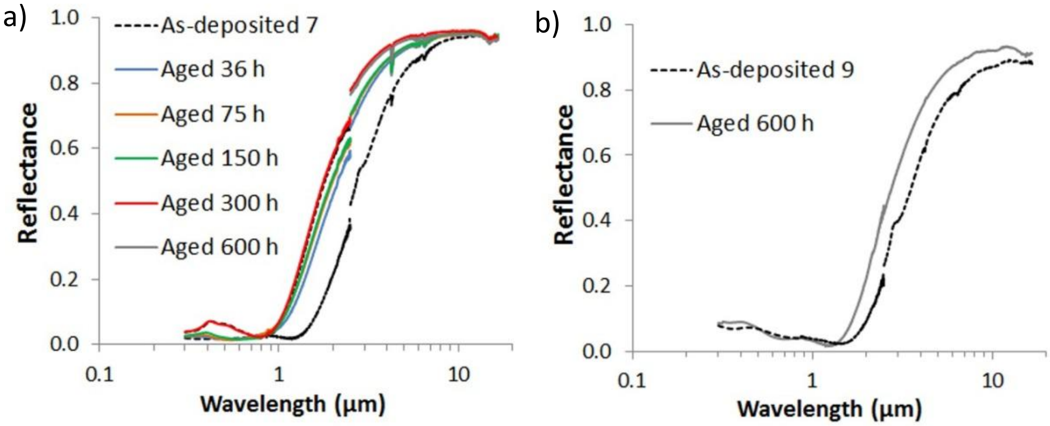

Figure 41. Reflectance curves for black chromium for a) absorber 7 on Ni-coated Cu substrate, and b) absorber 9 on SS substrate.

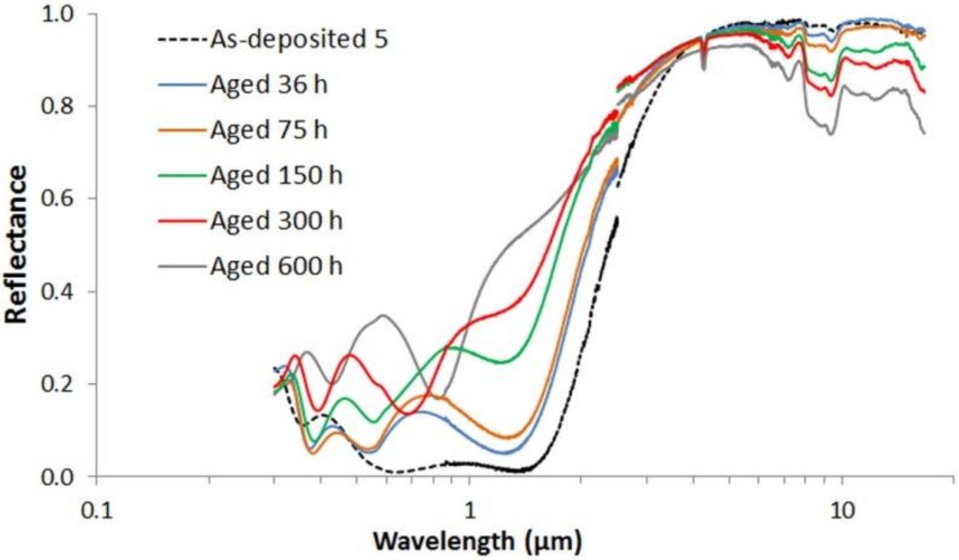

Figure 42. Reflectance curves for absorber 5, TiO_xN_y/SiO_x on Cu substrate.

6.2.2 Optical durability of industrial absorbers in accelerated ageing studies

The PC values calculated during the accelerated ageing studies at 278 °C are presented in Table 13 and Figure 43. In addition to the prolonged ageing studies at 278 °C, investigations were performed at 308 °C or 248 °C depending on the PC values according to [24]. The test procedure and qualification of the accelerated ageing test is presented in Table 14.

The sputtered CrO_xN_y and $TiAlSiO_xN_y$ on Al (absorbers 2, 6, and 10) and electroplated black chromium on SS (absorber 9) had a PC below 0.01 after 600 h, and thus they passed the accelerated ageing test without any significant changes in optical properties at the first test temperature. One of the $TiAlSiO_xN_y$ coatings on Al (absorber 11) slightly exceeded the PC limit of 0.01, but passed the test after the second test temperature. One of the sputtered CrO_xN_y coatings on Cu (absorber 1) showed only a small decline in optical properties and qualified after the second test temperature but the other (absorber 3) failed the accelerated ageing test. The effect of microstructure on this behaviour is discussed in section 7.2. The electroplated black chromium coating on Cu (absorber 7) showed a slow increase in PC values and the values slightly exceeded the 0.05 limit but it passed the test after the second test temperature. The PC values of the evaporated TiO_xN_y on Cu (absorber 5) increased substantially. In the case of CrO_x coating on anodized Al substrate (absorber 4), the PC value increased rapidly at the beginning of the ageing test and then stabilized.

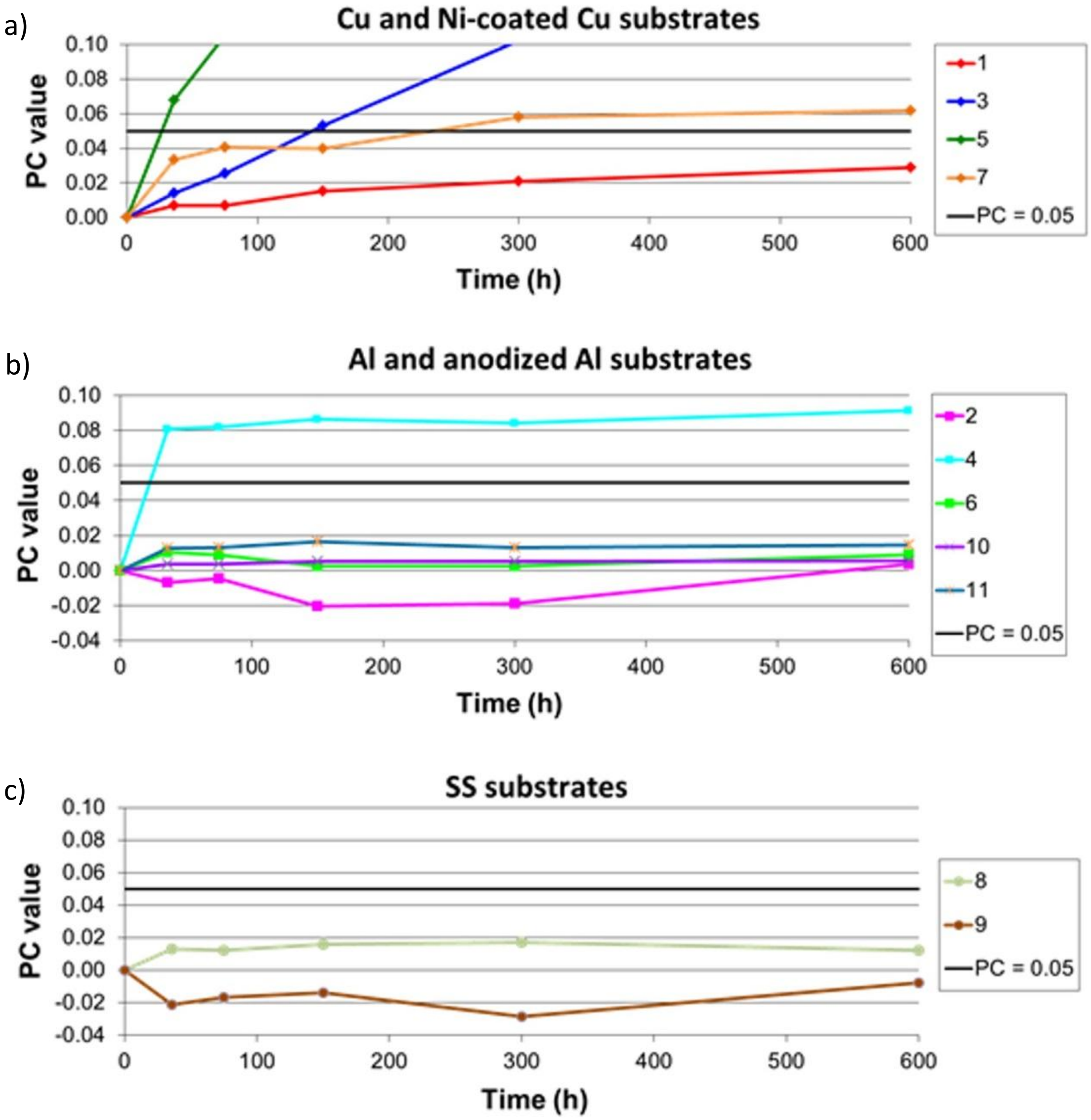

Figure 43. PC values during the accelerated ageing studies at 278 °C for the studied industrial absorbers on a) Cu and Ni-coated Cu, b) Al and anodized aluminium, and c) stainless steel substrates. The PC = 0.05 limit is marked on the graphs.

Table 14. Qualification of the accelerated ageing test with respect to thermal stability.

	PC (T_1, t_1) in 1st test at T_1 278 °C	PC in 2nd test at T_2 248 °C	PC in 2nd test at T_3 308 °C	Case in Fig. 13	Qualification	
1	0.029 after 600 h	-	0.040 after 342 h	b)	PC (T_3, t_3) ≥ PC (T_1, t_1)	**Pass**
2	0.004 after 600 h	-	-	a)	PC (T_1, 600 h) ≤ 0.01	**Pass**
3	0.026 after 75 h	0.047 after 272 h	-	c)	PC (T_2, t_2) > PC (T_1, t_1)	**Fail**
4	0.040 after 18 h *	0.062 after 105 h	-	c)	PC (T_2, t_2) > PC (T_1, t_1)	**Fail**
5	0.034 after 18 h *	0.136 after 105 h	-	c)	PC (T_2, t_2) > PC (T_1, t_1)	**Fail**
6	0.009 after 600 h	-	-	a)	PC (T_1, 600 h) ≤ 0.01	**Pass**
7	0.040 after 150 h	0.036 after 433 h		c)	PC (T_2, t_2) ≤ PC (T_1, t_1)	**Pass**
8	0.012 after 600 h		0.017 after 342 h	b)	PC (T_3, t_3) ≥ PC (T_1, t_1)	**Pass**
9	-0.008 after 600 h	-	-	a)	PC (T_1, 600 h) ≤ 0.01	**Pass**
10	0.006 after 600 h	-	-	a)	PC (T_1, 600 h) ≤ 0.01	**Pass**
11	0.015 after 600 h	-	0.015 after 342 h	b)	PC (T_3, t_3) ≥ PC (T_1, t_1)	**Pass**

***** As defined in [24], PC (T_1, t_1) was estimated from a graph for 18 h because the PC was > 0.05 after the first time period 36 h.

The activation energy was calculated according to the PC values in the two test temperatures by equation (6) and the service lifetime by equation (7) (Table 15). The stagnation temperature was assumed to be 185 °C as in Köhl *et al.* [18]. If the PC values remained below 0.05, it was not possible to define the activation energy for degradations of PC = 0.05 but the service lifetime could be evaluated as long and to last more than 25 years. The absorbers that qualified in the accelerated ageing test (absorbers 1, 2, and 6-11) are assumed to have a service lifetime of more than 25 years. Absorber 5 had a very low activation energy (<< 50 kJ/mol).

The very low activation energy can be assumed to suggest that more than one degradation process had contributed or that the degradation pattern was changed because of a physical change in the absorber [246]. Thus, the Arrhenius relationship is not valid for absorber 5 and it was not applicable (N/A) for determining the service lifetime.

Table 15. Activation energy calculated from PC values and service lifetime of the studied industrial solar absorbers (stagnation temperature 185 °C).

Absorber	Activation energy (kJ/mol)	Service lifetime (years)
1	-	> 25
2	-	> 25
3	55	14
4	94 *	12 *
5	N/A	N/A
6	-	> 25
7	73	47
8	-	> 25
9	-	> 25
10	-	> 25
11	-	> 25

* Activation energy was calculated according to [24] but Arrhenius behaviour is not valid for absorber 4 and thus the service lifetime estimation is unreliable.

The Arrhenius time transformations were calculated for absorbers in which the activation energy could be defined (absorbers 3-5 and 7) to ensure whether the Arrhenius relationship was accurate for the absorbers. The qualification scheme is based on the assumption that only one process of thermal degradation contributes to reduction in optical performance. The Arrhenius time transformations from 248 °C, 250 °C, and 308 °C to 278 °C are presented in Figure 44. All of the samples were tested according to ISO standard draft [24] at T_1 278 °C and at T_2 248 °C, and the activation energy was calculated according to these temperatures. For more information about the degradation process, the absorbers have also been studied at a higher temperature, at 308 °C, and some of the absorbers (3 and 4) have been studied at 250 °C. The Arrhenius time-transformed results at 248 °C and 250 °C are in good relation to 278 °C for absorbers 3, and 7. Hence, the Arrhenius relationship was valid for those absorbers in the temperature range of the accelerated ageing test from 248 °C to 278 °C. An exception was the evaporated TiO_xN_y on Cu (absorber 5, Figure 44 c), in which the activation energy suggested more than one ageing mechanism or phase change, and the Arrhenius time transformations to 278 °C were not valid at 248 °C after 200 h. After about 150 h at 278 °C, another process with higher activation energy seems to take over. For absorber 4 (Figure 44 b), degradation is activated at the beginning of the curve but then stabilised. This phenomenon creates a turn in the slope of the time-transformation graphs, which illustrates the behaviour of different activation energies. Thus, Arrhenius behaviour is not valid for absorber 4.

For the higher temperature of 308 °C, the Arrhenius time transformation results were quite well in relation with 278 °C for absorbers 3 and 7. Hence, the Arrhenius relationship was valid for absorbers 3 and 7 in the temperature range of about 250 °C to 300 °C. For absorber 5, the Arrhenius relationship was not valid at the higher temperature of 308 °C and there are uncertainties at the lower temperature of 248 °C, and thus it can be assumed that several degradation processes are involved. It should be noticed that absorbers 3-5 and 7 were defined [24] for study at the lower temperature of 248 °C, not at 308 °C.

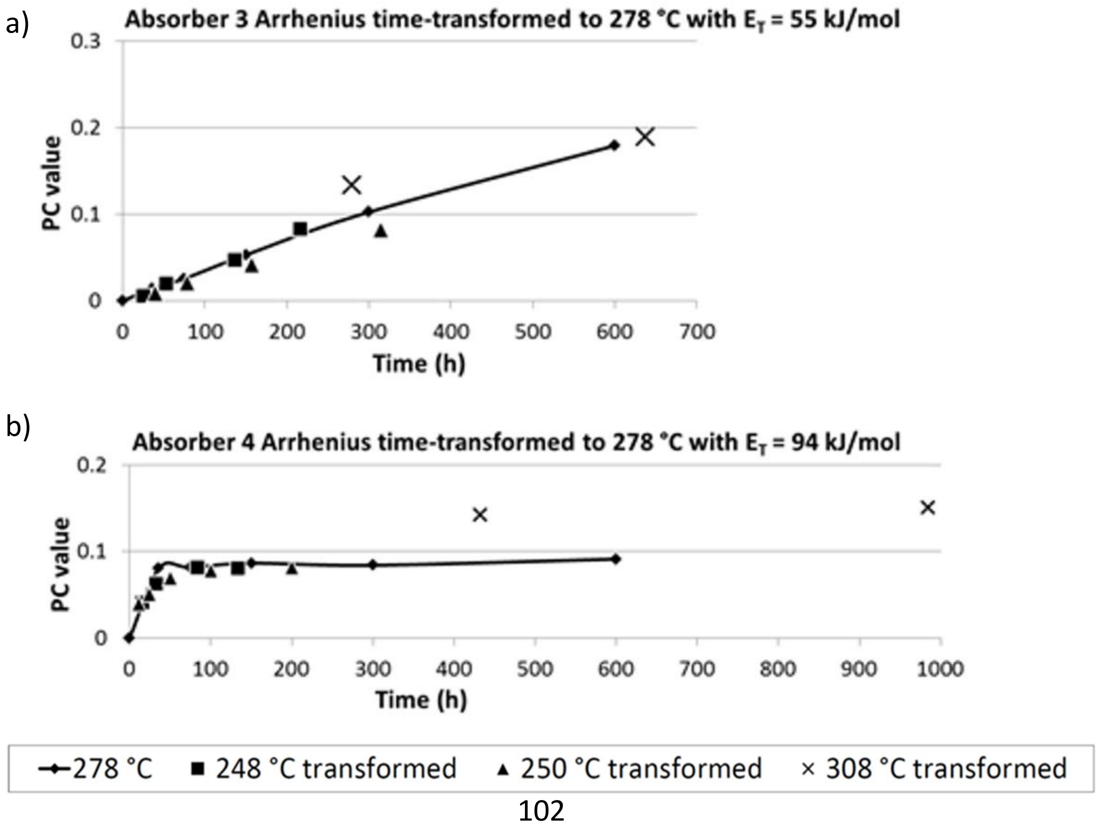

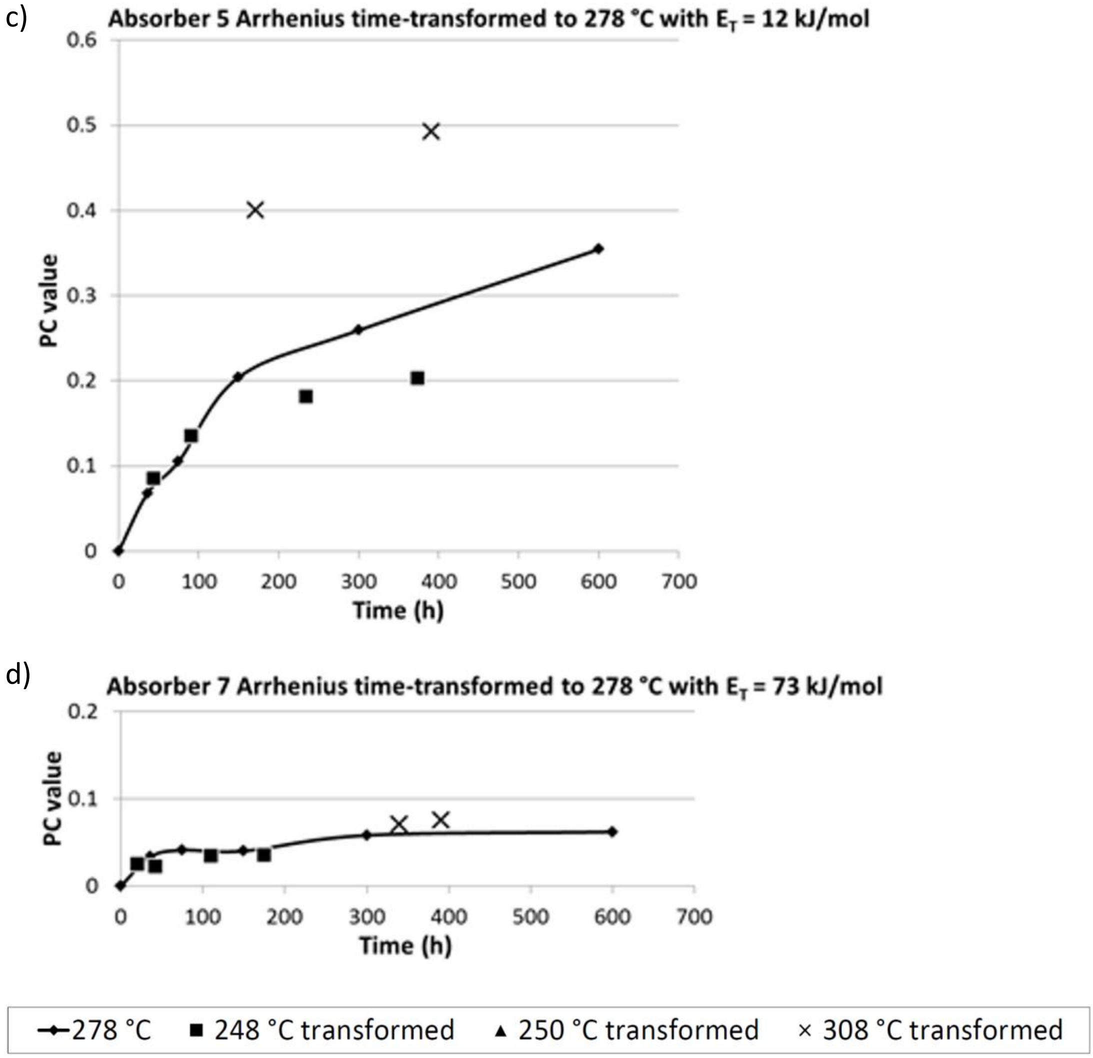

Figure 44. Arrhenius time transformations at 278 °C for a) sputtered CrO_xN_y on Cu: absorber 3, b) sputtered CrO_x on anodized Al: absorber 4, c) evaporated TiO_xN_y on Cu: absorber 5, and d) electroplated black chromium on Ni-coated Cu: absorber 5.

The accelerated ageing studies [24] included the calculation of activation energy from PC values using the two temperatures used in the qualification procedure. In addition, activation energies were determined separately for absorptance and emittance from the slopes of ln(Δα) or ln(ΔƐ) versus 1/T. Plots for estimating activation energy for industrial absorbers are presented in Figures 45 and 46. The difference in absorptance and emittance during ageing is expressed for a specific time in measurement points and using interpolation in appropriate cases. In most of the degraded absorbers (absorbers 2-5, and 7), the slope for the short-period heat treatment at 300-500 °C was gentler than the slope for the accelerated ageing studies at 248-308 °C or the preliminary ageing studies at 250 °C. This led to a lower activation energy for the short-period treatments. However, this may be dependent on the short-period ageing procedure, discussed in more detail in section 7.4.

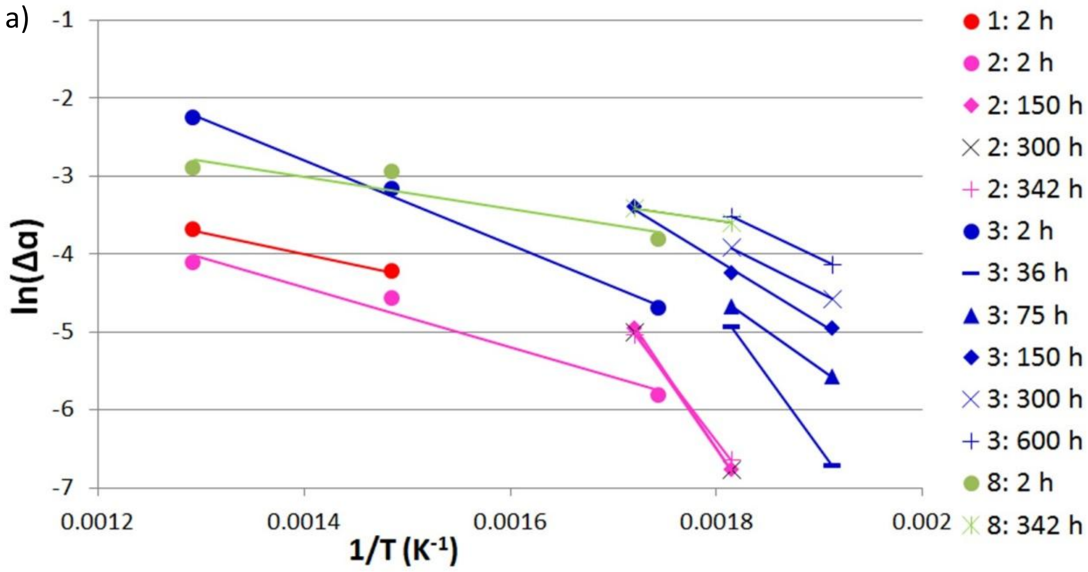

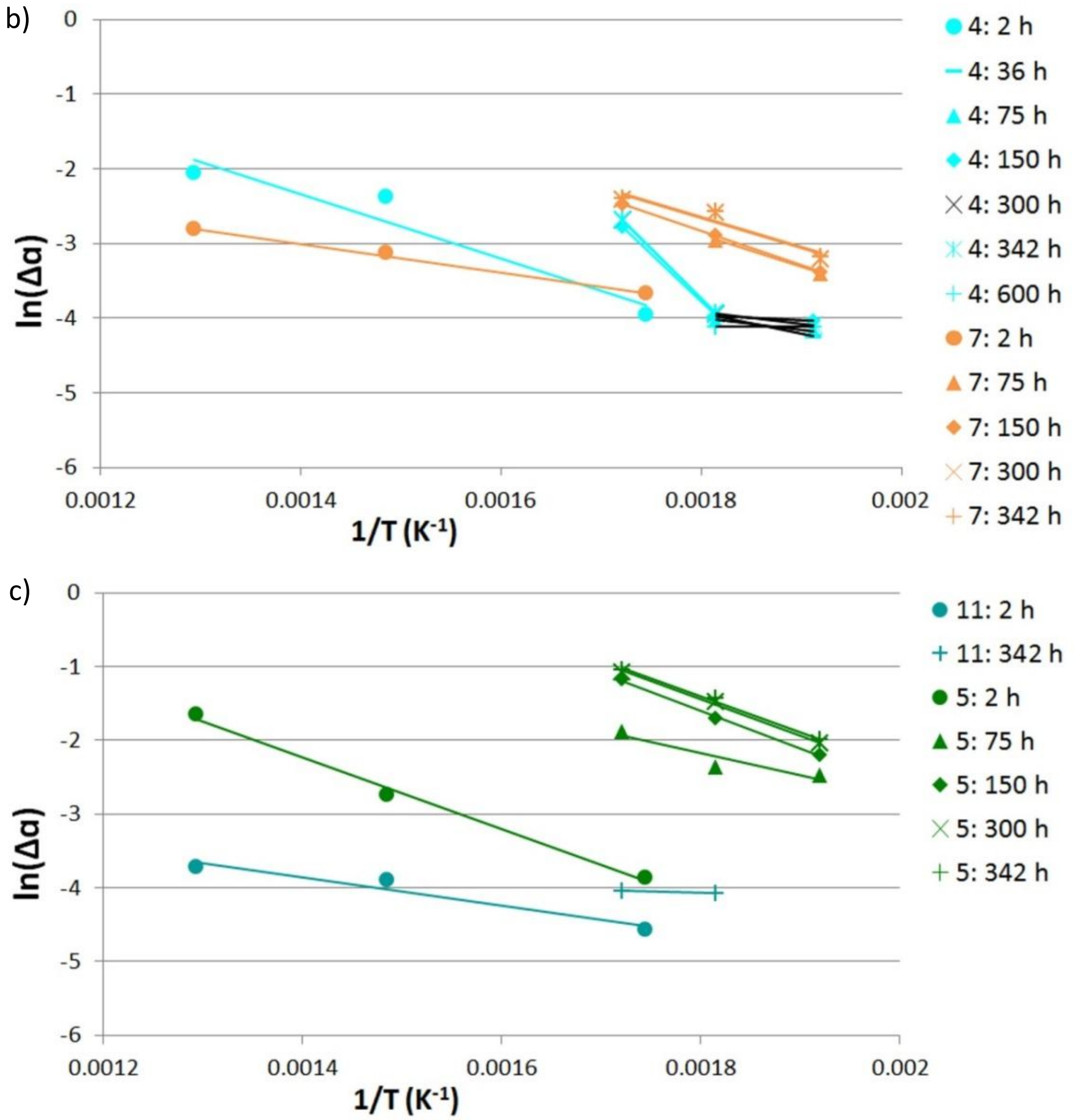

Figure 45. Plot of ln(Δα) versus 1/T and linear trend lines between ageing at different temperatures for a specific time for a) CrO_xN_y absorbers 1, 2, 3, and 8, b) CrO_x and black chrome absorbers 4 and 7, and c) TiO_xN_y and $TiAlSiO_xN_y$ absorbers 5 and 11.

CrO_xN_y-based absorber 1 degraded in solar absorptance only in the short-period heat treatment at 400-500 °C but remained unchanged at 300 °C and in the accelerated ageing studies. CrO_xN_y-based absorber 2 was degraded in solar absorptance at ≥ 278 °C for ≥ 150 h but remained unchanged for shorter durations at 278 °C and at the lower ageing temperature of 250 °C. CrO_xN_y-based absorber 3 degraded even at lower temperatures. The slope of difference in solar absorptance for absorber 3 for 36 h at 250-278 °C was steeper than the slopes for longer durations, and the slope of difference in thermal emittance for 36 h cannot be displayed because there was no degradation in thermal emittance at 250 °C after 36 h. CrO_xN_y-based absorber 8 was studied at ≥ 278 °C but it showed only very moderate changes in absorptance.

In CrO_x-based absorber 4 on anodized Al substrate, a change was obtained in the slope from 248-278 °C to 278-308 °C. At temperatures < 278 °C, the slope was gentle, nearly horizontal, but at temperatures > 278 °C, it was steeper. The slopes for absorber 4 at a certain temperature range in accelerated studies are quite parallel but they are located on the same level. Thus, a longer duration did not create a higher degradation in solar absorptance but the duration was rather insignificant in the time range studied. Only short-period heat treatments for 2 h obtained the lower level. In CrO_x-based (black chromium) absorber 7, the degradation of solar absorption exhibited a similar slope from 248 °C to 308 °C, and the duration of ageing influenced the level of the trend line slightly.

TiO_xN_y-based absorber 5 degraded in solar absorptance with quite a similar slope from 248 °C to 500 °C. $TiAlSiO_xN_y$-based absorber 11 showed a very small degradation in solar absorptance. Hence, the slope was gentle.

Changes in thermal emittance were obtained in absorbers 1, 3, and 5 on Cu substrates, and in absorber 4 on anodized Al substrate with a thin Al layer between the anodized Al oxide layer and the absorber coating. In the short-period heat treatments, absorbers 1 and 3 degraded at 400-500 °C but at 300 °C exposure thermal emittance did not increase. However, in longer durations in accelerated ageing studies, absorbers 1 and 3 degraded with quite a similar linear trend line from 250 °C to 308 °C. Absorber 5 showed quite parallel slopes for differences in thermal emittance which obtained a higher level during the exposure time. Absorber 4 had several different slopes for differences in thermal emittance. At a narrow temperature range from 248 °C to 250 °C, the slope was very steep, almost vertical, but from 248-250 °C to 278 °C it slowly became more horizontal as a function of exposure time. At > 278 °C, the slope levelled out and was located on the same level regardless of the exposure duration. Only short-period heat treatments for 2 h obtained a lower level but quite a similar slope than the “settled” slope at longer durations.

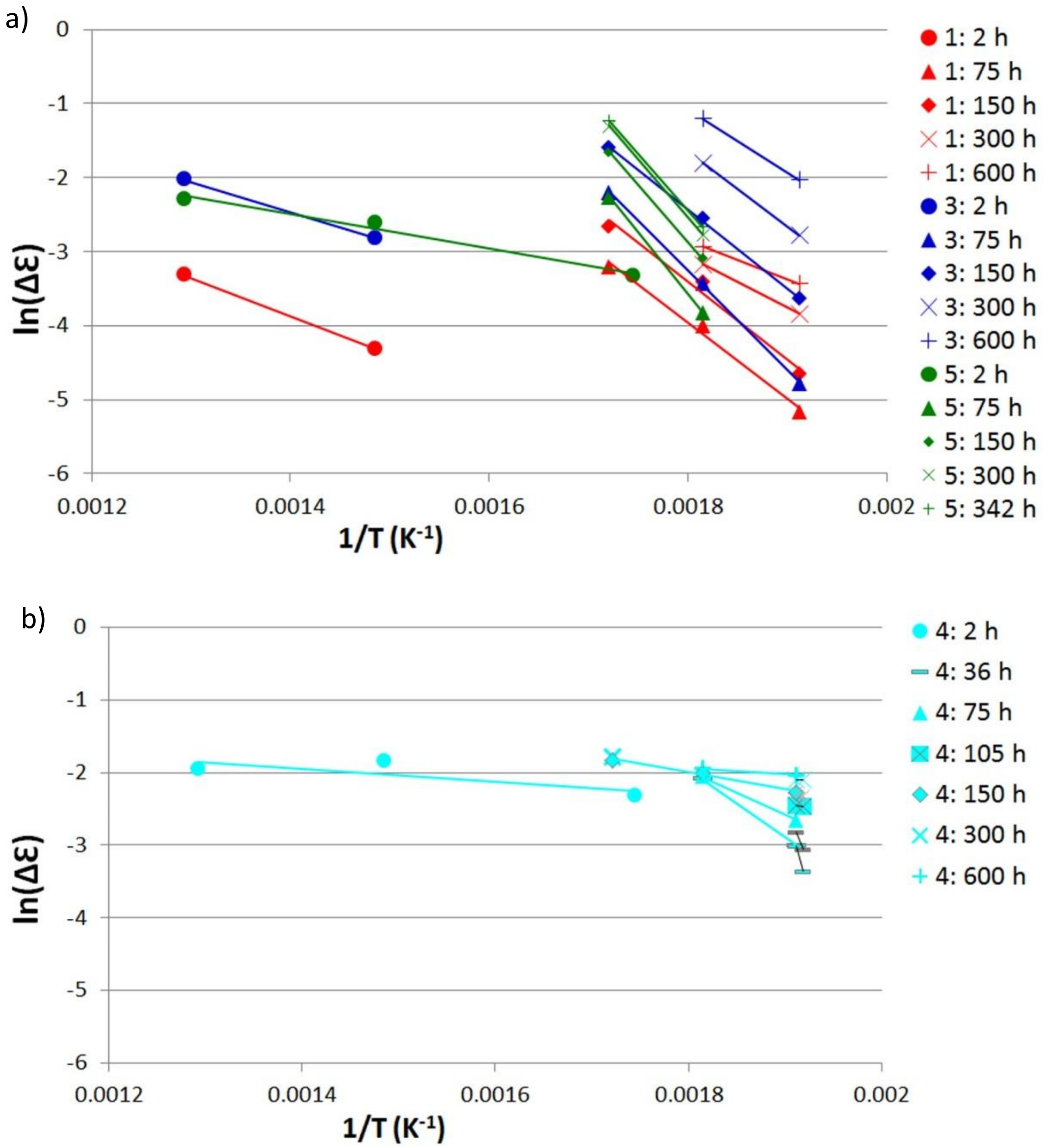

Figure 46. Plot of ln(ΔƐ) versus 1/T and linear trend lines between ageing at different temperatures for a specific time for a) absorbers 1, 3, and 5 on copper substrates, and b) absorber 4 on anodized Al substrate.

Table 16 shows the activation energies for absorptance and emittance. The activation energies are calculated from the slopes of ln(Δα) or ln(ΔƐ) versus 1/T (see Figures 45-46). The error range is estimated as a standard deviation of the activation energies with quite similar slopes. Up to 500 °C, there were only short-period heat treatments so the error was estimated to be ± 20 kJ/mol. In some cases, the error range was relatively high because of experimental uncertainties and interpolation of the results to meet a certain time period.

Table 16. Activation energies for industrial absorbers calculated for absorptance and emittance at elevated temperatures up to 500 °C.

Absorber	$E_T(\alpha)$ (kJ/mol)	$E_T(\varepsilon)$ (kJ/mol)
1	– (no degradation at < 300 °C) 20 ± 20 for 2 h at 400-500 °C	60 ± 20
2	150 ± 20 at < 300 °C 30 ± 20 for 2 h 300-500 °C	– (no degradation)
3	150 ± 20 for 36 h at < 300 °C 60 ± 20 at < 300 °C for 75-600 h 40 ± 20 for 2 h at 300-500 °C	90 ± 20 30 for 2 h at 300-500 °C
4	10 ± 10 at < 278 °C 110 ± 10 at ≥ 278 °C 40 ± 20 for 2 h at 300-500 °C	340 ± 20 at ≤ 250 °C for ≤ 50 h Decreases up to 10 ± 10 at higher temperatures or longer time
5	25 ± 10 for at ≤ 278 °C for < 150 h 40 ± 10 for at ≤ 278 °C for ≥ 150 h	10 ± 10 20 ± 10 for 2 h at 300-500 °C
6	260 ± 80 1) 10 ± 20 for 2 h 300-500 °C	– (no degradation)
7	40 ± 10 20 ± 20 for 2 h 300-500 °C	– (no degradation)
8	20 kJ/mol	– (no degradation)
9	– (no degradation)	– (no degradation)
10	– (no degradation)	– (no degradation)
11	20 ± 20	– (no degradation)

1) High standard deviation because of the very small degradation at 278 °C (α from 0.920 to 0.913 after 600 h) but at 308 °C still very insignificant but faster degradation to α = 0.903 after 342 h.

6.2.3 Changes in composition at elevated temperatures

The diffusion of oxygen and other elements was investigated by TOF-ERDA for as-deposited and aged industrial absorbers 1-7. Ageing was performed at 278 °C for 600 hours. Figure 47 shows the depth profile graphs of sputtered CrO_xN_y on Cu (absorbers 1 and 3), and Figure 48 those of evaporated TiO_xN_y on Cu (absorber 5). The ageing studies created changes in the composition. Copper diffused to the coating and the proportion of oxygen increased in the absorption layer in relation to the metallic chromium or titanium content. Aged absorbers with a CuO island formation have a rough surface, which leads to uncertainties in the TOF-ERDA depth profiles. Samples in TOF-ERDA are usually assumed to have smooth surfaces [271]. The distortion of Cu and O is based on the fact that TOF-ERDA sees a sample surface as a flat surface but islands create high surface roughness. For the aged depth profiles with island formation, the Cu inside the coating and the oxygen in the substrate comes from the CuO islands. In the case of aged absorbers with CuO islands, the amount of oxygen in the Cu substrate indicates the quantity of CuO islands on the surface. The O/Cu ratios for all of the as-deposited absorbers were zero but after ageing at 278 °C for 600 h, they were 0.11, 0.36, and 0.29 for absorbers 1, 3, and 5, respectively.

The composition of chromium oxy-nitride absorbers on Al substrate (absorbers 2 and 6) is presented in Figure 49. The depth profile of CrO_xN_y/SiO_x on Al (absorber 6) was fairly similar before and after ageing at 278 °C for 600 hours. CrO_xN_y/SnO_x on Al (absorber 2) suffered from slight oxidation in the absorption layer but in spite of this change, the coating passed the accelerated ageing test. A similar kind of oxidation in absorber coating was observed in the black chromium coating on Ni-coated Cu (absorber 7) (Figure 50).

As a substrate, the anodized aluminium/Al layer (as the IR reflector) aged during thermal exposure, with changes in optical properties as described in section 6.2.1. In sputtered CrO_x absorber 4, the composition of the anodized aluminium layer changed during the ageing test, as presented in Figure 51. The proportion of oxygen increased in comparison to the metallic aluminium in the major part of the anodized layer. In addition, aluminium seemed to form a layer between the anodized Al and CrO_x absorber layers. According to the TOF-ERDA measurements, the as-deposited anodized Al layer seems to be sub-stoichiometric alumina as in [242], and XRD results revealed metallic Al, Al_2O_3, and the remains of sulphides (Table 11). From the TOF-ERDA measurements, the O/Al ratio in the anodized aluminium layer was about 1 in the as-deposited coating whereas it was about 1.5 in the aged coating. An O/Al ratio of 1.5 corresponds to alumina, Al_2O_3. The TEM electron diffraction analysis of the selected area (SAED) and grazing incidence X-ray diffraction (XRD) revealed changes in the structure of the anodized Al layer, as presented in Figures 52 and 53. For the as-deposited anodized Al layer, SAED included amorphous rings. According to SAED, the aged anodized layer showed a diffraction pattern, and suggested a crystallized structure. For the as-deposited and aged absorber 4, the XRD pattern included peaks for aluminium (substrate) and chromium oxide (absorber coating). The silicon oxide anti-reflection coating did not show the peaks that represent an amorphous structure. For as-deposited absorber 4, the amorphous anodized aluminium oxide does not have peaks but ageing revealed crystallized gamma (γ) -Al_2O_3 peaks.

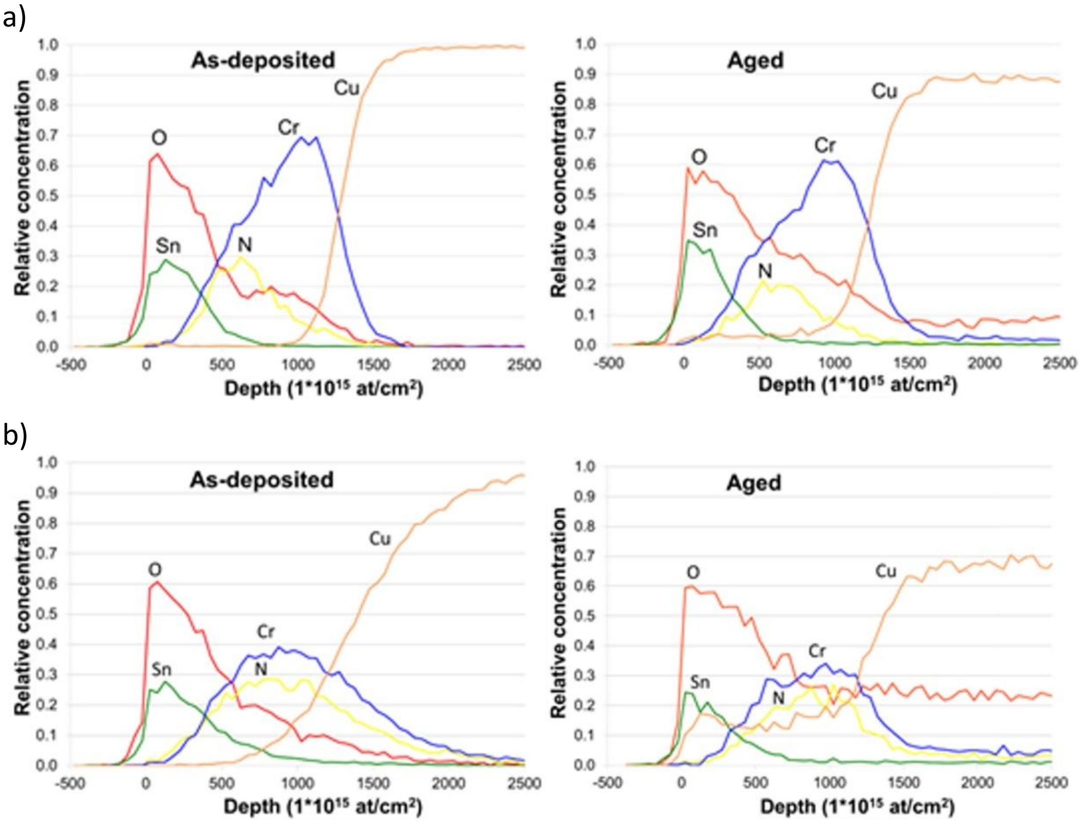

Figure 47. As-deposited and aged TOF-ERDA depth profile graphs for CrO_xN_y/SnO_x absorbers on Cu a) absorber 1, and b) absorber 3.

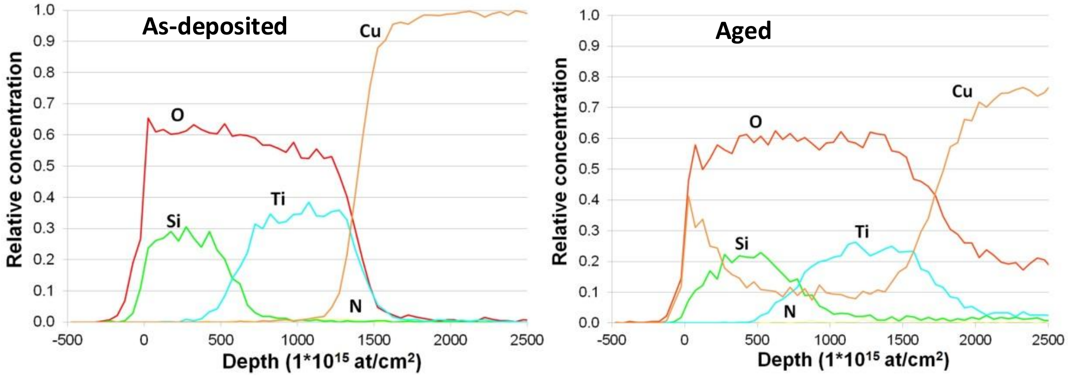

Figure 48. As-deposited and aged TOF-ERDA depth profile graphs for absorber 5: TiO_xN_y/SiO_x on Cu.

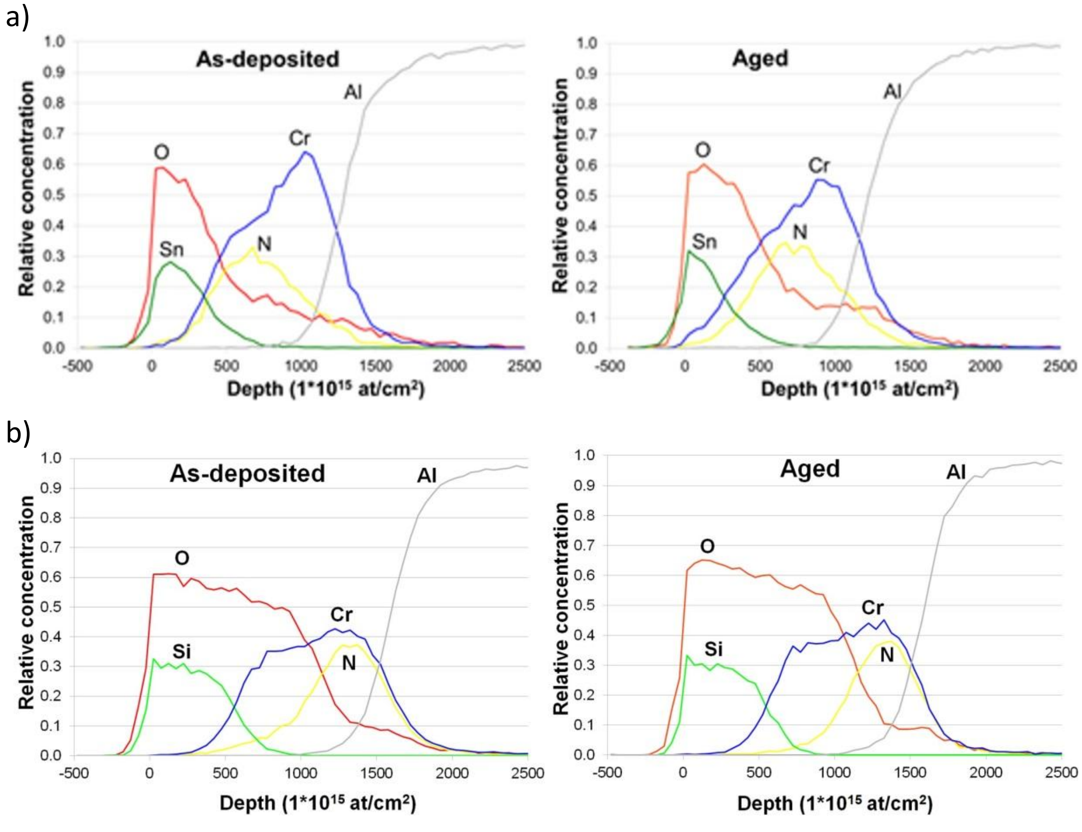

Figure 49. As-deposited and aged TOF-ERDA depth profile graphs for a) absorber 2: CrO_xN_y/SnO_x on Al, and b) absorber 6: CrO_xN_y/SiO_x on Al.

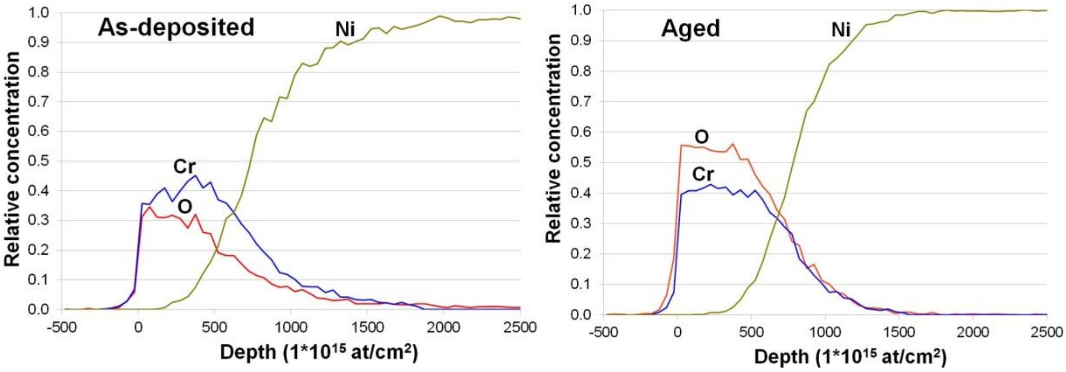

Figure 50. As-deposited and aged TOF-ERDA depth profile graphs for absorber 7: black chromium on Ni-coated Cu. The measurement depth was from the surface to the Ni layer.

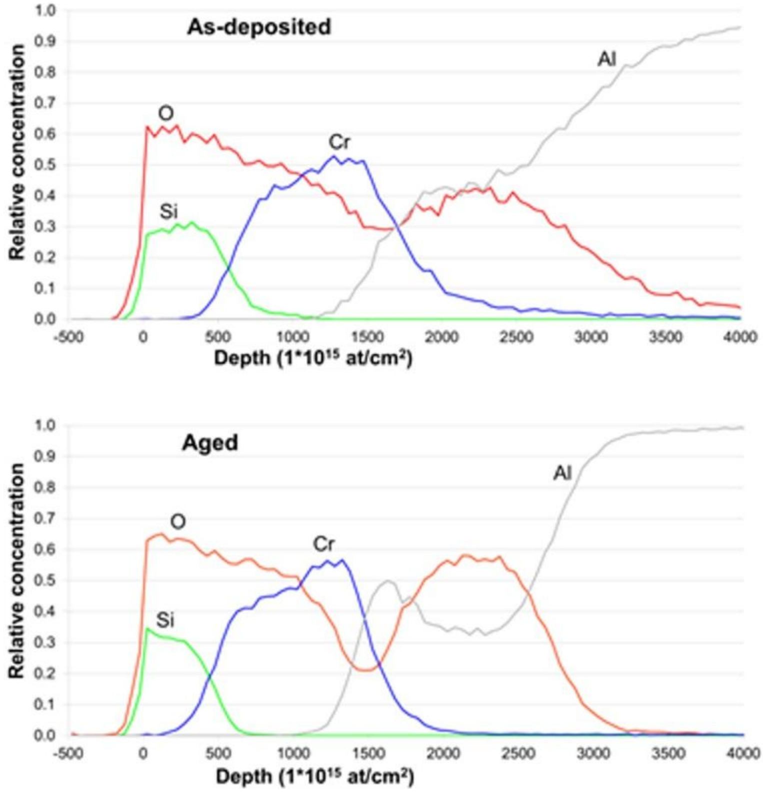

Figure 51. As-deposited and aged TOF-ERDA depth profile graphs for absorber 4: CrO_x/SiO_x on anodized Al.

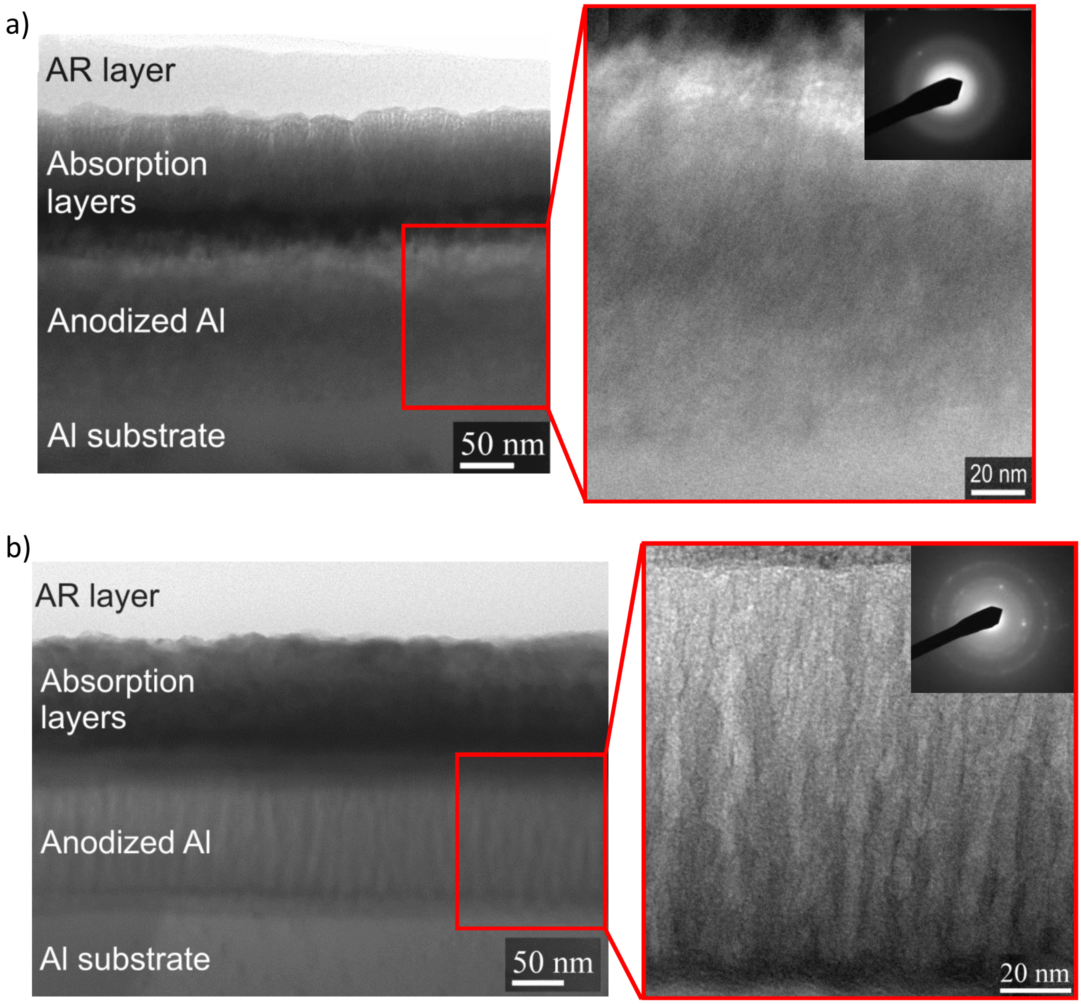

Figure 52. TEM images and SAED patterns for CrO_x/SiO_x absorber on anodized Al substrate (absorber 4) a) as-deposited, and b) aged at 278 °C for 600 hours. On the left, all of the coating layers and on the right, an insert of the anodized Al layer.

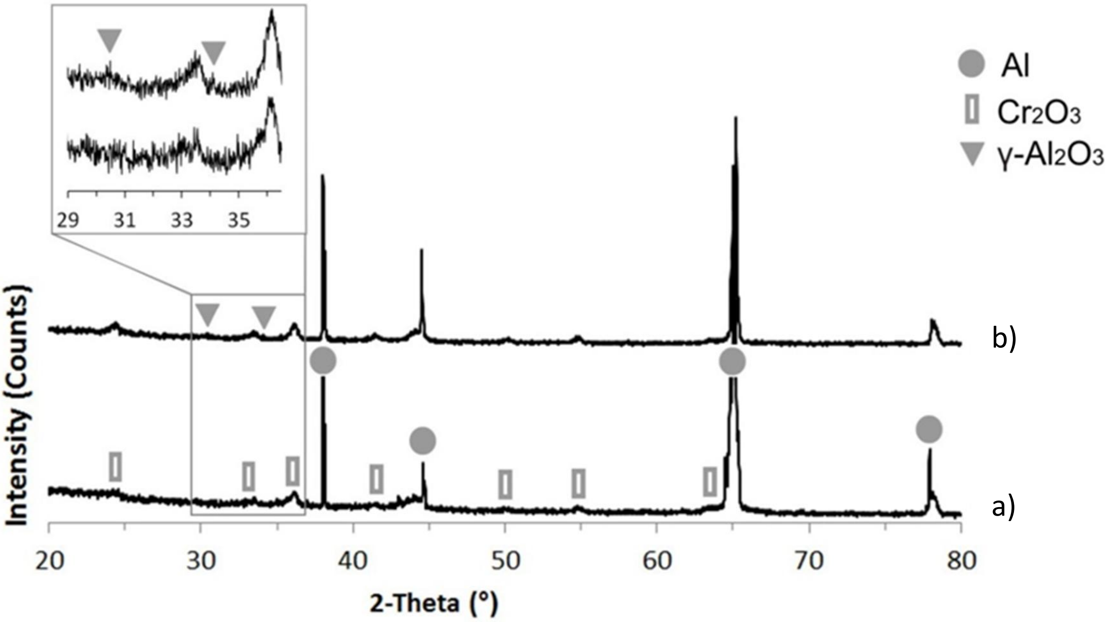

Figure 53. XRD patterns for CrO_x/SiO_x absorber on anodized Al substrate (absorber 4) a) as-deposited, and b) aged at 278 °C for 600 h.

The SAED patterns of the amorphous/crystalline structures of absorption layers before and after ageing are presented in Figure 54. The as-deposited absorption layers were crystalline. After ageing at 278 °C for 600 h, the CrO_xN_y absorption layers (absorber 1-3 and 6) remained quite similar showing a crystalline structure. D-values of the strongest rings were similar for each case. In the case of absorber 5, the aged TiO_xN_y coating seemed to have a decrease in crystallinity and became more amorphous (no clear diffraction rings). In absorber 4, d-values of the strongest rings seem to correspond rhombohedral Cr_2O_3 (ICDD PDF-4 database, reference code 00-006-0504). In the diffraction pattern of aged absorber 4, the separate spots most likely arise from the Al substrate, and are due to sample preparation.

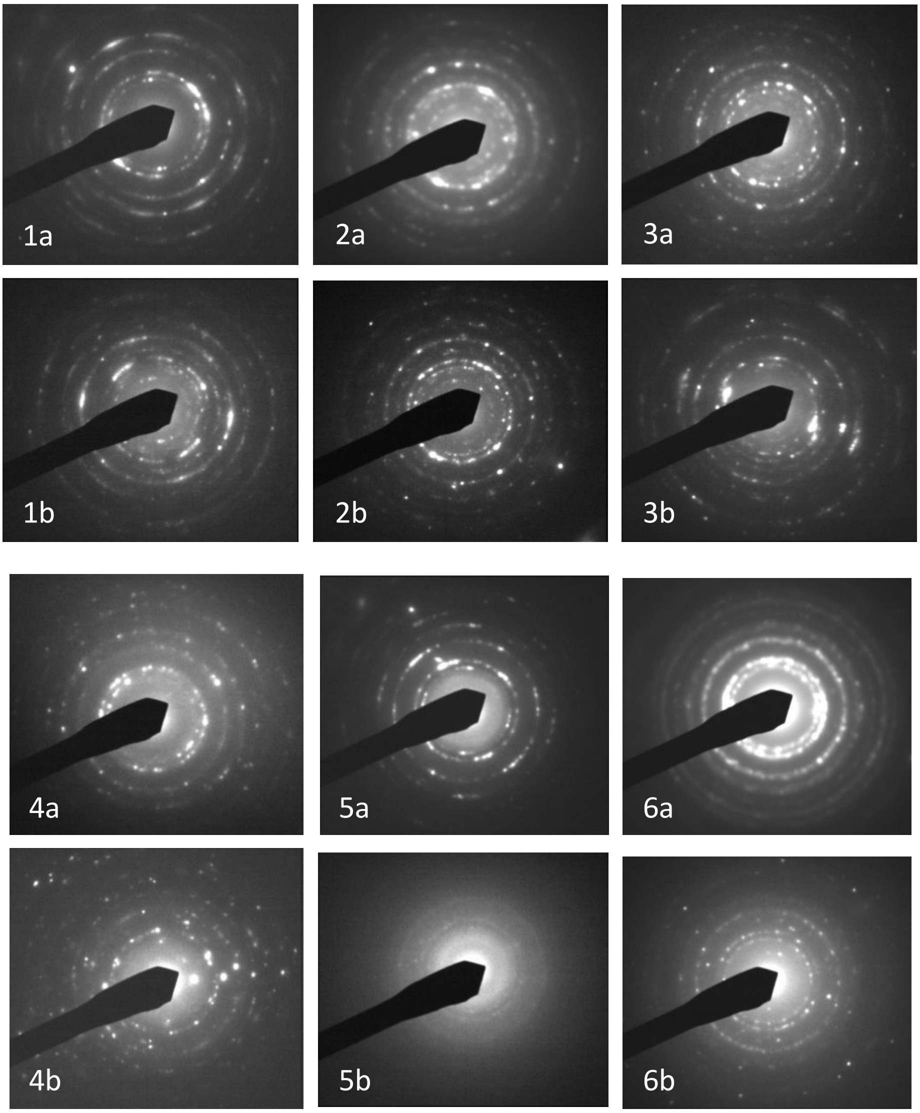

Figure 54. SAED patterns of absorber layers for absorbers 1-6: a) as-deposited and b) aged at 278 °C for 600 h.

The SAED patterns of the anti-reflection layers before and after ageing are presented in Figure 55. As-deposited tin oxide anti-reflection layers (absorbers 1-3) had sharp rings in a diffraction pattern, and thus they can be considered to be nanocrystalline. D-values of the strongest rings seem to correspond both SnO and SnO_2 compounds (ICDD PDF-4 database, reference codes 04-005-4540 and 00-041-1445). The as-deposited silicon oxide coatings (absorbers 4-6) had amorphous rings. During ageing, the structures of the anti-reflection coatings remained quite unchanged. Only the amorphous SiO_x AR layer of absorber 5 showed some sharp rings after ageing, which indicates crystallinity. A TEM image of aged absorber 5 is presented in Figure 56.

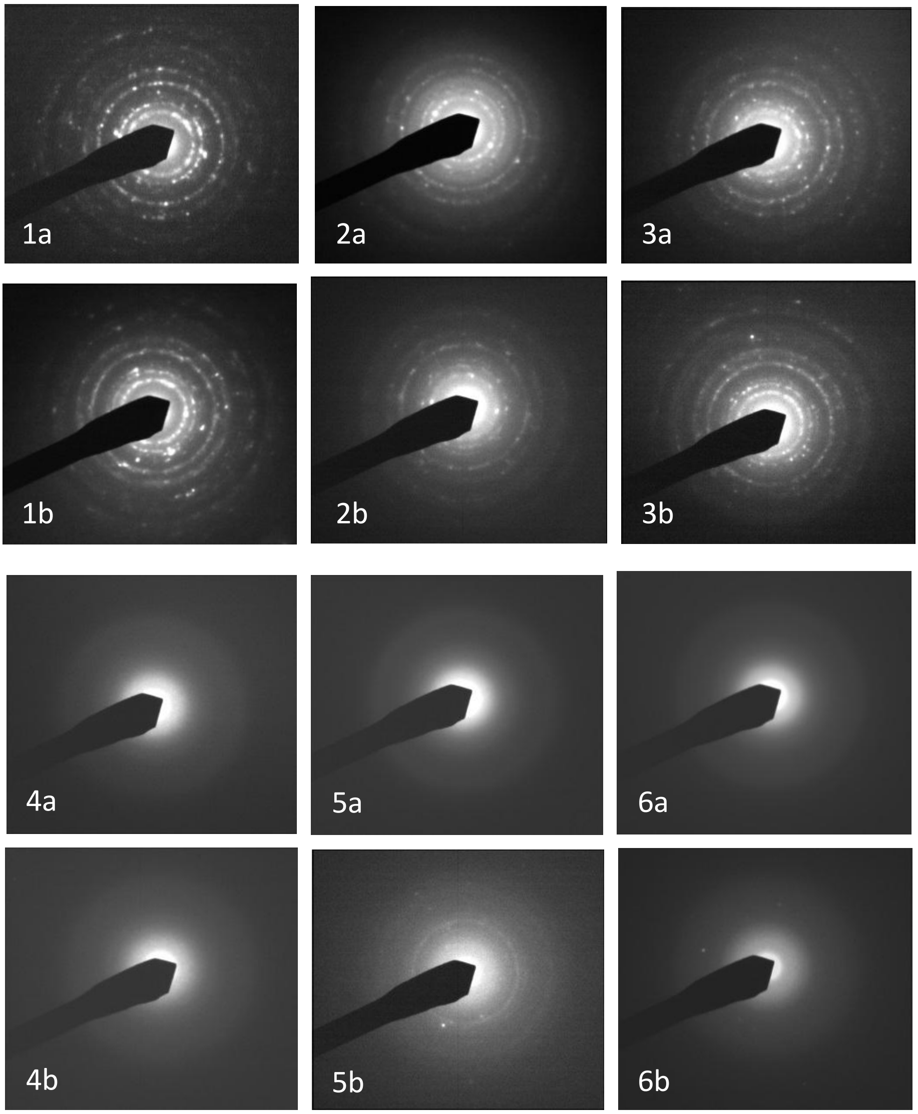

Figure 55. SAED patterns of anti-reflection layers for absorbers 1-6: a) as-deposited and b) aged at 278 °C for 600 h.

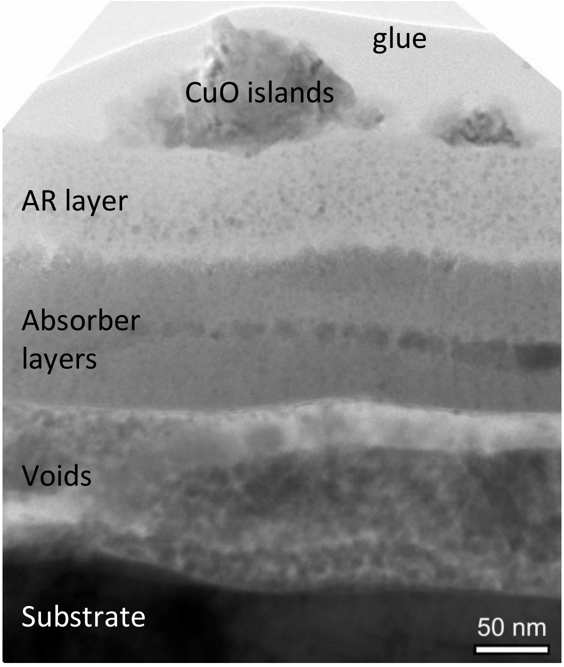

Figure 56. TEM image of aged (278 °C for 600 h) absorber 5.

The oxidation of chromium or titanium in the absorption layers was observed from the majority of the studied coatings using TOF-ERDA. Table 17 summarizes the ratios of oxygen before and after the ageing test at 278 °C for 600 hours for absorber and anti-reflection coatings. The oxygen content of the absorber layer was calculated as O/Cr (absorbers 1-4 and 6-7) or O/Ti (absorber 5), and of the anti-reflection layer as O/Sn (absorbers 1-3) or O/Si (absorbers 4-6). The oxygen/metal ratios were calculated by dividing the determined oxygen content of the certain coating layer (i.e. absorption or anti-reflection layer) by the measured metal or silicon content of the same layer. During ageing, the increase in oxygen content in the absorber layers in the sputtered CrO_xN_y on Cu and Al (absorbers 1-3 and 6) showed a wide variation, from about 10 % to 80 %. In the electroplated black chromium coating on Ni-coated Cu (absorber 7) and in one of the sputtered CrO_xN_y coatings (absorber 1), the O/Cr ratio increased by about 80 %. The sputtered CrO_x absorber coating on anodized Al (absorber 4) and evaporated TiO_xN_y on Cu (absorber 5) did not show any notable increase in the oxygen ratio in the absorption layer. The oxygen content in the anti-reflection coatings remained quite unchanged for the absorbers studied, except for the sputtered CrO_x/SiO_x absorber 4, in which the oxygen ratio increased by 15 %.

Table 17. Oxygen content of absorption and anti-reflection layers. Relative concentrations were measured by TOF-ERDA before and after ageing at 278 °C for 600 hours. Change is calculated from aged minus as-deposited values.

	Oxygen content of absorption layer O/Cr or O/Ti				**Oxygen content of AR layer O/Sn or O/Si**			
	As-dep.	**Aged**	**Change**	**Change %**	**As-dep.**	**Aged**	**Change**	**Change %**
1	0.27 ± 0.01	0.49 ± 0.07	0.22	81	2.05 ± 0.05	2.00 ± 0.03	-0.05	-2
2	0.33 ± 0.01	0.43 ± 0.05	0.10	30	1.92 ± 0.04	2.0 ± 0.2	0.08	4
3	0.26 ± 0.01	0.38 ± 0.06	0.12	46	1.93 ± 0.04	2.0 ± 0.4	0.07	4
4	0.81 ± 0.02	0.79 ± 0.07	-0.02	-2	1.83 ± 0.04	2.1 ± 0.1	0.27	15
5	1.59 ± 0.05	1.54 ± 0.4	-0.05	-3	2.19 ± 0.05	2.0 ± 0.6	-0.19	-9
6	0.81 ± 0.02	0.86 ± 0.07	0.05	6	2.02 ± 0.03	2.2 ± 0.1	0.18	9
7	0.69 ± 0.01	1.24 ± 0.07	0.55	80				

As the TOF-ERDA results revealed (Figures 47-48), copper substrate atoms had diffused outwards into the coating and/or through the coating to the surface. Similar phenomena were noticed with absorbers on Cu substrates (absorbers 1, 3, and 5) but not with absorbers on Ni-coated Cu, Al, anodized Al or stainless steel. In earlier studies, copper has been reported to diffuse through a coating [85, 174, 272]. Figure 57 and Table 18 show that the islands formed are copper oxide. Based on the O/Cu ratio, FESEM-EDS analyses indicate that the copper oxide phase formed was apparently CuO. Similar results have been published in the literature, when the CuO phase was confirmed by Raman spectroscopy [74] and XPS [76].

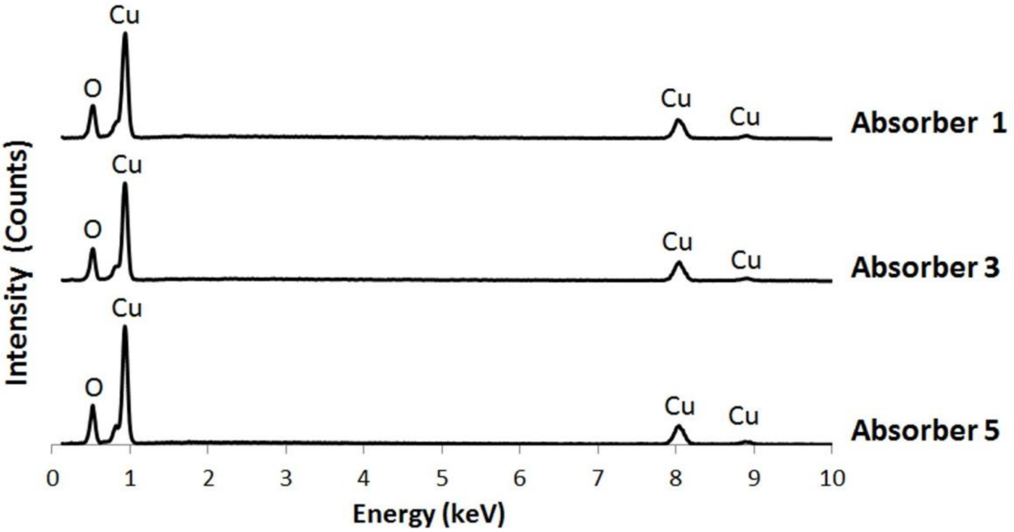

Figure 57. FESEM-EDS spectra of the islands of aged absorbers 1, 3, and 5 on copper substrates. Diffused copper formed CuO islands on the surface.

Table 18. FESEM-EDS analyses of the surface of as-deposited absorbers and islands of aged absorbers 1, 3, and 5 on copper substrates. EDS values are averages of three measurements with a standard deviation of ± 2 At.%. During the ageing test, copper diffused to the surface as islands and oxidized to CuO.

	Absorber 1		**Absorber 3**		**Absorber 5**	
Element	**Surface as-deposited (At.%)**	**Islands aged (At.%)**	**Surface as-deposited (At.%)**	**Islands aged (At.%)**	**Surface as-deposited (At.%)**	**Islands aged (At.%)**
O K	29	50	23	51	39	51
Cu K	50	50	56	49	49	49
Cr K	16	< 1	14	< 1	0	0
Ti K	0	0	0	0	6	< 1
Sn L	< 5	< 1	< 5	< 1	0	0
Si K	0	0	0	0	< 5	<1
N K	< 5	< 1	< 5	< 1	< 1	< 1

The islands were observed from the surface of absorbers with Cu substrates along the direction of rolling (Figure 58). In the case of copper substrates, islands of oxidized copper were formed along the rolling scratches of the substrate during the ageing test. Despite this diffusion, absorber 1 passed the accelerated ageing test, but absorbers 3 and 5 failed. The size of the CuO islands was on the submicron and micrometre scale (Figure 59). After 600 h exposure at 278 °C, the biggest islands were a couple of micrometres (about 2-3 µm) in height and coalesced with the subsequent islands in lines.

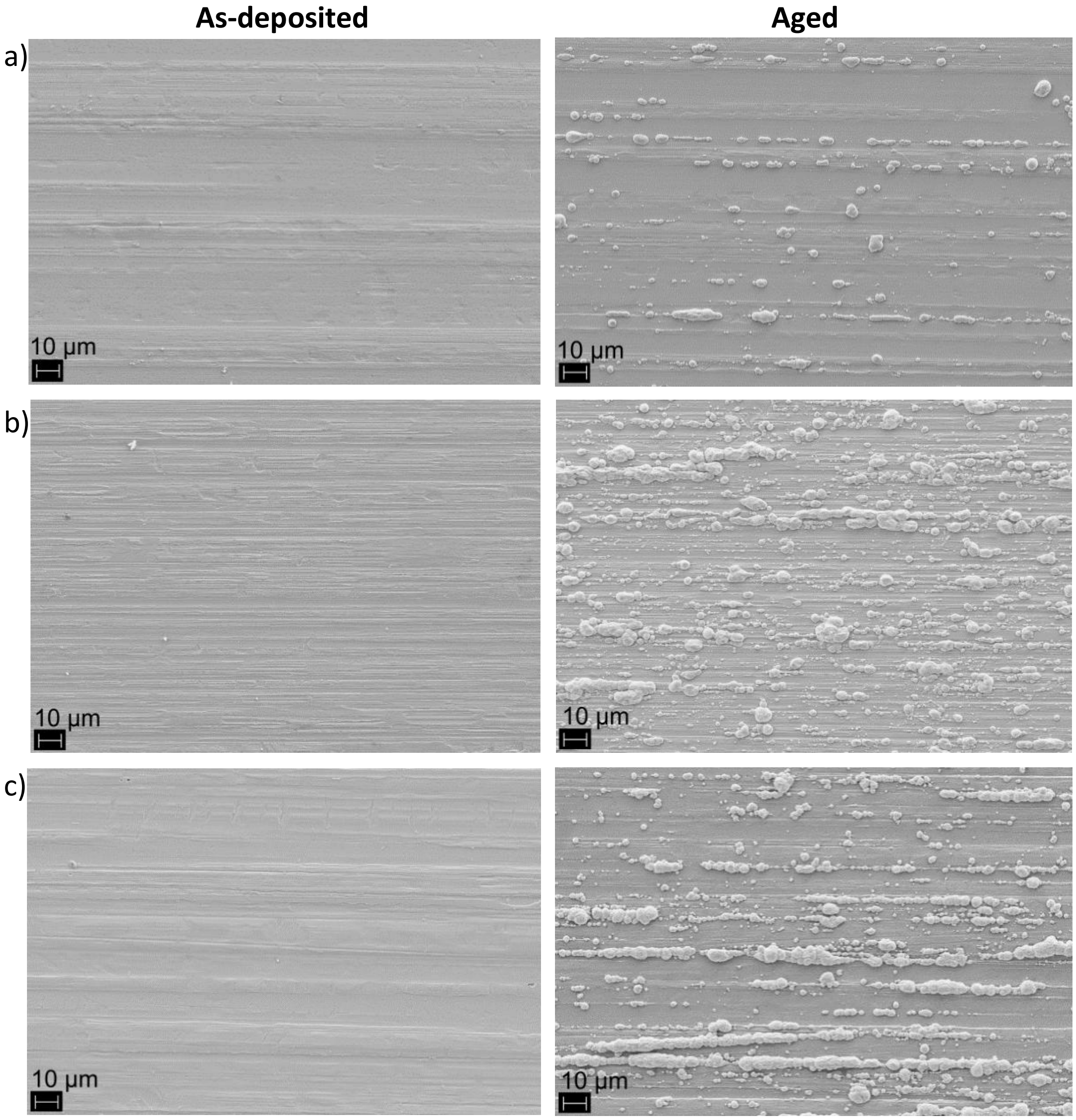

Figure 58. FESEM images of CrO_xN_y/SnO_x on Cu a) absorber 1, b) absorber 3, and TiO_xN_y/SiO_x on Cu c) absorber 5 from samples as-deposited and aged at 278 °C for 600 hours. The rolling direction of the substrates is horizontal in these pictures.

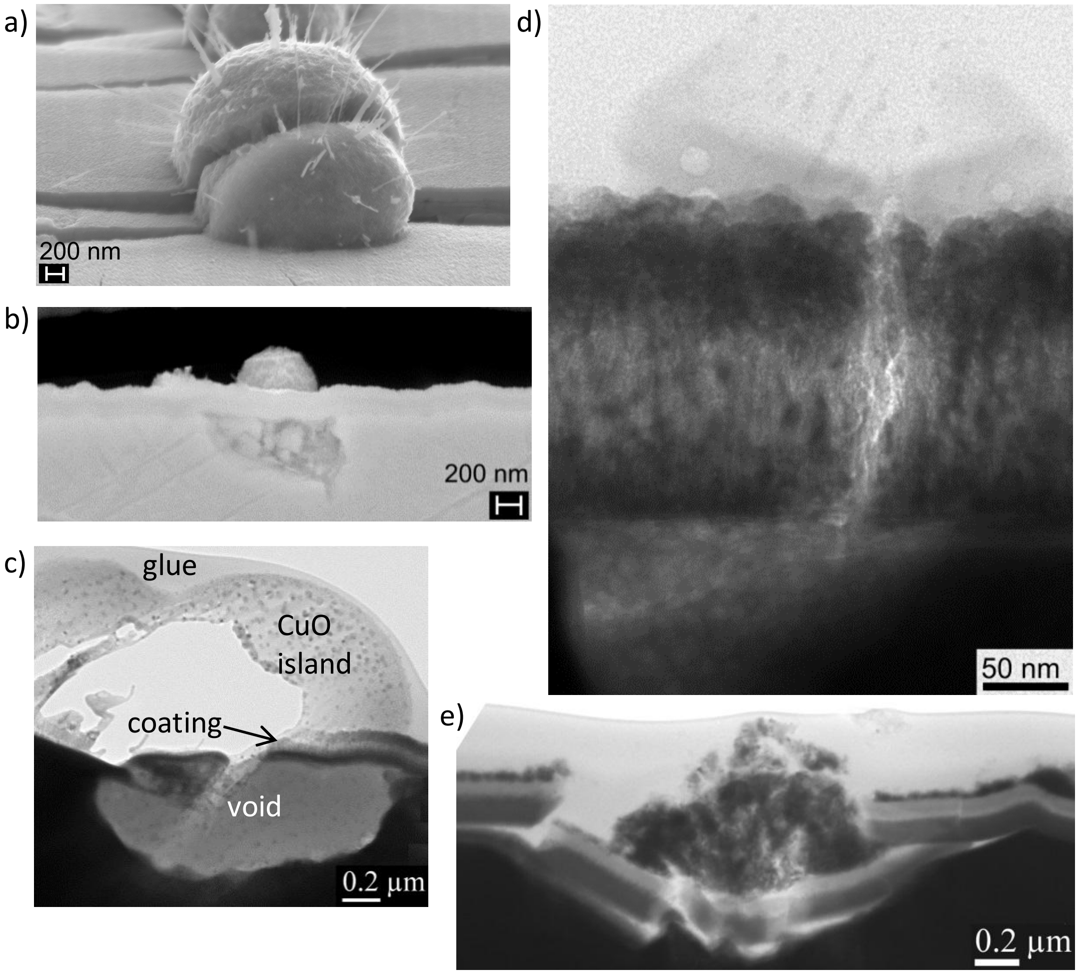

Figure 59. CuO islands on the absorber coating and voids under the coating after ageing at 278 °C for 600 h: a) FESEM image of bent absorber 1, b) FESEM image of cross-sectional, polished absorber 3, c) TEM image of absorber 1, d) TEM image of absorber 3, and e) TEM image of absorber 5.

Void formation was observed at the spot from where copper had diffused (see Figure 59). The substrate under the absorber coating was porous because copper atoms had diffused outwards. TEM-EDS analysis revealed mainly copper (~75 At.%), nitrogen (~20 At.%) and oxygen (< 5 At.%) in the void. Only minor ratios of chromium (< 1 At.%) were observed in the voids.

In the as-deposited interface of substrate and absorber coating, no metal oxide layer was observed or it was too thin to notice (< 2 nm). After ageing at 278 °C for 600 h, an oxide layer was observed on the aluminium substrates, as in [242]. The thickness of the aluminium oxide layer was approximately 5-10 nm. On the Cu substrates, no similar copper oxide layer was observed. Figure 60 presents the Cu and Al substrate interfaces with the absorber coatings before and after ageing.

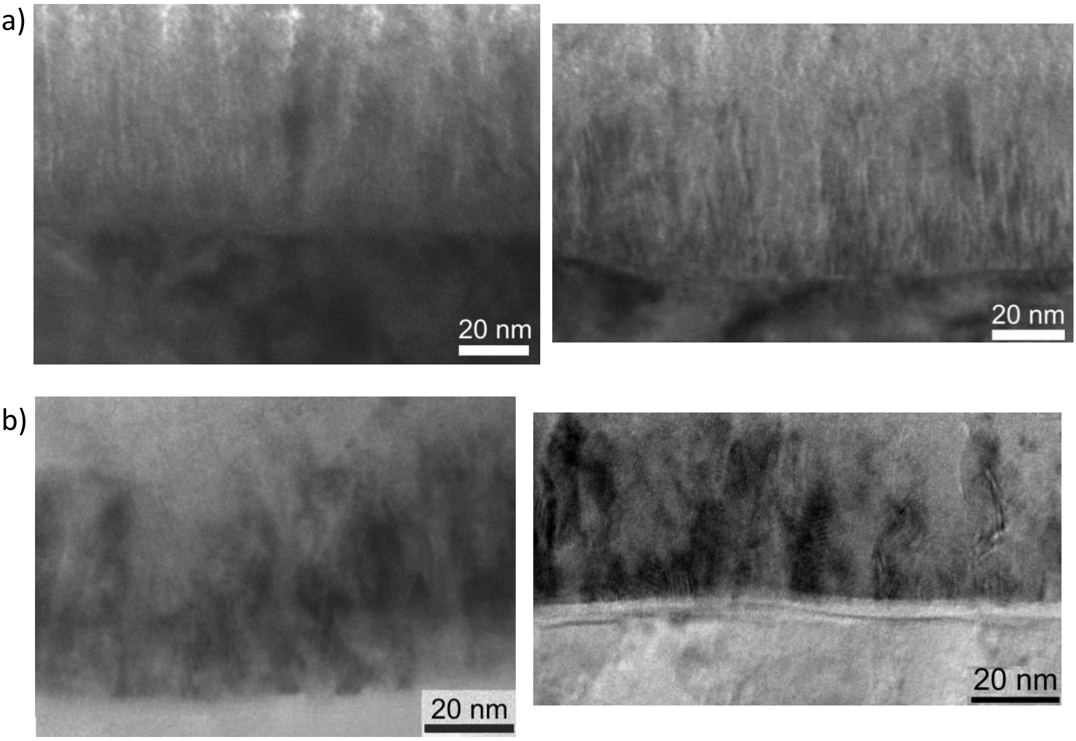

Figure 60. TEM images of interface of substrate and absorber coating before and after ageing at 278 °C for 600 h for a) absorber 1 on Cu substrate and b) absorber 6 on Al substrate.

6.2.4 Simulated changes in optical properties during thermal ageing

Simulations of optical properties were performed using CODE Coating Designer to reveal the connections between changes in optical properties and ageing mechanisms. The simulations modelled the behaviour in oxidation of the absorber coating or the IR reflector, CuO formation on the absorber coating, void formation in the substrate, and structural changes in the TiO_xN_y coating.

The simulated reflectance spectra for the oxidation of two different solar absorber coatings are presented in Figure 61. The simulated reference absorbers were a Cr_2O_3/Cr/Cr_2O_3 stack with layer thicknesses of 42.6 nm/12.3 nm/44.6 nm, respectively, and Cr particles in a Cr_2O_3 matrix with a graded structure. The optical properties and layer thicknesses of 3-layer Cr_2O_3/Cr/Cr_2O_3 were optimized with CODE Coating Designer. For the Cr_2O_3/Cr/Cr_2O_3 absorber, the simulated solar absorptance was 0.936 and thermal emittance 0.008. The oxidation of the Cr_2O_3/Cr/Cr_2O_3 stack was simulated by keeping the total thickness of the absorber coating constant but reducing the thickness of metallic Cr and increasing the thicknesses of the oxide layers. Two different oxidation ratios were used in the simulation for Cr_2O_3/Cr/Cr_2O_3: for a lower oxidation ratio, the layer thicknesses were 44.6 nm/8.3 nm/46.6 nm (oxidized 1) and for a more oxidized absorber 45.6 nm/6.3 nm/47.6 nm (oxidized 2). For the oxidized absorbers of Cr_2O_3/Cr/Cr_2O_3, the simulated solar absorptance values were 0.918 and 0.888, respectively, and thermal emittance was 0.007 for both. In the case of Cr particles in a Cr_2O_3 matrix, the total thickness of the absorber was 200 nm. The absorber had a graded structure from more metallic to dielectric towards the surface with different volume fractions of Cr particles. The initial structure was 30 % Cr for 100 nm/20 % Cr for 50 nm/10 % Cr for 50 nm in Cr_2O_3, the simulated solar absorptance was 0.836 and thermal emittance 0.016. The oxidation of Cr particles in a Cr_2O_3 matrix was simulated by decreasing the Cr content. For lower oxidation, the simulated absorber was 20 % Cr for 100 nm/10 % Cr for 100 nm (oxidized 3) and for a more oxidized absorber, 10 % Cr for 200 nm (oxidized 4). For the oxidized absorbers of Cr in a Cr_2O_3 matrix, the simulated solar absorptance values were decreased to 0.807 and 0.768, and thermal emittance to 0.012 and 0.011, respectively. In both simulation cases, the increased oxygen content shifted the spectrum towards lower wavelengths, made the interference fringes more pronounced and reduced solar absorptance but the thermal emittance remained almost unchanged.

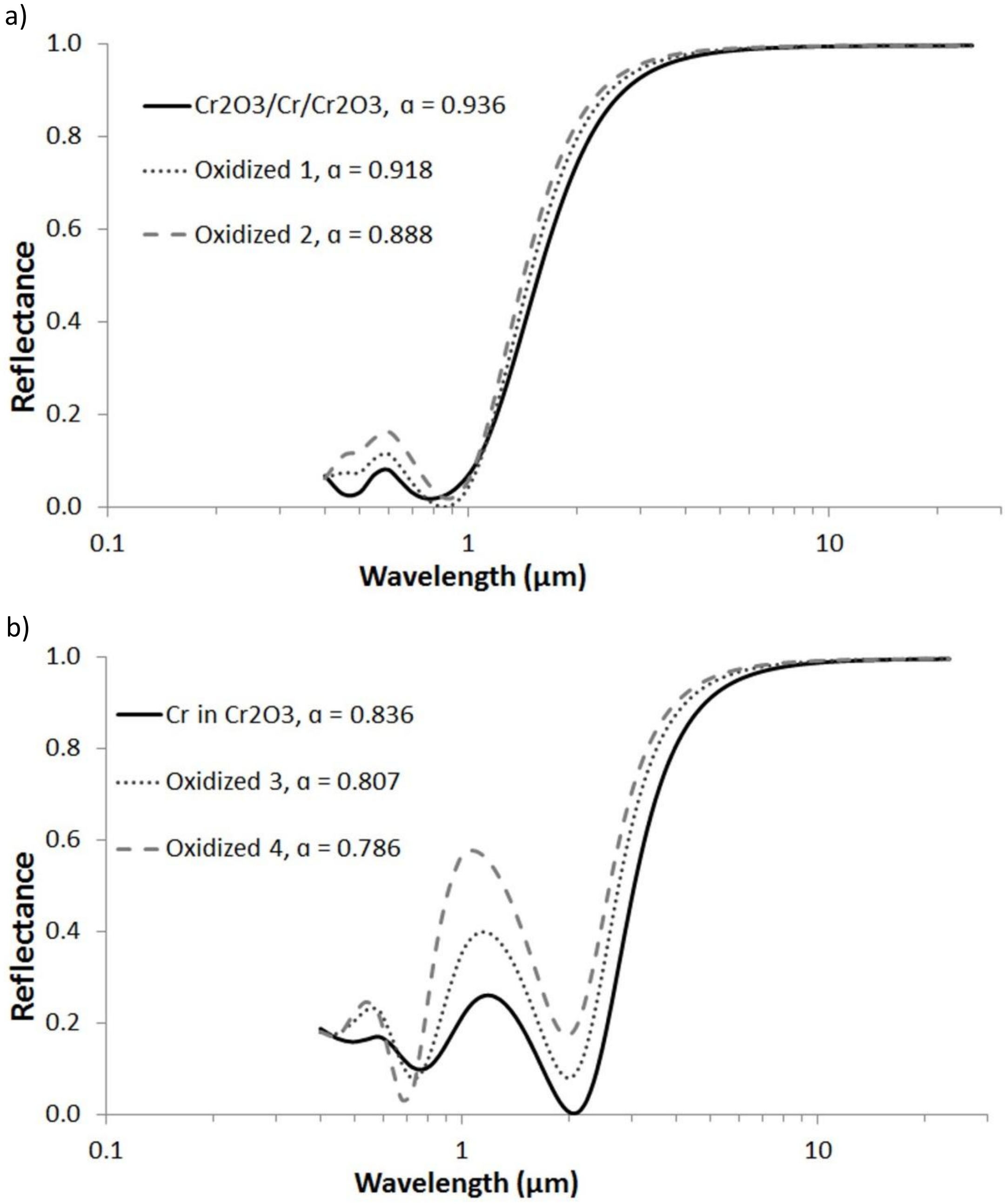

Figure 61. Simulated reflectance spectra for oxidation of solar absorber coatings: a) an optimized 3-layer stack of Cr_2O_3/Cr/Cr_2O_3, and b) the Bruggeman model of Cr particles in a Cr_2O_3 matrix with a gradient structure.

The coverage area of CuO islands in Figure 58 was 7 %, 20 %, and 15 % for absorbers 1, 3, and 5, respectively. The CuO islands were assumed to be hemispheres (see Figure 59). The diameters of the CuO islands were measured perpendicular to the rolling direction from Figure 58 for 50-70 islands larger than 1 µm. CuO islands of less than 1 µm in diameter were assumed to be insignificant. The average diameter of the CuO islands was 3 µm for aged absorbers 1, 3, and 5. The largest CuO islands were 6-8 µm in diameter (perpendicular to the rolling direction) but most likely they had been flattened from a hemispherical shape due to the coalescence of the islands. In cross-sectional analysis, the largest CuO islands were 2-3 µm in height. Thus, a diameter of 3 µm for a hemispherical island was used to estimate the thickness of the CuO layer on the surface if the islands were spread out uniformly as a layer on the surface of the absorber. The thicknesses of CuO layers would thus be 10 nm, 27 nm, and 20 nm for absorber 1, 3, and 5, respectively.

The simulated reflectance spectra for the formation of a uniform CuO layer on the surface of the absorber coating are presented in Figure 62. In the simulations, the reference absorber $Cr_2O_3/Cr/Cr_2O_3$ on Cu substrate was used, with and without a CuO layer on top. According to the estimation of the thickness of uniform CuO layers for absorbers 1, 5, and 3, thicknesses of 10 nm, 20 nm, and 30 nm were used in the simulations. Without the CuO layer, the simulated solar absorptance value was 0.936 and thermal emittance 0.008. With the CuO layer on top, the simulated solar absorptance values were 0.888, 0.808, and 0.738, respectively from 10 nm to 30 nm, and thermal emittance remained at 0.008. Thus, the uniform CuO layer on top of the absorber coating did decrease solar absorptance but the thermal emittance remained unchanged.

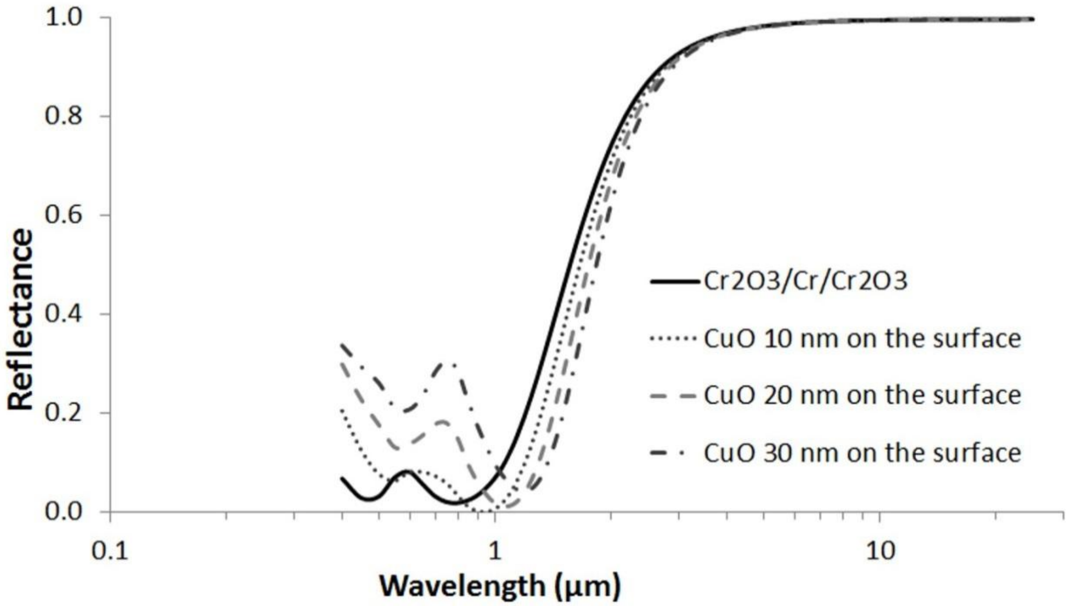

Figure 62. Simulated reflectance spectra for the formation of a uniform CuO layer on the surface of an optimized absorber coating. Simulations were performed using an optimized Cu substrate/Cr_2O_3/Cr/Cr_2O_3 absorber with and without a CuO layer on top.

Voids in the Cu substrate were simulated by using an air/Cu mixture layer or a damaged Cu layer between the Cu substrate and optimized 3-layer stack of Cr_2O_3/Cr/Cr_2O_3, as presented in Figure 63. The Bruggeman model was used in the air/Cu mixture, having 50 % air in the Cu matrix with a thickness of 200 nm or a gradient structure with four layers: 80 %, 50 %, 30 %, and 10 % air in Cu, with a thickness for each layer of 100 nm. The voids in the Cu substrate simulated by the air/Cu mixtures with the Bruggeman model reduced the reflectivity in the long-wavelength range but the thicker mixture also exhibited pronounced interference fringes in the short-wavelength range. Another way to simulate voids in the Cu substrate was to damage the surface layer of Cu by damping electrons in Cu from 170 cm^{-1} to 2750 cm^{-1} (correspond to mobilities of 48 and 3.4 cm^2/Vs, respectively) and converting the Cu into oxidized Cu by reducing the density of the electrons from $590*10^{20}$ cm^{-3} to $90*10^{20}$ cm^{-3} when the plasma frequency decreases from 72800 cm^{-1} to 27800 cm^{-1}. The simulations with damaged Cu reduced reflectivity significantly in the long-wavelength range and had only a slight effect on reflectance in the short-wavelength range.

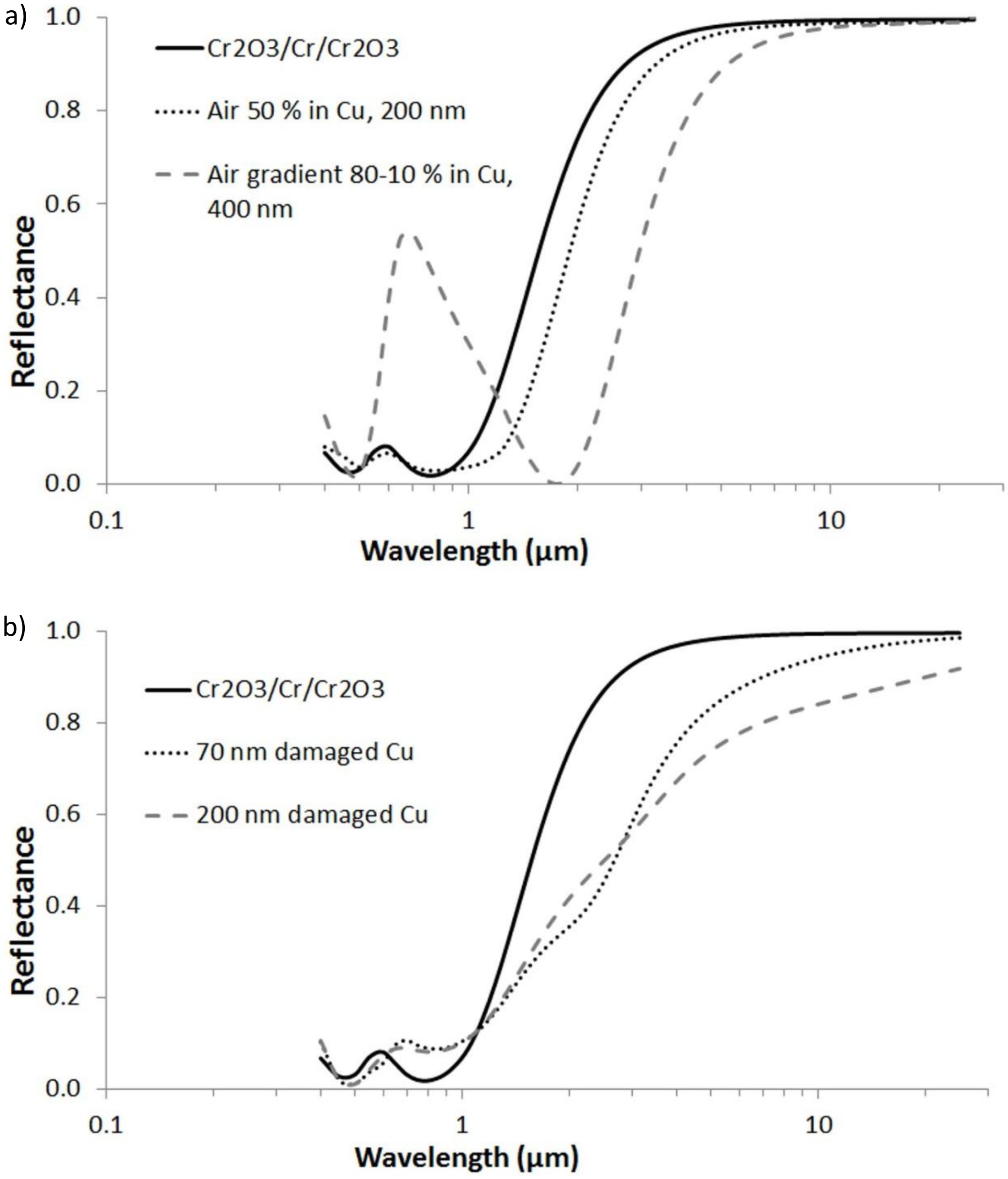

Figure 63. Simulated reflectance spectra for the formation of voids in the surface layer of Cu substrate under the optimized Cr_2O_3/Cr/Cr_2O_3 absorber coating. Simulations were performed using Cu substrate/voids in a Cu/Cr_2O_3/Cr/Cr_2O_3 stack. Voids in the Cu were simulated by using a) air/Cu mixtures with the Bruggeman model, and b) a damaged Cu layer having damped and reduced the density of electrons.

The simulated reflectance spectra for oxidation and the structural changes in the TiO_xN_y absorber are presented in Figure 64. The oxidation and structural changes in TiO_xN_y were simulated by the Bruggeman model with amorphous TiO_2 in a TiN matrix, a two-layer structure with TiN and amorphous TiO_2 layers, and with a totally oxidized TiO_2 layer. The oxidation of TiN in TiO_xN_y was simulated by increasing the amount of TiO_2 in the TiN matrix from 85 % to 95 %. As a consequence, the interference fringes became more pronounced. The two-layer structure with TiN and TiO_2 layers decreased solar absorptance significantly. An increase in the thickness of the oxide layer shifted the interference fringes.

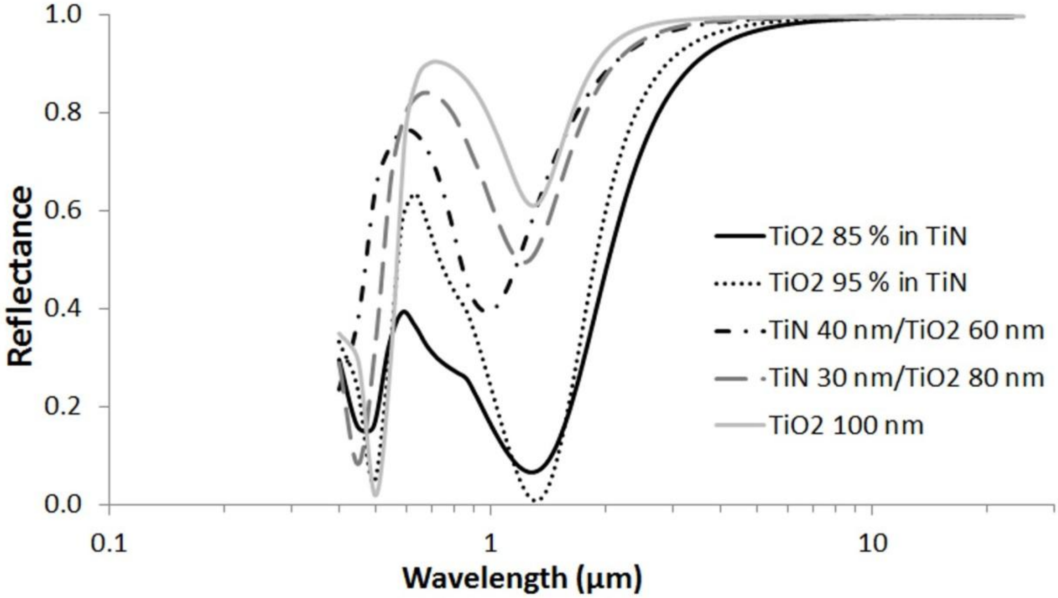

Figure 64. Simulated reflectance spectra for oxidation and possible structural changes of TiO_xN_y absorber on Cu substrate. Simulations were performed using the Bruggeman model of TiO_2 in a TiN matrix with a thickness of 100 nm, a two-layer structure of TiN/TiO_2, and a TiO_2 layer on Cu substrate.

Figure 65 presents the reflectance spectra simulations of an oxidized aluminium IR reflector on anodized aluminium substrate. The initial structure was Al substrate/140 nm Al_2O_3/35 nm Al/40 nm Cr 50 % in Cr_2O_3/40 nm Cr 25 % in Cr_2O_3/40 nm Cr_2O_3/60 nm SiO_2. The Al_2O_3 layer simulated the anodized aluminium oxide layer, Al layer was the IR reflector, graded Cr-Cr_2O_3 acted as the absorption coating and was prepared by the Bruggeman model, and SiO_2 was the anti-reflection layer. The removal of the Al layer (i.e. absorber coating directly on aluminium oxide) decreased the long-wavelength reflectivity and made the interference fringes more pronounced in the solar range. The oxidising of the Al layer was simulated by removing the Al layer and increasing the thickness of the Al_2O_3 layer to 175 nm. The oxidation of the Al layer caused a decrease in long-wavelength reflectivity and made the interference fringes more pronounced.

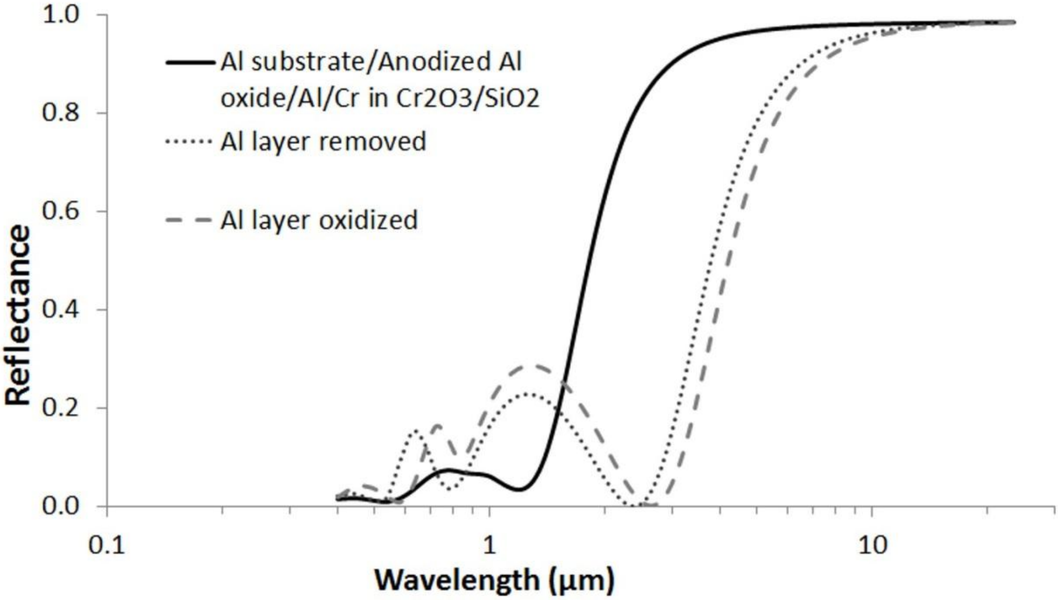

Figure 65. Simulated reflectance spectra for the oxidation of the Al reflector layer on anodized aluminium oxide. The absorber coating was simulated with the Bruggeman model using a graded structure of Cr in Cr_2O_3 and a SiO_2 anti-reflection layer.

6.3 Solar absorbers after short-period heat treatments at temperatures up to 500 °C

Short-period heat treatments were performed in a circulating air furnace at 200 °C, 300 °C, 400 °C, and 500 °C for two hours. 400 °C and 500 °C are beyond the scope for DHW and space heating applications, but they were used to generate information about ageing mechanisms in extreme temperatures and to provide further information for the development of high-temperature absorber coatings.

Changes in the industrial solar absorbers studied at 300 °C, 400 °C, and 500 °C for two hours corresponded well to the results of accelerated ageing. The absorbers which passed the accelerated ageing test (absorbers 2, 6, and 9-11 qualified after the first test temperature, and absorbers 1, 7, and 8 after the second test), remained quite unchanged even at 500 °C for 2 h. Correspondingly, the absorbers which did not pass the accelerated ageing test (absorbers 3-5) suffered from a severe decrease in optical selectivity, formation of CuO islands, and peeling of the coating from the substrate. The formation of CuO islands was observed after a two-hour exposure at ≥ 300 °C for industrial absorbers 1, 3, and 5, and for the experimental $CrO_x/Cr/CrO_x$ absorber. Even though the industrial copper-substrate absorbers showed island formation after 2 h at 300 °C, the experimental $TiAlSiO_xN_y/SiO_2$ on Cu did not show CuO island formation at 300 °C for 2 h, and after 400 °C for 2 h the CuO island formation was minor. Figure 66 presents the FESEM images of the experimental $TiAlSiO_xN_y/SiO_2$ and the most stable industrial absorber on Cu, CrO_xN_y/SnO_x (absorber 1) after a short-period heat treatment at 300 °C and 400 °C. For Ni-coated Cu (absorber 7), no formation of CuO islands was observed even at 500 °C for 2 h.

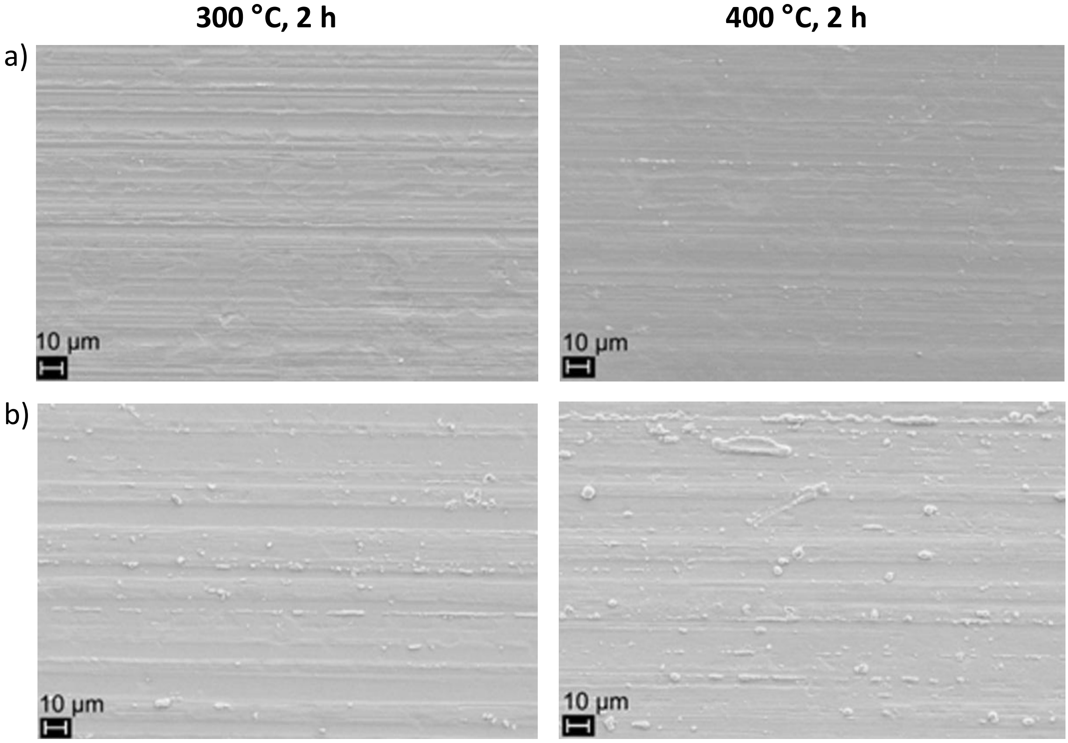

Figure 66. FESEM images of 300 °C and 400 °C for two-hour heat-treated absorbers on copper substrates a) experimental $TiAlSiO_xN_y/SiO_x$, and b) CrO_xN_y/SnO_x (industrial absorber 1). The rolling direction of the substrates is horizontal in these pictures.

The short-period PC values of the industrial absorbers at 300 °C, 400 °C, and 500 °C, and of the experimental sputtered $CrO_x/Cr/CrO_x$ absorber on Cu at 200 °C, 300 °C, 400 °C, and 500 °C are presented in Figure 67. The experimental $CrO_x/Cr/CrO_x$ absorber aged at the same rate as industrial TiO_xN_y on Cu up to 300 °C but degraded at 400 °C. It must be pointed out that the experimental absorber did not have any AR layer on the absorber coating. An AR coating would probably enhance the stability of the experimental absorber by preventing oxidation and diffusion.

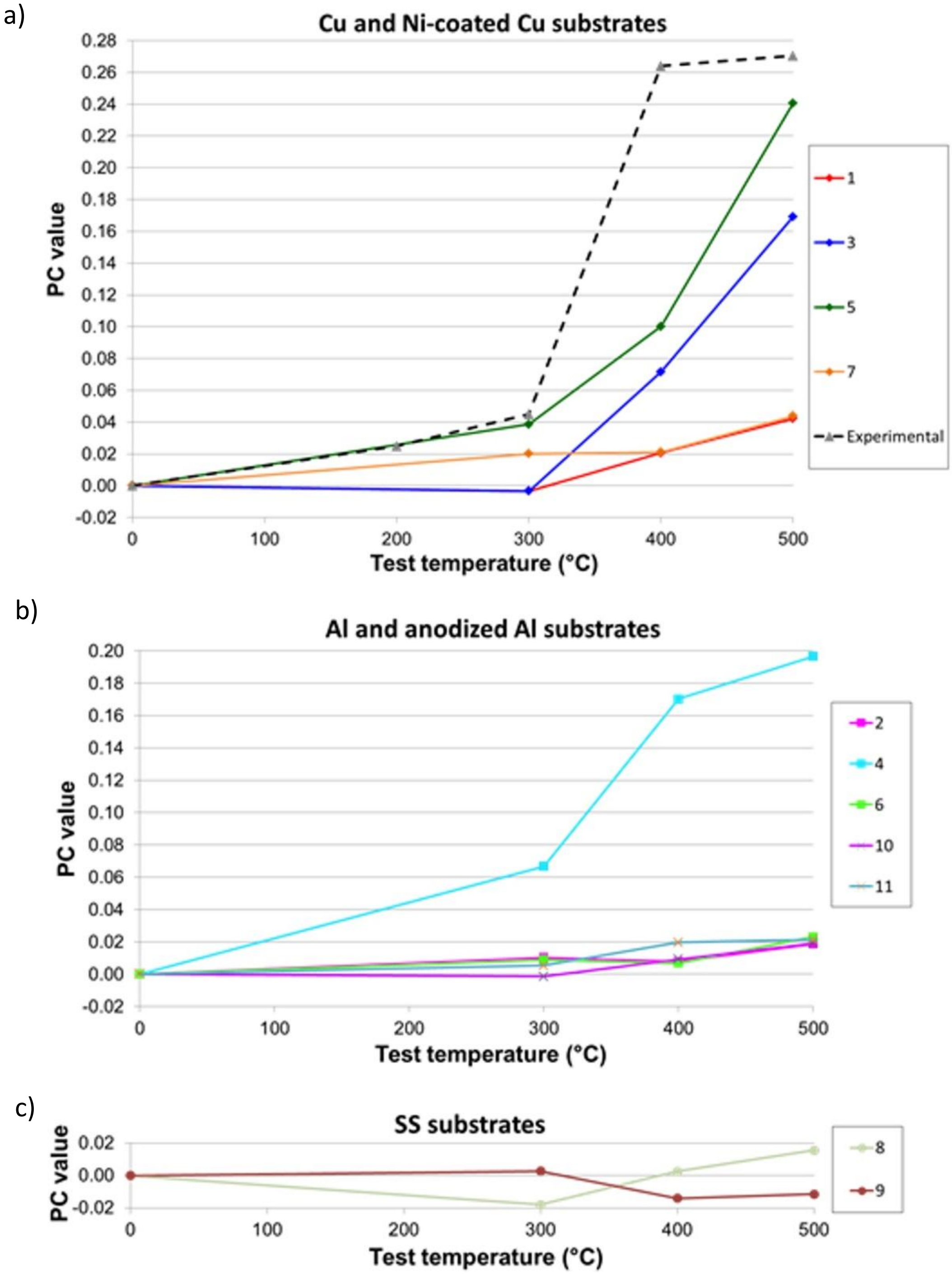

Figure 67. Calculated PC values after a 2 h exposure at 300 °C, 400 °C, and 500 °C for absorbers on a) Cu and Ni-coated Cu, b) Al and anodized Al, and c) stainless steel substrates.

Figure 68 shows the FESEM images of peeled coatings after two hours at 500 °C. In sputtered CrO_x on anodized Al (absorber 4), the SiO_x AR layer has been delaminated from the absorber coating, and in the evaporated TiO_xN_y on Cu (absorber 5), the absorber coatings have lost adhesion and have peeled off the substrate. The samples have been bent for FESEM sample preparation but such peeling was not observed in as-deposited or in other thermal treatments of the absorbers.

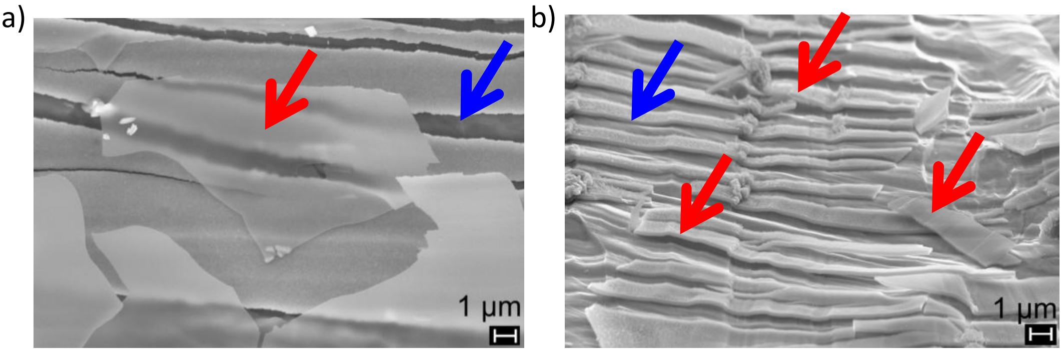

Figure 68. FESEM images after two hours at 500 °C a) sputtered CrO_x on anodized Al (absorber 4), and b) evaporated TiO_xN_y on Cu (absorber 5). The horizontal cracking of the coatings is due to sample preparation (blue arrows) but the coating layers have peeled off (red arrows).

6.4 Experimental diffusion barriers to prevent thermal ageing

Sputtered tantalum nitride and aluminium were studied as a diffusion barrier coating between copper substrate and a $CrO_x/Cr/CrO_x$ and/or $TiAlSiO_xN_y/SiO_x$ absorber coating. The cross-sectional FESEM images of the TaN_x and Al layers are presented in Figure 69. The experimental TaN_x coating had a columnar structure but seemed to be quite dense and fine-grained. Some defects were observed from the surface of the TaN_x coating. The experimental Al coating had a columnar structure with a higher surface roughness than the TaN_x coating.

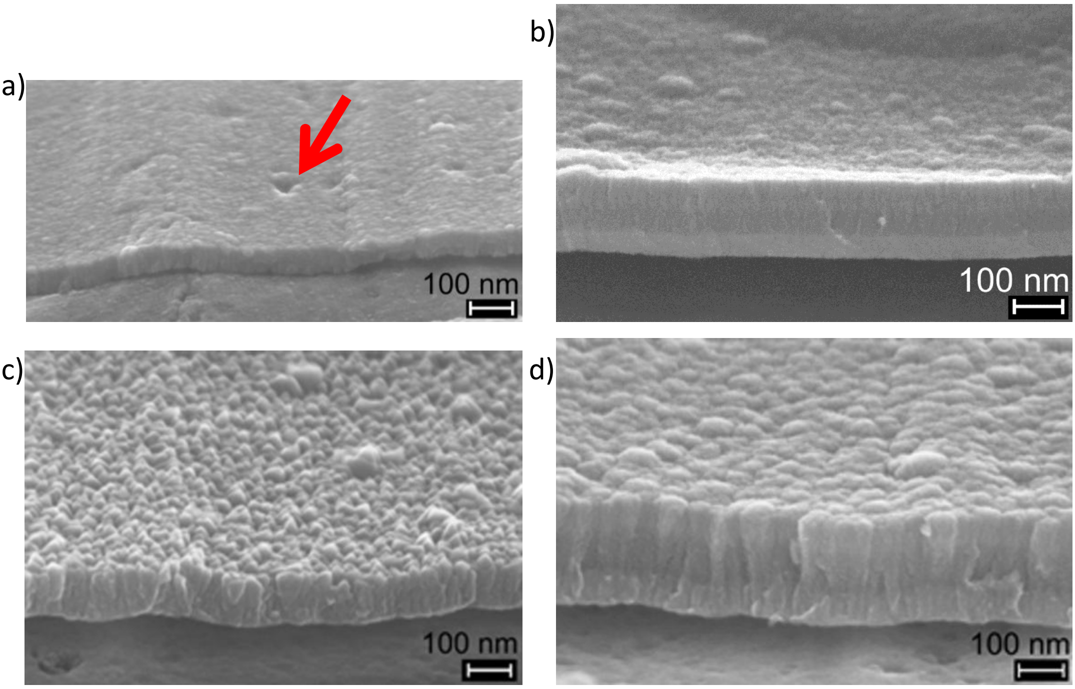

Figure 69. FESEM images of experimental diffusion barriers a) 60-nm-thick TaN_x layer on Cu, b) 40-nm-thick TaN_x layer between Cu and $CrO_x/Cr/CrO_x$ absorber coating, c) 100-nm-thick Al layer on Cu, and d) 100-nm-thick Al layer between Cu and $CrO_x/Cr/CrO_x$ absorber coating. The red arrow points out one of the observed defects in the TaN_x coating.

Solar absorptance and thermal emittance values are presented in Table 19 for as-deposited and for short-period thermal treated experimental absorbers with and without the TaN_x and Al diffusion barriers. Without any diffusion barrier, the optical properties for as-deposited $CrO_x/Cr/CrO_x$ on Cu was α = 0.80 and ε = 0.05, and for $TiAlSiO_xN_y/SiO_x$ on Cu α = 0.95 and ε = 0.05. The TaN_x and Al layers on Cu substrate reduced the optical selectivity of the as-deposited absorber structure. Thermal emittance increased with the thickness of the TaN_x layer. Without any absorber coating, the 20-nm-thick TaN_x layer on Cu had a thermal emittance of 0.05 and the 60-nm-thick TaN_x layer a thermal emittance of 0.17. A 60-nm-thick TaN_x layer between the Cu and $TiAlSiO_xN_y/SiO_x$ increased the thermal emittance from 0.05 to 0.20. Both the 100-nm- and 500-nm-thick Al layers increased the thermal emittance from 0.05 to about 0.10. According to CODE Coating Designer [244], Al layers increase the thermal emittance slightly between the Cu substrate and the experimental absorber used. The simulated emittance with a 100 nm Al layer was 0.02 and with a 500 nm Al layer 0.03.

Table 19. Solar absorptance and thermal emittance of the experimental absorbers on Cu with and without TaN_x or Al diffusion barrier for as-deposited and aged (2 h at 200 °C, 300 °C, 400 °C, and/or 500 °C) samples.

Diffusion barrier and absorber coating	**α, ε as-deposited**	**α, ε 200 °C**	**α, ε 300 °C**	**α, ε 400 °C**	**α, ε 500 °C**
without diffusion barrier $CrO_x/Cr/CrO_x$	0.80, 0.05	0.77, 0.04	0.78, 0.10	0.84, 0.52	0.90, 0.64
TaN_x (20 nm)/ $CrO_x/Cr/CrO_x$	0.77, 0.05	0.76, 0.07	0.72, 0.15		
TaN_x(40 nm)/ $CrO_x/Cr/CrO_x$	0.77, 0.06	0.77, 0.05	0.72, 0.13		
Al (100 nm)/ $CrO_x/Cr/CrO_x$	0.77, 0.11		0.74, 0.11	0.70, 0.14	0.61, 0.13
Al (500 nm)/ $CrO_x/Cr/CrO_x$	0.80, 0.10		0.80, 0.10	0.74, 0.09	0.78, 0.23
without diffusion barrier $TiAlSiO_xN_y/SiO_x$	0.95, 0.05		0.93, 0.04	0.92, 0.06	0.90, 0.10
TaN_x (20 nm)/ $TiAlSiO_xN_y/SiO_x$	0.94, 0.09		0.95, 0.09	0.93, 0.12	0.92, 0.75
TaN_x (40 nm)/ $TiAlSiO_xN_y/SiO_x$	0.94, 0.12		0.94, 0.13	0.93, 0.13	0.91, 0.21
TaN_x (60 nm)/ $TiAlSiO_xN_y/SiO_x$	0.94, 0.20		0.94, 0.18	0.91, 0.23	0.90, 0.28

Figure 70 presents reflectance spectra for experimental $CrO_x/Cr/CrO_x$ absorbers with and without TaN_x and Al diffusion barriers. The TaN_x layers shifted the interference fringes of as-deposited absorbers and made them more pronounced, which increased reflectance in the solar range. In heat treatments, reflectance in the long-wavelength range decreased (i.e. thermal emittance increased) at ≥ 300 °C for $CrO_x/Cr/CrO_x$ without the diffusion barriers in the solar range. First the interference fringes became pronounced and shifted at ≤ 300 °C and then flattened at 400-500 °C. A 20-nm-thick TaN_x layer decreased reflectance in the long-wavelength range even at 200 °C. A 40-nm-thick TaN_x layer showed a similar decrease of thermal reflectance at 300 °C. The as-deposited Al layers between the Cu substrate and $CrO_x/Cr/CrO_x$ absorber flattened reflectance curves in the long-wavelength range, which caused an increase of thermal emittance. The Al layers prevented a significant decrease of thermal reflectance up to 400-500 °C for 2 h. The experimental $CrO_x/Cr/CrO_x$ absorber with a 500-nm-thick Al layer showed optical degradation at 500 °C.

Figure 71 presents reflectance spectra for the experimental $TiAlSiO_xN_y/SiO_x$ absorber with and without TaN_x diffusion barrier layers. In the as-deposited $TaN_x/TiAlSiO_xN_y/SiO_x$ absorbers, the TaN_x layers flattened the slopes of the reflectance curves as a function of layer thickness, which decreased reflectance in the long-wavelength range (i.e. increased thermal emittance). In heat treatments, the reflectance of $TiAlSiO_xN_y/SiO_x$ remained quite unchanged with and without the TaN_x layer at 300 °C for 2 h. At 400 °C, a slight degradation of optical properties was observed for all $TiAlSiO_xN_y/SiO_x$ absorbers with and without the TaN_x layers. Thermal treatment at 500 °C for 2 h created higher degradation of optical properties but the degradation level was still moderate, except for 20 nm TaN_x. The 20-nm-thick TaN_x layer between the Cu substrate and $TiAlSiO_xN_y/SiO_x$ absorber degraded significantly and lost optical selectivity at 500 °C.

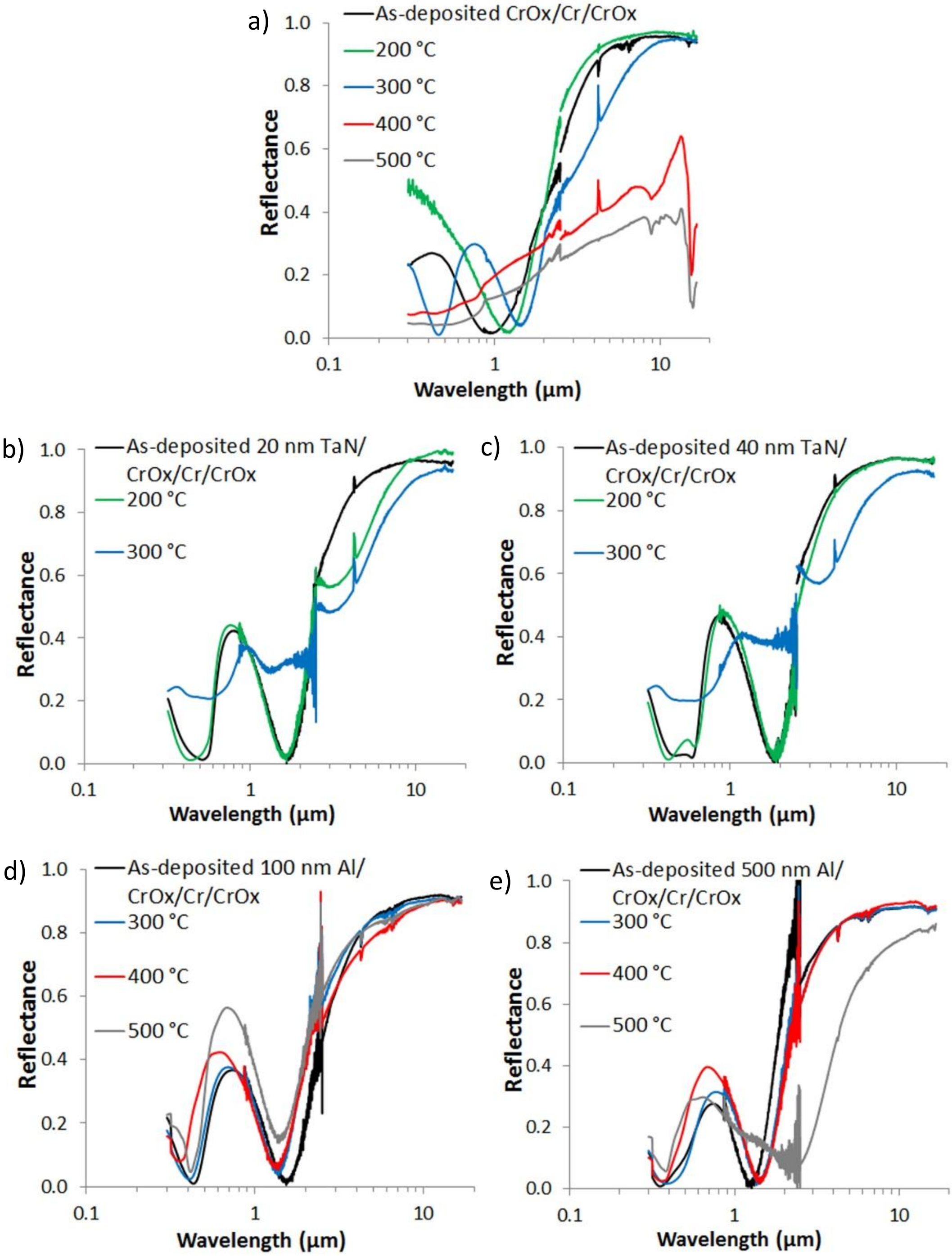

Figure 70. Reflectance curves for as-deposited and for two-hour heat-treated experimental CrO_x/Cr/CrO_x absorbers on Cu substrate: a) without a diffusion barrier layer at 200-500 °C, and with TaN_x diffusion barrier coating with a

thickness of b) 20 nm, c) 40 nm at 200-300 °C, and with an Al diffusion barrier coating with a thickness of d) 100 nm, and e) 500 nm at 300-500 °C.

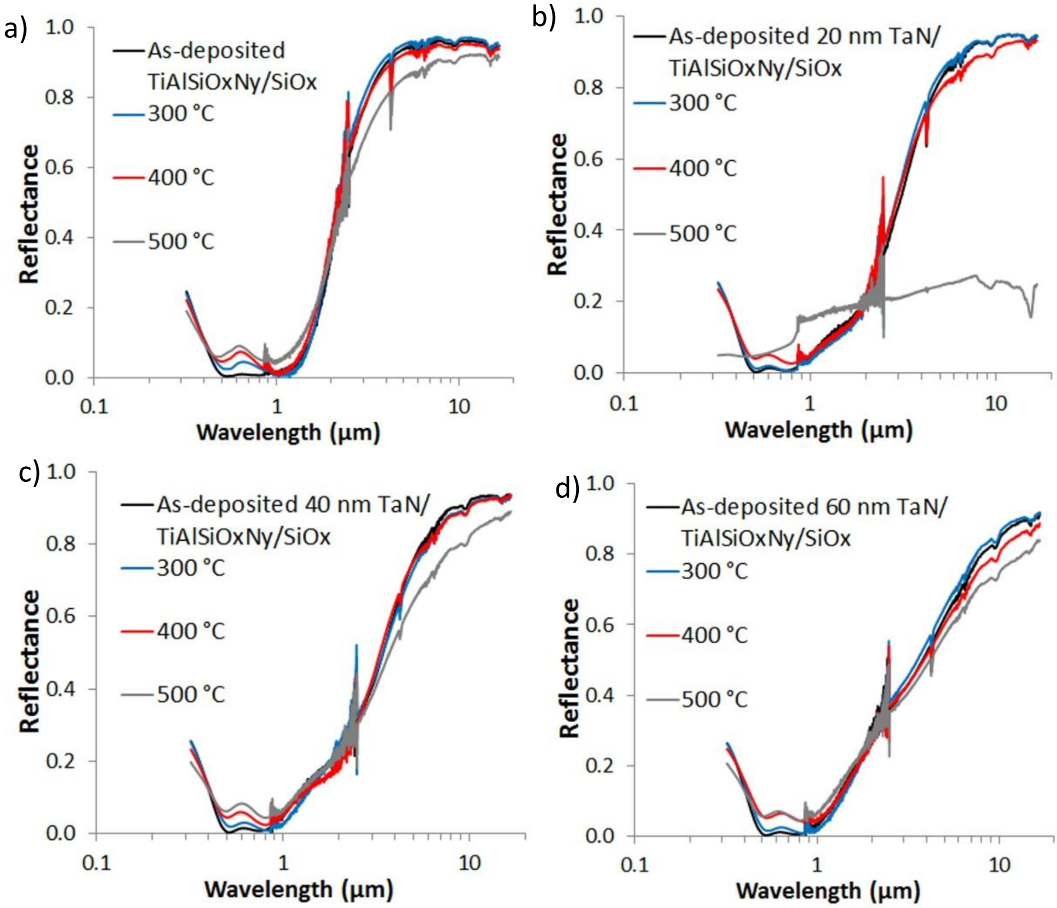

Figure 71. Reflectance curves for as-deposited and for two-hour heat-treated experimental $TiAlSiO_xN_y/SiO_x$ absorber at 300 °C, 400 °C, and 500 °C a) without a diffusion barrier layer, and with a TaN diffusion barrier coating with a thickness of b) 20 nm, c) 40 nm, and d) 60 nm on Cu substrate.

Activation energies were estimated separately for absorptance and emittance from the slopes of $\ln(\Delta\alpha)$ or $\ln(\Delta\varepsilon)$ versus 1/T. Plots for the experimental absorbers with and without the diffusion barrier coatings are presented in Figures 72 and 73. For the $CrO_x/Cr/CrO_x$ absorber, activation energy for a change in solar absorptance cannot be estimated with the existing ageing data. In addition, activation energy for a change in thermal emittance had uncertainties because of small changes within the error range, but the slopes presented in Figure 72 showed activation energy of 40 ± 10 kJ/mol for $CrO_x/Cr/CrO_x$ with and without 20 nm TaN_x. For $CrO_x/Cr/CrO_x$ with an Al layer, activation energy cannot be estimated because of uncertain results for the sample with a 100-nm-thick Al layer: Ɛ = 0.14 at 400 °C and Ɛ = 0.13 at 500 °C, which is within the error range of thermal emittance in the experimental $CrO_x/Cr/CrO_x$ absorber, and because the 500-nm-thick Al sample did not degrade in thermal emittance at 400 °C.

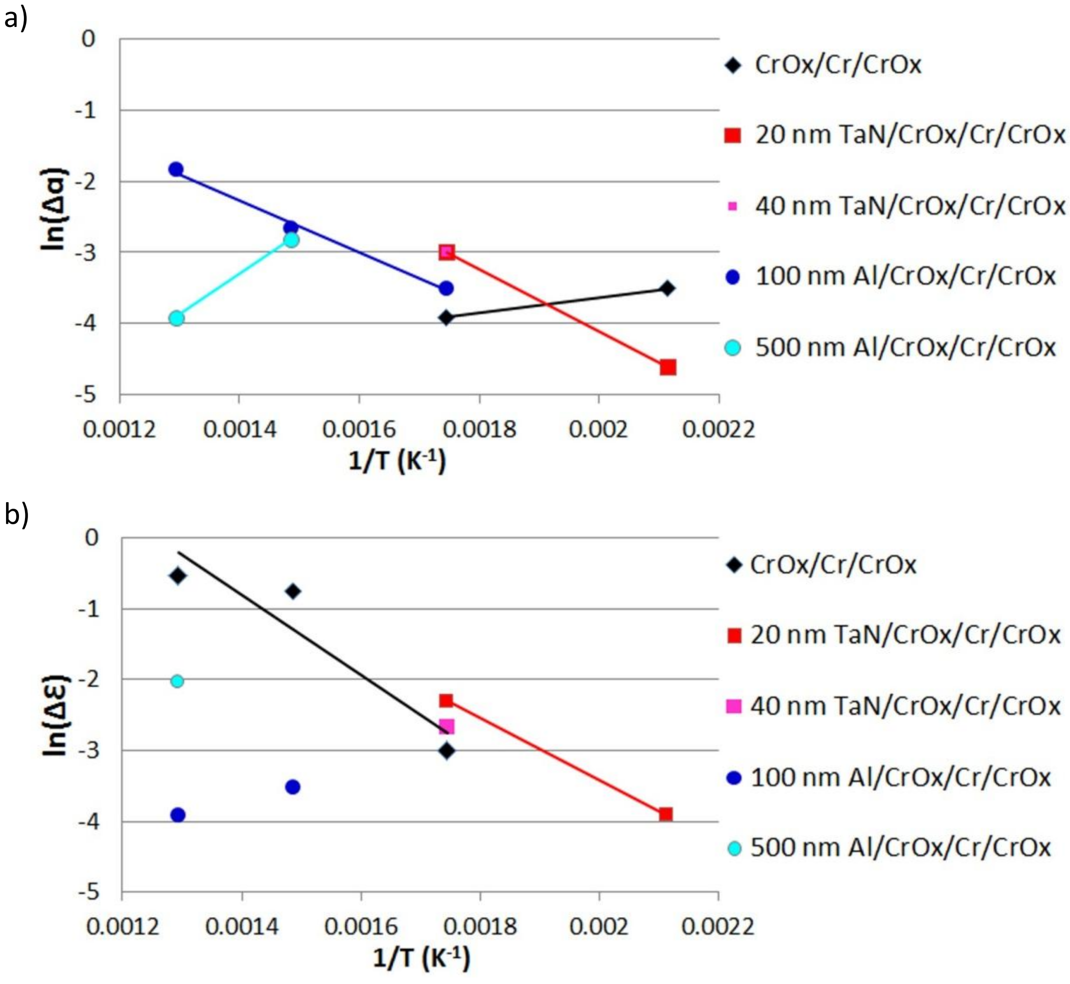

Figure 72. Plots a) ln(Δα) versus 1/T and b) ln(ΔƐ) versus 1/T in ageing at 200-500 °C for two hours for the experimental $CrO_x/Cr/CrO_x$ absorber with and without TaN_x and Al layers on Cu substrate.

For the TiAlSiO$_x$N$_y$/SiO$_x$ absorber, activation energy for a change in solar absorptance was 30 ± 15 kJ/mol with and without TaN$_x$ layers at 400-500 °C, see Figure 73. At < 400 °C, TiAlSiO$_x$N$_y$/SiO$_x$ with TaN$_x$ layers did not degrade in solar absorptance and also for the absorber without TaN$_x$ the degradation was slight. Activation energy for a change in thermal emittance was 80 ± 40 kJ/mol at 400-500 °C if all the slopes are estimated to have similar activation energy. Activation energy for a change in thermal emittance can also be divided into with and without a TaN$_x$ layer: for the TiAlSiO$_x$N$_y$/SiO$_x$ absorber 70 kJ/mol, and with a TaN$_x$ layer 90 ± 45 kJ/mol. At < 400 °C, TiAlSiO$_x$N$_y$/SiO$_x$ with TaN$_x$ layers did not degrade significantly in thermal emittance.

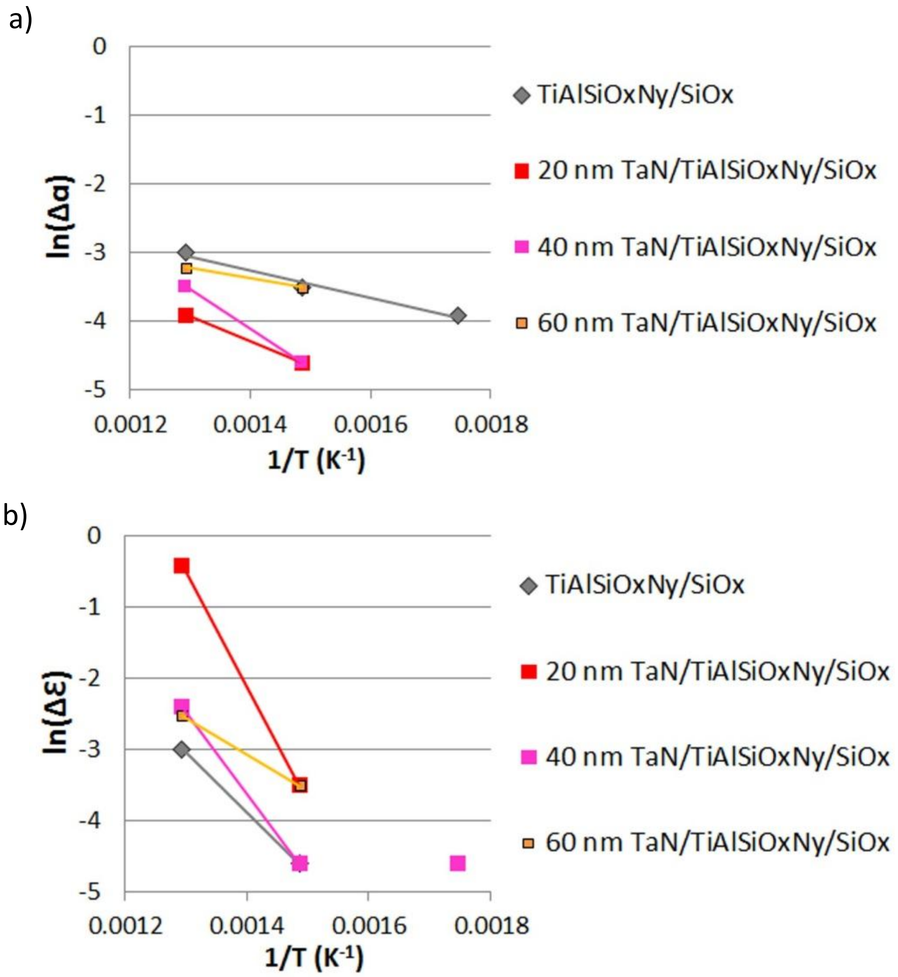

Figure 73. Plots a) ln(Δα) versus 1/T and b) ln(ΔƐ) versus 1/T in ageing at 300-500 °C for two hours for experimental TiAlSiO$_x$N$_y$/SiO$_x$ absorber with and without TaN$_x$ layer on Cu substrate.

Figure 74 illustrates the ageing rate of experimental absorbers with and without the TaN_x and Al diffusion barriers. The calculated PC values using equation (2) present the ageing rate. The sputtered TaN_x coating did not prevent or decelerate diffusion. The ageing properties were similar or even more aggressive with the TaN_x layer. CuO islands were observed on the coating surface after heat treatment at 300 °C for 2 h for the $CrO_x/Cr/CrO_x$ absorber with and without the TaN_x diffusion barrier. $TiAlSiO_xN_y/SiO_x$ on Cu without any diffusion barrier or with a TaN_x barrier layer of 20-60 nm prevented copper diffusion at 300 °C for 2 h. After 400 °C exposure for 2 h, minor CuO island formation was observed and the increase of thermal emittance values was very small, as presented in Table 19.

Aluminium acted as a diffusion barrier on copper according to the short-period ageing studies (Figure 74). Experimental coating without the Al layer degraded in lower temperatures faster than coatings with the Al barrier layer. The 100- and 500-nm-thick Al layers prevented Cu diffusion and retained optical selectivity for two hours at 300 °C, while without the Al layer, CuO island formation was observed. At higher temperatures (400 °C and 500 °C), the formation of CuO was observed but the Al diffusion barrier retarded the ageing mechanisms.

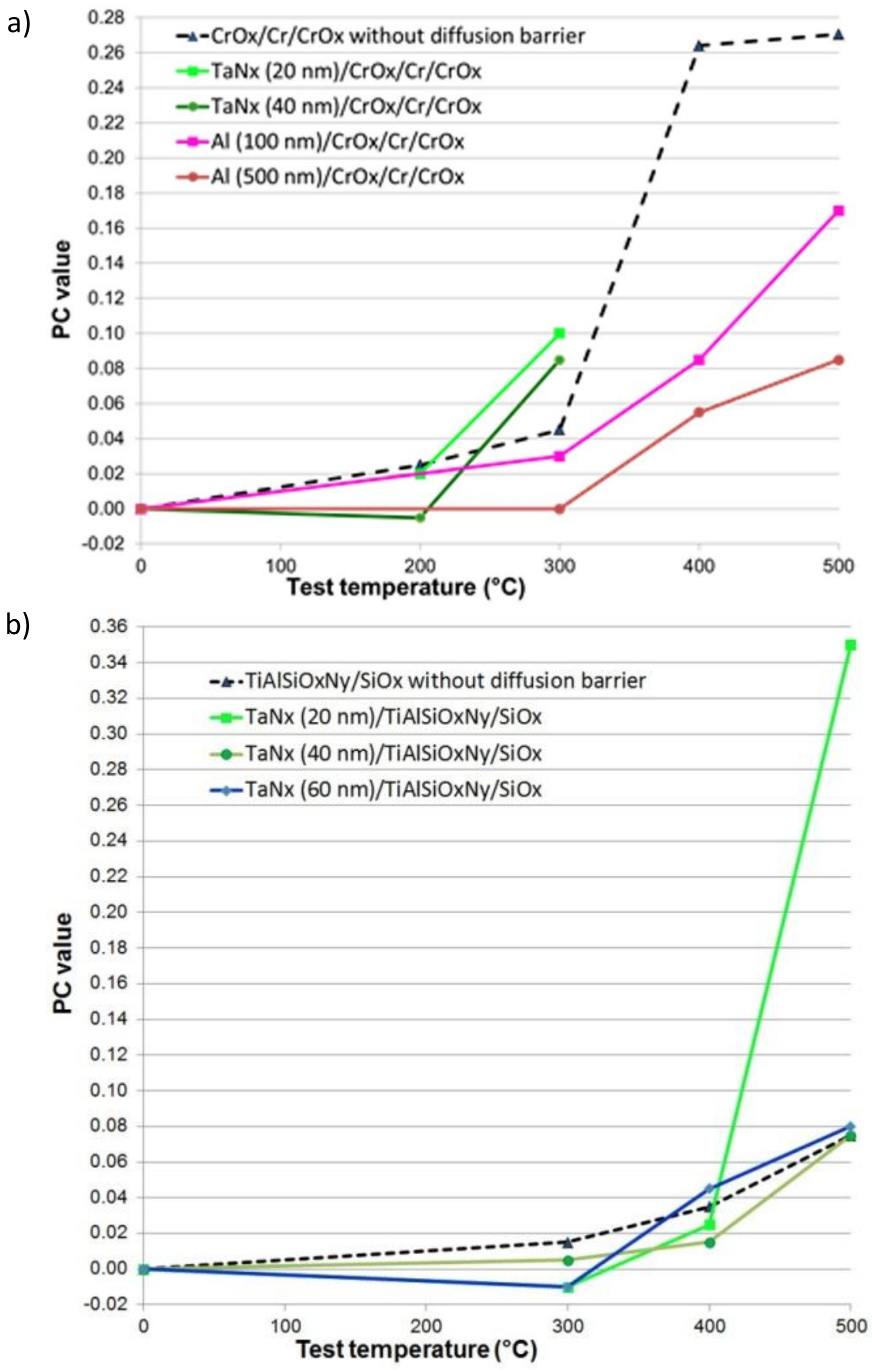

Figure 74. PC values of experimental coating structures in short-period heat treatments. TaN_x and Al were used as experimental diffusion barriers between Cu substrate and a) $CrO_x/Cr/CrO_x$, and b) $TiAlSiO_xN_y/SiO_x$ absorber coatings.

7 DISCUSSION

In this section, the ageing mechanisms at elevated temperatures (200-500 °C) are discussed. The microstructural aspects are compared to the compositional and optical ageing processes of the solar absorbers.

7.1 Ageing mechanisms at elevated temperatures (200-500 °C) in solar absorbers

Thermal exposure caused degradation processes in most of the absorber coatings. Thermal ageing mechanisms in air were 1) an increase in the oxygen/metal ratio in the absorber coatings, i.e. oxidation of the absorber coatings, 2a) the diffusion of copper substrate atoms into the coating layers or through the coating to the surface of the coating, and then 2b) the formation of CuO islands on the surface, and 2c) the formation of voids in the substrate 3) structural and chemical changes of anodized aluminium substrate with a thin Al reflector layer and TiO_xN_y absorber coating.

7.1.1 Oxidation of absorber coatings

During thermal exposure, an increase in the oxygen/metal ratio in the absorber coatings has been noticed for almost all of the industrial absorbers studied (see Table 17). In the literature, similar behaviour has been published: in a $CrO_x/Cr/CrO_x$ absorber, fine Cr crystallites oxidized [76], and in a black chromium absorber metallic Cr crystallites oxidized to chromium oxide [2, 22]. The oxidation mechanism of the absorber coating can be considered to cause a shift in the reflectance curve towards lower wavelengths during ageing due to a decrease in metal content inside the absorber coating. This behaviour is simulated in Figure 61 and suggested in [113, 270]. Another possible reason proposed in the literature is a modification of the refractive index of the matrix material in the cermet absorber as a result of structural change [113, 270] but structural changes other than oxidation of the absorption layer was not observed for Cr-based absorbers in this study (see Figure 54).

During ageing, the reflectance curves shifted more or less towards lower wavelengths in all of the absorbers studied (see Figures 37-42). The shifting of the reflectance spectra towards lower wavelengths correlated with the oxidation of Cr-based absorber coatings. The correlation between solar absorptance values

(Table 13) and oxidation of the absorber coatings (Table 17) is presented in Figure 75 after ageing at 278 °C for 600 h. A linear trend line is fitted to indicate the correlation between an increase in O/Cr ratio and solar absorptance. The O/Ti ratio was excluded from the trend line calculation because TiO_xN_y had structural and chemical changes as described in section 7.1.3. The increase in O/Cr ratio from TOR-ERDA measurements can be used to estimate the influence of chromium-based absorber coating oxidation on solar absorptance values.

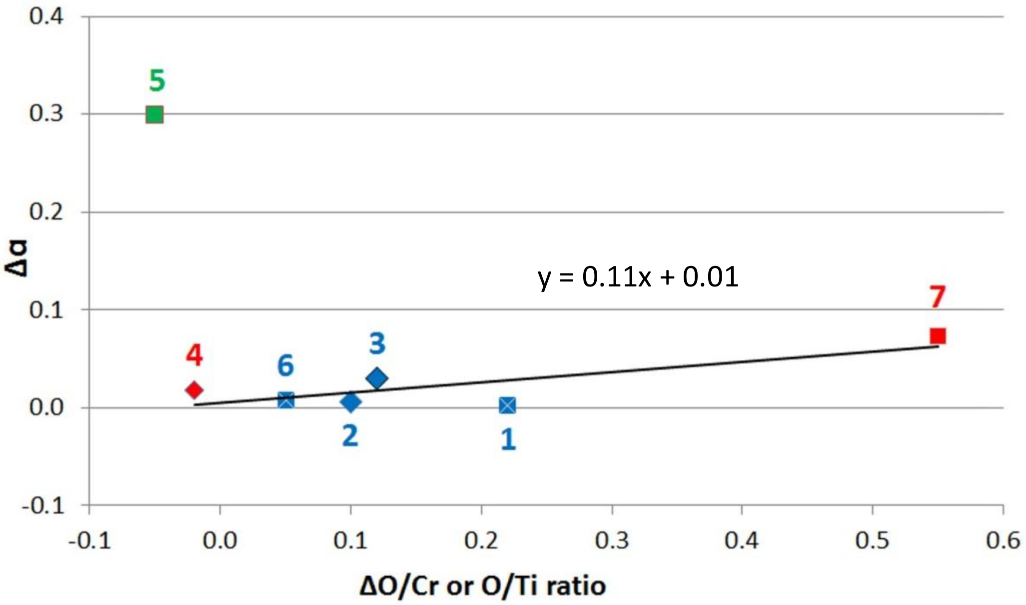

Figure 75. Correlation between change in solar absorptance and oxidation of the absorber coatings after ageing at 278 °C for 600 h. A linear trend line is fitted to Cr-based absorbers (excluding Ti-based absorber 5) to indicate the correlation between compositional changes and solar absorptance values. Blue markers are CrO_xN_y, red CrO_x, and green TiO_xN_y absorber coatings.

The activation energy for a change in solar absorptance can be considered to be equivalent to the activation energy of oxidation of an absorber coating. Thus, activation energy from the slope of ln(Δα) versus 1/T was examined and compared to oxidation values from the literature. Sputtered CrO_xN_y absorbers on Cu (absorbers 1 and 3) showed differences in microstructure (Figures 23-24) and durability (Table 15). According to the procedure in accelerated ageing studies, activation energy calculated from PC values could be defined only for absorber 3 because it degraded enough. It had an activation energy of 55 kJ/mol, and the Arrhenius time-transformations were well in line with each other (see Figure 44 a). Activation energies estimated from the slopes of ln(Δα) versus 1/T suggested

150 kJ/mol for 36 h at < 278 °C and 60 kJ/mol for longer durations or higher temperatures (see Figure 45 and Table 16). The difference (150 or 60 kJ/mol) in the activation energy was the consequence of a very small change at 250 °C after 36 h (at 250 °C α from 0.937 to 0.935 while at 278 °C α to 0.929) which may have been caused by errors in solar absorptance measurements (see error estimation of UV-Vis-NIR spectrometer in section 5.2.4). Absorber 1 did not degrade in solar absorptance in accelerated ageing studies but in short-period heat treatments at 400-500 °C it had an activation energy of 20 kJ/mol (see Figure 45 and Table 16). One of the CrO_xN_y absorbers on Cu passed (absorber 1) due to its denser coating structure but the other, with a more porous structure, failed (absorber 3). Similar kinds of CrO_xN_y absorbers on Al (absorbers 2 and 6) had activation energies for a change in solar absorptance of 150 kJ/mol and 260 kJ/mol respectively at 278-308 °C (the absorbers were not studied at a lower temperature) (see Figure 45 and Table 16). In the literature, Köhl *et al*. [18] studied the accelerated thermal ageing of a sputtered CrO_xN_y absorber on Cu at T_1 285 °C, and obtained an activation energy of 185 kJ/mol for the absorber. The absorber passed the test. [18] Activation energies for Cr oxidation to Cr_2O_3 have been reported to be 157 kJ/mol at 700-1100 °C [273], and 135 kJ/mol for oxidation of single crystalline Cr(110) films prepared by molecular beam epitaxy to epitaxial α-Cr_2O_3 in the temperature range from 127 °C to 427 °C [274]. Activation energy for oxidation in air of magnetron sputtered CrN was 51 kJ/mol at 500-800 °C [275], 98 kJ/mol at 350-800 °C [276], and 163 kJ/mol at 400-650 °C [277]. Non-stoichiometry in CrN_y has reported to lead to a reduced activation energy for oxidation compared to stoichiometric compounds [277]. The activation energies of oxidation in the literature showed a wide variation. In the case of gradient CrO_xN_y absorbers, according to these results it is not clear if Cr or CrN oxidized during the ageing. It is probable that the ageing process includes oxidation of both.

Longer thermal exposure or higher test temperatures would be needed to calculate the activation energy and the service lifetime for the absorbers that performed well, i.e. absorbers 1, 2, 6, and 8-11. Absorber 7 also passed the accelerated ageing test, and had a service lifetime of more than 25 years. It obtained an activation energy of 70 kJ/mol as calculated from PC values (see Table 15), and the slope of $\ln(\Delta\alpha)$ versus $1/T$ suggested 40 kJ/mol, while changes in thermal emittance were not observed (see Figures 45-46 and Table 16).

In the accelerated ageing test, most of the studied industrial solar absorbers had negligible or very small changes in solar absorptance values (Table 13), which indicates that the coatings are feasible for the common DHW and space heating applications of today. Only the evaporated TiO_xN_y coating on Cu (absorber 5), which suffered from structural changes in the absorber coating, had a significant decrease in absorptance. All of the absorbers studied which have suffered only oxidation of the absorber coating as the ageing mechanism (absorbers 2, 6-11), have a durability of more than 25 years (see Table 15). The increase in the O/Cr ratio in the absorption coating was as high as 80 % in the case of absorbers 1 and 7 but nevertheless both of them had a long predicted service lifetime (Tables 15 and 17). Thus, oxidation of the absorber coating without any structural changes can be considered as a minor ageing mechanism whose influence on the durability of absorbers is on an acceptable level.

7.1.2 Diffusion of the substrate material, island and void formation

During thermal exposure, the diffusion of copper substrate material through the coating, the formation of CuO islands on the coating and the formation of voids in the substrate have been observed for absorbers with Cu substrate. After an accelerated ageing test at 278 °C and short-period thermal treatments at 300 °C for two hours, CuO islands were observed from the surface of the absorbers with copper substrates along the direction of rolling. In applications other than solar absorbers, copper has been reported to diffuse through the coating and form an island (or *nodular defect*) [174, 272] during thermal exposure. In solar absorbers, Cu has been reported to diffuse and/or form CuO on the solar absorber surface [74, 76, 98].

Void formation was observed in the copper substrates under the coating layer as in [278]. The presence of Kirkendall voids in the substrate/absorber coating interface (see Figure 59) may support the outward diffusion of copper from the substrate. According to my studies, Kirkendall voids have not been reported before in solar thermal absorbers. It can be assumed that void formation weakens the adhesion between the substrate and coating but adhesion was not measured in this study. Figure 59 e) shows a coating which has collapsed into the formed void. In short-period thermal studies at 500 °C, industrial absorbers 4 and 5 suffered from reduced adhesion between the coating layers (absorber 4) or between the substrate and the absorber coating (absorber 5), and peeled off (see Figure 68). For absorber 4 this was probably due to different thermal expansion coefficients absorption layers and AR layer [76], resulting in crack formation and delamination [78]. For absorber 5, significant structural and chemical changes in the absorber coating [101] and void formation in copper substrate most likely affected the adhesion.

The diffusion process including formation of CuO islands and voids decreased the reflectance spectra in the IR range. The correlation between thermal emittance values (Table 13) and CuO island formation is presented in Figure 76 after ageing at 278 °C for 600 h. A linear trend line is fitted to indicate the correlation between compositional changes and thermal emittance values. Large CuO islands (diameter on a micrometre scale) created a distortion of copper and oxygen on the aged TOF-ERDA graphs of absorbers 1, 3, and 5 (see Figures 47-48). The amount of oxygen in the Cu substrate indicates the quantity of CuO islands on the rough surface, and thus O/Cu calculations from TOR-ERDA measurements can be used to estimate the influence of CuO island formation on thermal emittance values. Absorbers 1, 3, and 5 on Cu substrates formed CuO islands, and their thermal emittance increased as a function of the amount of CuO. Nevertheless, in addition to CuO islands, the diffusion process created voids in the substrate surface. The number of voids can be assumed to correlate with the number of islands, because the voids formed due to the outward diffusion of Cu through the coating.

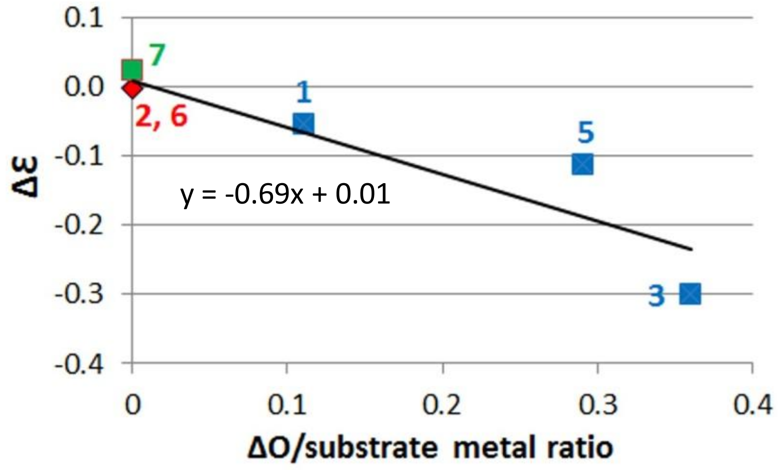

Figure 76. Correlation between change in thermal emittance and CuO island formation after ageing at 278 °C for 600 h. A linear trend line is fitted to indicate the correlation between compositional changes and thermal emittance values. The blue markers are the absorbers on the Cu substrate (absorbers 1, 3, and 5) which formed CuO islands during ageing. The red markers are the absorbers on Al (2 and 6) in which the O/Al composition remained unchanged. The green marker is the absorber on Ni-coated Cu (absorber 7) in which the O/Ni and O/Cu compositions remained unchanged.

The changes in thermal emittance may originate from void formation or the oxidation of copper in the islands (high thermal emittance of CuO [279]) or increased surface roughness [76]. Copper heated and covered with a thick copper oxide layer was reported to have an emittance of 0.78 [279]. However, if the CuO islands were spread out uniformly as a layer on the absorber surface (thickness < 30 nm), the thermal emittance would not increase significantly according to the simulations performed in this study (see Figure 62). Nevertheless, it can be assumed that the increase of thermal emittance resulted from the changes in the Cu substrate because it was not as reflective after the ageing process. This assumption is supported by the results that absorbers on Ni-coated Cu, Al or SS substrates did not show any significant changes in thermal emittance. The formation of voids in the Cu substrate was the most likely reason for the increase of thermal emittance, because voids in the Cu substrate can reduce reflectivity, as simulated in Figure 63.

For mid- and high-temperature applications, thermal emittance is a significant property because of the thermal losses due to the higher temperature difference between the collector and atmospheric air. At low stagnation temperatures (<< 200 °C), the equation with a quarter of the weight of thermal emittance (equation (1)) is used but for modern flat plate collectors with higher stagnation temperatures, the weight of thermal emittance has increased to half (equation (2)) [248]. It is likely that, for high temperature applications, the weight of thermal emittance should be considered to be even higher because of the high thermal losses. Due to the diffusion process of Cu substrate material, thermal emittance increased significantly for sputtered CrO_xN_y on Cu (absorber 3) (see Figures 36, 39 and 58).

The activation energy of a change in thermal emittance was observed in absorbers 1, 3, and 5 on the Cu substrate which had CuO and void formation during ageing. For absorber 1, the slope of $\ln(\Delta\varepsilon)$ versus $1/T$ suggested an activation energy of 60 kJ/mol at 250-500 °C, for absorber 3 90 kJ/mol at ≤ 308 °C, and for absorber 5 10-20 kJ/mol at 250-500 °C (see Figure 46 and Table 16). In the literature, the activation energy of Cu oxidation in air at 350-500 °C was 40 kJ/mol [280]. The activation energy of Cu oxidation was at quite the same level as the activation energies estimated in this study.

Aluminium substrates did not show similar diffusion, island or void formation processes. The reason appears to be that aluminium forms an oxide layer (see Figure 60), which acts as a barrier layer [242]. It is known that during the preparation or production of aluminium layers, foils or sheets, the formation of a thin oxide layer usually occurs. Often before the actual PVD coating process, metal ion etching is performed on the substrate to clean the substrate surface and improve the coating adhesion [281]. The studied sputtered industrial absorbers were probably ion-etched before the deposition process. Thus, in microstructural analysis we did not observe a natural aluminium oxide layer on the Al substrates from as-received samples but XPS measurements revealed an Al_2O_3 compound between the CrO_xN_y absorber coating and Al substrate (Table 11). The ageing studies at elevated temperatures accelerated the formation of an oxide layer [243], and a 5-10 nm thick aluminium oxide layer was observed after 600 h at 278 °C.

The as-deposited CrO_xN_y/SiO_x on Al substrate (absorber 6) had craters in the coating (see Figure 26). However, probably because of the aluminium oxide barrier layer formation, aluminium had not diffused outwards from the substrate, as presented in Figure 77. Absorber 6 passed the accelerated ageing test according to the first test temperature despite these defects in the coating. It is likely that the oxide layer formation on the aluminium substrate compensated for the defects in the coating.

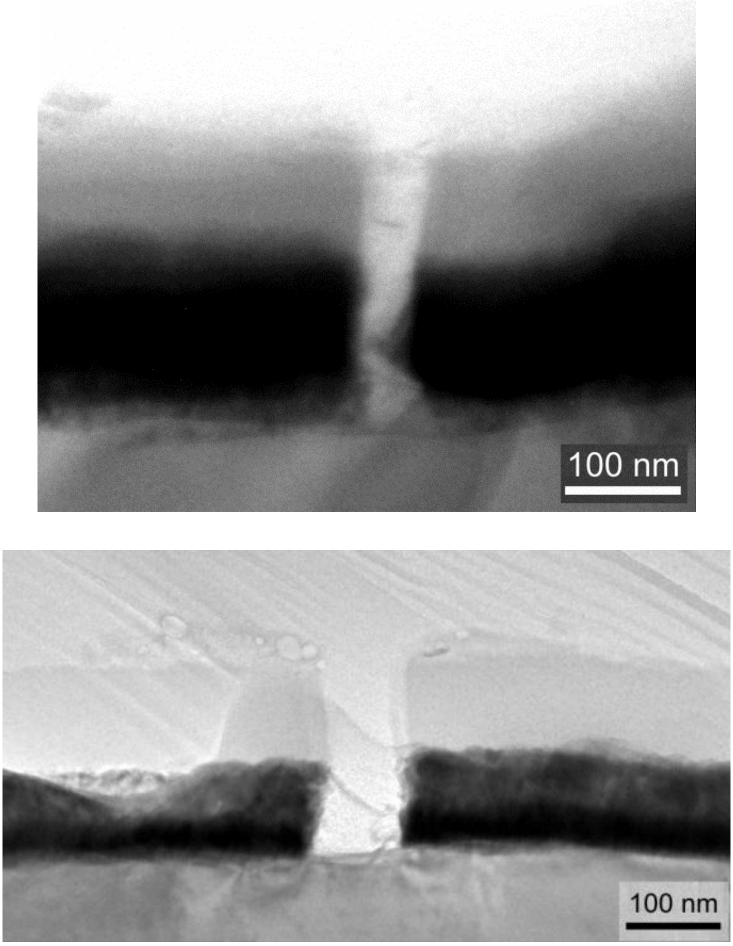

Figure 77. TEM images of two different defects through a CrO_xN_y/SiO_x coating on Al substrate (absorber 6) after ageing at 278 °C for 600 h.

The absorbers on stainless steel substrates did not show a substrate diffusion mechanism in the temperature range studied. As-deposited stainless steel absorbers (absorbers 8 and 9) obtained a higher thermal emittance ($\varepsilon_{\text{as-deposited}}$ = 0.223 and 0.140, respectively) than Cu or Al based absorbers [78]. However, the thermal emittance of the SS absorbers remained unchanged or even reduced during the ageing studies ($\varepsilon_{\text{aged 278 °C, 600 h}}$ = 0.194 and 0.109 for absorbers 8 and 9, respectively). For absorber 8, the slight decrease in solar absorptance values during the ageing studies ($\alpha_{\text{as-deposited}}$ = 0.960, $\alpha_{\text{aged 278 °C, 600 h}}$ = 0.933) was probably due to oxidation in the absorber coating similar to the other studied CrO_xN_y absorber coatings (absorbers 1-3 and 6) in this work, as simulated in Figure 61. Both of the SS absorbers passed the accelerated ageing test.

7.1.3 Structural and chemical changes in the coating layers or substrates

Major structural and chemical changes were observed from the TiO_xN_y absorber coating (industrial absorber 5) and the anodized aluminium substrate with a thin Al layer (industrial absorber 4).

TiO_xN_y absorber coating

TiO_xN_y has been reported to degrade first due to structural and chemical changes to TiN and TiO, after which they oxidize, and form crystalline rutile TiO_2. These in turn form a quasi-liquid film-substrate mixture with mobilized Cu in the interface region, and finally the film includes amorphous titanium oxides and crystalline copper oxides [101]. In this study for TiO_xN_y absorber 5, a similar transition from a crystalline to amorphous structure during ageing was revealed in SAED (see Figure 54).

Large CuO islands (diameter on a micrometre scale) created a distortion of copper and oxygen on the aged TOF-ERDA graph of absorber 5 (see Figure 48). The coating layers, especially the TiO_xN_y absorber coating, seemed to broaden during ageing. The distortion of CuO islands may be responsible for the broadening of the detected layers. However, a similar broadening was not observed in the other aged absorbers with CuO islands, as presented in Figure 47. Thus, it can be assumed that the TiO_xN_y layer may have extended in width during the thermal exposure in air due to structural and chemical changes.

The reflectance spectra of aged absorber 5 (Figure 42) had absorption peaks, which indicated structural and chemical changes. During ageing, in the solar wavelength range, the absorption decreased and the interference fringes became more pronounced and shifted. This indicates that the TiO_xN_y absorber coating had changed to a less absorbing material and there may also have been an increase in thickness of the absorption coating or a two-layer structure with TiN and TiO may have formed. The interference fringes became significant after the first thermal exposure period at 278 °C for 36 h, and were pronounced until 75 h with a small shift. After thermal exposure for ≥ 150 h, the shifting of the interference fringes became more significant, and also the activation energy for changes in solar absorptance increased (see Figure 45 and Table 16). This indicates that another structural ageing mechanism became dominant.

Figure 64 shows the simulations of different TiO_xN_y coatings on Cu. The evaporated TiO_xN_y absorber is very complex in structure as presented in [101], and its structural changes were complicated to model. The Bruggeman model with amorphous TiO_2 in a TiN matrix and a two-layer structure with TiN and amorphous TiO_2 layers were used in the simulation. Oxidation of TiN was simulated by increasing the amount of TiO_2 in the TiN matrix from 85 % to 95 %, and as a result, the interference fringes became more pronounced. The two-layer structure with TiN and TiO_2 layers decreased solar absorptance significantly and the increase in oxide or increase in thickness of the oxide layer shifted the interference fringes, similarly to the experimental data in Figure 42. In addition to changes in solar absorptance, a significant absorption peak was formed in the thermal emittance range, about 8-10 µm (Figure 42). The absorption peak increased during ageing. However, a similar absorption peak was not observed in aged absorbers 1 and 3 with CuO formation (Figure 39). Thus, it was assumed to be related to the quasi-liquid film-substrate mixture presented in [101] because chemical changes in the surface of the Cu substrate are more likely to affect the thermal emissivity range.

Lower thermal test temperatures would be needed to define the activation energy from PC values and the service lifetime for evaporated TiO_xN_y (absorber 5), which contributed more than one degradation process or phase changes at 278 °C. The Arrhenius relationship was not valid for absorber 5 (see Figures 44-46) in which another process with higher activation energy seems to take over after the knee in the 278 °C curve at about 150 h. Hence, it can be assumed that absorber 5 changed physically due to phase changes as in [101]. For absorber 5, the activation energy estimated from the slopes of $\ln(\Delta\alpha)$ versus 1/T suggested 25-40 kJ/mol and $\ln(\Delta\varepsilon)$ versus 1/T, 10-20 kJ/mol. Thus, the activation energy seems to be very low (see Figures 45-46 and Table 16). In the literature, activation energy for the oxidation in air of magnetron-sputtered TiN was 160-170 kJ/mol at 350-800 °C [276, 277]. However, the non-stoichiometry in TiN_y has been reported to lead to a reduced activation energy for oxidation compared to stoichiometric compounds [277].

Anodized aluminium substrate with a thin Al layer

Changes in the CrO_x absorber on anodized Al (absorber 4) degraded the optical properties of absorber 4 rapidly, and the absorber failed the accelerated ageing test. However, the time-transformations at 248 °C, 250 °C, and 278 °C corresponded well to each other but the graph is not linear (see Figure 44 b) as assumed in Arrhenius behaviour. CrO_x absorber on anodized Al (absorber 4) had activation energy of 94 kJ/mol as calculated from the PC values. Moreover, Arrhenius time-transformations (see Figure 44 b) and the estimation of activation energy from the slopes of $\ln(\Delta\alpha)$ or $\ln(\Delta\varepsilon)$ versus 1/T revealed more than one activation energy having an effect during the ageing process (see Figures 45-46 and Table 16). At 248-278 °C, the activation energy for the change in solar absorptance was 10 kJ/mol but at 278-308 °C, it was 110 kJ/mol. The longer duration did not create a higher degradation in solar absorptance and thus the duration was rather insignificant in the studied time range (36-600 h). This non-linear behaviour suggests that after the structural and chemical change in the anodized aluminium oxide layer has been completed, absorber 4 is quite stable at ≤ 278 °C.

Absorber 4 did not pass the accelerated ageing procedure because of the rapid changes in optical properties. The service lifetime was only 12 years but the estimation of the durability was unreliable because of the variation in activation energies during the thermal ageing, i.e. non-linear degradation behaviour as a function of time. Because the degradation behaviour of absorber 4 stabilized after the change in the anodized aluminium oxide layer, the true service lifetime may be longer than predicted according to the accelerated ageing procedure. Thus, because Arrhenius behaviour was not valid for absorber 4, the service lifetime estimation is unreliable. In any case, even at 248 °C it caused severe optical degradation.

The ageing behaviour and different activation energies for the CrO_x absorber on anodized Al (absorber 4) indicate chemical or structural changes which stabilize the stack after finishing. In absorber 4, the CrO_x/SiO_x coating layers seemed to be stable (no significant oxidation, see Table 17) and there was no island formation on the surface nor void formation in the substrate. Two different chemical/structural changes have been considered in this study to create degradation of thermal emittance during ageing (see Figures 36 and 40). One is a change revealed in the anodized aluminium oxide layer. TOF-ERDA results showed the oxidation of the sub-stoichiometric aluminium oxide (O/Al ratio 1) to correspond to Al_2O_3 (O/Al ratio 1.5), and the crystallization of the amorphous structure to the crystalline during thermal exposure in air (see Figure 52). XRD suggested γ-alumina formation but the peaks were very small (see Figure 53). Thus, the structure can be nanocrystalline and/or include also amorphous structure. The as-deposited anodized Al layer was probably sub-stoichiometric (or *nearly stoichiometric*) amorphous alumina as in [242, 282-284], and had a phase change towards crystalline γ-alumina during the thermal treatment in air [285, 286], as suggested by SAED and XRD (Figures 52 and 53). It is possible that the phase change in the anodized aluminium oxide layer affected the optical properties. The emittance of different types of anodized aluminium has been reported to vary between 0.055 and 0.82 [287]. However, it was not possible to confirm the relation between structural changes in anodized aluminium oxide and the increase in thermal emittance in this study.

Another possibility for the increase in thermal emittance of absorber 4 was the oxidation of a thin Al layer on the anodized aluminium oxide. The existence of the thin Al layer was not proved in this study but recounted by a manufacturer. The Al layer would act as an IR reflection layer on anodized aluminium oxide. The Al layer was probably too thin (nanometre scale) to be revealed by EDS, SAED, and TOF-ERDA analyses. XPS measurements suggested metallic Al but at the same depth Al_2O_3 also existed (Table 11). The TEM image in Figure 25 b) revealed a bright part in the top of the anodized aluminium oxide layer which can be the Al IR reflector layer. TOF-ERDA did not observe Al layer from as-deposited absorber 4 but observed oxidized Al layer from aged absorber 4 (see Figure 51). Most likely the as-deposited surface of anodized Al layer was rough and thus the interface between aluminium oxide (anodized layer) and Al layer (sputtered IR reflector) was uneven. The roughness of interfaces can influence on poor depth resolution in TOF-ERDA measurement. The cross-sectional TEM image (Figure 52 a) of as-deposited absorber 4 showed an unclear interface between aluminium oxide layer and assumed Al layer while it had a more clear interface after ageing (Figure 52 b). The similar effect is observed also in the interface between Al substrate and aluminium oxide layer (Figure 52) and it created sharpened depth profile between the substrate and aluminium oxide layer in TOF-ERDA measurements (Figure 51). Probably, during ageing the interfaces became sharper because of interdiffusion of oxygen between the layers. The simulation of oxidation of the aluminium IR reflector layer on aluminium oxide showed a similar increase in thermal emittance, as noted in experimental studies for absorber 4 (see Figures 40 and 65). The simulated oxidation also created pronounced interference fringes in the solar range. However, it can be assumed that the oxidation of the Al reflector layer on relatively thick oxide can increase thermal emittance. The oxidation process of the Al layer would be rapid but, after the formation of alumina, the stack would probably be quite stable and degradation of optical properties would stagnate. This kind of behaviour was noticed in this study for absorber 4.

7.2 Influence of microstructure on ageing properties

The microstructures of the sputtered and evaporated coatings studied were columnar. A columnar structure is typical for these coating methods but deposition parameters affect the density of the structure obtained [69]. Figure 78 presents the microstructures of sputtered coatings as a function of different coating parameters. High sputtering working pressures and low substrate temperatures in the deposition process promote the formation of a more columnar structure with intercolumnar and/or intergranular voids acting as fast diffusion paths. Coating structures with such open porosities are due to the low mobility of coating atoms (adatoms) caused by low homologous substrate temperatures (T/T_m), and the decreased amount of energetic particle bombardments due to the thermalization of coating atoms and energetic neutralized argon atoms (these originate from argon ions bombarding the sputtering target). [288]

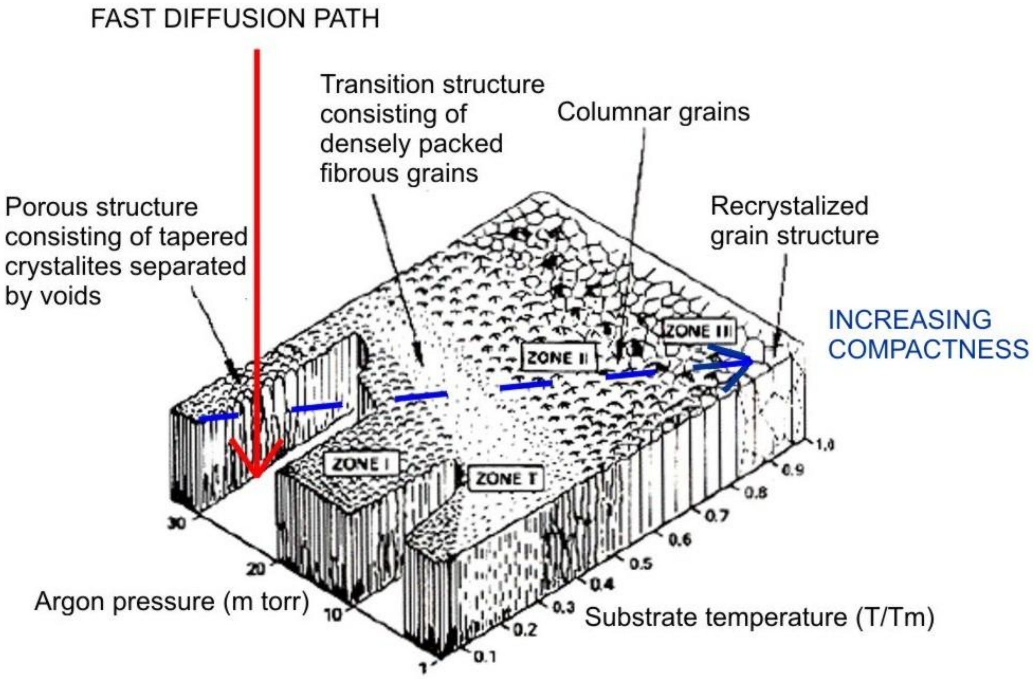

Figure 78. Schematic drawing of microstructures of any given sputtered coating as a function of different coating parameters. Denseness and compactness increase in the direction from left to right. High argon pressure or low substrate temperature creates a porous structure, which acts as a fast diffusion path. Modified from [69].

In this study, the copper and aluminium substrates studied were typical cold-rolled products. Substrate surface roughness from the rolling process or other defects in the substrate material affected the microstructure of the coating. The defects in the substrate surface can create a weaker point in the coating, causing ageing to be faster at this point. Very vulnerable points on the substrate surface were scratches along the rolling direction (see Figure 58). In the case of copper, especially at the edges of the scratches, there is no diffusion barrier effect due to the natural oxide layer. Along these scratches, the layer thickness could be thinner because of the shadowing effect [226] compared to the smoother parts of the absorber and thus the diffusion length may be smaller too. According to this result, a smoother substrate surface would probably reduce the defects in the coating, and thus retard the diffusion process. Hence, it can be assumed that production of a smoother substrate is more demanding and expensive. For, the price of rough quality (root mean square surface roughness of 0.25 µm RMS) aluminium substrate has been reported to be around 4 €/m^2 and smooth highly reflecting aluminium quality (0.02 µm RMS) about 10 €/m^2 [289]. The material cost of the substrate is significant in solar collector production [289].

7.2.1 Influence of microstructure of absorber coatings on ageing

The denseness of grain boundaries and packing density of the columnar structure affected the ageing properties of the studied absorbers. Both industrial absorbers 1 and 3 were CrO_xN_y/SnO_x absorbers on Cu but absorber 1 had smaller columns in width and a denser structure than absorber 3 (see Figures 23 and 24). Absorber 3 had bigger and more separated columns, and there was open porosity between the columns. The calculated densities (Table 10) correlated well with the microstructural analyses. The calculated density for the CrO_xN_y absorber coating for absorber 1 was 6.5 g/cm^3 and for absorber 3 it was 4.1 g/cm^3. The literature value for Cr is 7.15 g/cm^3, bulk hexagonal Cr_2O_3 is 5.2 g/cm^3 [290], for sputtered CrO_x coatings 2.8-7.3 g/cm^3 depending on the deposition parameters [291], for the bulk face-centred cubic CrN 6.2 g/cm^3 [292], and the sputtered CrN_y 3.2-6.5 g/cm^3 depending on deposition parameters [293, 294]. From the CrO_xN_y absorbers on Cu, absorber 1 was denser than absorber 3, as microstructural analysis indicated. The density of absorber 1 was at the upper limit of the reported densities of sputtered CrO_x and CrN coatings. The density of absorber 3 was at the midpoint of the sputtered literature density values. The difference in the densities of absorbers 1 and 3 may depend on differences in the deposition parameters of the sputtering or the nitrogen content in the absorber coating (see Figure 47). Absorber 1 has a Cr-rich CrO_x layer on Cu while absorber 3 has a CrN_y layer. CrN_y

has a smaller density in the literature than Cr or CrO_x, and for this reason the density of absorber 3 may be smaller. However, in the microstructural analysis, the porosity between the columns was observed from absorber 3 (see Figure 24), and this indicates differences in the deposition parameters. In absorber 1, the dense sputtered structure protected the substrate better from diffusion. Other sputtered CrO_xN_y coatings, absorbers 2 and 6, had densities of 5.0 and 5.2 g/cm^3 (Table 10), respectively, and the densities corresponded well with the microstructural analysis (Figure 25). Absorber 2 has some porosity between the columns while absorber 6 has quite a dense microstructure but several defects or craters in the coating (see Figure 26). Sputtered CrO_x coating (absorber 4) has a density of 5.4 g/cm^3 (Table 10), and columnar but quite a dense microstructure (Figure 25). The lack of CrN_y did not increase the density of absorber 4 higher than in the densest CrO_xN_y absorber 1 even though sputtered CrN_y has been reported to have a smaller density than sputtered CrO_x. However, CrO_x absorber 4 had a higher density than the other CrO_xN_y coatings (absorbers 2, 3, and 6).

Electroplated black chromium had a density of 1.6 g/cm^3 while the literature value for Cr is 7.15 g/cm^3 and for bulk hexagonal Cr_2O_3, 5.2 g/cm^3 [290]. The densities of electroplated black chromium depend strongly on the deposition parameters and Cr/Cr_2O_3 ratio (Cr denser than Cr_2O_3) achieved [295] but density values have not been reported in the open literature for electroplated black chromium. The calculated density of electroplated black chromium (absorber 7) was lower than the calculated densities of sputtered chromium oxide and chromium oxy-nitride coatings (absorbers 1-4 and 6), which can be explained by the flake-like microstructure (see Figure 30). Even though the black chromium coating in absorber 7 had a low density, copper was not observed to diffuse to the surface of the coating, most likely because of the thick Ni layer between the Cu substrate and black chromium coating. Thus, oxidation of the black chromium coating was significant (see Table 17) and degraded solar absorptance (Figures 35 and 41) but the effect on durability was still acceptable and the absorber passed the accelerated ageing test after the second exposure (Table 15).

Evaporated TiO_xN_y (absorber 5) had a density of 4.7 g/cm^3, while in the literature the density for bulk cubic TiO is 4.9 g/cm^3, sputtered TiO_x 3.2-4.6 g/cm^3 depending on the deposition parameters [296], bulk face-centred cubic TiN 5.2 g/cm^3 [297], and sputtered TiN_y 4.3-5.7 g/cm^3 depending on the deposition parameters [298, 299]. The literature values for TiO_xN_y coating deposited by an activated reactive evaporation process were 3.8-4.8 g/cm^3 depending on the deposition parameters [99]. Thus, absorber 5 has quite a high density for an evaporated TiO_xN_y coating but it is well within the literature values. Nevertheless, the density of absorber 5 was smaller than in most of the sputtered chromium-based absorbers (see Table 10).

The coating microstructure had a significant influence on the ageing properties of the absorbers. Table 20 summarizes the microstructures of industrial absorbers 1-7 as a function of changes in optical properties in ageing studies at 278 °C after 600 hours. The optical properties were determined with a PC value, and are listed from less-aged to most-aged absorbers. The open porosity between the columns acted as fast diffusion path, as illustrated in Figure 59 d). The as-deposited structure of the coatings is based on FESEM and TEM observations. It can be assumed that the coating method and parameters impacted the microstructure of the coating. With open porosity in the coating structure, Cu substrate atoms diffuse easily through the coating and form CuO islands and voids (see Figure 59), which increase thermal emittance, i.e. decrease reflectance at long wavelengths (Figure 39), as simulated in Figure 63.

Table 20 compares the changes in composition during accelerated ageing at 278 °C for 600 hours to the degradation of optical properties of industrial absorbers 1-7. Changes in the compositions correlated well with the changes in the optical properties of the different absorbers. The more the optical properties had degraded, the more the composition had changed during ageing. The reduction in absorptance was due to the oxidation of metallic chromium or titanium in the absorption coatings [85], as simulated by optical modelling in Figures 61 and 64. The graded structure of the coatings was lowered by oxidation (i.e. the composition profile became more homogeneous), which shifted the reflectance curve towards the lower wavelengths and reduced the absorptance (see Figures 37-42).

7.2.2 Influence of microstructure of anti-reflection coatings on ageing

Sputtered tin oxide anti-reflection coatings had a columnar structure and PECVD-coated or e-beam evaporated silicon oxide coatings had quite a smooth and homogeneous structure (see Figures 31 and 33). The differences between the microstructures were probably due to differences in the film growth of tin oxide and silicon oxide. Tin oxide grows in a columnar form with a crystalline structure (may also include amorphous structure) [300, 301], and silicon oxide as an amorphous glassy material with a smooth surface [302, 303].

Table 20. Microstructures of the as-deposited coatings and changes in composition during ageing as a function of PC values, and changes in optical properties after ageing at 278 °C for 600 hours. The higher the PC value, the more the absorber has aged. The dense coating structure was significantly more stable than the open columnar structure.

	$\Delta\alpha$, $\Delta\varepsilon$	PC	Structure as-deposited [1]	Differences in compositions after ageing
2	0.01, 0.00	0.004	Columnar, dense and fine-grained.	Small oxidation of the absorption layer and slight oxidation of the AR layer.
6	0.01, 0.00	0.009	Columnar absorption coating. AR coating homogeneous and quite smooth. Some	Slight oxidation of the absorption layer and the AR layer.
1	0.00, -0.05	0.029	Columnar, dense and fine-grained.	Significant oxidation of the absorption layer. Diffusion of copper through the coating and formation of CuO islands. Void formation in the substrate.
7	0.07, 0.02	0.062	Electroplated. Thick nickel layer and chromium particles on chromium oxide matrix. Rough top surface.	Significant oxidation of the absorption coating.
4	0.02, -0.14	0.091	Anodized aluminium oxide layer amorphous and sub-stoichiometric. A thin Al IR reflector. Absorption coating columnar and dense. AR coating homogeneous and quite smooth.	Oxidation and crystallization in the anodized aluminium layer and possible oxidation of the thin Al layer.
3	0.03, -0.30	0.179	Columnar, large columns and porosity between the columns.	Oxidation of absorber coating. Significant diffusion of copper through the coating and formation of CuO islands. Void formation in the substrate.
5	0.30, -0.11	0.354	Evaporated. Columnar absorption coating. AR coating homogeneous and quite smooth.	Chemical and structural changes in the absorber coating. Significant diffusion of copper through the coating and formation of CuO islands. Void formation in the substrate.

[1] Based on FESEM and TEM observations

The oxygen content of the anti-reflection coatings remained quite unchanged in the accelerated ageing studies and only a slight increase was noticed in the SiO_x AR coatings of absorbers 4 and 6 (Table 17). The calculated densities for the AR coatings were 6.2-6.5 g/cm^3 for sputtered tin oxide (absorbers 1-3, Table 12) while the literature values for bulk tetragonal SnO_2 are 6.9 g/cm^3 [304] and for DC magnetron sputtered SnO_x coatings 3.8-6.4 g/cm^3 depending on the deposition parameters [304]. The densities of the sputtered SnO_x AR coatings were well within the reported sputtered values and were quite high. The larger columns in the SnO_x AR layer of absorber 3 compared to fine-grained absorber 1 (see Figure 32) have a minor influence on density values: the density in fine-grained absorber 1 was 6.5 g/cm3 while it was 6.2 g/cm^3 in absorber 3.

The calculated density for the e-beam evaporated silicon oxide AR coating (absorber 4) was 2.8 g/cm^3 and for the PECVD-coated silicon oxide AR coatings (absorber 5 and 6) 1.8 and 2.5 g/cm^3, respectively (Table 12). The literature values for bulk SiO_2 are 2.2-2.7 g/cm^3 depending on the crystal structure [290], and for thermal CVD or PECVD-coated SiO_2 2.2 g/cm^3 [305]. The calculated density values are quite well within the reported values. The microstructures of all of the SiO_x AR layers were homogeneous and seemed in microstructural analyses to be dense (Figure 33). Absorber 4 had the highest density of SiO_x AR layer (2.8 g/cm^3). The density of the AR layer in absorber 6 was 2.5 g/cm^3 even when it had defects or craters in the coating (see Figure 26).

The composition and structure of the anti-reflection layers remained quite unchanged during ageing, as presented in Table 17 for oxygen ratios, and in Figure 55 for SAED patterns. The exception was the sharp rings in the SAED pattern of absorber 5 that were revealed after ageing but they probably originated from sample preparation. In the SAED pattern of absorber 5 crystallinity was revealed instead of an amorphous structure in the SiO_x anti-reflection layer but the sharp rings most likely came from transferred material due to ion bombardment during sample preparation. The FESEM image in Figure 56 reveals small spots in the AR layer of absorber 5 which correspond to residual bombarded material returned to the sample surface. Other possibilities could be diffused Cu from the substrate into the anti-reflection layer but the spots in the FESEM image seem more likely to be bombarded material.

7.3 Influence of diffusion barrier on ageing properties

Sputtered TaN_x and Al coatings were studied as diffusion barrier layers between the Cu substrate and experimental CrO_x/Cr/CrO_x and $TiAlSiO_xN_y$ absorbers. In addition to the experimental barrier coatings, an industrial electroplated Ni layer was studied as a diffusion barrier on Cu substrate.

The experimental CrO_x/Cr/CrO_x absorber and simulated CrO_x (45 nm)/Cr (30 nm)/CrO_x (45 nm) had differences in their reflectance spectra, as presented in Figure 22, even though the solar absorptance values (0.87 for the sputtered versus 0.86 for the simulated) and thermal emittance values (0.05 versus 0.01, respectively) were quite consistent. The difference in thermal emittance values can be explained by differences in the optical constants of the experimental and simulated Cu. The CODE Coating Designer database has optical values for quite an ideal Cu, which has been used in the simulations as a substrate. The simulated thermal emittance for Cu was 0.01 while the measured thermal emittance for cold-rolled Cu sheet was 0.05. Moreover, the optical values vary widely depending on the surface structure, as presented in Table 1 [106]. The difference in reflectance spectra in the short-wavelength range may be influenced by differences in the optical constants of the experimental and simulated chromium oxide and metallic chromium, or uncertainties in the thicknesses of the coating layers. By fitting the experimental data with CODE Coating Designer to meet the corresponding layers of Cr_2O_3/Cr/Cr_2O_3, for example the thicknesses of 40.8 nm/34.5 nm/76.8 nm roughly followed the experimental data, as presented in Figure 22. Even though the reproducibility of the experimental absorbers was acceptable (see section 6.1.2), the layer thickness values of 45 nm/30 nm/45 nm may have some uncertainties. The deposition rates of the experimental coating layers were calculated from cross-sectional FESEM samples from single coating layers, and they were about 3-4 nm/s for Cr and about 1 nm/s for CrO_x (see Table 4). However, the layer thicknesses achieved in the three-layer stack were estimated from cross-sectional FESEM images, and may have a wide error range because of inaccurate layer interfaces due to possible interdiffusion and interfacial roughness [306], as presented in Figure 34.

A thinner metallic Cr layer in the experimental three-layer stack would give higher solar absorptance, as described in the case of the optimized Cr_2O_3/Cr/Cr_2O_3 absorber with layer thicknesses of 42.6 nm/12.3 nm/44.6 nm, respectively (see section 6.2.4). It was decided to use the thicker Cr layer because it had better reproducibility in the deposition process. The higher solar absorptance with a thinner metallic Cr layer would explain the wide variation of solar absorptance degradation during ageing for the experimental $CrO_x/Cr/CrO_x$ absorber with and without the barrier coatings (see Table 19 and Figures 70 and 72). That is because the metallic Cr layer can became thinner by oxidation during ageing. The activation energy slopes for the change in thermal emittance had a wide variation (see Figure 72) because of the small changes in the range of ± 0.01, which is within the error range of thermal emittance measurements for the experimental $CrO_x/Cr/CrO_x$ absorber. The variation of activation energy slopes in Figure 73 was connected to the exceptional behaviour of 20 nm $TaN_x/TiAlSiO_xN_y/SiO_x$ at 500 °C, presented in Figure 71. This behaviour may be a consequence of chemical reactions, for example between Ta and Cu [307] or Ta and Al [308]. Since thermal emittance was affected significantly, reactions with Cu substrate are more likely to be the reason.

7.3.1 Sputtered tantalum nitride coatings

The sputtered experimental 20-60 nm thick TaN_x diffusion barrier between the Cu substrate and $CrO_x/Cr/CrO_x$ or $TiAlSiO_xN_y/SiO_x$ absorber coating did not prevent or decelerate Cu diffusion (see Figures 70-71 and Table 19). The ageing rate and formation of CuO islands was similar or even more aggressive with the TaN_x layer than without any diffusion barrier (see Figure 74). This result indicates that TaN_x acted as a fast diffusion path. A 20-nm-thick TaN_x layer between Cu and $CrO_x/Cr/CrO_x$ contributed to the decrease of long-wave reflectance at 200 °C while a similar absorber without a TaN_x layer did not suffer such phenomena (see Figure 70). A thicker, 40-nm-thick TaN_x layer between Cu and $CrO_x/Cr/CrO_x$ was stable at 200 °C for 2 h but suffered more severe degradation at 300 °C than the absorber without a TaN_x layer. The result was unexpected because the TaN_x coating seemed to be quite dense and fine-grained, even though it had some defects (see Figure 69). It has been reported previously that a 50-nm-thick Ta_2N is a stable diffusion barrier for Cu at 650 °C for 30 min in helium atmosphere [174]. The Ta_2N coating was magnetron sputtered reactively with a N_2 flow of 5 vol.% of Ar flow [174]. A similar reactive sputtering gas flow was used in this work. However, it must be pointed out that Holloway *et al.* [174] studied stability in a helium atmosphere, not in air.

The TaN_x diffusion barrier coating increased the thermal emittance of an as-deposited absorber due to the reduced IR reflector properties compared to Cu [106]. Thermal emittance increased with the TaN_x layer thickness due to the flattening of the reflectance spectra (Figure 71). The 20-nm-, 40-nm-, and 60-nm-thick TaN_x layers between the Cu and $TiAlSiO_xN_y/SiO_x$ increased the thermal emittance from 0.05 to 0.09, 0.12, and 0.20, respectively. It should be noted that when using a TaN_x layer, it would be necessary to change the absorber multilayer in order to obtain adequate optical properties. However, in this study the diffusion barriers were deposited between the Cu substrate and specified absorber to obtain comparative results of diffusion barrier properties. A thicker TaN_x layer could act better as a diffusion barrier, but even a 60-nm TaN_x layer increased thermal emittance significantly.

7.3.2 Sputtered aluminium coatings

Both 100-nm- and 500-nm-thick as-deposited Al layers between the Cu substrate and CrO_x/Cr/CrO_x absorber increased thermal emittance from 0.05 to about 0.10. The Al layers flattened the reflectance curves in the long-wavelength range, which influenced the increase of thermal emittance. The Al layer increased thermal emittance less than TaN_x because Al is a good IR reflector [106]. Sputtered, columnar Al increased the thermal emittance from 0.05 to about 0.10 probably because the sputtered, columnar surface was not as good an IR reflector as the smoother Al as a result of scattering [309].

Aluminium acted as a diffusion barrier on copper, according to the short-period ageing studies. Experimental coating without an Al layer degraded at lower temperatures and faster than coatings with an Al barrier layer. The 100- and 500-nm-thick Al layers prevented Cu diffusion and retained optical selectivity for two hours at 400 °C, while without the Al layer, CuO island formation was observed at 300 °C. At higher temperatures, the Al diffusion barrier retarded the ageing mechanisms. At 400 °C and 500 °C, it is more likely that intermetallic compounds formed between the Cu substrate and Al coating [310]. Moreover, stability at high-humidity and condensed water on an absorber must be studied [24] because Al absorbers have been reported to form aluminium hydroxide, which can have a strong influence on emittance [28]. It would be necessary to study the effect of both the high temperature and condensing humidity to be able to draw final conclusions about the durability of the Al diffusion barriers studied. Nevertheless, these results reveal that diffusion barriers can be used to prevent copper diffusion for future higher temperature solar thermal applications.

7.3.3 Electroplated nickel coating

A 3-µm-thick Ni layer prevented Cu diffusion in industrial absorber 7, as presented in Figures 41 and 50. The thick Ni layer was electrodeposited on the Cu substrate.

The Ni layer between the Cu substrate and black chromium acted as a diffusion barrier as reported earlier in [96]. However, a Ni-coated Cu substrate has a higher thermal emittance than a Cu substrate without the Ni layer [22]. Electroplating has environmental and health risks [311-313] but nickel-coating with a thickness on a micrometre scale would probably be demanding and slow to produce by PVD methods.

7.4 Activation energies in short-period heat treatments

The estimation of activation energy in short-period heat treatments at 300-500 °C had a statistical distortion when compared to the results of the accelerated ageing tests (see Figures 45-46 and Table 16). Degradation at 300 °C seemed to be higher and at 500 °C lower than expected according to the results of accelerated ageing studies. This behaviour can be explained by differences in the experimental procedures of the exposures.

In the accelerated ageing studies, the samples were put into a hot furnace and removed to room temperature after a certain time period. In contrast, in the short-period heat treatments, the samples were placed in a cold furnace and then the furnace was heated to the testing temperature. The heating rates varied from 7.1 °C/min to 6.0 °C/min at 300-500 °C. After maintaining the exposure temperature for two hours, the samples were cooled inside the furnace with cooling rates from 1.7 °C/min to 2.4 °C/min at 300-500 °C. Thus, the two-hour exposure in the short-period heat treatments loaded more thermal stress to the absorber samples because of prolonged exposure due to the heating and cooling period. When comparing activation energies of short-period heat treatments with each other, the thermal load seems to be relatively higher at 300 °C than at 500 °C even though the actual exposure time at elevated temperature (including heating and cooling) at 300 °C was about 280 min, at 400 °C about 310 min, and at 500 °C 345 min. During the short-period thermal treatment at 300 °C, the cooling rate was slowest which may have added the thermal load. Thus, it can be assumed that activation energies should be higher in short-period heat treatments to correspond to the values of accelerated ageing studies in absorbers 2, 3, 4, 6, 7, and 8. Most likely absorber 1 is affected by similar behaviour and the estimation of activation energy according to short-period heat treatments is too low. Titanium-based absorbers 5 and 11 had slightly steeper slopes (i.e. higher activation energy) in short-period heat treatments, which may indicate other ageing mechanisms at 400-500 °C.

8 CONCLUSIONS

Emerging solar thermal applications, such as solar cooling and industrial process heating, require higher operating temperatures than traditional DHW and space heating applications. Thus, demands for temperature stability in solar absorbers will become higher in the future. PVD solar absorber coatings with dense structures have great potential for use in advanced solar collectors at elevated temperatures. The studied temperature range was 200-500 °C. The whole stack of the absorber plate: the substrate material, the possible diffusion barrier layer, the absorption layer and the AR layer all had a significant influence on ageing behaviour at elevated temperatures.

i) Substrate material

The substrate material was the most significant individual factor in thermal ageing phenomena. At about 300 °C, it was found that copper easily diffused through the coating and formed CuO islands on the coating surface. As a consequence of the outward diffusion of copper, voids were formed in the copper substrate at the interface of the substrate and the coating. This diffusion mechanism increased thermal emittance. The increase in thermal emittance can be explained most probably by the void formation in the substrate because the formed rough substrate surface did not act as a good IR reflector. In addition, the high ε of copper oxide has been considered to affect the optical properties but in the simulation performed, void formation seemed to be the most significant factor. According to studies by the author, in actual exposure outdoors at the operating temperatures of traditional DHW and space heating applications with flat plate collectors (operating temperature < 100 °C), copper diffusion and CuO island formation has not been reported for solar absorbers.

In thermal exposure in air, aluminium formed a natural thin (< 10 nm) oxide layer, which acted as a diffusion barrier. The stainless steel substrate was stable at elevated temperatures but has a higher initial thermal emittance than copper or aluminium.

ii) Density and stability of the coating layers

The role of a dense and closely packed coating structure and diffusion barrier would be to slow down the diffusion and oxidation reactions that cause changes in absorber composition and thus reduce optical selectivity. The density of the absorber coating played a significant role in temperature degradation because the dense absorber coating decelerated the diffusion processes even without a diffusion barrier layer. In a dense, fine-grained and closely packed sputtered CrO_xN_y/SnO_x coating (industrial absorber 1), copper diffusion was negligible during the accelerated ageing studies, and the absorber had a long lifetime (> 25 years). Meanwhile, a similar but more porous sputtered CrO_xN_y/SnO_x coating (industrial absorber 3) obtained significant diffusion reactions, which led to reduced durability resulting in a lifetime of 14 years. On the basis of all these results, it can be assumed that dense coating layers (including a possible diffusion barrier) effectively prevent the ageing of copper substrate absorbers.

A sputtered $TiAlSiO_xN_y$ coating is conventionally used in the tool industry. In these studies, it had a very stable coating structure as a solar absorber. The optical properties of $TiAlSiO_xN_y/SiO_x$ on aluminium substrate remained almost constant in the accelerated ageing test at 278 °C for 600 h (Table 13). A similar absorber coating was used on copper substrate as a reference without a diffusion barrier in experimental short-period thermal studies. The $TiAlSiO_xN_y/SiO_x$ on Cu substrate withstood 2 h at 300 °C without CuO island formation. After 2 h at 400 °C, the island formation was minor and the influence on the optical properties was negligible. In comparison, in industrial CrO_xN_y/SnO_x (absorbers 1 and 3) and TiO_xN_y/SiO_x (absorber 5), CuO island formation was observed after 2 h at 300 °C.

As diffusion barrier layers, an electroplated 3-µm-thick nickel or a sputtered aluminium coating on copper substrate prevented copper diffusion effectively. The results clearly indicate that diffusion barriers can be used to prevent copper diffusion in high-temperature solar thermal applications.

The oxidation of the metallic chromium, titanium or titanium-aluminium of the absorber coatings lowered the graded structure i.e. decreased metal content of the absorber coating. This reduced solar absorptance by a shift of the reflectance curve towards shorter wavelengths due to the increase in oxide content inside the absorber coating. However, oxidation of the absorber coating without other chemical or structural changes can be considered a minor ageing mechanism which influences the durability of the absorbers at an acceptable level.

The materials used in the absorber should be stable because possible phase changes may have an influence on optical properties. In this study, the evaporated TiO_xN_y absorber coating and anodized aluminium substrate with a thin Al layer as IR reflector demonstrated chemical and phase changes at 278 °C, and both of these industrial absorbers suffered from reduced durability in the accelerated ageing studies. As a conclusion, coating layers need to be dense and stable to prevent temperature-induced diffusion processes and physical changes.

9 SUGGESTIONS FOR FUTURE WORK

At elevated temperatures, solutions should be prepared to control diffusion and oxidation during the lifetime of the absorber surface. However, it is known that there are ageing mechanisms other than high temperature, i.e. humidity and the microclimate of the collector. In the case of humidity, corrosion mechanisms have been reported in absorber coatings on aluminium substrates. This study is restricted to temperature-dependent ageing alone, and for future applications other ageing mechanisms should also be studied. At high operating temperatures (> 250 °C) solar concentrators are required, and it would be reasonable to use evacuated or noble gas filled collectors to reduce oxidizing and minimize thermal losses. Future work should concentrate on ageing mechanisms at high temperatures in a vacuum because it is not well known how the diffusion process and oxidation behave separately as ageing mechanisms. For high-temperature solar applications, the possible phase changes should be studied at operating temperatures, which may be higher than those studied in this work. Furthermore, phase changes for every absorber should be determined with X-ray diffraction (XRD) suitable for thin films, and adhesion should be measured. For accurate simulation of absorbers and fitting the models to the experimental data, deposited single layers of each absorber coating material on glass would be required. The adjustment of a suitable optical constant model should be possible with single layer optical constants of materials deposited by certain devices and settings. Then, the exact modelling with multilayer or graded absorbers could take into account the interaction or mixing of adjacent layers.

In future studies, W and Mo diffusion barriers should be investigated because they are highly IR reflecting, are assumed to have good high-temperature stability without the formation of binary compounds with Cu and have low self-diffusion coefficients. W or Mo should be studied as IR reflectors on stainless steel absorbers to produce more a selective absorber coating on SS. However, metallic interlayers might oxidize at high temperatures in air, and thus it would be interesting to study nitrides or carbides of W and Mo even though they are not as good IR reflectors as the metals. Concerning the deposition of absorber coatings, other PVD or CVD methods should be investigated. The replacement of electroplated hexavalent black chromium with PVD- or CVD-coating would be suitable for environmental and health reasons. The diffusion barrier properties of amorphous and non-columnar coating structures produced by, for example, vacuum cathodic arc or atomic layer deposition methods might enhance the high-temperature stability of the coatings.

10 REFERENCES

[1] European Solar Thermal Industry Federation (ESTIF): Solar Thermal Markets in Europe - Trends and Market Statistics 2010. Available at: http://www.estif.org. Accessed (2.11.2012).

[2] Lee, K.D. Preparation and characterization of black chrome solar selective coatings, *Journal of the Korean Physical Society* 51 (2007), 135-144.

[3] Zhang, Q.C., Hadavi, M.S., Lee, K.D., Shen, Y.G. Zr-ZrO_2 cermet solar coatings designed by modelling calculations and deposited by dc magnetron sputtering, *Journal of Physics D: Applied Physics* 36 (2003), 723-729.

[4] Moise, V., Cloots, R., Rulmont, A. Study of the electrochemical synthesis of selective black coatings absorbing solar energy, *International Journal of Inorganic Materials* 3 (2001), 1323-1329.

[5] Newby, K.R. Functional chromium plating, *Met Finish* 97 (1999), 223-247.

[6] Zeng, Z., Liang, A., Zhang, J. A review of recent patents on trivalent chromium plating, *Recent Patents on Materials Science* 2 (2009), 50-57.

[7] Abdel Hamid, Z. Electrodeposition of black chromium from environmentally electrolyte based on trivalent chromium salt, *Surface and Coatings Technology* 203 (2009), 3442-3449.

[8] Bayati, M.R., Shariat, M.H., Janghorban, K. Design of chemical composition and optimum working conditions for trivalent black chromium electroplating bath used for solar thermal collectors, *Renewable Energy* 30 (2005), 2163-2178.

[9] Eugénio, S., Rangel, C.M., Vilar, R., Quaresma, S. Electrochemical aspects of black chromium electrodeposition from 1-butyl-3-methylimidazolium tetrafluoroborate ionic liquid, *Electrochim Acta* 56 (2011), 10347-10352.

[10] Kalogirou, S.A. Solar thermal collectors and applications, *Progress in Energy and Combustion Science* 30 (2004), 231-295.

[11] Teixeira, V., Sousa, E., Costa, M.F., Nunes, C., Rosa, L., Carvalho, M.J., Collares-Pereira, M., Roman, E., Gago, J. Spectrally selective composite coatings of Cr–Cr_2O_3 and Mo–Al_2O_3 for solar energy applications, *Thin Solid Films* 392 (2001), 320-326.

[12] Teixeira, V., Sousa, E., Costa, M.F., Nunes, C., Rosa, L., Carvalho, M.J., Collares-Pereira, M., Roman, E., Gago, J. Chromium-based thin sputtered composite coatings for solar thermal collectors, *Vacuum* 64 (2002), 299-305.

[13] Nunes, C., Teixeira, V., Prates, M.L., Barradas, N.P., Sequeira, A.D. Graded selective coatings based on chromium and titanium oxynitride, *Thin Solid Films* 442 (2003), 173-178.

[14] Graf, W., Brucker, F., Köhl, M., Tröscher, T., Wittwer, V., Herlitze, L. Development of large area sputtered solar absorber coatings, *Journal of Non-Crystalline Solids* 218 (1997), 380-387.

[15] Wäckelgård, E., Niklasson, G.A., Granqvist, C.G. Selectively solar-absorbing coatings. In: Gordon, J., editor. Solar Energy - The state of the art. 1st ed., *ISES position papers, James & James, London, UK,* (2001), 109-144.

[16] Koželj, M., Vuk, A.Š., Jerman, I., Orel, B. Corrosion protection of Sunselect, a spectrally selective solar absorber coating, by (3-mercaptopropyl)trimethoxysilane, *Solar Energy Materials and Solar Cells* 93 (2009), 1733-1742.

[17] Juang, R., Yeh, Y., Chang, B., Chen, W., Chung, T. Preparation of solar selective absorbing coatings by magnetron sputtering from a single stainless steel target, *Thin Solid Films* 518 (2010), 5501-5504.

[18] Köhl, M., Heck, M., Brunold, S., Frei, U., Carlsson, B., Möller, K. Advanced procedure for the assessment of the lifetime of solar absorber coatings, *Solar Energy Materials and Solar Cells* 84 (2004), 275-289.

[19] Ecoheatcool Work Package 1, The European heat market - Final report, *Euroheat & Power,* EU Intelligent Energy Europe Programme (2006), 1-73.

[20] European Solar Thermal Technology Platform (ESTTP). Solar heating and cooling for a sustainable energy future in Europe, Revised version, *Sixth framework programme, Brussels, Belgium,* (2009), 1-121.

[21] Carlsson, B. Proposal for ISO standard. Solar energy – Materials for flat plate collectors – Qualification test procedure for solar absorber surface durability. *Updated CD draft,* (1998), 1-32.

[22] Carlsson, B., Frei, U., Köhl, M., Möller, K. Accelerated life testing of solar energy materials - Case study of some selective materials for DHW-systems, *IEA SHCP Task X* (1994), 1-263.

[23] Brunold, S., Frei, U., Carlsson, B., Möller, K., Köhl, M. Accelerated life testing of solar absorber coatings: Testing procedure and results, *Solar Energy* 68 (2000), 313-323.

[24] European Committee for Standardization. Draft BS EN 12975-3-1 Thermal solar systems and components - Solar collectors - Part 3-1: Qualification of solar absorber surface durability, (2011), 1-34.

[25] SpeedColl project: Entwicklung beschleunigter Alterungstestverfahren für solarthermische Kollektoren und deren Komponenten. Available at: http://www.speedcoll.de/. Accessed (13.9.2012).

[26] Barshilia, H.C., Selvakumar, N., Rajam, K.S., Biswas, A. Optical properties and thermal stability of TiAlN/AlON tandem absorber prepared by reactive DC/RF magnetron sputtering, *Solar Energy Materials and Solar Cells,* 92 (2008), 1425-1433.

[27] Lee, Y.K., Latt, K.M., Osipowicz, T., Sher-Yi, C. Study of diffusion barrier properties of ternary alloy ($Ti_xAl_yN_z$) in $Cu/Ti_xAl_yN_z/SiO_2/Si$ thin film structure, *Materials Science in Semiconductor Processing* 3 (2000), 191-194.

[28] Ruesch, F. Absorber coatings: Task X procedure and test results of newly developed coatings. *SMEThermal 2012 Conference 7.2.2012, Berlin, Germany,* (2012).

[29] Duffie, J.A. and Beckman, W.A. editors. Solar engineering of thermal processes, 2nd ed., *John Wiley & Sons, Inc., New York, USA,* (1991), 1-936.

[30] Jayakumar, P. editor. Solar energy - Resource assessment handbook, 1st ed., *APCTT,* (2009), 1-117.

[31] International Organization for Standardization. ISO 9845-1, Solar energy. Reference solar spectral irradiance at the ground at different receiving conditions. Part 1: Direct normal and hemispherical solar irradiance for air mass 1,5, *International Organization for Standardization* (1992), 1-14.

[32] Richtmyer, F.K., Kennard, E.H., Lauritsen, T. editors. Introduction to modern physics, 5th ed., *McGraw-Hill, New York, USA,* (1955), 1-752.

[33] Peuser, F.A., Remmers, K.H., Schnauss, M. editors. Solar thermal systems - Successful planning and construction, 1st ed., *Solarpraxis AG, Berlin, Germany* (2002), 1-377.

[34] Caouris, Y.G. 3.04 - Low Temperature Stationary Collectors. In: Sayigh, A., editor. Comprehensive Renewable Energy. 1st ed., *Elsevier, Oxford, UK*, (2012), 103-147.

[35] Powell, R.W., Ho, C.Y., Liley, P.E. Thermal conductivity of selected materials, *National standard reference data series - National Bureau of standards 8,* 20402 (1966), 1-169.

[36] Peet, M.J., Hasan, H.S., Bhadeshia, H.K.D.H. Prediction of thermal conductivity of steel, *International Journal of Heat and Mass Transfer* 54 (2011), 2602-2608.

[37] Kurzböck, M., Wallner, G.M., Lang, R.W. Black pigmented polypropylene materials for solar absorbers, *Energy Procedia* 30 (2012), 438-445.

[38] Grabmayer, K., Wallner, G.M., Nitsche, D. Black absorber materials based on polypropylene. *IEA-SHC Task 39 Newsletter* 8 (2011), 9-9.

[39] Kahlen, S., Wallner, G.M., Lang, R.W. Aging behavior of polymeric solar absorber materials - Part 1: Engineering plastics, *Solar Energy* 84 (2010), 1567-1576.

[40] Kahlen, S., Wallner, G.M., Lang, R.W. Aging behavior of polymeric solar absorber materials - Part 2: Commodity plastics, *Solar Energy* 84 (2010), 1577-1586.

[41] Resch, K. and Wallner, G.M. Thermotropic layers for flat-plate collectors - A review of various concepts for overheating protection with polymeric materials, *Solar Energy Materials and Solar Cells* 93 (2009), 119-128.

[42] Eaton, C.B. and Blum, H.A. The use of moderate vacuum environments as a means of increasing the collection efficiencies and operating temperatures of flat-plate solar collectors, *Solar Energy* 17 (1975), 151-158.

[43] Benz, N., Beikircher, T., Aghazadeh, B. Aerogel and krypton insulated evacuated flat-plate collector for process heat production, *Solar Energy* 58 (1996), 45-48.

[44] Benz, N. and Beikircher, T. High efficiency evacuated flat-plate solar collector for process steam production, *Solar Energy* 65 (1999), 111-118.

[45] Vestlund, J., Rönnelid, M., Dalenbäck, J. Thermal performance of gas-filled flat plate solar collectors, *Solar Energy* 83 (2009), 896-904.

[46] Vestlund, J., Dalenbäck, J., Rönnelid, M. Thermal and mechanical performance of sealed, gas-filled, flat plate solar collectors, *Solar Energy* 86 (2012), 13-25.

[47] Buderus homepage. Available at: http://www.buderus.com. Accessed (3.1.2013).

[48] SRB Energy homepage. Available at: http://www.srbenergy.com/. Accessed (3.1.2013).

[49] TPV Solar homepage. Available at: http://www.tvpsolar.com/. Accessed (3.1.2013).

[50] Kennedy, C.E. Review of mid- to high-temperature solar selective absorber materials, *National Renewable Energy Laboratory, Colorado, USA* (2002), 1-58.

[51] Hutchins, M.G. Spectrally selective solar absorber coatings, *Applied Energy* 5 (1979), 251-262.

[52] Meinel, A.B. and Meinel, M.P. editors. Applied Solar Energy: An Introduction, *Addison-Wesley*, (1976), 1-651.

[53] Seraphin, B.O. Chemical vapor deposition of thin semiconductor films for solar energy conversion, *Thin Solid Films* 39 (1976), 87-94.

[54] Randich, E. and Allred, D.D. The CVD ZrB_2 as a selective solar absorber. *International conference on Metallurgical Coatings, 6.-10.4.1981, San Francisco, USA,* (1981).

[55] Randich, E. and Allred, D.D. Chemically vapor-deposited ZrB_2 as a selective solar absorber, *Thin Solid Films* 83 (1981), 393-398.

[56] Randich, E. and Pettit, R.B. Solar selective properties and high temperature stability of CVD ZrB_2, *Solar Energy Materials* 5 (1981), 425-435.

[57] Kennedy, C.E. and Price, H. Progress in development of high-temperature solar-selective coating. *Proceedings of the ISEC 2005, International Solar Energy Conference* 6.-12.8.2005*, Orlando, USA,* (2005).

[58] Pettit, G.D., Cuomo, J.J., Distefano, T.H., Woodall, J.M. Solar absorbing surfaces of anodized dendritic tungsten, *IBM Journal of Research and Development* 22 (1978), 372-377.

[59] Sai, H., Yugami, H., Kanamori, Y., Hane, K. Solar selective absorbers based on two-dimensional W surface gratings with submicron periods for high-temperature photothermal conversion, *Solar Energy Materials and Solar Cells* 79 (2003), 35-49.

[60] Harding, G.L. and Lake, M.R. Sputter etched metal solar selective absorbing surfaces for high temperature thermal collectors, *Solar Energy Materials* 5 (1981), 445-464.

[61] Janai, M., Allred, D.D., Booth, D.C., Seraphin, B.O. Optical properties and structure of amorphous silicon films prepared by CVD, *Solar Energy Materials* 1 (1979), 11-27.

[62] Seraphin, B.O. Chemical vapor deposition of spectrally selective surfaces for high temperature photothermal conversion, *Thin Solid Films* 57 (1979), 293-297.

[63] Mattox, D.M. and Kominiak, G.J. Deposition of semiconductor films with high solar absorptivity, *Journal of Vacuum Science and Technology* 12 (1975), 182-185.

[64] Gilbert, L.R., Messier, R., Roy, R. Black germanium solar selective absorber surfaces, *Thin Solid Films* 54 (1978), 149-157.

[65] Goldschmidt, D. Amorphous germanium as a medium temperature solar selective absorber, *Thin Solid Films* 90 (1982), 139-143.

[66] Reddy, G.B., Pandya, D.K., Chopra, K.L. Chemically deposited PbS-antireflection layer selective absorbers, *Solar Energy Materials* 15 (1987), 153-162.

[67] McMahon, T.J. and Jasperson, S.N. PbS-Al selective solar absorbers, *Applied Optics* 13 (1974), 2750-2751.

[68] Bogaerts, W., Van Haute, A., Pacolet, M. Absorber surfaces and durability of solar heat collectors, *Commission of the European communities,* Report number EUR 8353 EN, Luxembourg (1983), 1-70.

[69] Thornton, J.A. and Lamb, J.L. Thermal stability studies of sputter-deposited multilayer selective absorber coatings, *Thin Solid Films* 96 (1982), 175-183.

[70] Selvakumar, N., Barshilia, H.C., Rajam, K.S., Biswas, A. Structure, optical properties and thermal stability of pulsed sputter deposited high temperature HfO_x/Mo/HfO_2 solar selective absorbers, *Solar Energy Materials and Solar Cells* 94 (2010), 1412-1420.

[71] Nunes, C., Teixeira, V., Collares-Pereira, M., Monteiro, A., Roman, E., Martin-Gago, J. Deposition of PVD solar absorber coatings for high-efficiency thermal collectors, *Vacuum* 67 (2002), 623-627.

[72] Schön, J.H., Binder, G., Bucher, E. Performance and stability of some new high-temperature selective absorber systems based on metal/dielectric multilayers, *Solar Energy Materials and Solar Cells* 33 (1994), 403-416.

[73] Nuru, Z.Y., Arendse, C.J., Muller, T.F.G., Maaza, M. Structural and optical properties of Al_xO_y/Pt/Al_xO_y multilayer absorber, *Materials Science and Engineering: B* 177 (2012), 1194-1199.

[74] Barshilia, H.C., Selvakumar, N., Vignesh, G., Rajam, K.S., Biswas, A. Optical properties and thermal stability of pulsed-sputter-deposited Al_xO_y/Al/Al_xO_y multilayer absorber coatings, *Solar Energy Materials and Solar Cells* 93 (2009), 315-323.

[75] Chandra, A. and Mishra, M. Solar absorption behaviour of multilayer stacks, *Energy Conversion and Management* 25 (1985), 387-390.

[76] Barshilia, H.C., Selvakumar, N., Rajam, K.S. Structure and optical properties of pulsed sputter deposited $Cr_xO_y/Cr/Cr_2O_3$ solar selective coatings, *Journal of Applied Physics* 103 (2008), 023507-1-023507-11.

[77] Schmidt, R.N. and Park, K.C. High-temperature space-stable selective solar absorber coatings, *Applied Optics* 8 (1965), 917-925.

[78] Selvakumar, N. and Barshilia, H.C. Review of physical vapor deposited (PVD) spectrally selective coatings for mid- and high-temperature solar thermal applications, *Solar Energy Materials and Solar Cells* 98 (2012), 1-23.

[79] Farooq, M. and Lee, Z.H. Computations of the optical properties of metal/insulator-composites for solar selective absorbers, *Renewable Energy* 28 (2003), 1421-1431.

[80] Adsten, M., Joerger, R., Järrendahl, K., Wäckelgård, E. Optical characterization of industrially sputtered nickel–nickel oxide solar selective surface, *Solar Energy* 68 (2000), 325-328.

[81] Buhrman, R.A. Physics of solar selective surfaces. In: Böer, K.W., editor. Advances in Solar Energy, *American Solar Energy Society, New York, USA* (1986), 207-282.

[82] Trotter Jr., D.M. and Sievers, A.J. Spectral selectivity of high-temperature solar absorbers, *Applied Optics* 19 (1980), 711-728.

[83] Refractive Index Database. Available at: http://refractiveindex.info. Accessed (16.4.2013).

[84] Julkarnain, M., Hossain, J., Sharif, K.S., Khan, K.A. Optical properties of thermally evaporated Cr_2O_3 thin films, *Canadian Journal on Chemical Engineering & Technology* 3 (2012), 81-85.

[85] Zajac, G., Smith, G.B., Ignatiev, A. Refinement of solar absorbing black chrome microstructure and its relationship to optical degradation mechanisms, *Journal of Applied Physics* 51 (1980), 5544-5554.

[86] Granqvist, C.G. Coatings of ultrafine chromium particles: efficient selective absorbers of solar energy, *Physica Skripta* 16 (1977), 163-164.

[87] Smith, G.B., McPhedran, R.C., Derrick, G.H. Surface structure and the optical properties of black chrome, *Applied Physics A* 36 (1985), 193-204.

[88] Lee, K.D., Jung, W.C., Kim, J.H. Thermal degradation of black chrome coatings, *Solar Energy Materials and Solar Cells* 63 (2000), 125-137.

[89] Batec Solar A/S homepage. Available at: http://www.batec.dk/. Accessed (29.10.2012).

[90] Jafari, S. and Rozati, S.M. Characterization of black chrome films prepared by electroplating technique., *World Renewable Energy Congress* 8.-13.5.2011*, Linköping, Sweden,* (2011).

[91] Materials Technology, Inc. homepage. Available at: http://www.mtisolar.com/. Accessed (29.10.2012).

[92] Energie Solaire SA homepage. Available at: http://www.energie-solaire.com/. Accessed (29.10.2012).

[93] Bacon, D. and Ignatiev, A. The role of the substrate in the optical degradation of solar absorbing black chrome, *Solar Energy Materials* 9 (1983), 3-19.

[94] Baral, A. and Engelken, R. Modeling, Optimization, and comparative analysis of trivalent chromium electrodeposition from aqueous glycine and formic acid baths, *Journal of the electrochemical society* 152 (2005), C504-C512.

[95] Oelhafen, P. and Schüler, A. Nanostructured materials for solar energy conversion, *Solar Energy* 79 (2005), 110-121.

[96] Muehlratzer, A., Goerler, G.P., Erben, E., Zeilinger, H. Selection of a black chrome bath for continuous tube-plating and the properties of the coatings deposited from it, *Solar Energy* 27 (1981), 115-120.

[97] Smith, G.B. and Ignatiev, A. Black chromium-molybdenum: A new stable solar absorber, *Solar Energy Materials* 4 (1981), 119-133.

[98] Wu, L., Gao, J., Liu, Z., Liang, L., Xia, F., Cao, H. Thermal aging characteristics of CrN_xO_y solar selective absorber coating for flat plate solar thermal collector applications, *Solar Energy Materials and Solar Cells* 114 (2013), 186-191.

[99] Lazarov, M., Raths, P., Metzger, H., Spirkl, W. Optical constants and film density of TiN_xO_y solar selective absorbers, *Journal of Applied Physics* 77 (1995), 2133-2137.

[100] Lazarov, M.P., Sizmann, R., Frei, U. Optimization of SiO_2-TiN_xO_y-Cu interference absorbers: numerical and experimental results, *Proceedings of the Society of Photo-Optical Instrumentation Engineers* 2017 (1993), 345-356.

[101] Schellinger, H., Lazarov, M., Kiank, H., Sizmann, R. Thermal and chemical metallic - dielectric transitions of TiN_xO_y Cu absorber tandems, *SPIE, Optical Materials Technology for Energy Efficiency and Solar Energy Conversion XII* 2017 (1993), 366-376.

[102] Assmann, W., Reichelt, T., Eisenhammerb, T., Huber, H., Mahr, A., Schellingerb, H., Wohlgemuth, R. ERDA of solar selective absorbers, *Nuclear Instruments and Methods in Physics Research B* 113 (1996), 303-307.

[103] Metson, J.B. and Prince, K.E. SIMS depth profiling of TiO_xN_y films, *Surface and Interface Analysis* 28 (1999), 159-162.

[104] Sievers, A.J. Thermal radiation from metal surfaces, *The Journal of the Optical Society of America* 68 (1978), 1505-1516.

[105] Smalley, R. and Sievers, A.J. The total hemispherical emissivity of copper, *The Journal of the Optical Society of America* 68 (1978), 1516-1518.

[106] Cverna, F. editor. Thermal properties of metals, 1st ed., *ASM International, Ohio, USA*, (2002), 1-560.

[107] Ramanathan, K.G. and Yen, S.H. High-temperature emissivities of copper, aluminum, and silver, *The Journal of the Optical Society of America* 67 (1977), 32-38.

[108] Wijewardane, S. and Goswami, D.Y. A review on surface control of thermal radiation by paints and coatings for new energy applications, *Renewable and Sustainable Energy Reviews* 16 (2012), 1863-1873.

[109] Palik, E.D. editor. Handbook of optical constants of solids I, 1st ed., *Academic Press, Orlando*, (1985).

[110] Palik, E.D. editor. Handbook of optical constants of solids II, 1st ed., *Academic Press, Orlando, Florida, USA*, (1991).

[111] Sala, A. editor. Radiant properties of materials: tables of radiant values for black body and real materials, 1st ed., *Elsevier, New York, USA* (1986), 1-479.

[112] Farooq, M., Green, A.A., Hutchins, M.G. High performance sputtered Ni : SiO_2 composite solar absorber surfaces, *Solar Energy Materials and Solar Cells* 54 (1998), 67-73.

[113] Antonaia, A., Castaldo, A., Addonizio, M.L., Esposito, S. Stability of W-Al_2O_3 cermet based solar coating for receiver tube operating at high temperature, *Solar Energy Materials and Solar Cells* 94 (2010), 1604-1611.

[114] Antonaia A., Esposito S., inventors. Method for producing a cermet-based spectrally selective coating and material thus obtained. ENEA (Italy's National Agency for New Technologies, Energy, and the Environment), assignee. International patent WO 2009/107157 A2., (2009)

[115] Archimede Solar Energy Homepage. Available at: http://www.archimedesolarenergy.com/. Accessed (7.12.2012).

[116] Siemens homepage. Available at: http://www.energy.siemens.com. Accessed (5.1.2013).

[117] Barshilia, H.C., Selvakumar, N., Rajam, K.S., Biswas, A. Spectrally selective NbAlN/NbAlON/Si_3N_4 tandem absorber for high-temperature solar applications, *Solar Energy Materials and Solar Cells* 92 (2008), 495-504.

[118] Yin, Y., Pan, Y., Hang, L.X., McKenzie, D.R., Bilek, M.M.M. Direct current reactive sputtering Cr–Cr_2O_3 cermet solar selective surfaces for solar hot water applications, *Thin Solid Films* 517 (2009), 1601-1606.

[119] Inal, O.T., Mabon, J.C., Robino, C.V. Thermal degradation of solar collector surfaces, *Thin Solid Films* 83 (1981), 399-414.

[120] Fan, J.C.C. Selective black absorbers using rf-sputtered Cr_2O_3/Cr cermet films, *Applied Physics Letters* 30 (1977), 511-513.

[121] McKenzie, D.R. Gold, silver, chromium, and copper cermet selective surfaces for evacuated solar collectors, *Applied Physics Letters* 34 (1979), 25-28.

[122] Selvakumar, N., Santhoshkumar, S., Basu, S., Biswas, A., Barshilia, H.C. Spectrally selective CrMoN/CrON tandem absorber for mid-temperature solar thermal applications, *Solar Energy Materials and Solar Cells* 109 (2013), 97-103.

[123] Bittar, A., Cochrane, D., Caughley, S., Vickeridge, I. Study of TiO_xN_y thin film selective surfaces produced by ion assisted deposition, *Journal of Vacuum Science and Technology A: Vacuum, Surfaces and Films* 15 (1997), 223-229.

[124] Blickensderfer, R., Deardorff, D.K., Lincoln, R.L. Spectral reflectance of TiN_x and ZrN_x films as selective solar absorbers, *Solar Energy* 19 (1977), 429-432.

[125] Mammadov, F. Study of selective surface of solar heat receiver, *International Journal of Energy Engineering* 2 (2012), 138-144.

[126] Barshilia, H.C., Selvakumar, N., Rajam, K.S., Sridhara Rao, D.W., Muraleedharan, K., Biswas, A. TiAlN/TiAlON/Si_3N_4 tandem absorber for high temperature solar selective applications, *Applied Physics Letters* 89 (2006), 191909-1-191909-3.

[127] Barshilia, H.C., Selvakumar, N., Rajam, K.S. Thermal stability of TiAlN/TiAlON/Si_3N_4 tandem absorbers prepared by reactive direct current magnetron sputtering, *Journal of Vacuum Science & Technology A: Vacuum, Surfaces, and Films* 25 (2007), 383-390.

[128] Barshilia, H.C., Selvakumar, N., Rajam, K.S., Sridhara Rao, D.V., Muraleedharan, K. Deposition and characterization of TiAlN/TiAlON/Si_3N_4 tandem absorbers prepared using reactive direct current magnetron sputtering, *Thin Solid Films* 516 (2008), 6071-6078.

[129] Selvakumar, N., Barshilia, H.C., Rajam, K.S., Biswas, A. Spectrally selective TiAlN/CrAlON/Si_3N_4 tandem absorber for high temperature solar applications. In: Vijay, V.K.and Garg, H.P., editors. Renewable Energy Environment for Sustainable Development. 1st ed., *Narosa Publishing House, India* (2008), 469-477.

[130] Hao, L., Wang, S.M., Jiang, L., Liu, X., Li, H., Li, Z. Preparation and thermal stability on non-vacuum high temperature solar selective absorbing coatings, *Chinese Science Bulletin* 54 (2009), 1451-1454.

[131] Hao, L., Du, M., Liu, X., Wang, S., Jiang, L., Lü, F., Li, Z., Mi, J. Thermal stability of nitride solar selective absorbing coatings used in high temperature parabolic trough current, *Science China Technological Sciences* 53 (2010), 1507-1512.

[132] Rebouta, L., Capela, P., Andritschky, M., Matilainen, A., Santilli, P., Pischow, K., Alves, E. Characterization of TiAlSiN/TiAlSiON/SiO_2 optical stack designed by modelling calculations for solar selective applications, *Solar Energy Materials and Solar Cells* 105 (2012), 202-207.

[133] Andritschky M., Rebouta L., Pischow K., inventors. Method for providing a thermal absorber. International patent, (2011).

[134] Savo-Solar Oy homepage. Available at: http://www.savosolar.fi/. Accessed (29.11.2012).

[135] Zhao, S. and Wäckelgård, E. The optical properties of sputtered composite of Al-AlN, *Solar Energy Materials and Solar Cells* 90 (2006), 1861-1874.

[136] Yue, S., Yueyan, S., Fengchun, W. High-temperature optical properties and stability of Al_xO_y-AlN_x-Al solar selective absorbing surface prepared by DC magnetron reactive sputtering, *Solar Energy Materials and Solar Cells* 77 (2003), 393-403.

[137] Zhang, Q.C. Stainless-steel-AlN cermet selective surfaces deposited by direct current magnetron sputtering technology, *Solar Energy Materials and Solar Cells* 52 (1998), 95-106.

[138] Eisenhammer, T., Haugeneder, A., Mahr, A. High-temperature optical properties and stability of selective absorbers based on quasicrystalline AlCuFe, *Solar Energy Materials and Solar Cells,* 54 (1998), 379-386.

[139] Wäckelgård, E. and Hultmark, G. Industrially sputtered solar absorber surface, *Solar Energy Materials and Solar Cells* 54 (1998), 165-170.

[140] Craighead, H.G. and Buhrman, R.A. Optical properties of selectively absorbing Ni/Al_2O_3 composite films, *Applied Physics Letters* 31 (1977), 423-425.

[141] Craighead, H.G., Bartynski, R., Buhrman, R.A., Wojcik, L., Sievers, A.J. Metal/insulator composite selective absorbers, *Solar Energy Materials* 1 (1979), 105-124.

[142] Zhang, Q. and Shen, Y.G. High performance W-AlN cermet solar coatings designed by modelling calculations and deposited by DC magnetron sputtering, *Solar Energy Materials and Solar Cells* 81 (2004), 25-37.

[143] Wang, J., Wei, B., Wei, Q., Li, D. Optical property and thermal stability of Mo/Mo-SiO_2/SiO_2 solar-selective coating prepared by magnetron sputtering, *Physica Status Solidi A* 208 (2011), 664-667.

[144] Esposito, S., Antonaia, A., Addonizio, M.L., Aprea, S. Fabrication and optimisation of highly efficient cermet-based spectrally selective coatings for high operating temperature, *Thin Solid Films* 517 (2009), 6000-6006.

[145] Xinkang, D., Cong, W., Tianmin, W., Long, Z., Buliang, C., Ning, R. Microstructure and spectral selectivity of Mo–Al_2O_3 solar selective absorbing coatings after annealing, *Thin Solid Films* 516 (2008), 3971-3977.

[146] Lanxner, M. and Elgat, Z. Solar selective absorber coating for high service temperatures, produced by plasma sputtering, *SPIE, Optical Materials Technology for Energy Efficiency and Solar Energy Conversion IX* 1272 (1990), 240-249.

[147] Selvakumar, N., Manikandanath, N.T., Biswas, A., Barshilia, H.C. Design and fabrication of highly thermally stable HfMoN/HfON/Al_2O_3 tandem absorber for solar thermal power generation applications, *Solar Energy Materials and Solar Cells* 102 (2012), 86-92.

[148] Lazarov M.P., Mayer I.V., inventors. Material consisting of chemical compounds, comprizing a metal from group IV A of the periodic system, nitrogen and oxygen, and processes for its preparation. U.S. patent 5,670,248. (1997)

[149] Lazarov M.P., Mayer I.V., inventors. Method for depositing thin layers of a material consisting of chemical compounds comprising a metal from group IV of the periodic system, nitrogen and oxygen onto heatable substrates. U.S. patent 5,776,556. (1998)

[150] Fan, J.C.C. Selective black absorbers using MgO/Au cermet films, *Applied Physics Letters* 29 (1976), 478-480.

[151] Thornton, J.A. and Lamb, J.L. Sputter-deposited Pt-Al_2O_3 selective absorber coatings, *Thin Solid Films* 83 (1981), 377-385.

[152] Liu, Y., Wang, C., Xue, Y. The spectral properties and thermal stability of NbTiON solar selective absorbing coating, *Solar Energy Materials and Solar Cells* 96 (2012), 131-136.

[153] Garnich, F. and Sailer, E. Cu-SiO_2/Cu-cermet selective absorbers for solar photothermal conversion, *Solar Energy Materials* 20 (1990), 81-89.

[154] Harding, G.L. A sputtered copper-carbon selective absorbing surface for evacuated collectors, *Solar Energy Materials* 7 (1982), 123-128.

[155] Harding, G.L. and Window, B. Graded metal carbide solar selective surfaces coated onto glass tubes by a magnetron sputtering system, *Journal of Vacuum Science and Technology* 16 (1979), 2101-2104.

[156] McKenzie, D.R. Effect of substrate on graphite and other solar selective surfaces, *Applied Optics* 17 (1978), 1884-1888.

[157] Schüler, A., Videnovic, I.R., Oelhafen, P., Brunold, S. Titanium-containing amorphous hydrogenated silicon carbon films (a-Si:C:H/Ti) for durable solar absorber coatings, *Solar Energy Materials and Solar Cells* 69 (2001), 271-284.

[158] Kennedy C.E., inventor. High temperature solar selective coatings. Renewable Energy Laboratory (NREL), a Division of the Midwest Research Institute, assignee. US patent WO/2009/051595 A1. (2009).

[159] Biswas, A., Bhattacharyya, D., Barshilia, H.C., Selvakumar, N., Rajam, K.S. Spectroscopic ellipsometric characterization of TiAlN/TiAlON/Si_3N_4 tandem absorber for solar selective applications, *Applied Surface Science* 254 (2008), 1694-1699.

[160] Ramberg, C.E., Blanquet, E., Pons, M., Bernard, C., Madar, R. Application of equilibrium thermodynamics to the development of diffusion barriers for copper metallization (invited), *Microelectronic Engineering* 50 (2000), 357-368.

[161] Holubář, P., Jílek, M., Šíma, M. Nanocomposite nc-TiAlSiN and nc-TiN-BN coatings: their applications on substrates made of cemented carbide and results of cutting tests, *Surface and Coatings Technology* 120–121 (1999), 184-188.

[162] Rebouta, L., Pitães, A., Andritschky, M., Capela, P., Cerqueira, M.F., Matilainen, A., Pischow, K. Optical characterization of TiAlN/TiAlON/SiO_2 absorber for solar selective applications, *Surface and Coatings Technology* 211 (2012), 41-44.

[163] Yoo, Y.H., Le, D.P., Kim, J.G., Kim, S.K., Vinh, P.V. Corrosion behavior of TiN, TiAlN, TiAlSiN thin films deposited on tool steel in the 3.5 wt.% NaCl solution, *Thin Solid Films* 516 (2008), 3544-3548.

[164] Man, B.Y., Guzman, L., Miotello, A., Adami, M. Microstructure, oxidation and H_2-permeation resistance of TiAlN films deposited by DC magnetron sputtering technique, *Surface and Coatings Technology* 180–181 (2004), 9-14.

[165] Zhu, D. and Zhao, S. Chromaticity and optical properties of colored and black solar-thermal absorbing coatings, *Solar Energy Materials and Solar Cells* 94 (2010), 1630-1635.

[166] Zhu, D., Mao, F., Zhao, S. The influence of oxygen in $TiAlO_xN_y$ on the optical properties of colored solar-absorbing coatings, *Solar Energy Materials and Solar Cells* 98 (2012), 179-184.

[167] Yin, Y., Hang, L., Zhang, S., Bui, X.L. Thermal oxidation properties of titanium nitride and titanium-aluminum nitride materials - A perspective for high temperature air-stable solar selective absorber applications, *Thin Solid Films* 515 (2007), 2829-2832.

[168] Vennemann, A., Stock, H.-R., Kohlscheen, J., Rambadt, S., Erkens, G. Oxidation resistance of titanium-aluminium-silicon nitride coatings, *Surface and Coatings Technology* 174–175 (2003), 408-415.

[169] Chen, J.K., Chang, C.L., Shieh, Y.N., Tsai, K.J., Tsai, B.H. Structures and properties of (TiAlSi)N films, *Procedia Engineering* 36 (2012), 335-340.

[170] Barshilia, H.C., Ghosh, M., Shashidhara, Ramakrishna, R., Rajam, K.S. Deposition and characterization of TiAlSiN nanocomposite coatings prepared by reactive pulsed direct current unbalanced magnetron sputtering, *Applied Surface Science* 256 (2010), 6420-6426.

[171] Zhu, L., Hu, M., Ni, W., Liu, Y. High temperature oxidation behavior of $Ti_{0.5}Al_{0.5}N$ coating and $Ti_{0.5}Al_{0.4}Si_{0.1}N$ coating, *Vacuum* 86 (2012), 1795-1799.

[172] Caron, R.N. and Staley, J.T. Effects of composition, processing, and structure on properties of nonferrous alloys, *Materials Selection and Design, ASM Handbook* 20 (1997), 383-415.

[173] Weber, E.R. Transition metals in silicon, *Applied Physics A* 30 (1983), 1-22.

[174] Holloway, K., Fryer, P.M., Cabral, C., Jr., Harper, J.M.E., Bailey, P.J., Kelleher, K.H. Tantalum as a diffusion barrier between copper and silicon: Failure mechanism and effect of nitrogen additions, *Journal of Applied Physics* 71 (1992), 5433-5444.

[175] Tan, C.M. and Roy, A. Electromigration in ULSI interconnects, *Materials Science and Engineering: R: Reports* 58 (2007), 1-75.

[176] Istratov, A.A. and Weber, E.R. Electrical properties and recombination activity of copper, nickel and cobalt in silicon, *Applied Physics A: Materials Science & Processing* 66 (1998), 123-136.

[177] Bryner, J., Profunser, D.M., Vollmann, J., Mueller, E., Dual, J. Characterization of Ta and TaN diffusion barriers beneath Cu layers using picosecond ultrasonics, *Ultrasonics,* 44 (2006), e1269-e1275.

[178] Gill, W.N. and Plawsky, J.L. Design of diffusion barriers, *Thin Solid Films* 515 (2007), 4794-4800.

[179] Chang, C.A. Formation of copper silicides from Cu(100)/Si(100) and Cu(111)/Si(111) structures, *Journal of Applied Physics* 67 (1990), 566-569.

[180] Holloway, K. and Fryer, P.M. Tantalum as a diffusion barrier between copper and silicon, *Applied Physics Letters* 57 (1990), 1736-1738.

[181] Moshfegh, A.Z. and Akhavan, O. Bias sputtered Ta modified diffusion barrier in Cu/Ta(V_b)/Si(111) structures, *Thin Solid Films* 370 (2000), 10-17.

[182] Laurila, T., Zeng, K., Kivilahti, J.K. Failure mechanism of Ta diffusion barrier between Cu and Si, *Journal of Applied Physics* 88 (2000), 3377-3384.

[183] Lane, L.C., Nason, T.C., Yang, G.-R., Lu, T.-M., Bakhru, H. Secondary ion mass spectrometry study of the thermal stability of Cu/refractory metal/Si structures, *Journal of Applied Physics* 69 (1991), 6719-6721.

[184] Gardner, D.S., Onuki, J., Kudoo, K., Misawa, Y., Vu, Q.T. Encapsulated copper interconnection devices using sidewall barriers, *Thin Solid Films* 262 (1995), 104-119.

[185] Chuang, J., Tu, S., Chen, M. Sputter-deposited Mo and reactively sputter-deposited Mo-N films as barrier layers against Cu diffusion, *Thin Solid Films* 346 (1999), 299-306.

[186] Song, S., Liu, Y., Mao, D., Ling, H., Li, M. Diffusion barrier performances of thin Mo, Mo-N and Mo/Mo-N films between Cu and Si, *Thin Solid Films* 476 (2005), 142-147.

[187] He, Y. and Feng, J.Y. Diffusion barrier performances of direct current sputter-deposited Mo and MoxN films between Cu and Si, *Journal of Crystal Growth,* 263 (2004), 203-207.

[188] Couach, M., Khoder, A.F., Monnier, F., Sergent, M., Chevrel, R., Le Lay, L., Dubots, P. Investigation of the structure of the Nb barrier of chevrel phase composite, *Physica C: Superconductivity* 153–155, Part 1 (1988), 463-464.

[189] Xie, Q., Jiang, Y., De Keyser, K., Detavernier, C., Deduytsche, D., Ru, G., Qu, X., Tu, K.N. The effect of sputtered W-based carbide diffusion barriers on the thermal stability and void formation in copper thin films, *Microelectronic Engineering* 87 (2010), 2535-2539.

[190] Lee, C., Liu, D., Deng, R. Diffusion barrier of sputtered W film for Cu Schottky contacts on InGaP layer, *Thin Solid Films* 468 (2004), 216-221.

[191] Uekubo, M., Oku, T., Nii, K., Murakami, M., Takahiro, K., Yamaguchi, S., Nakano, T., Ohta, T. WN_x diffusion barriers between Si and Cu, *Thin Solid Films* 286 (1996), 170-175.

[192] Ezer, Y., Härkönen, J., Sokolov, V., Saarilahti, J., Kaitila, J., Kuivalainen, P. Diffusion barrier performance of thin Cr films in the Cu/Cr/Si structure, *Materials Research Bulletin* 33 (1998), 1331-1337.

[193] So, W.W., Choe, S., Chuang, R., Lee, C.C. An effective diffusion barrier metallization process on copper, *Thin Solid Films* 376 (2000), 164-169.

[194] Len, V.S.C., Hurley, R.E., McCusker, N., McNeill, D.W., Armstrong, B.M., Gamble, H.S. An investigation into the performance of diffusion barrier materials against copper diffusion using metal-oxide-semiconductor (MOS) capacitor structures, *Solid-State Electronics* 43 (1999), 1045-1049.

[195] Chen, K., Yu, Y., Mu, H., Luo, E.Z., Sundaravel, B., Wong, S.P., Wilson, I.H. Preferentially oriented and amorphous Ti, TiN and Ti/TiN diffusion barrier for Cu prepared by ion beam assisted deposition (IBAD), *Surface and Coatings Technology* 151–152 (2002), 434-439.

[196] Braud, F., Torres, J., Palleau, J., Mermet, J.L., Mouche, M.J. Ti-diffusion barrier in Cu-based metallization, *Applied Surface Science,* 91 (1995), 251-256.

[197] Henderson, L.B. and Ekerdt, J.G. Time-to-failure analysis of 5 nm amorphous Ru(P) as a copper diffusion barrier, *Thin Solid Films* 517 (2009), 1645-1649.

[198] He, G., Yao, L., Song, Z., Li, Y., Xu, K. Diffusion barrier performance of nano-structured and amorphous Ru–Ge diffusion barriers for copper metallization, *Vacuum* 86 (2012), 965-969.

[199] Chang, C.A. and Hu, C.K. Reaction between Cu and $TiSi_2$ across different barrier layers, *Applied Physics Letters* 57 (1990), 617-619.

[200] Li, J., Strane, J.W., Russell, S.W., Hong, S.Q., Mayer, J.W. Observation and prediction of first phase formation in binary Cu-metal thin films, *Journal of Applied Physics* 72 (1992), 2810-2816.

[201] Apblett, C., Muira, D., Sullivan, M., Ficalora, P.J. Reaction of Cu-Ti bilayer films in vacuum and hydrogen, *Journal of Applied Physics* 71 (1992), 4925-4932.

[202] Ono, H., Nakano, T., Ohta, T. Diffusion barrier effects of transition metals for Cu/M/Si multilayers (M=Cr, Ti, Nb, Mo, Ta, W), *Applied Physics Letters* 64 (1994), 1511.

[203] Auciello, O., Chevacharoenkul, S., Ameen, M.S., Duarte, J. Controlled ion beam sputter deposition of W/Cu/W layered films for microelectronic applications, *Journal of Vacuum Science & Technology A: Vacuum, Surfaces, and Films* 9 (1991), 625-631.

[204] Lin, S. and Lee, C. Characteristics of sputtered Ta–B–N thin films as diffusion barriers between copper and silicon, *Applied Surface Science,* 253 (2006), 1215-1221.

[205] Ikeda, S., Palleau, J., Torres, J., Chenevier, B., Bourhila, N., Madar, R. TEM studies of the microstructure evolution in plasma treated CVD TiN thin films used as diffusion barriers, *Solid-State Electronics* 43 (1999), 1063-1068.

[206] Wang, Y., Zhao, C., Cao, F., Shao, L. Effect of substrate temperature on the thermal stability of Cu/Zr-N/Si contact system, *Materials Letters* 62 (2008), 418-421.

[207] Kim, D.J., Kim, Y.T., Park, J.W. Nanostructured Ta-Si-N diffusion barriers for Cu metallization, *Journal of Applied Physics* 82 (1997), 4847-4851.

[208] Yan, H., Tay, Y.Y., Jiang, Y., Yantara, N., Pan, J., Liang, M.H., Chen, Z. Copper diffusion barrier performance of amorphous Ta-Ni thin films, *Applied Surface Science* 258 (2012), 3158-3162.

[209] Chen, C. and Liu, C. Diffusion barrier properties of amorphous ZrCN films for copper metallization, *Journal of Non-Crystalline Solids* 351 (2005), 3725-3729.

[210] Stavrev, M., Fischer, D., Preuß, A., Wenzel, C., Mattern, N. Study of nanocrystalline Ta(N,O) diffusion barriers for use in Cu metallization, *Microelectronic Engineering* 33 (1997), 269-275.

[211] Kattelus, H.P. and Nicolet, M.A. Diffusion barriers in semiconductor contact metallization. In: Gupta, D. and Ho, P.S., editors. Diffusion phenomena in thin films and microelectronic materials. 1st ed., *Noyes Publications, New Jersey, USA* (1988), 432-498.

[212] Kwak, M.Y., Shin, D.H., Kang, T.W., Kim, K.N. Characteristics of TiN barrier layer against Cu diffusion, *Thin Solid Films* 339 (1999), 290-293.

[213] Yang, W.L., Wu, W., Liu, D., Wu, C., Ou, K.L. Barrier capability of TaN_x films deposited by different nitrogen flow rate against Cu diffusion in $Cu/TaN_x/n^+$–p junction diodes, *Solid-State Electronics* 45 (2001), 149-158.

[214] Kuo, Y., Huang, J., Lin, S., Lee, C., Lee, W. Diffusion barrier properties of sputtered TaN_x between Cu and Si using TaN as the target, *Materials Chemistry and Physic* 80 (2003), 690-695.

[215] Laurila, T., Zeng, K., Kivilahti, J.K., Molarius, J., Riekkinen, T., Suni, I. Tantalum carbide and nitride diffusion barriers for Cu metallisation, *Microelectronic Engineering* 60 (2002), 71-80.

[216] Laurila, T., Zeng, K., Kivilahti, J.K., Molarius, J., Suni, I. TaC as a diffusion barrier between Si and Cu, *Journal of Applied Physics* 91 (2002), 5391-5399.

[217] Suh, B., Lee, Y., Hwang, J., Park, C. Properties of reactively sputtered WN_x as Cu diffusion barrier, *Thin Solid Films* 348 (1999), 299-303.

[218] Ecke, R., Schulz, S.E., Hecker, M., Gessner, T. Development of PECVD WN_x ultrathin film as barrier layer for copper metallization, *Microelectronic Engineering* 64 (2002), 261-268.

[219] Sun, Y.-M., Lee, S.Y., Lemonds, A.M., Engbrecht, E.R., Veldman, S., Lozano, J., White, J.M., Ekerdt, J.G., Emesh, I., Pfeifer, K. Low temperature chemical vapor deposition of tungsten carbide for copper diffusion barriers, *Thin Solid Films* 397 (2001), 109-115.

[220] Qingxiang, W., Shuhua, L., Xianhui, W., Zhikang, F. Diffusion barrier performance of amorphous W-Ti-N films in Cu metallization, *Vacuum* 84 (2010), 1270-1274.

[221] Chen, C. and Liu, C. Characterization of sputtered nano-crystalline zirconium carbide as a diffusion barrier for Cu metallization, *Journal of Electronic Materials* 34 (2005), 1408-1413.

[222] Alén, P., Ritala, M., Arstila, K., Keinonen, J., Leskelä, M. The growth and diffusion barrier properties of atomic layer deposited NbN_x thin films, *Thin Solid Films* 491 (2005), 235-241.

[223] Zhou, J., Chen, H., Li, Y. Diffusion barrier performance of nanoscale TaN_x thin-film, *Transactions of Nonferrous Metals Society of China* 17 (2007), 733-738.

[224] Chung, H.-C. and Liu, C.-P. Effect of crystallinity and preferred orientation of Ta_2N films on diffusion barrier properties for copper metallization, *Surface and Coatings Technology* 200 (2006), 3122-3126.

[225] Kirkendall, E., Thomassen, L., Uethegrove, C. Rates of diffusion of copper and zinc in alpha brass, *Transactions of the American Institute of Mining and Metallurgical Engineers* 133 (1939), 186-203.

[226] Mattox, D.M. 9 - Atomistic film growth and some growth-related film properties. In: Mattox, D.M., editor. Handbook of Physical Vapor Deposition (PVD) Processing. 2nd ed., *William Andrew Publishing, Westwood, New Jersey, USA,* (1998), 472-568.

[227] Feinstein, L.G. and Bindell, J.B. The failure of aged Cu-Au thin films by Kirkendall porosity, *Thin Solid Films* 62 (1979), 37-47.

[228] Li, D., Liu, C., Conway, P.P. Characteristics of intermetallics and micromechanical properties during thermal ageing of Sn-Ag-Cu flip-chip solder interconnects, *Materials Science and Engineering: A* 391 (2005), 95-103.

[229] Chopra, R., Ohring, M., Oswald, R.S. Observation of a marker shift in a Cu-Sn thin film diffusion couple by Auger electron spectroscopy methods, *Thin Solid Films* 86 (1981), 43-47.

[230] Zeng, K., Stierman, R., Chiu, T.C., Edwards, D., Ano, K., Tu, K.N. Kirkendall void formation in eutectic SnPb solder joints on bare Cu and its effect on joint reliability, *Journal of Applied Physics* 97 (2005), 024508-1-024508-8.

[231] Philofsky, E. Intermetallic formation in gold-aluminum systems, *Solid-State Electronics* 13 (1970), 1391-1394.

[232] Tang, W., He, A., Liu, Q., Ivey, D.G. Room temperature interfacial reactions in electrodeposited Au/Sn couples, *Acta Materialia* 56 (2008), 5818-5827.

[233] Sheen, M.T., Chang, C.M., Teng, H.C., Kuang, J.H., Hsieh, K.C., Cheng, W.H. The influence of thermal aging on joint strength and fracture surface of Pb/Sn and Au/Sn solders in laser diode packages, *Journal of Electronic Materials* 31 (2002), 895-902.

[234] Paul, A., van Dal, M.J.H., Kodentsov, A.A., van Loo, F.J.J. The Kirkendall effect in multiphase diffusion, *Acta Materialia* 52 (2004), 623-630.

[235] Weinberg, K., Böhme, T., Müller, W.H. Kirkendall voids in the intermetallic layers of solder joints in MEMS, *Computational Materials Science* 45 (2009), 827-831.

[236] Murali, S., Srikanth, N., Vath III, C.J. Effect of wire size on the formation of intermetallics and Kirkendall voids on thermal aging of thermosonic wire bonds, *Materials Letters* 58 (2004), 3096-3101.

[237] Ji, H., Li, M., Wang, C., Bang, H.S., Bang, H.S. Comparison of interface evolution of ultrasonic aluminum and gold wire wedge bonds during thermal aging, *Materials Science and Engineering: A* 447 (2007), 111-118.

[238] Wang, S.H., Matlock, D.K., Olson, D.L. An analysis of the critical conditions for diffusion-induced void formation in Ni-Cu laminate composites, *Materials Science and Engineering A* 167 (1993), 139-145.

[239] Choi, I.D., Matlock, D.K., Olson, D.L. An analysis of diffusion-induced porosity in Cu-Ni laminate composites, *Materials Science and Engineering: A* 124 (1990), L15-L18.

[240] Andersson, A., Ekström, H.E., Grönhaug, S., Gullman, L.O., Söderberg, L., Karsson, Å., Knutsson, L., Lindstrand, E., Reuterdahl, H. editors. MNC handbook nr 12 - Aluminium konstructions- och materiallära, 1st ed., *MNC Metallnormcentralen and SIS Standardiseringskommissionen i Sverige, Stockholm, Sweden*, (1983).

[241] Greenpeace International. Concentrating solar power: global outlook 09, *Greenpeace International, Solar PACES and ESTELA,* 3rd joint report (2009), 1-88.

[242] Poinern, G.E.J., Ali, N., Fawcett, D. Progress in nano-engineered anodic aluminum oxide membrane development, *Materials* 4 (2011), 487-526.

[243] Lugscheider, E., Krämer, G., Barimani, C., Zimmermann, H. PVD coatings on aluminium substrates, *Surface and Coatings Technology* 74-75 (1995), 497-502.

[244] W. Theiss Hard- and Software homepage. Available at: http://www.mtheiss.com/. Accessed (25.4.2013).

[245] Musil, J., Baroch, P., Vlček, J., Nam, K.H., Han, J.G. Reactive magnetron sputtering of thin films: present status and trends, *Thin Solid Films* 475 (2005), 208-218.

[246] Carlsson, B., Möller, K., Köhl, M., Frei, U., Brunold, S. Qualification test procedure for solar absorber surface durability, *Solar Energy Materials and Solar Cells* 61 (2000), 255-275.

[247] Brunold, S., Frei, U., Carlsson, B., Möller, K., Köhl, M. Round robin on accelerated life testing of solar absorber surface durability, *Solar Energy Materials and Solar Cells* 61 (2000), 239-253.

[248] Köhl, M. Durability of solar energy materials, *Renewable Energy* 24 (2001), 597-607.

[249] Köhl, M., Carlsson, B., Jorgensen, G., Czanderna, A.W. editors. Performance and durability assessment: Optical materials for solar thermal systems, 1st ed., *Elsevier Ltd.*, (2004).

[250] Roos, A. Use of an integrating sphere in solar energy research, *Solar Energy Materials and Solar Cells* 30 (1993), 77-94.

[251] Roos, A. Chapter 2.1 - Optical properties and measurements. In: Köhl, M., Carlsson, B., Jorgensen, G., Czanderna, A.W., editors. Performance and durability assessment. 1st ed., *Elsevier, Amsterdam*, (2004), 19-55.

[252] Roos, A., Ribbing, C.G., Bergkvist, M. Errors in integrating sphere measurements due to sphere geometry and sample texture. In: M. G. Hutchins, editor. *Solar Optical Materials, Pergamon, Oxford, UK,* (1988), 143-150.

[253] Gindele, K., Köhl, M., Mast, M. Spectral reflectance measurements using an integrating sphere in the infrared, *Applied Optics* 24 (1985), 1757-1760.

[254] Jokinen, J., Keinonen, J., Tikkanen, P., Kuronen, A., Ahlgren, T., Nordlund, K. Comparison of TOF-ERDA and nuclear resonance reaction techniques for range profile measurements of keV energy implants, *Nuclear Instruments and Methods in Physics Research Section B: Beam Interactions with Materials and Atoms* 119 (1996), 533-542.

[255] Ziegler, J.F., Biersack, J.P., Littmark, U. editors. The stopping and range of ions in matter, 1st ed., *Pergamon Press., New York, USA,* (1985).

[256] Lynch, D.W. and Hunter, W.R. An introduction to the data for several metals. In: Palik, E.D., editor. Handbook of optical constants of solids II. *Ebook, Academic Press., USA,* (1997), 341-419.

[257] Ribbing, C.G. and Roos, A. Copper oxides (Cu_2O, CuO). In: Palik, E.D., editor. Handbook of optical constants of solids II. 1st ed., *Academic Press, Burlington, USA,* (1991), 875-882.

[258] Lynch, D.W. and Hunter, W.R. Introduction to the data for several metals. In: Palik, E.D., editor. Handbook of optical constants of solids III. *Ebook, Academic Press., USA,* (1998), 233-286.

[259] Palik, E.D. editor. Handbook of optical constants in solids, *Ebook, Academic Press., USA,* (1991).

[260] Bruggeman, D.A.G. Berechnung verschiedener physikalischer Konstanten von heterogenen Substanzen, *Annalen der Physik* 25 (1935), 636-679.

[261] Niklasson, G.A., Granqvist, C.G., Hunderi, O. Effective medium models for the optical properties of inhomogeneous materials, *Applied Optics* 20 (1981), 26-30.

[262] Granqvist, C.G. Optical properties of cermet materials, *Journal de Physique* C1 (1981), 247-284.

[263] Quinn, J.J. and Yi, K.S. Free electron theory of metals. In: Quinn, J.J. and Yi, K.S., editors. Solid state physics. XIV ed., Springer, Berlin, Germany (2009), 79-107.

[264] Sha, C.H. and Lee, C.C. Microstructure and surface treatment of 304 stainless steel for electronic packaging, *Journal of Electronic Packaging* 133 (2011), 021005-1-021005-4.

[265] Peng, X., Yan, J., Zhou, Y., Wang, F. Effect of grain refinement on the resistance of 304 stainless steel to breakaway oxidation in wet air, *Acta Materialia* 53 (2005), 5079-5088.

[266] Movchan, B.A. and Demchishin, A.V. Study of the structure and properties of thick vacuum condensates of nickel, titanium, tungsten, aluminium oxide and zirconium dioxide, *Physics of Metals and Metallography* 28 (1969), 83-90.

[267] Lampert, C.M. and Washburn, J. Microstructure of a black chrome solar selective absorber, *Solar Energy Materials* 1 (1979), 81-92.

[268] Ding, D., Cai, W., Long, M., Wu, H., Wu, Y. Optical, structural and thermal characteristics of Cu–$CuAl_2O_4$ hybrids deposited in anodic aluminum oxide as selective solar absorber, *Solar Energy Materials and Solar Cells* 94 (2010), 1578-1581.

[269] Wäckelgård, E. Characterization of black nickel solar absorber coatings electroplated in a nickel chlorine aqueous solution, *Solar Energy Materials and Solar Cells* 56 (1998), 35-44.

[270] Gampp, R., Oelhafen, P., Gantenbein, P., Brunold, S., Frei, U. Accelerated aging tests of chromium containing amorphous hydrogenated carbon coatings for solar collectors, *Solar Energy Materials and Solar Cells* 54 (1998), 369-377.

[271] Mizohata, K. Progress in elastic recoil detection analysis. Academic dissertation. *University of Helsinki*. *Helsinki, Finland,* (2012).

[272] Vuoristo, P., Mäntylä, T., Kettunen, P. Adhesion and structure of rf-sputtered magnesium oxide coatings on various metal substrates, *Journal of Vacuum Science & Technology A* 4 (1986), 2932-2937.

[273] Young, D. editor. High temperature oxidation and corrosion of metals, 1st ed., *Elsevier, Great Britain,* (2008), 1-592.

[274] Stierle, A. and Zabel, H. Kinetics of Cr_2O_3 growth during the oxidation of Cr(110), *Europhysics Letters* 37 (1997), 365-370.

[275] Kacsich, T., Lieb, K.P., Schaper, A., Schulte, O. Oxidation of thin chromium nitride films: kinetics and morphology, *Journal of Physics: Condensed Matter* 8 (1996), 10703-10719.

[276] Otani, Y. and Hofmann, S. High temperature oxidation behaviour of $(Ti_{1-x}Cr_x)N$ coatings, *Thin Solid Films* 287 (1996), 188-192.

[277] Hones, P., Zakri, C., Schmid, P.E., Lévy, F., Shojaei, O.R. Oxidation resistance of protective coatings studied by spectroscopic ellipsometry, *Applied Physics Letters* 76 (2000), 3194-3196.

[278] Bateni, M.R., Mirdamadi, S., Ashrafizadeh, F., Szpunar, J.A., Drew, R.A.L. Oxidation behaviour of titanium coated copper substrate, *Surface and Coatings Technology* 139 (2001), 192-199.

[279] Baukal, C.E.J. editor. Oxygen-enhanced combustion, 2nd ed., *CRC Press, Taylor & Francis Group, Boca Raton, Florida, USA,* (2013), 1-792.

[280] Tylecote, R.F. The oxidation of copper at 350 °C-900 °C in air, *Journal of the Institute of Metals* 78 (1950), 327-50.

[281] Knotek, O., Löffler, F., Krämer, G. Multicomponent and multilayer physically vapour deposited coatings for cutting tools, *Surface and Coatings Technology* 54–55 (1992), 241-248.

[282] Uchi, H., Kanno, T., Alwitt, R.S. Structural features of crystalline anodic alumina films, *Journal of the electrochemical sosiety* 148 (2001), B17-B32.

[283] Hickmott, T.W. Electrolyte effects on charge, polarization, and conduction in thin anodic Al_2O_3 films. I. Initial charge and temperature-dependent polarization, *Journal of Applied Physics* 102 (2007), 093706-1-093706-1.

[284] Hakimizad, A., Raeissi, K., Ashrafizadeh, F. Characterization of aluminum anodized layers modified in sulfuric and phosphoric acid baths and their effect on conventional electrolytic coloring, *Surface and Coatings Technology* 206 (2012), 2438-2445.

[285] Wang, X. and Han, G. Fabrication and characterization of anodic aluminum oxide template, *Microelectronic Engineering* 66 (2003), 166-170.

[286] Kim, Y., Kim, C., Kim, P., Yi, J. Effect of preparation conditions on the phase transformation of mesoporous alumina, *Journal of Non-Crystalline Solids* 351 (2005), 550-556.

[287] Gustavsen, A. and Berdahl, P. Spectral emissivity of anodized aluminum and the thermal transmittance of aluminum window frames, *Nordic Journal of Building Physics* 3 (2003), 1-12.

[288] Thornton, J.A. The microstructure of sputter-deposited coatings, *The Journal of Vacuum Science and Technology A* 4 (1986), 3059-3065.

[289] Boström, T., Wäckelgård, E., Westin, G. Solution-chemical derived nickel–alumina coatings for thermal solar absorbers, *Solar Energy* 74 (2003), 497-503.

[290] Vacuum Engineering & Materials Co., Inc. Thin film evaporation guide. Available at: http://www.vem-co.com. Accessed (15.10.2013).

[291] Hones, P., Diserens, M., Lévy, F. Characterization of sputter-deposited chromium oxide thin films, *Surface and Coatings Technology* 120-121 (1999), 277-283.

[292] Bertrand, G., Savall, C., Meunier, C. Properties of reactively RF magnetron-sputtered chromium nitride coatings, *Surface and Coatings Technology* 96 (1997), 323-329.

[293] Cunha, L., Andritschky, M., Pischow, K., Wang, Z., Zarychta, A., Miranda, A.S., Cunha, A.M. Performance of chromium nitride based coatings under plastic processing conditions, *Surface and Coatings Technology* 133–134 (2000), 61-67.

[294] Chekour, L., Nouveau, C., Chala, A., Labidi, C., Rouag, N., Djouadi, M.A. Growth mechanism for chromium nitride films deposited by magnetron and triode sputtering methods, *Surface and Coatings Technology* 200 (2005), 241-244.

[295] Mandich, N.V. and Snyder, D.L. Electrodeposition of chromium. In: Schlesinger, M. and Paunovic, M., editors. Modern Electroplating. 5th ed., *John Wiley & Sons, Inc., New Jersey, USA* (2010), 205-248.

[296] Zakrzewska, K. Nonstoichiometry in TiO_{2-y} studied by ion beam methods and photoelectron spectroscopy, *Advances in Materials Science and Engineering* 2012 (2012), 1-13.

[297] Deniz, D. Texture evolution in metal nitride (aluminum nitride, titanium nitride, hafnium nitride) thin films prepared by off-normal incidence reactive magnetron sputtering. Dissertation. *University of New Hampshire*. *USA*, (2008), 1-159.

[298] Patsalas, P., Charitidis, C., Logothetidis, S. The effect of substrate temperature and biasing on the mechanical properties and structure of sputtered titanium nitride thin films, *Surface and Coatings Technology* 125 (2000), 335-340.

[299] Popović, M., Novaković, M., Traverse, A., Zhang, K., Bibić, N., Hofsäss, H., Lieb, K.P. Modifications of reactively sputtered titanium nitride films by argon and vanadium ion implantation: Microstructural and opto-electric properties, *Thin Solid Films* 531 (2013), 189-196.

[300] Yamazaki, T., Okumura, H., Jin, C., Nakayama, A., Kikuta, T., Nakatani, N. Effect of density and thickness on H_2-gas sensing property of sputtered SnO_2 films, *Vacuum* 77 (2005), 237-243.

[301] Jin, C., Yamazaki, T., Ito, K., Kikuta, T., Nakatani, N. H_2S sensing property of porous SnO_2 sputtered films coated with various doping films, *Vacuum* 80 (2006), 723-725.

[302] Wang, X., Masumoto, H., Someno, Y., Hirai, T. Microstructure and optical properties of amorphous TiO_2-SiO_2 composite films synthesized by helicon plasma sputtering, *Thin Solid Films* 338 (1999), 105-109.

[303] Jeong, S., Kim, J., Kim, B., Shim, S., Lee, B. Characterization of SiO_2 and TiO_2 films prepared using rf magnetron sputtering and their application to anti-reflection coating, *Vacuum* 76 (2004), 507-515.

[304] Toshinari, Y., Tomoyasu, F., Yanbai, S., Chengji, J., Toshio, K., Noriyuki, N. Effective surface area of SnO_2-sputtered films evaluated by measurement of physical adsorption isotherms, *Japanese Journal of Applied Physics* 45 (2006), 9180-9184.

[305] Franssila, S. Part II: Materials. In: Franssila, S., editor. Introduction to microfabrication. 1st ed., *John Wiley & Sons, Ltd., England* (2004), 33-90.

[306] Jiang, H., Michette, A., Pfauntsch, S., Wang, Z., Zhu, J., Li, D. Determination of the evolution of layer thickness errors and interfacial imperfections in ultrathin sputtered Cr/C multilayers using high-resolution transmission electron microscopy, *Optics express* 19 (2011), 11815-11824.

[307] Kwon, K.W., Lee, H.J., Ryu, C., Sinclair, R. Characteristics of Ta as an underlayer for Cu interconnects, *Advanced metallization for ULSI applications* 14 (1998), 711-716.

[308] Colgan, E.G. and Mayer, J.W. Thin-film reactions of Al with Co, Cr, Mo, Ta, Ti, and W, *Journal of Materials Research* 4 (1989), 815-820.

[309] Smith, D.Y., Shiles, E., Inokuti, M. The optical properties of metallic aluminum. In: Edward D. Palik, editor. Handbook of Optical Constants of Solids. 1st ed., *Academic Press, Burlington, USA,* (1997), 369-406.

[310] Chen, C.-Y. and Hwang, W.-S. Effect of annealing on the interfacial structure of aluminum-copper joints, *Materials Transactions* 48 (2007), 1938-1947.

[311] Gambelunghe, A., Piccinini, R., Ambrogi, M., Villarini, M., Moretti, M., Marchetti, C., Abbritti, G., Muzi, G. Primary DNA damage in chrome-plating workers, *Toxicology* 188 (2003), 187-195.

[312] Wu, F.Y., Wu, W.Y., Kuo, H.W., Liu, C.S., Wang, R.Y., Lai, J.S. Effect of genotoxic exposure to chromium among electroplating workers in Taiwan, *Science of The Total Environment* 279 (2001), 21-28.

[313] Dhal, B., Thatoi, H.N., Das, N.N., Pandey, B.D. Chemical and microbial remediation of hexavalent chromium from contaminated soil and mining/metallurgical solid waste: A review, *Journal of Hazardous Materials* 250–251 (2013), 272-291.

Tampereen teknillinen yliopisto
PL 527
33101 Tampere

Tampere University of Technology
P.O.B. 527
FI-33101 Tampere, Finland

ISBN 978-952-15-3313-6
ISSN 1459-2045